

Electronic Thesis and Dissertation Repository

4-13-2022 11:00 AM

Effect of Structural Nonlinearities on Flutter of Cable-Supported Bridges

Sébastien Maheux, *The University of Western Ontario*

Supervisor: El Damatty, Ashraf, *The University of Western Ontario*

Co-Supervisor: King, J. Peter C., *The University of Western Ontario*

A thesis submitted in partial fulfillment of the requirements for the Doctor of Philosophy degree in Civil and Environmental Engineering

© Sébastien Maheux 2022

Follow this and additional works at: <https://ir.lib.uwo.ca/etd>



Part of the [Civil Engineering Commons](#), and the [Structural Engineering Commons](#)

Recommended Citation

Maheux, Sébastien, "Effect of Structural Nonlinearities on Flutter of Cable-Supported Bridges" (2022). *Electronic Thesis and Dissertation Repository*. 8460.
<https://ir.lib.uwo.ca/etd/8460>

This Dissertation/Thesis is brought to you for free and open access by Scholarship@Western. It has been accepted for inclusion in Electronic Thesis and Dissertation Repository by an authorized administrator of Scholarship@Western. For more information, please contact wlsadmin@uwo.ca.

Abstract

It is well known that cable-supported bridges, like suspension bridges and cable-stayed bridges, are structures that are highly sensitive to wind. This is why there has been an important research effort over the past decades on aeroelastic instability phenomena in bridges like flutter. This has allowed the safe design of long-span bridges with respect to wind effects. Nonetheless, the analysis methods that have become the norm in the field of bridge engineering, such as flutter analysis and wind tunnel tests, rely on some simplifications to facilitate analysis. For example, they assume a linear structural behavior of the bridge structure. Therefore, this research project aims at developing a better understanding of the effect of structural nonlinearities on the wind stability of these bridges. To do so, a new experimental approach able to account for structural nonlinearities of bridges is elaborated for wind tunnel tests. First, a numerical method based on large-displacement finite element analysis is developed to characterize the nonlinear structural behavior of cable-supported bridges. The research focuses on geometric nonlinearities, which are more of a concern for these bridges. It is found that single-span suspension bridges behave more nonlinearly. Secondly, it is shown that the nonlinear behavior obtained from the numerical method can be scaled to be utilized for dynamic section model tests in the wind tunnel that account for the nonlinear structural behavior of the bridge. This led to the development of a springing system able to mechanically reproduce this nonlinear behavior in the wind tunnel. A new experimental apparatus for section model tests was designed and fabricated for this purpose. This section model test rig was utilized at the Boundary Layer Wind Tunnel Laboratory (BLWTL) of the University of Western Ontario. This proved the possibility of accounting for structural nonlinearities when conducting dynamic section model tests. It is demonstrated that structural nonlinearities have an effect on the dynamic response as well as on the critical velocity for flutter. This research project therefore provides to bridge designers an effective tool for the assessment of the influence of structural nonlinearities on the aeroelastic stability of cable-supported bridges.

Keywords

Cable-supported bridge, Suspension bridge, Structural nonlinearities, Geometric nonlinearities, Bridge aeroelasticity, Section model tests, Instabilities, Flutter.

Summary for Lay Audience

Cable-supported bridges, such as suspension bridges and cable-stayed bridges, are commonly used in our modern road networks for the crossing of major obstacles. These structures can be very long, and it is not uncommon to have bridges spanning distances over 1 km. These bridges are therefore very flexible, what makes them vulnerable to wind actions. In order to ensure the safety of such long bridges, engineers utilize techniques that can be either run on a computer using a numerical representation of a bridge or performed in a wind tunnel using scale models of bridges. The stability of bridges when subjected to wind is one of the main concerns for which engineers have utilized these methods. The approaches rely on some simplifications that ease their utilization, especially pertaining to how the bridge structure behaves. Consequently, this project aims at developing a new approach for studying the stability of bridges for which the structural behavior is modeled accurately. At first, a numerical approach is elaborated to characterize with good accuracy the behavior of cable-supported bridges. Then, the results of this new numerical techniques were utilized for the development of a new method for testing bridges in the wind tunnel. By comparing it to typical wind tunnel tests for bridges, this new innovative wind tunnel test approach is utilized to demonstrate the effect of accounting for an accurate bridge structural behavior on the stability of bridges. It is believed that this research will eventually lead to safer bridge designs against wind.

Co-Authorship Statement

This thesis has been prepared in accordance with the regulations for an integrated-article format thesis as stipulated by the School of Graduate and Postdoctoral Studies at the University of Western Ontario. The co-authorship statements for the research chapters in this thesis are given below.

Chapter 3 – Nonlinear Structural Vertical-Torsional Coupling

The development of the numerical approach presented in this chapter as well as its computer implementation were made by S. Maheux. Similarly, the finite element models of cable-supported bridges were elaborated by him. S. Maheux ran the analyses and processed the results. The initial and final versions of chapter 3 were written by S. Maheux. The roles of Prof. A. El Damatty, Dr. J. P. C. King and Prof. F. Brancaeloni included supervision and reviewing of the initial and final versions of the chapter. This chapter was published in the peer-reviewed journal *Engineering Structures*:

S. Maheux, J. P. C. King, A. El Damatty, and F. Brancaeloni, “Assessment of nonlinear structural vertical-torsional coupling in cable-supported bridges,” *Engineering Structures*, vol. 219, p. 110800, 2020.

Chapter 4 – Theory for Nonlinear Section Model Tests

The development and validation of the theory presented in this chapter were made by S. Maheux. Result analysis and writing were conducted by S. Maheux. Prof. A. El Damatty, Dr. J. P. C. King and Prof. F. Brancaeloni supervised the research and provided feedback to S. Maheux on the manuscript of this chapter.

A journal paper co-authored by S. Maheux, J. P. C. King, A. El Damatty and F. Brancaeloni and entitled “Theory for nonlinear section model tests in the wind tunnel for cable-supported bridges” has been submitted to *Engineering Structures*, a peer-reviewed journal (submission on August 13, 2021).

Chapter 5 – Design of Test Rig for Nonlinear Section Model Tests

S. Maheux elaborated the idea for a mechanical device required for nonlinear section model tests of bridges. He also developed the mathematical procedure to determine the configuration of the mechanical device to be utilized for nonlinear section model tests. S. Maheux designed a new experimental rig to be used for nonlinear section model tests, which

was fabricated by the University Machine Services (UMS) of the University of Western Ontario under the supervision of S. Maheux. This chapter was completely written by S. Maheux. Prof. A. El Damatty, Dr. J. P. C. King and Prof. F. Brancaeloni supervised the work and provided comments on the initial and final versions of the manuscript.

A journal paper co-authored by S. Maheux, J. P. C. King, A. El Damatty and F. Brancaeloni and entitled “Design of test rig for nonlinear section model tests in the wind tunnel for cable-supported bridges” will be submitted to the peer-reviewed journal *Engineering Structures*.

Chapter 6 – Nonlinear Section Model Tests

S. Maheux conducted the section model tests at the Boundary Layer Wind Tunnel Laboratory (BLWTL) of the University of Western Ontario. This was done with the assistance of the staff members of the BLWTL. The wind tunnel tests results were processed and analyzed by S. Maheux. The initial and final versions of this chapter were prepared by S. Maheux with feedback from Prof. A. El Damatty, Dr. J. P. C. King and Prof. F. Brancaeloni. Supervision was also provided by Prof. A. El Damatty, Dr. J. P. C. King and Prof. F. Brancaeloni.

A journal paper co-authored by S. Maheux, J. P. C. King, A. El Damatty and F. Brancaeloni and entitled “Nonlinear section model tests in the wind tunnel for cable-supported bridges” will be submitted to the peer-reviewed journal *Engineering Structures*.

Appendix B – Nonlinear Structural Coupling for Non-Analogous Modes

Numerical analyses included in this appendix were performed by S. Maheux, and result processing was also conducted by him. The manuscript in its initial and final versions were prepared by S. Maheux. The roles of Prof. A. El Damatty, Dr. J. P. C. King and Prof. F. Brancaeloni included supervision and reviewing the manuscript.

A conference paper co-authored by S. Maheux, J. P. C. King, A. El Damatty and F. Brancaeloni and entitled “Nonlinear coupling in cable-supported bridges for non-analogous modes” has been submitted to the *IABSE Congress Nanjing 2022* organized by the International Association for Bridge and Structural Engineering (submission on March 1, 2022).

Appendix C – Validation of New Experimental Bridge Rig

The wind tunnel results presented in this chapter were obtained by S. Maheux. The first half of the results were measured during S. Maheux’s master’s research at the *Université de Sherbrooke*. With the assistance of the staff members of the BLWTL, S. Maheux measured the second half of the wind tunnel results at the BLWTL of the University of Western Ontario.

Dr. M. AbuGazia helped with 10 % of the wind tunnel tests at the BLWTL. Processing and analysis of the wind tunnel results were carried out by S. Maheux. Additionally, S. Maheux prepared the initial and final versions of this appendix. The roles of Prof. A. El Damatty, Dr. J. P. C. King and Prof. F. Brancaeloni included supervision and reviewing the different versions of this appendix.

A conference paper co-authored by S. Maheux, J. P. C. King, A. El Damatty, F. Brancaeloni and M. AbuGazia and entitled “Comparison of wind tunnel results for the development of a new section model test rig for bridges” has been submitted to the *CSCE 2022 Annual Conference* organized by the Canadian Society for Civil Engineering (submission on April 16, 2022).

Les recherches connues sur les lois du choc et de la résistance des fluides n'offrent pas les moyens d'apprécier, avec l'exactitude qui serait à désirer, l'action des vents sur les ponts suspendus.

–Claude-Louis Navier, 1830

Acknowledgments

It would not have been possible for me to successfully complete my Ph.D. journey without the help, support and contribution of many individuals. First and foremost, I would like to extend my sincere gratitude to my supervisors, Prof. Ashraf El Damatty and Dr. J. Peter C. King, who have always been supportive, understanding and available for me. I am also grateful to them for giving me such freedom in the realization of my Ph.D. project and for letting me work on a subject for which I have a genuine passion, i.e., cable-supported bridge engineering. I would like to thank them for supporting me throughout my research internships in Italy, England and Vancouver. I feel lucky to have had the opportunity to spend almost 20 % of my Ph.D. away from campus so that I could collaborate with the best engineers in my field. I also recognize the chance I have had to work with Dr. J. Peter C. King to perpetuate the tradition of excellence in bridge innovation carried by Prof. Alan Davenport and Dr. King for so many years at the University of Western Ontario. Thank you Peter for volunteering some of your time to my Ph.D. project. It has been greatly appreciated, and your immense experience and knowledge of the field of bridge aeroelasticity have been valuable to keep me on the right track.

Additionally, this research project would not have been possible without the financial support of the Natural Sciences and Engineering Research Council of Canada (NSERC), the *Fonds de recherche du Québec - Nature et technologies* (FRQNT), the *ministère des Transports du Québec* (MTQ), the Boundary Layer Wind Tunnel Laboratory (BLWTL) at the University of Western Ontario, the Faculty of Engineering at the University of Western Ontario, Mitacs, COWI North America and the Mensa Canada Scholarship Programme. I also want to thank Compute Ontario and Compute Canada for providing some of the computational resources used for this project.

Aside from my supervisors, I am very grateful to another of my mentors, Prof. Fabio Brancaleoni, who has been an unofficial supervisor for the last three years of my Ph.D. project. I would like to thank him for hosting me for two research internships at E.D.In., an engineering firm he founded in Rome. Your guidance regarding the structural design of cable-supported bridges has definitely contributed to the success I have had with my research. I would also like to thank the engineers at E.D.In. for their help and hospitality, especially my close friends, Mr. Andrea Del Vecchio and Mr. Francesco Caiulo, who have been very supportive. I would also like to acknowledge Prof. Achille Paolone from the *Sapienza Università di Roma* for acting as a co-host for my second internship in Rome. It is worth mentioning that, if it had not been of the late Prof. Giovanni Solari for connecting me

with Prof. Brancaleoni, my research internships in Italy would not have happened. I want to thank him for this as well as for inviting me to visit him at the *Università degli di Studi di Genova* in 2019. From the same university, I also have to thank Dr. Stefano Brusco for his support and friendship.

I would like to acknowledge the contribution of many individuals from the different offices of COWI around the world. From COWI Denmark, I want to thank Dr. Allan Larsen for taking the time in the early stages of my project to discuss my research and provide me with the structural data of an existing suspension bridge. I am also grateful to Mr. David MacKenzie and Mr. Ian Firth for hosting me for one month in the summer of 2019 at COWI UK's office in London, England. I would like to thank the engineers at COWI UK, especially Mr. Daniel Green for his help with my research. At COWI North America in North Vancouver, I am very grateful to Dr. Hisham Ibrahim and Ms. Anne-Marie Langlois for being part of my research project through a partnership between COWI North America and Mitacs.

Additionally, I must acknowledge the extraordinary support I have received for my wind tunnel tests from the staff members at the Boundary Layer Wind Tunnel Laboratory (BLWTL) of the University of Western Ontario. My thanks go to Mr. Peter Case, Mr. Darren Garnham, Dr. Lingzhe Kong, Mr. Anthony Burggraaf and Mr. Andrew Klazinga. For the fabrication of a new section model test rig utilized in this research, I want to acknowledge the University Machine Services (UMS) at the University of Western Ontario, especially Mr. Ian J. Vinkenvleugel.

For providing me with one of the bridge models utilized for this research project, I am grateful to Prof. Sébastien Langlois of the *Université de Sherbrooke*, my master's supervisor. For his support and giving me my first opportunity to work on cable-supported bridges as an undergraduate research student, I would also like to thank Dr. Frédéric Légeron, my master's co-supervisor. For encouraging me to be more active within the International Association for Bridge and Structural Engineering (IABSE), I would like to thank Prof. F. Michael Bartlett. I would also like to say thank you to my graduate student colleagues at the University of Western Ontario, especially Dr. Mohamed AbuGazia, Mr. Wesam AbdElhamid Mohamed, Mr. Chu Peng and Dr. Ahmed Shehata.

Finally, I want to express my deepest gratitude to my parents, Richard Maheux and Lorraine Lachance, as well as my brother, Marc-Antoine Maheux, for their unconditional support, encouragements, and patience throughout my Ph.D. journey. Allision Loveridge, I would like to thank you for your encouragement and for supporting me with everything ranging from reviewing my writings to helping me with my wind tunnel tests. Thank you for your love

and for having been my number one fan in the last laps of this endurance race that has been my Ph.D. thesis.

Table of Contents

Abstract	ii
Summary for Lay Audience	iii
Co-Authorship Statement	iv
Acknowledgments	viii
Table of Contents	xi
List of Tables	xvi
List of Figures	xviii
List of Appendices	xxii
List of Abbreviations	xxiii
List of Symbols	xxiv
Preface	xxix
1 Introduction	1
1.1 Context	1
1.2 Definition of Research Project	3
1.3 Objectives of Research Project	4
1.4 Original Contributions	4
1.5 Thesis Structure	5
1.5.1 Nonlinear Structural Vertical-Torsional Coupling	5
1.5.2 Theory for Nonlinear Section Model Tests	6
1.5.3 Design of Test Rig for Nonlinear Section Model Tests	6
1.5.4 Nonlinear Section Model Tests	6
1.5.5 Appendices	7
2 Literature Review	8
2.1 Aerodynamic and Aeroelastic Phenomena	8
2.1.1 Static Phenomena	8
2.1.2 Dynamic Phenomena	9

2.2	Wind Tunnel Tests	10
2.2.1	Dimensional Analysis and Similitude	10
2.2.2	Full-Aeroelastic Model Tests	12
2.2.3	Section Model Tests	13
2.2.4	Other Wind Tunnel Test Approaches	15
2.2.5	Computational Fluid Dynamics (CFD)	16
2.3	Force Modeling for Flutter Analysis	16
2.3.1	Linear Approaches	16
2.3.2	Aerodynamic Nonlinearities	17
2.3.3	Nonlinear Approaches	18
2.4	Flutter Analysis	19
2.4.1	Modeling Approaches	19
2.4.2	Nonlinear Flutter Analysis	21
2.5	Structural Nonlinearities in Long-Span Bridges	22
2.6	Summary on Flutter and Structural Nonlinearities	23
3	Nonlinear Structural Vertical-Torsional Coupling	25
3.1	Introduction	25
3.2	Nonlinear Generalized Stiffness	27
3.2.1	One-Mode Analysis	28
3.2.2	Two-Mode Analysis for Vertical and Torsional Modes	31
3.2.3	Verification of Nonlinear Distortion for \mathbf{u}_{nl}	32
3.2.4	Calculation of Derivatives in $\tilde{\mathbf{K}}_{V\theta}^t$	32
3.2.5	Generalization for More Than Two Modes	34
3.3	Numerical Models of Cable-Supported Bridges	35
3.3.1	Modeling Approach of Suspension Bridges	36
3.3.2	Modeling Approach of Cable-Stayed Bridges	38
3.4	Reference Displacements for Nonlinear Generalized Stiffness Parameters	38
3.5	Results for Nonlinear Generalized Stiffness Analysis	41
3.5.1	Effect of Mean Aerodynamic Loads	42
3.5.2	Effect of Hydraulic Buffers	43
3.5.3	One-Mode Analysis of Suspension Bridges	43
3.5.4	One-Mode Analysis of Cable-Stayed Bridges	43
3.5.5	Two-Mode Analysis of Suspension Bridges	45
3.5.6	Two-Mode Analysis of Cable-Stayed Bridges	47
3.5.7	Effect of Lateral Modes on Vertical-Torsional Coupling	51

3.6	Discussion	53
3.6.1	Influence of Mean Aerodynamic Loads and Buffers on Nonlinear Generalized Stiffness Parameters	53
3.6.2	One-Mode Analysis of Suspension Bridges	53
3.6.3	One-Mode Analysis of Cable-Stayed Bridges	57
3.6.4	Nonlinear Vertical-Torsional Coupling in Suspension Bridges	58
3.6.5	Nonlinear Vertical-Torsional Coupling in Cable-Stayed Bridges	59
3.6.6	Suspension Bridges vs Cable-Stayed Bridges	60
3.6.7	Nonlinear Generalized Stiffness Parameters and Stability of Cable-Supported Bridges	60
3.7	Conclusions	61
4	Theory for Nonlinear Section Model Tests	63
4.1	Introduction	63
4.2	Section Model Tests for Assessing the Effect of Structural Nonlinearities	67
4.2.1	Why Section Model Tests Over Other Testing Approaches?	67
4.2.2	Role of Section Model Tests in Bridge Design and Research	68
4.2.3	Structural Nonlinearities vs Aerodynamic Nonlinearities	69
4.3	Nonlinear Generalized Stiffness	70
4.3.1	Overview of Numerical Approach	71
4.3.2	Numerical Models of Cable-Supported Bridges	74
4.3.3	Results for Two-Mode Analysis of Single-Span Suspension Bridges	75
4.4	Theory for Nonlinear Section Model Tests	79
4.4.1	Modal Equations of Full Bridge	79
4.4.2	Generalized Aerodynamic Forces	82
4.4.3	Full-Bridge Dynamic Equations for a Nonlinear Two-Mode Aeroelastic System	87
4.4.4	Nonlinear Dynamic Equations of Full-Scale Section Model	88
4.4.5	Effective Distributed Mass	89
4.4.6	Different Mode Normalization for Full-Bridge Dynamic Equations	90
4.4.7	Discussion on Nonlinear Modal Dynamic Problem	93
4.4.8	Scaling of Nonlinear Generalized Stiffness Parameters	94
4.5	Validation of Assumptions Used in the Theory for Nonlinear Section Model Tests	96
4.5.1	Full-Bridge Mean Wind Response	96
4.5.2	Comparison for Effective Distributed Mass	98

4.5.3	Shape Similarity for Vertical and Torsional Modes	102
4.5.4	Mean Wind Response from Section Model Tests	104
4.5.5	Buffeting Force Vector	106
4.6	Example and Discussion on Scaled Nonlinear Generalized Behavior	109
4.6.1	Example of Scaled Nonlinear Generalized Behavior for Bridge SU4c	109
4.6.2	Comparison Between Linear and Nonlinear Cases for Bridge SU4c .	110
4.6.3	Implications of Nonlinear Structural Behavior on Testing Procedure	111
4.7	Conclusions	113
5	Design of Test Rig for Nonlinear Section Model Tests	115
5.1	Introduction	115
5.2	Scaled Nonlinear Generalized Structural Behavior	117
5.2.1	Nonlinear Generalized Stiffness	119
5.2.2	Mode Correction Factors for Nonlinear Generalized Stiffness	122
5.2.3	Effective Distributed Mass	123
5.2.4	Scaling of Nonlinear Generalized Stiffness	124
5.3	Springing System for Nonlinear Section Model Tests	125
5.3.1	Target Scaled Properties for Inclined Spring System	125
5.3.2	Resultant Forces for Inclined Spring System	127
5.3.3	Prestressing of Inclined Spring System	129
5.3.4	Fitting Procedure for Nonlinear Spring Configuration	130
5.4	Steps for Determining Test Parameters for Nonlinear Section Model Tests .	131
5.5	Nonlinear Spring Configurations for Single-Span Suspension Bridges	133
5.6	Discussion on Requirements Needed for a Nonlinear Section Model Test Rig	137
5.7	Design of New Section Model Test Rig	138
5.8	Conclusions	142
6	Nonlinear Section Model Tests	145
6.1	Introduction	145
6.2	Overview of Theory for Nonlinear Section Model Tests	148
6.2.1	Nonlinear Generalized Stiffness	149
6.2.2	Mode Correction Factors	150
6.2.3	Effective Distributed Mass Properties	151
6.2.4	Scaled Nonlinear Generalized Stiffness Behavior	151
6.3	Experimental Apparatus for Nonlinear Section Model Tests	152
6.3.1	Calibration Procedure for Nonlinear Spring Configuration	152
6.3.2	Description of Nonlinear Section Model Test Rig	154

6.4	Experimental Program	156
6.4.1	Boundary Layer Wind Tunnel Laboratory at the University of Western Ontario	156
6.4.2	Bridge Section Models	156
6.4.3	Validation of Nonlinear Section Model Test Rig	157
6.4.4	Linear Section Model Tests	158
6.4.5	Nonlinear Section Model Tests	159
6.5	Results	162
6.5.1	Static Aerodynamic Coefficients	162
6.5.2	Old Bridge Rig vs New Bridge Rig for Linear Tests	163
6.5.3	Structural Behavior for Nonlinear Section Model Tests	166
6.5.4	Mean and Peak Displacements for Dynamic Tests	166
6.5.5	Linear and Nonlinear Dynamic Responses When Flutter Is Reached	172
6.6	Discussion	176
6.6.1	Static Aerodynamic Coefficients of Bridge Section Models	176
6.6.2	Validity of the New Section Model Test Rig	176
6.6.3	Process of Conducting Nonlinear Section Model Tests	177
6.6.4	Linear Dynamic Tests vs Nonlinear Dynamic Tests	177
6.7	Conclusions	180
7	Conclusion	182
7.1	Summary	182
7.2	Contributions	184
7.3	Recommendations for Future Work	185
	Bibliography	187
	Appendices	204
	Curriculum Vitae	270

List of Tables

3.1	Description of cable-supported bridges	36
3.2	Description of finite element models of cable-supported bridges	37
3.3	Midspan displacements under mean wind loads at 60 m/s	40
3.4	Reference displacements for the presentation of nonlinear generalized stiffness parameters	41
4.1	Description of cable-supported bridges	75
4.2	Description of finite element models of single-span suspension bridges	76
4.3	Midspan displacements under mean aerodynamic loads at high wind speed for an angle of attack of 0°	97
4.4	Comparison of effective distributed mass properties (first symmetric vertical-torsional modal pair)	100
4.5	Comparison of mode correction factors (first symmetric vertical-torsional modal pair)	103
5.1	Description of cable-supported bridges	133
6.1	Description of cable-supported bridges	157
6.2	Full-scale test parameters for section model tests	159
6.3	Flutter wind speeds for linear and nonlinear tests (full scale)	169
A.1	General information for suspension bridge SU1	208
A.2	Natural frequencies and mode shapes for suspension bridge SU1	210
A.3	General information for suspension bridge SU2	211
A.4	Natural frequencies and mode shapes for suspension bridge SU2	213
A.5	General information for suspension bridge SU3a	214
A.6	Natural frequencies and mode shapes for suspension bridge SU3a	216
A.7	General information for suspension bridge SU3b	217
A.8	Natural frequencies and mode shapes for suspension bridge SU3b	219
A.9	General information for suspension bridge SU3c	220
A.10	Natural frequencies and mode shapes for suspension bridge SU3c	222
A.11	General information for suspension bridge SU4a	223
A.12	Natural frequencies and mode shapes for suspension bridge SU4a	225
A.13	General information for suspension bridge SU4b	226
A.14	Natural frequencies and mode shapes for suspension bridge SU4b	228
A.15	General information for suspension bridge SU4c	229

A.16	Natural frequencies and mode shapes for suspension bridge SU4c	231
A.17	General information for suspension bridge SU4d	232
A.18	Natural frequencies and mode shapes for suspension bridge SU4d	234
A.19	General information for cable-stayed bridge CS1	235
A.20	Natural frequencies and mode shapes for cable-stayed bridge CS1	237
A.21	General information for cable-stayed bridge CS2	238
A.22	Natural frequencies and mode shapes for cable-stayed bridge CS2	240
B.1	Description of cable-supported bridges	244
C.1	Full-scale test parameters for dynamic tests of bridge SU2	261

List of Figures

2.1	Typical wind response of a cable-supported bridge	10
2.2	Wind tunnel tests for bridges	11
2.3	Two-dimensional flutter analysis	20
2.4	Fishbone model of a bridge	20
3.1	Normalized generalized displacement grid for two-mode analysis	33
3.2	Midspan displacements under mean wind loads for bridge SU2	39
3.3	Effect of mean aerodynamic loads on one-mode nonlinear generalized stiffnesses of bridges SU1 and SU2	42
3.4	Effect of hydraulic buffers on one-mode nonlinear generalized stiffnesses of bridge SU3b	43
3.5	One-mode nonlinear generalized stiffness analysis of suspension bridges	44
3.6	One-mode nonlinear generalized stiffness analysis of cable-stayed bridges	46
3.7	Two-mode nonlinear generalized stiffness analysis of bridge SU2 for modes VS1 and $\theta S1$	47
3.8	Two-mode nonlinear generalized stiffness analysis of bridge SU3b for modes VS1 and $\theta S1$	48
3.9	Two-mode nonlinear generalized stiffness analysis of bridge SU3b for modes VA1 and $\theta A1$	48
3.10	Comparison of diagonal nonlinear generalized stiffness terms for suspension bridges	49
3.11	Comparison of off-diagonal nonlinear generalized stiffness terms for suspension bridges	50
3.12	Two-mode nonlinear generalized stiffness analysis of bridge CS1 for modes VS1 and $\theta S1$	51
3.13	Comparison of diagonal nonlinear generalized stiffness terms for cable-stayed bridges	52
3.14	Comparison of off-diagonal nonlinear generalized stiffness terms for cable-stayed bridges	52
3.15	Effect of lateral modes on two-mode nonlinear generalized stiffnesses	54
3.16	Hanger and stay cable tensions for one-mode nonlinear generalized stiffness analysis	56
3.17	One-mode nonlinear generalized stiffness for bridges SU3a, SU3b and SU3c (vertical modes)	57

4.1	Dynamic system of a bridge section model	72
4.2	Nonlinear generalized stiffness terms for single-span suspension bridges	77
4.3	Displacements and aerodynamic forces for a bridge deck	83
4.4	Comparison of typical mode shapes for a full bridge and a section model	89
4.5	Midspan displacements under mean aerodynamic loads for bridge SU2	99
4.6	Maximum bridge-deck displacements under mean aerodynamic loads	105
4.7	Bridge-deck displacement profile for mean aerodynamic loads at 60 m/s	105
4.8	Time histories of effective buffeting forces per unit length	108
4.9	Power spectral density of effective buffeting forces per unit length	109
4.10	Scaled nonlinear generalized behavior for bridge SU4c	110
4.11	Analysis of nonlinear behavior for the scaled section model of bridge SU4c . .	112
5.1	Dynamic system of a bridge section model	120
5.2	Comparison of typical mode shapes for a full bridge and a section model	122
5.3	Spring configuration for nonlinear section model tests	126
5.4	Free-body diagram of the nonlinear springing system	129
5.5	Nonlinear spring configurations for the single-span suspension bridges	135
5.6	Comparison between target and spring-modeled scaled nonlinear generalized behavior for bridge SU4c	136
5.7	Comparison between target and spring-modeled scaled nonlinear generalized behavior for bridge SU4d	136
5.8	Three-dimensional model of new section model test rig	138
5.9	Description of new section model test rig	140
5.10	Possible adjustments for the new section model test rig	141
5.11	Mechanism of new section model test rig	142
5.12	Torsion arm of new section model test rig	143
5.13	Air bushing cart of new section model test rig	143
6.1	Spring configuration for nonlinear section model tests	153
6.2	New section model test rig	155
6.3	Bridge models utilized for nonlinear section model tests	157
6.4	Nonlinear spring configurations for the first symmetric modal pairs of the sus- pension bridges	160
6.5	Sign convention for displacements and forces	163
6.6	Static aerodynamic coefficients (turbulent flow)	163
6.7	Flutter derivatives of bridge SU2 (smooth flow)	164

6.8	Linear dynamic response of bridge SU2 for modes VS1 and TS1 and a smooth flow (full scale)	165
6.9	Setup for measuring nonlinear structural behavior	167
6.10	Comparison between target nonlinear behavior and experimental nonlinear behavior	168
6.11	Linear and nonlinear dynamic responses of bridge SU2 for a smooth flow . . .	169
6.12	Linear and nonlinear dynamic responses of bridge SU2 for a turbulent flow . .	170
6.13	Linear and nonlinear dynamic responses of bridge SU4c for a smooth flow . . .	170
6.14	Linear and nonlinear dynamic responses of bridge SU4c for a turbulent flow . .	171
6.15	Linear and nonlinear dynamic responses of bridge SU4d for a smooth flow . . .	171
6.16	Linear and nonlinear dynamic responses of bridge SU4d for a turbulent flow . .	172
6.17	Flutter dynamic response of bridge SU2 for a smooth flow	173
6.18	Flutter dynamic response of bridge SU4c for a smooth flow	174
6.19	Flutter dynamic response of bridge SU4d for a smooth flow	175
A.1	Finite element models of suspension bridge SU1	208
A.2	Pushover analysis for suspension bridge SU1 (w/o buffers)	209
A.3	Finite element models of suspension bridge SU2	211
A.4	Pushover analysis for suspension bridge SU2 (w/o buffers)	212
A.5	Finite element models of suspension bridge SU3a	214
A.6	Pushover analysis for suspension bridge SU3a (w/o buffers)	215
A.7	Finite element models of suspension bridge SU3b	217
A.8	Pushover analysis for suspension bridge SU3b (w/o buffers)	218
A.9	Finite element models of suspension bridge SU3b	220
A.10	Pushover analysis for suspension bridge SU3c (w/o buffers)	221
A.11	Finite element models of suspension bridge SU4a	223
A.12	Pushover analysis for suspension bridge SU4a (w/o buffers)	224
A.13	Finite element models of suspension bridge SU4b	226
A.14	Pushover analysis for suspension bridge SU4b (w/o buffers)	227
A.15	Finite element models of suspension bridge SU4c	229
A.16	Pushover analysis for suspension bridge SU4c (w/o buffers)	230
A.17	Finite element models of suspension bridge SU4d	232
A.18	Pushover analysis for suspension bridge SU4d (w/o buffers)	233
A.19	Finite element models of cable-stayed bridge CS1	235
A.20	Pushover analysis for cable-stayed bridge CS1	236
A.21	Finite element models of cable-stayed bridge CS2	238
A.22	Pushover analysis for cable-stayed bridge CS2 (w/o buffers)	239

B.1	Nonlinear generalized stiffness terms of suspension bridges for analogous vertical and torsional modes	246
B.2	Nonlinear generalized stiffness terms of suspension bridges for non-analogous vertical and torsional modes	248
B.3	Nonlinear generalized stiffness terms of suspension bridges for same-type modes	251
C.1	Section model test rig at the <i>Université de Sherbrooke</i>	257
C.2	Section model test rigs at the Boundary Layer Wind Tunnel Laboratory	258
C.3	Section model of bridge SU2 for $\lambda_L = 1/70$	259
C.4	Section model of bridge SU2 inside the wind tunnels	259
C.5	Static test rig of the Boundary Layer Wind Tunnel Laboratory	260
C.6	Sign convention for displacements and forces	263
C.7	Static aerodynamic coefficients of bridge SU2	264
C.8	Flutter derivatives of bridge SU2 for vertical motion (smooth flow)	265
C.9	Flutter derivatives of bridge SU2 for rotational motion (smooth flow)	266
C.10	Dynamic response of bridge SU2 for modes VS1 and TS1 and a smooth flow (full scale)	267
C.11	Dynamic response of bridge SU2 for modes VS1 and TS1 and a turbulent flow (full scale)	267

List of Appendices

A	Finite Element Models of Cable-Supported Bridges	204
B	Nonlinear Structural Coupling for Non-Analogous Modes	241
C	Validation of New Experimental Bridge Rig	254

List of Abbreviations

BLWTL	Boundary Layer Wind Tunnel Laboratory of the University of Western Ontario
CEVA	Complex eigenvalue analysis
CFD	Computational fluid dynamics
DCM	Distributed cable mass
DOF	Degree of freedom
IABSE	International Association for Bridge and Structural Engineering
LCM	Lumped cable mass
MAC	Modal assurance criterion
PSD	Power spectral density
VIV	Vortex-induced vibration

List of Symbols

A_i	Moment flutter derivatives (non-normalized form)
A_i^*	Moment flutter derivatives (normalized form)
B	Bridge-deck width
C_{L0}	Lift coefficient at an angle of attack of 0°
C'_L	Slope of the lift coefficient
C_{D0}	Drag coefficient at an angle of attack of 0°
C_{M0}	Moment coefficient at an angle of attack of 0°
C'_M	Slope of the lift coefficient
D	Lateral force per unit length applied to the bridge deck
D_{se}	Self-excited drag force per unit length
F_H	Horizontal resultant force of the springing system
F_V	Vertical resultant force of the springing system
F_{sb}	Force in bottom springs
F_{st}	Force in top springs
Fr	Froude number
H_i	Lift force flutter derivatives (non-normalized form)
H_i^*	Lift force flutter derivatives (normalized form)
$J_{V\theta}$	Error function of nonlinear least-squares problem
K	Reduced frequency
\mathbf{K}	Stiffness matrix
\mathbf{K}_G	Geometric stiffness matrix linearized about the dead-load configuration
\mathbf{K}_S	Elastic stiffness matrix linearized about the dead-load configuration
$\tilde{\mathbf{K}}_{V\theta}^t$	Two-mode nonlinear generalized stiffness matrix
$\tilde{\mathbf{K}}_{ij}^t$	Two-mode nonlinear generalized stiffness matrix
$\tilde{\mathbf{K}}_m^t$	Nonlinear generalized stiffness matrix for m selected modes
L	Characteristic dimension
L	Vertical force per unit length applied to the bridge deck
L_b	Buffeting lift force per unit length
L_{br}	Length of the bridge
L_m	Length of the section model
L_s	Mean aerodynamic lift force per unit length
L_{sb}	Initial length of bottom springs
L_{sb}^H	Initial horizontal distance of bottom springs
L_{sb}^V	Initial vertical distance of bottom springs

L_{sbi}	Final length of bottom springs
L_{sbi}^H	Final horizontal distance of bottom springs
L_{sbi}^V	Final vertical distance of bottom springs
L_{se}	Self-excited lift force per unit length
L_{span}	Main span length
L_{st}	Initial length of top springs
L_{st}^H	Initial horizontal distance of top springs
L_{st}^V	Initial vertical distance of top springs
L_{sti}	Final length of top springs
L_{sti}^H	Final horizontal distance of top springs
L_{sti}^V	Final vertical distance of top springs
M	Torsional moment per unit length applied to the bridge deck
M_b	Buffeting moment per unit length
M_s	Mean aerodynamic moment per unit length
M_{se}	Self-excited moment per unit length
M_θ	Resultant moment of the springing system
\overline{M}	Moment per unit length
$\overline{MAC}_{V\theta}$	Modal assurance criterion between one vertical mode and one torsional mode
\overline{MMI}	Mass moment of inertia per unit length
\overline{MMI}_{deck}	Mass moment of inertia per unit length of the bridge deck
\mathbf{M}	Mass matrix
N	Number of samples considered for $J_{V\theta}$
P_i^*	Drag force flutter derivatives (normalized form)
R^2	Uncentered coefficient of determination
Re	Reynolds number
S_{yj}	Power spectral density of vertical displacement or rotation
\overline{S}_{fj}^b	Power spectral density of effective buffeting force or moment per unit length
U	Mean wind speed
U_R	Reduced velocity
U_{cr}	Flutter wind speed
\mathbf{U}_M	Upper-triangular matrix obtained from Cholesky factorization of \mathbf{M}
a_j	Modal load coefficient
a_{sb}	Initial horizontal position of bottom springs
a_{st}	Initial horizontal position of top springs
b_{cl}	Half of the distance between the cables at deck level
d_b	Lever arm of bottom springs

d_t	Lever arm of top springs
f	Frequency
f_j	Natural frequency calculated at the dead-load configuration
f_j^*	Mass-corrected nonlinear restoring vertical force or moment
\bar{f}	Force per unit length
\bar{f}_j	Nonlinear restoring vertical force or moment per unit length
\bar{f}_j^*	Mass-corrected nonlinear restoring vertical force or moment per unit length
\bar{f}_j^b	Effective buffeting force or moment per unit length
\tilde{f}_j	Generalized restoring force
\mathbf{f}_{SG}	Internal force vector of nonlinear geometric structure
g	Gravitational acceleration
h	Vertical displacement
k_j^*	Mass-corrected tangent stiffness
k_{sb}	Stiffness of bottom springs
k_{st}	Stiffness of top springs
\bar{k}_j	Stiffness per unit length
\bar{k}_j^*	Mass-corrected tangent stiffness per unit length
\tilde{k}_j	Linear generalized stiffness
\tilde{k}_j^t	Tangent nonlinear generalized stiffness
m_j^*	Modified effective mass or mass moment of inertia
\bar{m}	Mass per unit length
\bar{m}_{cable}	Mass per unit length for a main cable
\bar{m}_{deck}	Mass per unit length of the bridge deck
\bar{m}_j	Effective mass or mass moment of inertia per unit length
\bar{m}_j^*	Modified effective mass or mass moment of inertia per unit length
\tilde{m}_j	Generalized mass
\tilde{m}_j^*	Modified generalized mass
\mathbf{m}	Diagonal matrix for the mass functions of the different structural elements
p	Horizontal displacement
\tilde{p}_j	Generalized force
\tilde{p}_j^b	Generalized buffeting lift force or moment
\tilde{p}_j^s	Generalized mean aerodynamic lift force or moment
\tilde{p}_j^{se}	Generalized self-excited lift force or moment
\mathbf{p}	External force vector
$\mathbf{p}_{V\theta}$	Modal force vector for two modes
$\mathbf{p}_{V\theta}^m$	Modal force vector for two modes

\mathbf{p}_{ij}	Modal force vector for two modes
\mathbf{p}_j	Modal force vector for one mode
\mathbf{p}_j^m	Modal force vector for one mode
\mathbf{p}_m	Modal force vector for m selected modes
$\tilde{\mathbf{p}}_{V\theta}$	Generalized modal force vector for two modes
$\tilde{\mathbf{p}}_m$	Generalized modal force vector for m selected modes
s	Dimensionless time
s_j	Curved coordinate for generalized force of mode j
t	Time
u	Lateral wind fluctuations
u_y	Lateral displacement
u_z	Vertical displacement
\mathbf{u}	Displacement vector
\mathbf{u}_{deck}	Displacement vector containing displacement functions of the deck
\mathbf{u}_{nl}	Nonlinear displacement vector
w	Vertical wind fluctuations
x	Position along the bridge deck
y_j	Displacement or rotation of section model
y_j^d	Dynamic displacement or rotation of section model
y_j^s	Static displacement or rotation of section model
z_j	Generalized displacement
z_j^d	Dynamic generalized displacement for mode j
z_j^s	Static generalized displacement for mode j
\mathbf{z}	Generalized displacement vector
Γ_j^k	Mode correction factor for the generalized restoring force
Γ_{j2}^k	Mode correction factor for the generalized mass
ΔL_{sbi}	Elongation of bottom springs
ΔL_{sb}^p	Displacement prestress of bottom springs
ΔL_{sti}	Elongation of top springs
ΔL_{st}^p	Displacement prestress of top springs
Φ	Modal matrix
α	Torsional rotation
α_s	Angle of attack
α_s	Static rotation of the bridge deck
β_j	Mode correction factor for the generalized displacement
θ_x	Torsional rotation

λ_L	Geometric scale
λ_U	Velocity scale
λ_f	Frequency scale
μ	Dynamic viscosity of air
ξ	Damping ratio
ξ_j	Damping ratio of mode j
ρ	Density of air
$\sigma_{V\theta}$	Standard error of the regression
σ_{yj}^2	Variance of vertical displacement or rotation
ϕ	Küssner function
ϕ_{Jk}	Buffeting indicial function
Φ_j	Mode shape vector calculated at the dead-load configuration
χ_{Jk}	Aerodynamic admittance function
\mathcal{X}_j	Deck displacement vector in direction j for mode j
ω	Angular frequency of oscillation
ω_j	Natural angular frequency calculated at the dead-load configuration
ψ_j^k	Modal function of the bridge deck in direction k for mode j
$\psi_j^{k,cable}$	Modal function of the cables in direction k for mode j
Ψ_j	Vector containing the modal functions for the deck displacements
Ψ_j^{all}	Vector of the modal functions for the displacements of all structural elements
$[\]'$	Derivative with respect to function variable
$[\]\dot{\ }$	Time derivative
$[\]^T$	Transpose of matrix or vector

Preface

Being raised in a small town that is home of the *Pont Perrault*, the second longest covered bridge in Canada, I believe that it was meant for me to study and work in the field of bridge engineering. Not too far away at about 100 km northwest of this covered bridge can be found two major structures that have kept impressing me by their sheer size and beauty. The first one, the *Pont de Québec*, will certainly always fascinate me with its history and for having the world's longest span for a cantilever bridge. The other structure is the *Pont Pierre-Laporte*, the longest suspension bridge in Canada. Its elegance that originates from the slenderness and apparent lightness of its suspension system was the triggering point for my interest in cable-supported bridges, which are undoubtedly the “sexiest” bridges ever built.

Unknowingly in 2010, I began my civil engineering studies at the *Université de Sherbrooke*, where one of the only researchers in Canada specialized in cable-supported bridges was professor at the time. His name is Dr. Frédéric Légeron, and in 2012, he gave me my first chance to work on such bridges when I was an undergraduate researcher. This brought me to do a master's about the aeroelastic stability of long-span bridges. Inevitably, this also led me to write this Ph.D. thesis on the same subject at the University of Western Ontario. My Ph.D. experience has brought me even closer to my little boy's dream of designing cable-supported bridges.

Being at the junction of structural engineering, bridge engineering and wind engineering, the research presented in this thesis is relevant to any bridge engineers, wind engineers and researchers interested in very long cable-supported bridges, either suspension bridges or cable-stayed bridges. More specifically, anyone with experience with nonlinear analysis of cable-supported bridges, bridge aeroelasticity and wind tunnel testing of bridges should find information and conclusions of interest in this Ph.D. thesis.

Chapter 1

Introduction

1.1 Context

Cable-supported bridges, like suspension bridges and cable-stayed bridges, are important elements of our modern transportation networks that have developed over the years. Due to the great distances that cable-supported bridges can span, they are utilized for the crossing of major obstacles such as rivers, fjords and valleys. This is made possible, technically and economically, by the inherent lightness of cable structures as these structures provide an effective utilization of material. This is explained by the fact that these bridges mostly carry loads using cables, which are good in tension, the most effective way for a structural element to resist an external force. The use of cables in long-span bridges and their slenderness, originating from their length, make them very flexible. From this fact, cable-supported bridges are quite effective at resisting earthquakes. Conversely, their flexibility makes them sensitive to the actions of wind. From being able to span great distances, these structures are usually located in open locations where strong winds are often encountered. Consequently, it is of paramount importance to account for wind effects in the design of the complex structures that are cable-supported bridges.

Early in the development of modern suspension bridges at the beginning of the 1800s, it was clear that long-span bridges were seen as complex structures. Engineers relied on empirical approaches and experience for their design as accurate design methods were not available [1]. This had inevitably led to collapses of many early suspension bridges mainly due to brittle material, overloading and dynamic wind actions. In the 1820s, Claude-Louis Navier, a famous French engineer mostly known for the Navier-Stokes equations, was mandated to study the suspension bridge system after the failure of the *Pont des Invalides*, crossing the River Seine in Paris [2]. In his report to the *Direction générale des Ponts et Chaussées et des mines*, Navier was the first to develop a mathematical model for suspension bridges, more specifically for the unstiffened suspension bridge. However, at the time, the equations of his model could not be utilized for the purpose of designing a modern suspension bridge having a stiffening girder, i.e., a stiffened suspension bridge. It is worth mentioning that, in his report [2], Navier recommends that cable-stayed bridges should be avoided. He made this recommendation based on the numerous collapses as well as on the observation that this structural system cannot be calculated using the mathematical tools available at that time.

Because of Navier's recommendation, it was needed to wait until the 1950s before seeing modern cable-stayed bridges being built again.

Additionally, in his report [2], Navier mentions that the analytical approaches that had been available for the analysis of suspension bridges could not account for the complicated dynamic actions of wind. This is why, until almost the end of the 1800s, the design of suspension bridges had been done through experience. For example, John A. Roebling designed the Brooklyn Bridge, which opened in 1883, using simplified calculations and physical scale models [3]. It is only towards the end of the nineteenth century with the development of the elastic theory and deflection theory of suspension bridges that analytical design approaches became predominant [4]. At the beginning of the twentieth century, the adoption of the deflection theory, originally developed by Josef Melan and made available for design purposes by David B. Steinman [5], had led to a rapid increase in span length and slenderness for cable-supported bridges. This is when dynamic wind oscillations started to be encountered again in suspension bridges. Unlike their predecessors who had relied on empirical rules and experience, the engineers of this era had used analytical methods, and they had somehow been overconfident of their designs determined by analysis. This was especially the case with regard to dynamic wind effects as only static wind forces were considered at the time [3]. The George Washington Bridge, designed by Othmar Ammann, was one of those wind-sensitive bridges.

After modifying the deflection theory to include the effect of horizontal wind forces, Leon S. Moisseiff showed that the main cables in a suspension bridge contribute to the lateral stiffness of a bridge and help resist horizontal wind loads [6]. This had led to a further increase in slenderness that culminated with the Tacoma Narrows Bridge. It is well known that, during its short life, the Tacoma Narrows Bridge had experienced dynamic vertical oscillations for being too flexible and having an H-shaped bridge-deck cross section prone to wind-generated vortices. The Tacoma Narrows Bridges eventually collapsed in 1940 due to torsional flutter [7, 8]. This led Prof. F. Burt Farquharson to develop modern wind tunnel testing approaches for long-span bridges as he was involved in the engineering investigation for Tacoma [9]. As a result, wind tunnel tests have then been utilized in the design process of cable-supported bridges.

Since the collapse of Tacoma, important research efforts have been dedicated to understanding dynamic wind effects in cable-supported bridges. Nowadays, the standard approaches for checking the dynamic response of bridges under turbulent wind originate from the frequency-domain buffeting theory developed by Prof. Alan G. Davenport [10]. Regarding aeroelastic stability, the flutter derivative technique originally elaborated by Prof. Robert H.

Scanlan [11] is still central to the analytical techniques utilized to predict flutter, an instability phenomenon characterized by large dynamic oscillations and caused by aerodynamic self-excited forces. These analytical techniques and wind tunnel approaches have made possible the safe construction of long suspension bridges, like the Great Belt Bridge [12] and Akashi Kaikyo Bridge [13], as well as long cable-stayed bridges, like the *Pont de Normandie* [14] and Russky Bridge [15]. Now, even longer spans are possible by using vented-box girders made out of multiple longitudinal boxes with airfoil-shaped cross sections that are interconnected with crossbeams, an idea of William C. Brown. The bridge deck of the Çanakkale Bridge [16], the longest suspension bridge in the world with a main span of 2023 m, is an example as it is equipped with a twin-box girder. A triple-box girder was considered for the Messina Strait Bridge, which, with a main span of 3300 m, is the longest proposed suspension bridge for which a detailed design exists [17].

As discussed in the previous paragraph, main spans for cable-supported bridges are getting longer, which makes the issue of aeroelastic stability even more important in order to ensure safe and reliable bridge structures for the public. The analytical approaches and wind tunnel techniques utilized nowadays in bridge engineering assume a linear behavior for cable-supported bridges. This appears reasonable for most cable-supported bridges, but this might be inappropriate for bridges with very long main spans. This is because very long-span bridges are intrinsically nonlinear due to their cable system as it is known that the cable system dominates the structural behavior of a bridge for longer spans [17]. Considering that cables have a greater influence on the structural behavior in the case of very long cable-supported bridges, it seems reasonable to think that their aeroelastic stability could be impacted, and such nonlinear effects should be accounted for in the prediction of instabilities in the case of very long bridges.

1.2 Definition of Research Project

Indeed, there is a possibility that a stronger nonlinear behavior in cable-supported bridges has an effect on the predicted critical wind speed for an instability. In other words, the structural nonlinearities in long-span bridges could change the onset of flutter, and neglecting them could lead to erroneous stability predictions in the case of bridges with very long main spans. Not only that the critical velocity could be impacted by structural nonlinearities, but these nonlinearities could trigger nonlinear structural dynamic phenomena that have never been observed in bridges. If such nonlinear dynamic phenomena are possible, it would be relevant to ask whether they could interact with aerodynamic and aeroelastic effects.

Similar to what happened when dynamic wind actions were not considered in the design of suspension bridges, instability predictions for long-span bridges are currently carried out without including structural nonlinearities. Therefore, this doctoral research project aims at providing an assessment of the effect of structural nonlinearities on flutter instability of long cable-supported bridges. This research focuses on geometric nonlinearities, which are more of a concern for long cable-supported bridges. This project begins with an assessment of structural nonlinearities in cable-supported bridges using numerical analysis in order to find bridges that are more critical to nonlinear effects. From there, it is believed that an experimental approach is the most convenient way to assess the effect of structural nonlinearities due to the difficulty to analytically represent aerodynamic forces involved in flutter for large bridge-deck amplitudes of vibration. Consequently, following theoretical developments for a new experimental approach in the wind tunnel able to account for structural nonlinearities, it is required to develop a new experimental apparatus for this new method. By testing bridges that exhibit a stronger nonlinear behavior using this experimental approach, it will be possible to determine whether the aeroelastic stability of cable-supported bridges can be impacted by structural nonlinearities.

1.3 Objectives of Research Project

This research project has four main objectives which are as follows:

1. Quantify structural nonlinearities in cable-supported bridges in terms of dynamic properties using nonlinear finite element analysis;
2. Develop the theory required to account for structural nonlinearities when conducting wind tunnel tests of bridges;
3. Design an experimental apparatus for wind tunnel tests of bridges able to represent the nonlinear structural behavior of a cable-supported bridge;
4. Conduct nonlinear wind tunnel tests in order to study the effect of structural nonlinearities on the aeroelastic stability of cable-supported bridges experimentally.

1.4 Original Contributions

From this research project, six original contributions will be produced:

1. Numerical approach to quantify structural nonlinearities in cable-supported bridges;

2. Assessment of structural nonlinearities for suspension bridges and cable-stayed bridges of various span lengths;
3. Theoretical approach for section model tests in the wind tunnel for cable-supported bridges able to account for the nonlinear structural behavior;
4. Numerical method for the calibration of a mechanical device for nonlinear section model tests able to model the nonlinear structural behavior of a cable-supported bridge;
5. Experimental rig for nonlinear section model tests in the wind tunnel for cable-supported bridges;
6. Assessment of the influence of structural nonlinearities on the aeroelastic stability of long-span bridges using nonlinear section model tests.

1.5 Thesis Structure

This integrated-article format thesis is comprised of a literature review chapter, four main research chapters, a concluding chapter and three appendices. In chapter 2, a literature review pertaining to this research project is made in order to demonstrate the gap in knowledge with respect to the effect of structural nonlinearities on the aeroelastic stability of bridges.

1.5.1 Nonlinear Structural Vertical-Torsional Coupling

Chapter 3 presents a preliminary investigation of structural nonlinearities in long-span bridges, more specifically for nonlinear vertical-torsional coupling. This is done using a simplified practical approach. The approach relies on nonlinear pushover analyses that are conducted for the geometrically nonlinear finite element models of five suspension bridges and two cable-stayed bridges. This approach allows determining the nonlinear stiffness parameters of equivalent systems having between one and three degrees of freedom (lateral, vertical and torsional). It provides an effective method to determine bridges that are more nonlinear and are likely more critical for their flutter response to be impacted by the nonlinear structural behavior. Since the proposed technique relies on the modes of vibration and can account for the interaction between the vertical and torsional effects, it can also be used to judge which ones of the bridges considered are the most susceptible to nonlinear mode coupling under wind loads.

1.5.2 Theory for Nonlinear Section Model Tests

Chapter 4 presents the theoretical developments for a new type of section model test for bridges that accounts for geometric nonlinearities of the bridge structure. This theory for nonlinear section model tests starts from two-mode nonlinear generalized stiffness parameters obtained using nonlinear pushover analysis, which need to be scaled using a specifically developed procedure. Using eleven numerical models of cable-supported bridges (nine suspension bridges and two cable-stayed bridges), the assumptions made in the theory for nonlinear tests are then validated. The proposed scaling procedure is also tested.

1.5.3 Design of Test Rig for Nonlinear Section Model Tests

Chapter 5 discusses the development of a new experimental apparatus for nonlinear section model tests that will allow studying the interaction between nonlinear structural effects and aeroelastic effects. After reviewing the theoretical developments for nonlinear section model tests, a numerical procedure to determine the parameters of a mechanical system able to model the nonlinear structural behavior for section model tests is developed. The procedure was tested for four single-span suspension bridges with main spans ranging from 1.2 km to 3.0 km. Following a discussion on the characteristics needed for a nonlinear section model test rig, a design of such a test rig is briefly presented.

1.5.4 Nonlinear Section Model Tests

Chapter 6 presents an experimental assessment of the effect of structural nonlinearities on the aeroelastic stability and wind response of cable-supported bridges. This is achieved by using nonlinear section model tests, which account for the nonlinear structural behavior of the bridge under consideration. First, the theoretical developments required for nonlinear section model tests of bridges are briefly reviewed. Then, the experimental apparatus utilized for nonlinear wind tunnel tests is described, which includes a short description of the calibration procedure used for the mechanical device required for nonlinear tests. Three different suspension bridge configurations are tested. The first is for a single-box girder suspension bridge, and the second and third are for two twin-box girder suspension bridges having different span lengths. By comparing the results of linear tests to those of nonlinear tests, it is possible to assess the effect of structural nonlinearities.

1.5.5 Appendices

Following the concluding chapter, where the main conclusions and recommendations are discussed, can be found three appendices in which additional information regarding this project is given. Firstly, a detailed description is presented in appendix A for the eleven cable-supported bridges utilized for this research as well as for the corresponding finite element models. Secondly, appendix B discusses an assessment of nonlinear structural vertical-torsional coupling for non-analogous modes of vibration in suspension bridges. This is done in order to validate that nonlinear structural coupling in cable-supported bridges is stronger in the case of analogous modes, therefore confirming that an assessment of the effect of structural nonlinearities on the aeroelastic stability of bridges should focus on analogous modes. Lastly, the validation of the new experimental rig for section model tests is presented in appendix C. This is achieved by comparing wind tunnel test results for the existing experimental rig to those of the new one.

Chapter 2

Literature Review

The main function of bridge decks in suspension bridges and cable-stayed bridges is to carry the gravity loads from vehicles, which are eventually transferred to the ground through the tower foundations and abutments. This is achieved through a cable system. As mentioned before, the efficiency of cable systems allows cable-supported bridges to span great distances, but it has the inconvenience of making these structures sensitive to wind actions due to their flexibility. Considering that they are often located where high winds can be encountered, it is therefore of paramount importance to adequately study the aerodynamic and aeroelastic behavior of cable-supported bridges.

2.1 Aerodynamic and Aeroelastic Phenomena

Obviously, the bridge deck of a cable-supported bridge is one of the critical structural elements with regard to the actions of wind. This is why it is important to characterize aerodynamic forces caused by wind on it. It is of common practice to separate the actions of wind on bridge decks into three components: mean aerodynamic forces or static forces, buffeting forces and self-excited forces. Buffeting forces correspond to forces relative to wind fluctuations, whereas self-excited forces are aerodynamic forces associated with the motion of the bridge deck. It is worth noting that this separation of wind effects on bridge decks is relevant for linear aerodynamic force models as individual aerodynamic effects are not as easily distinguishable in the case of nonlinear force models. Mean aerodynamic forces, buffeting forces and self-excited forces need to be accounted for in the assessment of the dynamic response of a bridge subjected to turbulent wind, i.e., the buffeting response. These aerodynamic forces induce straining actions in a bridge, but they can also lead to other static and dynamic phenomena, especially instabilities.

2.1.1 Static Phenomena

Static instabilities due to wind in bridges are phenomena that are analogous to column buckling. Such instability happens when the effective stiffness, the cumulative effect of structural stiffness and aerodynamic stiffness, of a bridge becomes nil. Any further increase of the mean aerodynamic forces will therefore lead to very large bridge-deck displacements and likely to bridge collapse. This phenomenon is referred to as an aerostatic instability

[18–20]. This instability happens due to the variation of the mean aerodynamic forces with the angle of attack. A special case of aerostatic instability is torsional divergence, which occurs when any additional static torsional moment is greater than what can be resisted by the torsional stiffness of the bridge [21].

2.1.2 Dynamic Phenomena

The dynamic phenomena of greater concern for the decks of cable-supported bridges are vortex-induced vibration (VIV), galloping and flutter. VIVs are caused by forces associated with the periodic shedding of vortices on a structural element like a bridge deck. Resonance occurs when the shedding frequency of vortices is close to one of the natural frequencies of the bridge [21]. In the vicinity of the natural frequencies, the bridge-deck motion causes the airflow to interact vigorously with the structure. Consequently, vortex shedding synchronizes with the vibrational frequency of the bridge deck. In this case, the shedding of vortices is governed by the bridge-deck movement. This phenomenon is known as lock-in. Because the amplitudes of motion are limited for VIVs in bridges, they are unlikely to lead to bridge collapse, but they can cause fatigue problems [22].

Galloping is an aeroelastic instability that produces bridge-deck vibrations of large amplitudes mainly in a direction perpendicular to the mean wind flow [22]. The phenomenon is caused by the interaction between the airflow and the motion of the bridge deck. This instability is not typical of long cable-supported bridges as its critical wind speed is typically much more than the one for flutter.

Flutter is an aeroelastic instability characterized by large amplitudes of motion caused by the extraction of oscillatory energy by the bridge deck from the airflow it is subjected to [23]. Flutter can therefore be described as a self-excited instability. In the case of bridges, torsional flutter and coupled flutter are the most common types of flutter [22]. Torsional flutter involves one torsional mode of vibration causing large torsional rotations of the bridge deck, whereas coupled flutter involves the aeroelastic coupling of one vertical mode of vibration and one torsional mode. If a bridge is subjected to wind with a speed greater than or equal to its critical flutter wind speed, this will result in major structural damage and even bridge collapse.

Typically, bridge decks experience VIVs over a small range of relatively low wind speeds as illustrated in fig. 2.1 [24]. Passed this range of wind speeds, buffeting of the bridge deck is the phenomenon of importance until the wind speed is high enough to trigger a divergent-type instability like an aerostatic instability, galloping or flutter. Typically, flutter

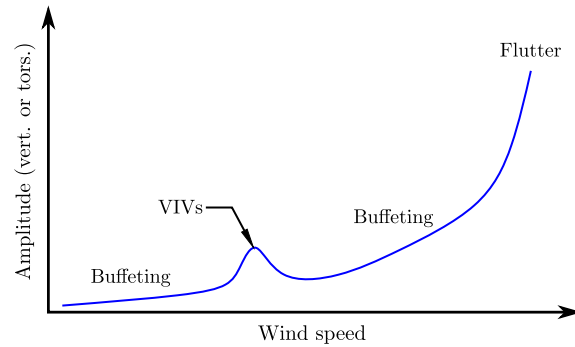


Figure 2.1: Typical wind response of a cable-supported bridge

is the critical phenomenon since its critical wind speed is usually less than those for an aerostatic instability and galloping. Due to the large amplitudes of vibration in the vicinity of the flutter wind speed, structural nonlinearities could impact the flutter behavior of a bridge.

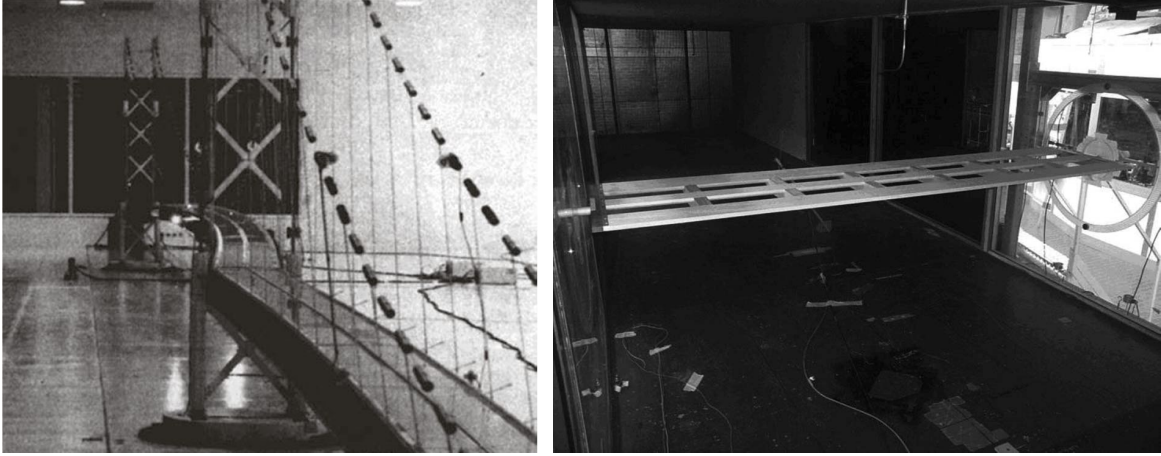
For this reason, the following sections in this literature review chapter will focus on flutter and structural nonlinearities in cable-supported bridges. The tools utilized for flutter analysis and their recent evolution are discussed. Section 2.2 quickly reviews wind tunnel testing techniques with an emphasis on flutter and structural nonlinearities. Then, a discussion regarding the force modeling of self-excited forces, which are utilized in flutter analysis approaches is presented in section 2.3. In section 2.4, flutter analysis procedures for bridges are discussed. Finally, a discussion on structural nonlinearities in cable-supported bridges is presented in section 2.5.

2.2 Wind Tunnel Tests

The use of wind tunnel tests played an important role in the investigation of the collapse of the Tacoma Narrows Bridge [9, 25]. Since this bridge collapse, wind tunnel tests have been an essential tool for bridge engineers in the design of cable-supported bridges. His involvement with the Tacoma Narrows Bridge had led Prof. F. Burt Farquharson, one of the pioneers for wind tunnel testing of bridges, to develop the two most common types of wind tunnel tests, which are full-aeroelastic model tests and section model tests [9]. Examples of these types of tests are presented in fig. 2.2.

2.2.1 Dimensional Analysis and Similitude

For practical reasons, wind tunnel tests are conducted on scale models of cable-supported bridges. It is therefore required to satisfy similitude requirements based on dimensional anal-



(a) Full-aeroelastic model [26]

(b) Section model [27]

Figure 2.2: Wind tunnel tests for bridges

ysis so that wind tunnel test results are representative of the full-scale bridge. Consequently, aerodynamic and structural parameters must be scaled appropriately.

Scaling Parameters

Since air at atmospheric pressure is typically utilized in wind tunnel tests [21], the density scale λ_ρ is unity. According to [21], the geometric scale λ_L , velocity scale λ_U and frequency scale λ_f are expressed as:

$$\lambda_L = \frac{L_m}{L_p} \quad \lambda_U = \frac{U_m}{U_p} \quad \lambda_f = \frac{f_m}{f_p} \quad (2.1)$$

where subscript m refers to the model; subscript p refers to the prototype or full-scale bridge; L is a characteristic dimension; U is the mean wind speed; f is the frequency. To account for the effect of time appropriately, dimensional analysis dictates that the reduced frequency similitude (or Strouhal number similitude) must be satisfied [21]. The reduced frequency similitude is expressed mathematically as:

$$\left(\frac{L_m f_m}{U_m} \right) = \left(\frac{L_p f_p}{U_p} \right) \quad (2.2)$$

From eq. 2.2, it is concluded that $\lambda_f = \lambda_U / \lambda_L$. When gravity effects are important for the dynamic behavior of a bridge, e.g., in the case of a full-aeroelastic model of a suspension bridge, it is required to satisfy the Froude number similitude, with the Froude number defined as:

$$Fr = \frac{U^2}{Lg} \quad (2.3)$$

where Fr is the Froude number; g is the gravitational acceleration. When the Froude number similitude is respected, it can be demonstrated that $\lambda_U = \sqrt{\lambda_L}$ and $\lambda_f = 1/\sqrt{\lambda_L}$. Additionally, it is worth mentioning that it is not possible to meet the Reynolds number similitude for wind tunnel tests satisfying the Froude number similitude [21]. In the Reynolds number similitude, the Reynolds number is defined as:

$$Re = \frac{\rho UL}{\mu} \quad (2.4)$$

where Re is the Reynolds number; ρ is the density of air; μ is the dynamic viscosity of air. The violation of the Reynolds number is typical for wind tunnel tests of bridges. To minimize the effect of this violation, the scale model should be as large as possible [22].

Structural Parameters

Similarly, the structural parameters of the prototype bridge, such as the mass, mass moment of inertia and damping ratio, must be scaled. Therefore, the following equations must be satisfied [22]:

$$\frac{\bar{m}_m}{\bar{m}_r} = \lambda_L^2 \quad \frac{\overline{MMI}_m}{\overline{MMI}_r} = \lambda_L^4 \quad \frac{\xi_m}{\xi_r} = 1 \quad (2.5)$$

where \bar{m} is the mass per unit length; \overline{MMI} is the mass moment of inertia per unit length; ξ is the damping ratio. Similar equations can be derived for the stiffness parameters (axial, bending and torsional). It is also possible to derive scaling equations for the force per unit length \bar{f} and moment per unit length \bar{M} [28]:

$$\frac{\bar{f}_m}{\bar{f}_r} = \lambda_U^2 \lambda_L \quad \frac{\bar{M}_m}{\bar{M}_r} = \lambda_U^2 \lambda_L^2 \quad (2.6)$$

2.2.2 Full-Aeroelastic Model Tests

Full-aeroelastic model tests are performed using a scale model of the entire bridge that includes the most important structural elements like the towers, bridge deck and cable system [29]. The scale model required for these tests is flexible and can reproduce the most

important modes of vibration of the bridge prototype. The calibration of a full-aeroelastic model is made using a finite element model of the bridge prototype [22]. As shown in fig. 2.2a for the model of the Akashi KaiKyo Bridge, a full-aeroelastic model stands on the floor of the wind tunnel. For these tests, the bridge model can be subjected to a smooth flow or a turbulent atmospheric boundary layer flow. They are able to account for three-dimensional effects of the flow conditions and modes of vibration. These tests are utilized for obtaining the dynamic response of a bridge subjected to wind as well as for assessing its stability. Due to their size and complexity, full-aeroelastic model tests are expensive [21]. This is why they are generally utilized toward the end of the design process of a cable-supported bridge in order to validate its aerodynamic and aeroelastic behavior [22].

As long as the Froude number scaling is satisfied, full-aeroelastic models are able to model geometric nonlinearities of the structure because all the important bridge elements are included and gravity effects are appropriately scaled. However, it should be noted that it is not physically possible for the towers and bridge deck in cable-supported bridges to have the correct scaled axial stiffness at the same time as the correct scaled bending stiffness. For these structural elements, the standard practice is to scale them to match the scaled bending stiffness. It follows that the geometric stiffness is erroneous for these structural elements. Only the geometric stiffness of cables is properly modeled since only the correct scaled axial stiffness is needed for cables as they have negligible bending stiffness. Considering the cost of full-aeroelastic models and the fact that they cannot properly account for geometric nonlinearities in their current form, it appears that full-aeroelastic model tests are not suitable for an initial experimental study on the effect of structural nonlinearities on the aeroelastic stability.

2.2.3 Section Model Tests

Section model tests are performed using a rigid segment of a bridge deck, which is attached to an experimental rig at its ends [30]. An example of a section model is given in fig. 2.2b. For static tests, the section model is attached to a rigid experimental rig equipped with load cells in order to be able to measure the static force coefficients. In the case of dynamic tests, the section model is suspended by a springing system at its ends. Since the stiffness is provided through an external adjustable springing system, the Froude number scaling is not required, and only the reduced frequency similitude has to be met for dynamic section model tests. It is also worth noting that section models can be fabricated at larger scales in comparison to full-aeroelastic models, therefore reducing Reynolds number effects.

Smooth flow or grid-generated turbulent flow can be utilized for section model tests [31].

Typically, only one vertical mode and one torsional mode can be modeled in dynamic section model tests. In some studies [32, 33], a lateral mode has also been included. Moreover to the static force coefficients, section model tests can also be utilized to measure the flutter derivatives [11] and aerodynamic admittance functions [34], measure the wind and motion-induced surface pressures using pressure taps [28, 35], assess the stability [30] and predict the dynamic response of the bridge deck [31]. From this, the versatility of section model tests appears evident. Supplemental to their versatility, their simplicity and relative affordability have made this type of wind tunnel tests the most common approach for testing bridges.

Despite their simplicity, there have been some improvements made to how section model tests are conducted. A dynamometric section model was developed in order to be able to effectively measure the aerodynamic forces [36]. Such a section model is especially interesting for the measurements of flutter derivatives using forced-vibration tests. Since a dynamic movement is imposed to the section model for these tests, using a dynamometric section model makes it easier to differentiate the aerodynamic forces from the inertial forces by minimizing the initial forces that are measured. Additionally, an innovative section model test rig that can be used to study the dynamic response and flutter as well as measure the flutter derivatives using the free- and forced-vibration approaches was developed [33, 37–39]. In [40, 41], another forced-vibration rig is discussed, but its particularity is that it can be used for arbitrary motion. Also, an approach to determine the center of rotation to be used for section model tests is analyzed in [42, 43]. This is especially of interest for bridges exhibiting lateral-torsional modes of vibration like simple suspension bridges often utilized for pedestrians.

Section model tests for bridges assume a linear structural behavior. However, a slight nonlinear structural behavior in torsion for large rotations greater than 15° is observed for the section model test rig in [44–46]. The nonlinear torsional behavior comes from the kinematics of the mechanisms utilized for this section model test rig, and it is consequently not representative of an actual cable-supported bridge. Nevertheless, considering that it allows large amplitudes of vibration, this rig is interesting for studying aerodynamic nonlinearities and nonlinear flutter. Another example of a section model test rig able of large displacements is the one in [47, 48]. As this rig has a linear structural behavior, it is relevant for the study of aerodynamic nonlinearities. In a different civil engineering application of section model tests, a pendulum system is utilized to represent the swaying stiffness of a transmission line conductor [49]. This makes this experimental rig geometrically nonlinear.

Unlike in the field of bridge engineering, there have been different section model test studies accounting for nonlinear structural behavior for airfoils in the field of aeronautics. Different

types of nonlinearities have been tested, which include freeplay nonlinearity [50–53], bilinear behavior [50, 54–56], parabolic behavior [51] and cubic behavior [57, 58]. Among these studies, it should be noted that Schwartz et al. [54] demonstrated that the flutter velocity of an airfoil for a hardening bilinear structural behavior is less than for the linear case. It is worth noting that there was only a difference of 14 % between the two stiffness values of the bilinear system used in [54]. Additionally, for these nonlinear experimental studies on airfoils, it appears that the nonlinear structural behavior utilized for the wind tunnel tests does not seem to have been calibrated with respect to the behavior of actual aircraft structural elements.

The versatility offered by the section model test procedure and its affordability make this testing approach very interesting for an experimental study on the effect of structural nonlinearities on flutter. Indeed, the flexibility offered by the possibility to easily adjust the experimental rig at the ends of the section model could allow accounting for structural nonlinearities. This would be done by developing a nonlinear mechanical device as similarly done in the aeronautics studies discussed at the end of the previous paragraph. However, in this case, a nonlinear structural behavior representative of the prototype bridge would have to be mechanically modeled.

2.2.4 Other Wind Tunnel Test Approaches

Taut-strip models, which are intermediate between section and full-aeroelastic models, are sometimes used [59]. For such models, only the bridge deck is considered, and the stiffness of the model is provided using taut wires or tubes. These tests can reproduce the three-dimensional effects on the bridge deck. However, it would be difficult to consider taut-strip model tests for a study on the effect of structural nonlinearities on flutter. This is because the taut wires or tubes utilized for these tests already possess their own nonlinear behavior, which is likely to be different than the one for a cable-supported bridge.

More recently, a multi-supported aeroelastic model was developed to study VIVs for vertical modes [60], but such an approach is not suitable for assessing flutter. This is because only vertical modes can be properly scaled in such a model since it is only supported along its length with vertical flexible spring supports. Moreover, real-time hybrid tests, similar to what is used in structural engineering, are currently under development [61, 62]. In such tests, the aeroelastic system would be partially modeled in the lab and partially represented in a numerical model. For these hybrid tests, the nonlinear structural behavior could be simulated, but the development of this method is not completed, and once completed, it is likely that such an experimental approach will be expensive and complicated to use.

2.2.5 Computational Fluid Dynamics (CFD)

Because of today's computational capabilities, computational fluid dynamics (CFD) is becoming very interesting for bridge engineering applications (e.g. [63–68]). For example, static coefficients, flutter derivatives, pressure distributions and flow visualization for bridge decks can be obtained using CFD. Nevertheless, CFD results should be validated using wind tunnel tests [22, 26]. Therefore, wind tunnel experiments are still important for the assessment of the aeroelastic stability of bridges.

2.3 Force Modeling for Flutter Analysis

Flutter assessment for bridges requires the study of motion-induced aerodynamic forces, commonly called self-excited forces. In the aeronautical field, theoretical formulations (e.g. [69]) are available while bridge aeroelasticity relies on force models based on experimental coefficients or functions measured using wind tunnel tests or CFD.

2.3.1 Linear Approaches

For flutter analysis, linear formulations of self-excited forces are usually employed. Scanlan's approach based on flutter derivatives [11, 70] is the standard approach for modeling these forces in bridge engineering. Mathematically, Scanlan's approach is expressed as follows:

$$D_{se}(t) = \frac{1}{2}\rho U^2 B \left(KP_1^* \frac{\dot{p}}{U} + KP_2^* \frac{B\dot{\alpha}}{U} + K^2 P_3^* \alpha + K^2 P_4^* \frac{p}{B} + KP_5^* \frac{\dot{h}}{U} + K^2 P_6^* \frac{h}{B} \right) \quad (2.7)$$

$$L_{se}(t) = \frac{1}{2}\rho U^2 B \left(KH_1^* \frac{\dot{h}}{U} + KH_2^* \frac{B\dot{\alpha}}{U} + K^2 H_3^* \alpha + K^2 H_4^* \frac{h}{B} + KH_5^* \frac{\dot{p}}{U} + K^2 H_6^* \frac{p}{B} \right) \quad (2.8)$$

$$M_{se}(t) = \frac{1}{2}\rho U^2 B^2 \left(KA_1^* \frac{\dot{h}}{U} + KA_2^* \frac{B\dot{\alpha}}{U} + K^2 A_3^* \alpha + K^2 A_4^* \frac{h}{B} + KA_5^* \frac{\dot{p}}{U} + K^2 A_6^* \frac{p}{B} \right) \quad (2.9)$$

where $D_{se}(t)$, $L_{se}(t)$ and $M_{se}(t)$ are respectively the self-excited drag force, self-excited lift force and self-excited moment per unit length; t is the time; ρ is the density of air; U is the mean wind speed; B is the bridge-deck width; $K = \omega B/U$ is the reduced frequency; $\omega = 2\pi f$ is the angular frequency of oscillation; P_i^* , H_i^* and A_i^* ($i = 1, \dots, 6$) are the flutter derivatives, which are functions of the reduced velocity $U_R = U/(fB)$; f is the frequency of oscillation; $p = p(t)$, $h = h(t)$ and $\alpha = \alpha(t)$ are the horizontal, vertical and torsional displacements; the overdot denotes the time derivative. This model is utilized in the frequency domain since

the flutter derivatives are frequency dependent. It should be noted that it can only predict the stability limit, i.e., the post-flutter response cannot be obtained. The identification of flutter derivatives is well established. They can either be measured using free-vibration tests [11, 27, 70] or forced-vibration tests [36, 71].

In the time domain, the linearized quasi-steady approach is the simplest model [72]. Unlike Scanlan's formulation, the unsteady effects of the self-excited forces are not considered in this model. Therefore, it is not suitable for the flutter analysis of bridges. To take into account the unsteady effects in the time domain, convolution formulations were proposed. Either the indicial functions [73–75] or rational functions [76–78] could be employed. These functions are usually identified indirectly from the flutter derivatives using a least-squares approach (e.g. [79]). Direct measurement of indicial functions [80] were shown to be possible, but the experimental approach required is complicated. It is worth noting that the identification of such functions may be difficult for bluff deck sections [81]. Additionally, Wu and Kareem [82] mention that neither the indicial function approach nor the rational function approach is superior as both are able to provide reliable flutter predictions.

Equations 2.7–2.9 consider the superposition of the contributions from the different displacement components to the self-excited forces. When used for buffeting analysis, the linear models discussed in this section also assume the superposition of the self-excited forces at different frequencies. For limited amplitudes of motion, it was demonstrated that the superposition holds very well for the self-excited lift force and moment of a single-box girder deck, whereas discrepancies were observed for the drag force due to its small magnitude [83].

2.3.2 Aerodynamic Nonlinearities

The conclusions in [83] indicate that linear self-excited force models are sufficient for buffeting analysis and predicting the stability limit as long as the amplitude of motion is not too large. For larger amplitudes, the self-excited forces behave nonlinearly as demonstrated by the dependence of flutter derivatives with respect to the amplitude of motion [84–91]. Nonlinearities with respect to the frequency of oscillation [87] and the velocity of the bridge deck [38] were also observed. Studies in [92–96] demonstrated the hysteretic behavior of aerodynamic force coefficients when the self-excited effects are included.

Additionally, many experimental studies have been conducted on the nonlinear flutter response of bridges [67, 90, 95, 97–101]. For a typical flutter response, the bridge motion becomes divergent at the critical wind speed. This has been described as hard flutter in

the literature. In comparison, nonlinear flutter behavior is characterized by limit-cycle oscillations, i.e., the amplitude of motion of the bridge deck stabilizes at a specific value for a specific wind speed. The amplitude of motion for the post-flutter response increases gradually as the wind speed is increased. This type of flutter response is qualified as soft flutter. This behavior is caused by the aerodynamic nonlinearities related to the amplitude of motion, especially in rotation.

It is worth noting that these experimental studies have only focused on aerodynamic nonlinearities, and structural nonlinearities have not been discussed. In these studies, structural nonlinearities are only mentioned with regard to verifications that stiffness and damping nonlinearities of the section model test rig are small and negligible compared to aerodynamic nonlinearities [90, 102–104]. It should also be noted that there has never been an experimental assessment considering a nonlinear structural behavior representative of a cable-supported bridge.

2.3.3 Nonlinear Approaches

In order to consider the nonlinearities of self-excited forces, nonlinear force models are required. The simplest nonlinear model is the nonlinear quasi-steady approach [72]. Since it neglects the unsteady effects, more advanced models should be used such as the band superposition method [105–109]. This method separates the evaluation of the aerodynamic forces into low-frequency and high-frequency components. It considers the large amplitude nonlinearities and unsteady effects. For the low-frequency forces, a quasi-steady approach is used to consider the large amplitude effect. For the high-frequency contribution, the forces are evaluated at the low-frequency effective angle of attack employing an unsteady force model (e.g. rational functions or rheological models). This means that the coefficients or functions of the unsteady force model are required at multiple angles of attack, which demands many wind tunnel tests.

Guo et al. [89] and Wu et al. [110] developed nonlinear amplitude-dependent flutter derivatives, which can be used to predict the post-flutter amplitude, but this force model cannot give the time history of the response. Zhang [111] proposed multistage indicial functions to represent amplitude nonlinearities. Being a time-domain model, the time history can be calculated as well as the post-flutter amplitude. Also, nonlinear convolution models relying on Volterra series were proposed for a representation of the self-excited forces in the time domain [112–114] and in the frequency domain [115], but they are advanced models.

A nonlinear approach relying on hysteresis loops of dynamic aerodynamic coefficients, which

include the contribution of self-excited forces, was proposed [116, 117]. Its effectiveness at representing nonlinearities is questionable since it lumps the nonlinear effects from different sources (e.g. large amplitude, turbulence and deck motions) into one single parameter. Additionally, time-domain models using artificial intelligence are presented in [118, 119]. Such models make it difficult to analyze the model parameters, and they have the inconvenience of losing the physical interpretation of the phenomena involved.

Furthermore, a generalized nonlinear aerodynamic force model was developed to predict nonlinear flutter [93, 94, 120]. It accounts for the static aerodynamic effects, dynamic aerodynamic effects caused the motion of the bridge deck, aerodynamic added mass effects and unsteady effects. Its calibration appears to be a challenging process since it is needed to determine over 400 parameters.

In the study of limit-cycle oscillations associated with torsional flutter for bluff bridge-deck sections, Gao et al. [103, 121] came up with an elegant way to model the nonlinear self-excited moment by adding to the flutter derivative approach cubic terms relative to the rotation and rotational velocity of the bridge deck. However, as this mathematical formulation only consider one degree of freedom (DOF), it is only suitable for the study of torsional flutter. Gao et al. [122] reutilized this idea of adding nonlinear contributions to the flutter derivative model, but in this case, accounting for two DOFs, which are the vertical displacement and torsional rotation. By considering two DOFs, it makes the calibration process more difficult in comparison to the one-DOF case.

From this brief overview of the different modeling techniques for the nonlinear aerodynamic forces involved in flutter, it is evident that nonlinear force models to study flutter are more difficult to implement. It should also be noted that this is still a field in development.

2.4 Flutter Analysis

2.4.1 Modeling Approaches

For the flutter analysis of bridges, different modeling approaches are available. As a first estimate, empirical simplified formulas can be employed [123, 124]. For a better understanding of the phenomenon, two-dimensional analysis can be used. In this case, a three-DOF system (horizontal, vertical and torsional) representing the bridge deck is considered (fig. 2.3). However, it is typical to neglect the effect of the lateral displacement and drag force. Dynamic properties of this simplified model are set according to the modes of vibration of the full bridge. Such models are useful to assess the most important aerodynamic

coefficients for flutter. For 2D analysis using the flutter derivatives, a complex eigenvalue analysis (CEVA) [125], the step-by-step approach [126, 127] or the system decoupling approach [128] can be used. For 2D flutter analysis in the time domain, numerical integration is required.

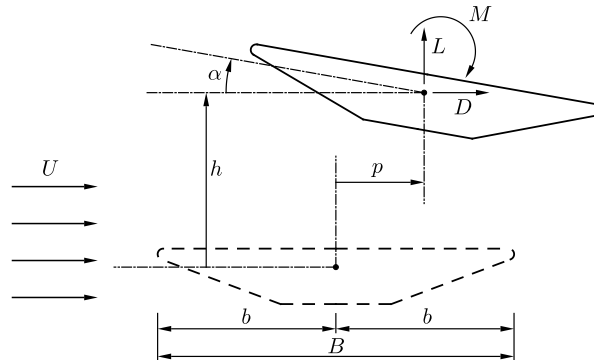


Figure 2.3: Two-dimensional flutter analysis

To consider the structural behavior of the full bridge on flutter, three-dimensional models are needed. For 3D flutter analysis, some researchers have used the finite-strip method [129, 130], but the finite element method is much more common. Using the finite element method, a fishbone model, where the bridge deck is modeled using frame elements connected to the cable system through rigid links (fig. 2.4), is typically employed for flutter analysis (e.g. [131–133]). Using the flutter derivatives, the flutter wind speed can be obtained using two equivalent approaches: CEVA (e.g. [131]) and determinant method (e.g. [134]). It is possible to use a multi-mode analysis [131, 134, 135] or a full-model analysis [136, 137]. The difficulty with the multi-mode method is to decide how many and which modes of the bridge are important for a good flutter prediction. Numerical integration is again used in the time domain [78, 138], which is more computationally intensive than a frequency-domain analysis.

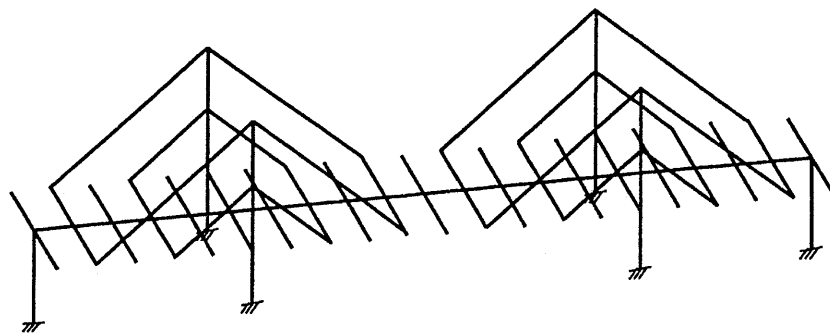


Figure 2.4: Fishbone model of a bridge [130]

2.4.2 Nonlinear Flutter Analysis

Limited studies have been conducted on nonlinear 3D flutter analysis. Chen and Kareem [105] presented flutter analyses using the band superposition method, which means aerodynamic nonlinearities were considered. However, a linear structure was assumed. For the case tested, the effect of aerodynamic nonlinearities on the critical flutter velocity is small. Similarly, a generalized nonlinear aerodynamic force model was utilized for time-domain analysis to study the effect of aerodynamic nonlinearities [93, 94]. Zhang [111] also demonstrated that the effect of aerodynamic nonlinearities on the critical velocity is much less important than the effect of the mean aerodynamic forces, which changes the angle of attack leading to different aerodynamic parameters for the self-excited forces along the bridge deck.

Some analyses have been carried out considering the geometric nonlinearities of the bridge. First, the static equilibrium under the dead loads and mean aerodynamic loads is determined by conducting a nonlinear static analysis. This deformed configuration under static loads is considered for the evaluation of the stiffness matrix (mechanical and geometric contributions) used in the flutter analysis. Then, the flutter analysis can be performed using the flutter derivatives and CEVA [133, 139–141]. Instead, Salvatori and Borri [142] conducted an analysis in the time domain using indicial functions, but the bridge was linearized at the deformed state under static loads. Thus, the previous studies do not consider the geometric nonlinearities in the dynamic analysis of flutter. Using a simplified model of a bridge and indicial functions, Salvatori and Spinelli [143] conducted a flutter analysis taking into account geometric nonlinearities for the static and dynamic analyses. Because of that, the post-flutter response or limit-cycle oscillations can be obtained. Similar results based on finite element analysis were obtained in [111, 144]. Arena et al. [145, 146] presented similar conclusions using a nonlinear continuum formulation of a suspension bridge.

Employing indicial functions, Chobsilprakob et al. [144] carried out a flutter analysis of a suspension bridge considering the geometric and material nonlinearities, but important simplifications were used. The effect of mean wind loads were neglected, and the aerodynamic properties of a rectangular section were assumed for the bridge deck. The initial force applied in the analysis was chosen to ensure an excursion in the material nonlinear range, which is not representative of a real wind event. For these specific conditions, it was shown numerically that the structural nonlinearities decrease the flutter wind speed.

Numerical studies for nonlinear 3D flutter analysis accounting for aerodynamic and structural nonlinearities are difficult due to the fact that the simulation of structural nonlinearities is more adapted to time-domain analysis. However, the nonlinear time-domain aerodynamic

models are more challenging to utilize. It is also worth noting that nonlinear 3D flutter analyses accounting for structural nonlinearities have never been verified experimentally.

2.5 Structural Nonlinearities in Long-Span Bridges

For the analysis of cable-supported bridges, it is important to account for geometric nonlinearities (P- Δ , cable sag and large displacement effects) [147], and to assess the collapse load, material nonlinearities should also be modeled (e.g. [148]). Nevertheless, geometric nonlinearities are more important for long-span bridges due to the fact that their cable systems are designed to remain elastic [149]. For very long cable-supported bridges like the Messina Strait Bridge [17], nonlinear geometric analysis could be utilized for some critical load cases in order to check the static structural performance. Additionally, for slender towers, geometric nonlinearities have a non-negligible effect on the tower moment distributions [149, 150]. Even the nonlinear concrete behavior in the case of concrete towers has an influence on the moment distributions [151]. Another source of nonlinearities in cable-supported bridges comes from the longitudinal hydraulic buffers, whose function is to limit longitudinal deck motions [12, 17, 151].

For the static analysis of cable-stayed bridges for vertical loads, large displacement effects are more important than the other geometric nonlinearities on the behavior of the bridge deck [152]. However, when geometric and material nonlinearities are accounted for, the material nonlinear effects appear first and geometric nonlinearities are small [148], even for a 1400 m cable-stayed span [153]. Similar conclusions were obtained for a cable-stayed suspension bridge subjected to vertical loads [154]. This is explained by the in-plane structural effectiveness of the cable-stayed system [149]. Similarly, Brownjohn [155] showed that the geometric nonlinear effect on the bridge deck is also small in the case of static vertical loads on a suspension bridge. For static wind loads, it has been shown by some researchers that geometric nonlinearities affect the aerostatic stability of cable-stayed and suspension bridges [18–20, 153]. For a suspension bridge having for cross section a stiffening truss, it was demonstrated that material nonlinearities can also affect the aerostatic stability [156]. This is due to the large drag forces on stiffening trusses.

In dynamic analyses, material nonlinearities slightly reduce the response of long-span bridges to earthquakes [157]. For geometric nonlinearities, Brownjohn [155] mentions that they are negligible for common level of dynamic response. However, using continuum formulations, some researchers in mathematics and engineering demonstrated that nonlinear dynamic effects related to the geometric nonlinearities, such as internal resonance, could lead to large

oscillations. For cable-stayed bridges, some researchers were able to simulate a nonlinear interaction between the deck and cables [158–162]. Suspension bridges with inclined main cables are also susceptible to nonlinear dynamic phenomena [163–165]. Furthermore, due to nonlinear dynamic effects, it has been demonstrated that vertical energy in a suspension bridge can be transferred to torsional modes causing large torsional vibrations [166–169]. These large torsional vibrations associated with nonlinear vertical-torsional coupling are possible if a certain energy threshold is respected [169]. Using a continuum model of a narrow 1400 m suspension bridge, Capsoni et al. [170] demonstrated that aeroelastic effects and such resonance can lead to unexpected unstable conditions in specific cases.

It seems that such nonlinear dynamic effects have never been experienced on an actual structure. However, a transition from an antisymmetric instability mode to a symmetric instability mode was observed in the case of a full-aeroelastic model of a double-main-span suspension bridge [171]. According to [172, 173], it would be caused by internal resonance due to the nonlinearities of the aeroelastic system. This phenomenon would be different than the flutter mode transition of [174] associated with two flutter instability modes having the same critical wind speed. The phenomenon discussed in [171–173] has led to recent studies on aerodynamic nonlinearities and nonlinear flutter that were discussed in sections 2.3.2 and 2.3.3.

2.6 Summary on Flutter and Structural Nonlinearities

Until now, the research carried out on nonlinear flutter considering structural nonlinearities has mainly been about the evaluation of the flutter wind speed for the nonlinear static deck deflection and the simulation of the nonlinear dynamic post-flutter response. This has been done in the case of long-span bridges with main spans between 1 km to 2 km. It has aimed at assessing the stiffening or softening effects associated with geometric nonlinearities on flutter. Regarding nonlinear structural dynamic effects such as internal resonance and nonlinear vertical-torsional coupling, the research has mostly been theoretical, and it has been conducted for suspension bridges with a maximum span length of 1.4 km. Consequently, for long-span bridges with main spans greater than 2 km, it is not known to what extent the nonlinear structural behavior can influence the flutter onset and flutter nonlinear dynamic response.

Similar to what happened when dynamic wind actions were not considered in the design of suspension bridges due to a gap in knowledge, the influence of structural nonlinearities on the stability of cable-supported bridges under wind actions is not well understood. Considering

that even weakly nonlinear systems can exhibit nonlinear dynamic phenomena [175], it seems relevant to develop a better comprehension of the interaction between structural nonlinearities and aeroelastic effects. This is especially the case for very long bridges as they could be more susceptible to nonlinear vertical-torsional coupling since their torsional-to-vertical frequency ratio decreases significantly as their span lengths increase [176]. This can be achieved by using numerical analysis to characterize the nonlinear structural behavior of long cable-supported bridges. This nonlinear structural behavior obtained numerically can then be utilized for an experimental study of the interaction between aeroelastic and nonlinear structural effects using the section model testing procedure, what has never been realized.

Chapter 3

Nonlinear Structural Vertical-Torsional Coupling

3.1 Introduction

Due to their flexibility, cable-supported bridges are quite effective at resisting earthquakes, but they are vulnerable to wind actions. Even though this fact had been learned by experience by suspension bridge designers of the 1800s, it had been somehow forgotten even by noted bridge engineers like Othmar Amman and Leon Moisseiff [1, 3]. Both designed by Amman, one of the greatest engineers of New York City bridges, the Bronx-Whitestone Bridge and the George Washington Bridge in its single deck configuration had suffered from vertical oscillations due to wind. On November 7, 1940, Moisseiff's infamous Tacoma Narrows Bridge collapsed due to dynamic wind actions. In the bridge engineering community, it is generally accepted that torsional flutter was responsible in the case of Tacoma [7, 8, 11]. However, using Tacoma as case study, mathematicians have shown that dynamic vertical forcing can lead to large torsional oscillations due to nonlinear vertical-torsional mode coupling associated with geometric nonlinearities [166–169]. For simulating this structural dynamic instability, simplified models or continuum models based on systems of nonlinear partial differential equations were used. Using a continuum model, it was demonstrated that flutter was likely responsible for Tacoma [170]. Nevertheless, the authors of [166–169] raise a point not considered in the wind design of long-span bridges, i.e., possible large oscillations caused by structural coupling between the modes of vibration because of structural nonlinearities. The nonlinear effect described previously seems to be attributed to internal parametric resonance, a dynamic instability [170]. The possible occurrence of internal resonance has also been demonstrated in cable-stayed bridges [160–162]. Additionally, suspension bridges with inclined main cables can exhibit nonlinear dynamic phenomena such as internal resonance [163–165].

To the author's knowledge, such large torsional oscillations from a vertical forcing because of nonlinear structural effects have never been demonstrated experimentally. However, a transition from an antisymmetric flutter mode to a symmetric flutter mode was observed on a full-aeroelastic model of a double-main-span suspension bridge [171]. This phenomenon seems to be different than the flutter mode transition described in [174] which was explained by the fact that the antisymmetric and symmetric flutter modes have the same critical wind speed. It appears that the flutter mode transition of [171] would be internal resonance caused

by the aerodynamic and/or structural nonlinearities of the aeroelastic-structural bridge system [172].

For cable-supported bridges, structural nonlinearities can arise from different sources. There are geometric nonlinearities (P- Δ , cable sag and large displacement effects) and material nonlinearities (e.g. steel yielding and nonlinear concrete behavior) [147]. Material nonlinearities are more important for small- and medium-span bridges especially in the case of seismic excitation. For bridges with longer spans, nonlinear geometric effects are generally of greater concern. For example, the geometric stiffness contribution of the main cables in suspension bridges evolves nonlinearly, and for very long-span bridges like the Messina Strait Bridge [17], it could be relevant to check the static structural performance for some of the critical load cases using nonlinear geometric analysis. Another example when geometric nonlinearities should be considered for long-span bridges occurs with bridges having very slender towers [149, 150]. Furthermore, the nonlinear concrete behavior should also be accounted for in the case of concrete towers [151]. For static wind loads on cable-supported bridges, it has been shown that the critical wind speed for aerostatic instability, an aerodynamic instability analogous to column buckling, can significantly be reduced due to geometric nonlinearities when compared to linear analysis [18–20].

As discussed in the previous paragraph, it is relatively common to utilize nonlinear analysis to determine the static behavior of long-span bridges. For dynamic analysis, the structural response is usually obtained considering the linearized stiffness about the dead-load configuration of the bridge, which is determined using large displacement analysis. Nonlinear dynamic analysis is utilized in specific cases, e.g., for the seismic response of long-span bridges having hydraulic buffers since buffers behave like nonlinear springs under rapidly varying dynamic actions [12, 17, 151]. Unlike for seismic analysis, dynamic analyses for wind effects typically consider a linear structure since frequency-domain analysis procedures are generally employed in the design process for assessing phenomena such as buffeting (e.g. [10, 31]) and flutter (e.g. [134, 136, 139, 140]). Time-domain approaches for buffeting analysis are sometimes used (e.g. [177]), but they are demanding in terms of computational time compared to frequency-domain analysis. To the author's knowledge, such time-domain analyses are carried out assuming a linear behavior for the bridge when used by bridge designers.

Similar to what happened when dynamic wind actions were not considered in the design of suspension bridges, wind analyses of long-span bridges are currently carried out without including the structural nonlinearities. Considering the results obtained by mathematicians regarding large torsional response caused by nonlinear structural coupling between the

modes of vibration [166–169], it appears that further research is needed on the possible interaction between structural nonlinearities and wind phenomena such as buffeting and flutter. Having a better understanding of nonlinear structural phenomena in long-span bridges is of practical engineering value considering the very long spans of recent projects like the Çanakkale Bridge and Messina Strait Bridge.

Thus, this chapter presents an initial investigation based on static analysis of the nonlinear vertical-torsional coupling in long-span bridges. The main objective of this study is to provide an analysis procedure that can be used to compare the level of nonlinear structural coupling and structural nonlinearity for different bridge structures. The proposed approach relies on nonlinear finite element analysis, an engineering tool which can model complex structures, such as cable-supported bridges, accurately unlike continuum models.

First, the theoretical development for the calculation of nonlinear generalized stiffness parameters that accounts for nonlinear vertical-torsional coupling is made. Then, through static pushover analysis, the nonlinear generalized stiffness parameters are calculated for five suspension bridges and two cable-stayed bridges. Nonlinear vertical and torsional stiffness parameters are obtained individually and in a coupled manner. Comparing the nonlinear generalized stiffness parameters for each bridge allows identifying the bridges with the strongest nonlinear structural coupling that are likely more susceptible to a structural dynamic instability.

3.2 Nonlinear Generalized Stiffness

In the case of static analysis, the displacement at a specific location on the bridge (e.g. at midspan), can be used as a nonlinearity measure by comparing linear and nonlinear static responses. Such an approach was used in [148] for a cable-stayed bridge subjected to live loads. For dynamic analysis, the displacement time history at a specific location can still be used to compare linear and nonlinear responses, but it does not provide synthetic information about the potential vertical-torsional mode coupling in long-span bridges. Nonlinear normal modes [178, 179] could provide a way to assess this nonlinear coupling in a more synthetic manner, but nonlinear normal mode calculations are not readily available in finite element codes, especially commercial codes, and therefore would require a specific development.

However, it is possible to make use of the linear modes of vibration to study the nonlinear vertical-torsional mode coupling in cable-supported bridges. Using the modes of vibration and nonlinear static analysis, which are available in most finite element codes, nonlinear

generalized stiffness parameters can be calculated as shown in the following subsections. The idea of using the linear modes of vibration for studying the nonlinear behavior of cable-supported bridges was initially developed in [155], but was limited to mode-by-mode analysis. Therefore, in the following subsections, a method inspired by the work in [155] is developed to account simultaneously of one vertical mode and one torsional mode, which allows the coupling between the selected modes. A generalization of the proposed method for more than two modes is also presented.

Additionally, it should be mentioned that, in this study, only geometric nonlinearities are considered for the assessment of nonlinear vertical-torsional coupling. This choice is made because material nonlinearities are unlikely to happen, especially under wind loads, in a properly designed structure. This assumption is reasonable considering that the main structural component in suspension and cable-stayed bridges, the cable system, is designed elastically due to the fact that the breaking strain of steel cable wires is very small with a typical value of 4 % [149]. Therefore, only nonlinear geometric analysis is required in the proposed method.

3.2.1 One-Mode Analysis

Before developing the approach to calculate the two-mode nonlinear generalized parameters for cable-supported bridges, a rectified and improved version of the one-mode method of [155] is presented.

The method relies on the application of a static load proportional to one of the modes of vibration of the bridge finite element model under consideration. This is done in order to quantify the nonlinear behavior in terms of dynamic properties. However, at first, let us consider the static application of a modal load to a linear bridge structure as follows:

$$\mathbf{K}\mathbf{u} = \mathbf{p}_j \quad \text{with} \quad \mathbf{p}_j = a_j \omega_j^2 \mathbf{M}\boldsymbol{\phi}_j \quad (3.1)$$

where \mathbf{K} and \mathbf{M} are respectively the stiffness matrix and mass matrix of the bridge obtained using the finite element method; \mathbf{u} is the displacement vector; a_j is a real coefficient; $\omega_j = 2\pi f_j$ is the natural angular frequency of mode $\boldsymbol{\phi}_j$ calculated at the dead-load configuration; f_j is the natural frequency of mode $\boldsymbol{\phi}_j$. For a cable-supported bridge, we have that $\mathbf{K} = \mathbf{K}_S + \mathbf{K}_G$ where \mathbf{K}_S and \mathbf{K}_G are respectively the elastic and geometric stiffness matrices linearized about the dead-load configuration.

Mode $\boldsymbol{\phi}_j$ is normalized such that the maximum displacement/rotation of the bridge deck

is unity. The maximum displacement is used for horizontal and vertical modes, whereas rotation is considered for torsional modes. Because $\mathbf{K}\boldsymbol{\phi}_j = \omega_j^2\mathbf{M}\boldsymbol{\phi}_j$, it follows that the displacement vector in eq. 3.1 is $\mathbf{u} = a_j\boldsymbol{\phi}_j$. Therefore, it is concluded that a_j corresponds to the maximum linear deck displacement caused by the load vector \mathbf{p}_j as defined in eq. 3.1. This physical interpretation facilitates choosing the range of values for a_j to be used in the analysis. This is not possible for the procedure in [155] because a_j has no physical interpretation due to the usage of mass-normalized modes.

The displacement vector \mathbf{u} can be written in terms of the modal coordinates using eq. 3.2:

$$\mathbf{u} = \sum_{k=1}^n \boldsymbol{\phi}_k z_k = \boldsymbol{\Phi} \mathbf{z} \quad (3.2)$$

By substituting eq. 3.2 into eq. 3.1 then premultiplying both sides of eq. 3.1 by $\boldsymbol{\Phi}^T$, n uncoupled static equations are obtained. Due to the orthogonality properties of \mathbf{M} and the fact that \mathbf{p}_j is a modal load vector proportional to the mass matrix, only one uncoupled equation has to be considered since the other equations have generalized loads equal to zero. Therefore, the solution of eq. 3.1 in terms of the modal coordinates is:

$$\tilde{k}_j z_j = \tilde{p}_j \quad \text{and} \quad \mathbf{u} = \boldsymbol{\phi}_j z_j \quad (3.3)$$

where $\tilde{k}_j = \boldsymbol{\phi}_j^T \mathbf{K} \boldsymbol{\phi}_j = \omega_j^2 \tilde{m}_j$ is the generalized stiffness; z_j is the generalized coordinate; $\tilde{p}_j = a_j \omega_j^2 \tilde{m}_j$ is the generalized load; $\tilde{m}_j = \boldsymbol{\phi}_j^T \mathbf{M} \boldsymbol{\phi}_j$ is the generalized mass. Rearranging eq. 3.3 provides an indirect way of calculating the generalized stiffness \tilde{k}_j from linear static analysis without using the stiffness matrix directly:

$$\tilde{k}_j = \frac{\tilde{p}_j}{z_j} \quad (3.4)$$

A similar approach can be used for characterizing in a practical manner a nonlinear generalized stiffness for a nonlinear geometric system:

$$\mathbf{f}_{SG}(\mathbf{u}_{nl}) = \mathbf{p}_j \quad \text{with} \quad \mathbf{p}_j = a_j \omega_j^2 \mathbf{M} \boldsymbol{\phi}_j \quad (3.5)$$

where $\mathbf{f}_{SG}(\mathbf{u}_{nl})$ is the internal force vector of the nonlinear geometric system; \mathbf{u}_{nl} is the nonlinear displacement vector obtained from nonlinear static analysis using the Newton-

Raphson method, for example.

However, for the nonlinear case shown in eq. 3.5, the displacement vector is not exactly proportional to ϕ_j since distortions will be caused by the geometric nonlinearities. Considering that the displacements that will be considered are significantly smaller than the span length, the nonlinear displacement vector can be reasonably approximated as:

$$\mathbf{u}_{nl} \approx \phi_j z_j \quad (3.6)$$

Premultiplying both sides of eq. 3.6 by $\phi_j^T \mathbf{M}$, the generalized coordinate for the displacement vector caused by \mathbf{p}_j is obtained:

$$z_j = \frac{\phi_j^T \mathbf{M} \mathbf{u}_{nl}}{\tilde{m}_j} \quad (3.7)$$

Using the mass matrix in eq. 3.7 allows having consistent units in the procedure as explained in more detail in section 3.2.3. Then, the tangent nonlinear generalized stiffness \tilde{k}_j^t as a function of z_j is calculated as:

$$\tilde{k}_j^t(z_j) = \frac{d\tilde{p}_j}{dz_j} = \omega_j^2 \tilde{m}_j \frac{da_j}{dz_j} \quad (3.8)$$

By using different values for the coefficient a_j , the nonlinear relationship \tilde{p}_j vs z_j can be calculated, and then, using finite differences, \tilde{k}_j^t is evaluated. It should be mentioned that, due to the normalization used for the modes, the generalized coordinate z_j is equal to the maximum deck displacement in the direction under consideration in the nonlinear geometric case.

The derivative da_j/dz_j in eq. 3.8 can be interpreted as a relative measure of the nonlinear contribution of $\tilde{k}_j^t(z_j)$ with respect to the linear generalized stiffness \tilde{k}_j because:

$$\frac{da_j}{dz_j} = \frac{\tilde{k}_j^t}{\omega_j^2 \tilde{m}_j} = \frac{\tilde{k}_j^t}{\tilde{k}_j} \quad (3.9)$$

3.2.2 Two-Mode Analysis for Vertical and Torsional Modes

The calculation of the nonlinear generalized stiffness can also be extended to two modes. This is done in order to assess the nonlinear vertical-torsional mode coupling. Therefore, in this section, we are interested in one vertical mode $\boldsymbol{\phi}_V$ and one torsional mode $\boldsymbol{\phi}_\theta$. This choice is also justified from the fact that vertical and torsional effects are the most important regarding the wind response and stability of bridges. In this case, the nonlinear static equation to solve is:

$$\mathbf{f}_{SG}(\mathbf{u}_{nl}) = \mathbf{p}_{V\theta} \quad (3.10)$$

$$\mathbf{p}_{V\theta} = \mathbf{p}_V + \mathbf{p}_\theta = a_V \omega_V^2 \mathbf{M} \boldsymbol{\phi}_V + a_\theta \omega_\theta^2 \mathbf{M} \boldsymbol{\phi}_\theta \quad (3.11)$$

The nonlinear displacement vector (i.e. the solution of $\mathbf{f}_{SG}(\mathbf{u}_{nl}) = \mathbf{p}_{V\theta}$) is approximated as:

$$\mathbf{u}_{nl} \approx \boldsymbol{\phi}_V z_V + \boldsymbol{\phi}_\theta z_\theta = \boldsymbol{\Phi}_{V\theta} \mathbf{z}_{V\theta} \quad (3.12)$$

where $\boldsymbol{\Phi}_{V\theta} = [\boldsymbol{\phi}_V \ \boldsymbol{\phi}_\theta]$ and $\mathbf{z}_{V\theta} = [z_V \ z_\theta]^\top$. By premultiplying eq. 3.12 by $\boldsymbol{\Phi}_{V\theta}^\top \mathbf{M}$, the generalized displacements can be calculated due to the orthogonality property of the modal matrix $\boldsymbol{\Phi}_{V\theta}$ with respect to \mathbf{M} :

$$(\boldsymbol{\Phi}_{V\theta}^\top \mathbf{M} \boldsymbol{\Phi}_{V\theta}) \mathbf{z}_{V\theta} = \boldsymbol{\Phi}_{V\theta}^\top \mathbf{M} \mathbf{u}_{nl} \quad (3.13)$$

$$z_V = \frac{\boldsymbol{\phi}_V^\top \mathbf{M} \mathbf{u}_{nl}}{\tilde{m}_V} \quad \text{and} \quad z_\theta = \frac{\boldsymbol{\phi}_\theta^\top \mathbf{M} \mathbf{u}_{nl}}{\tilde{m}_\theta} \quad (3.14)$$

Then, the two-mode nonlinear generalized stiffness matrix $\tilde{\mathbf{K}}_{V\theta}^t$, which is a function of $\mathbf{z}_{V\theta}$, can be evaluated:

$$\tilde{\mathbf{K}}_{V\theta}^t(\mathbf{z}_{V\theta}) = \frac{\partial \tilde{\mathbf{p}}_{V\theta}}{\partial \mathbf{z}_{V\theta}} = \begin{bmatrix} \frac{\partial \tilde{p}_V}{\partial z_V} & \frac{\partial \tilde{p}_V}{\partial z_\theta} \\ \frac{\partial \tilde{p}_\theta}{\partial z_V} & \frac{\partial \tilde{p}_\theta}{\partial z_\theta} \end{bmatrix} \quad (3.15)$$

It should be noted that $\tilde{\mathbf{p}}_{V\theta} = \boldsymbol{\Phi}_{V\theta}^\top \mathbf{p}_{V\theta} = [\tilde{p}_V \ \tilde{p}_\theta]^\top = [a_V \omega_V^2 \tilde{m}_V \ a_\theta \omega_\theta^2 \tilde{m}_\theta]^\top$. By varying a_V and a_θ , the relationship for $\tilde{\mathbf{p}}_{V\theta}$ as a function of $\mathbf{z}_{V\theta}$ can be determined. $\tilde{\mathbf{K}}_{V\theta}^t$ can be thought

as the stiffness matrix of an equivalent two-degree-of-freedom system. It should be noted that the fact of considering two modes in the modal load allows studying the nonlinear mode coupling as demonstrated by the off-diagonal terms in eq. 3.15.

3.2.3 Verification of Nonlinear Distortion for \mathbf{u}_{nl}

By expressing the mass matrix by its Cholesky factorization, i.e., $\mathbf{M} = \mathbf{U}_M^T \mathbf{U}_M$ where \mathbf{U}_M is an upper-triangular matrix, eq. 3.13 becomes:

$$(\mathbf{U}_M \Phi_{V\theta})^T (\mathbf{U}_M \Phi_{V\theta}) \mathbf{z}_{V\theta} = (\mathbf{U}_M \Phi_{V\theta})^T (\mathbf{U}_M \mathbf{u}_{nl}) \quad (3.16)$$

Equation 3.16 can be viewed as the least squares solution of:

$$\begin{bmatrix} \mathbf{U}_M \phi_V & \mathbf{U}_M \phi_\theta \end{bmatrix} \begin{bmatrix} z_V \\ z_\theta \end{bmatrix} = \mathbf{U}_M \mathbf{u}_{nl} \quad (3.17)$$

Therefore, the uncentered coefficient of determination R^2 for eq. 3.17 can be used for judging whether \mathbf{u}_{nl} is not too distorted in comparison with the linear combination of the modes, i.e., the nonlinear distortions are sufficiently small such that the use of eq. 3.12 is reasonable. Consequently, the closer R^2 is to 1, the better is the approximation utilized in eq. 3.12.

Also, it is worth noting that the units are consistent ($M^{1/2}L$) in eq. 3.17 even though \mathbf{u}_{nl} contains displacements and rotations when frame elements are considered in the finite element model. Thus, eqs. 3.14 and 3.17 are preferred to a direct least squares solution of eq. 3.12. For one-mode analysis, eq. 3.7 can be modified to obtain an equation analogous to eq. 3.17 from which R^2 can be calculated.

3.2.4 Calculation of Derivatives in $\tilde{\mathbf{K}}_{V\theta}^t$

For two-mode analysis, the derivatives in the tangent stiffness matrix $\tilde{\mathbf{K}}_{V\theta}^t$ cannot be calculated directly. This is because the generalized displacements z_V and z_θ are not distributed across a uniform grid as shown in fig. 3.1. The reason is that the loads are controlled in the proposed approach using the coefficients a_V and a_θ and not the generalized displacements. However, it is considered that the generalized loads \tilde{p}_V and \tilde{p}_θ are defined across a uniform grid.

Each point (z_V, z_θ) in fig. 3.1 corresponds to different combinations of \tilde{p}_V and \tilde{p}_θ . We define

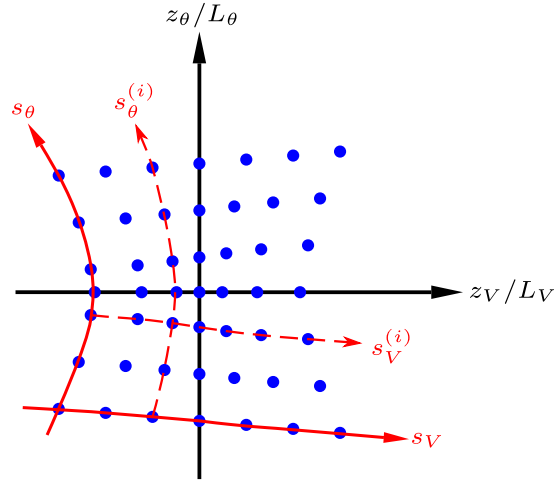


Figure 3.1: Normalized generalized displacement grid for two-mode analysis

the curved coordinates s_V and s_θ in the plane formed by the normalized quantities z_V/L_V and z_θ/L_θ where $L_V = z_{Vmax} - z_{Vmin}$ and $L_\theta = z_{\theta max} - z_{\theta min}$. The coordinate s_V corresponds to a path in the plane $z_V/L_V - z_\theta/L_\theta$ when \tilde{p}_V is increased and \tilde{p}_θ is kept constant. Similarly, s_θ is the curved coordinate when \tilde{p}_θ is increased and \tilde{p}_V is constant. The curved paths $s_V^{(i)}$ and $s_\theta^{(i)}$ can be calculated incrementally using:

$$s_V^{(i)} = \sum \sqrt{\left(\frac{\Delta z_{VV}^{(i)}}{L_V}\right)^2 + \left(\frac{\Delta z_{\theta V}^{(i)}}{L_\theta}\right)^2} \quad (3.18)$$

$$s_\theta^{(i)} = \sum \sqrt{\left(\frac{\Delta z_{V\theta}^{(i)}}{L_V}\right)^2 + \left(\frac{\Delta z_{\theta\theta}^{(i)}}{L_\theta}\right)^2} \quad (3.19)$$

where $\Delta z_{VV}^{(i)}$ and $\Delta z_{\theta V}^{(i)}$ are the increments in z_V and z_θ between two consecutive points along $s_V^{(i)}$; $\Delta z_{V\theta}^{(i)}$ and $\Delta z_{\theta\theta}^{(i)}$ are the increments in z_V and z_θ along $s_\theta^{(i)}$. Doing so, the curved coordinates can be calculated for each point (z_V, z_θ) corresponding to different combinations of \tilde{p}_V and \tilde{p}_θ .

For calculating the first row in $\tilde{\mathbf{K}}_{V\theta}^t$, the chain rule is employed:

$$\begin{aligned} \frac{\partial \tilde{p}_V}{\partial s_V} &= \frac{\partial \tilde{p}_V}{\partial z_V} \frac{\partial z_V}{\partial s_V} + \frac{\partial \tilde{p}_V}{\partial z_\theta} \frac{\partial z_\theta}{\partial s_V} \\ \frac{\partial \tilde{p}_V}{\partial s_\theta} &= \frac{\partial \tilde{p}_V}{\partial z_V} \frac{\partial z_V}{\partial s_\theta} + \frac{\partial \tilde{p}_V}{\partial z_\theta} \frac{\partial z_\theta}{\partial s_\theta} \end{aligned} \quad (3.20)$$

Solving for $\partial\tilde{p}_V/\partial z_V$ and $\partial\tilde{p}_V/\partial z_\theta$ in eq. 3.20, the following equation is obtained for calculating the first row in $\tilde{\mathbf{K}}_{V\theta}^t$. In eq. 3.21, $\partial\tilde{p}_V/\partial s_\theta$ is zero by definition.

$$\begin{bmatrix} \frac{\partial\tilde{p}_V}{\partial z_V} \\ \frac{\partial\tilde{p}_V}{\partial z_\theta} \end{bmatrix} = \begin{bmatrix} \frac{\partial z_V}{\partial s_V} & \frac{\partial z_\theta}{\partial s_V} \\ \frac{\partial z_V}{\partial s_\theta} & \frac{\partial z_\theta}{\partial s_\theta} \end{bmatrix}^{-1} \begin{bmatrix} \frac{\partial\tilde{p}_V}{\partial s_V} \\ \frac{\partial\tilde{p}_V}{\partial s_\theta} \end{bmatrix} \quad (3.21)$$

The derivatives on the right-hand side of eq. 3.21 can be evaluated by finite differences. The same procedure can be used to obtain the second row of $\tilde{\mathbf{K}}_{V\theta}^t$. Doing so for each point (z_V, z_θ) , the relationship for $\tilde{\mathbf{K}}_{V\theta}^t$ vs $\mathbf{z}_{V\theta}$ is obtained.

3.2.5 Generalization for More Than Two Modes

The calculation of nonlinear generalized stiffness parameters can be generalized to any combination of modes. In this case, the nonlinear static equation is solved for a modal load that accounts for m selected modes:

$$\mathbf{f}_{SG}(\mathbf{u}_{nl}) = \mathbf{p}_m \quad \text{with} \quad \mathbf{p}_m = \sum_{k=1}^m a_k \omega_k^2 \mathbf{M} \boldsymbol{\phi}_k \quad (3.22)$$

The following equation is used to approximate the displacement vector \mathbf{u}_{nl} :

$$\mathbf{u}_{nl} \approx \sum_{k=1}^m \boldsymbol{\phi}_k z_k = \boldsymbol{\Phi}_m \mathbf{z}_m \quad (3.23)$$

Premultiplying eq. 3.23 by $\boldsymbol{\Phi}_m^T \mathbf{M}$ yields:

$$z_k = \frac{\boldsymbol{\phi}_k^T \mathbf{M} \mathbf{u}_{nl}}{\tilde{m}_k} \quad \text{for} \quad k = 1, 2, \dots, m \quad (3.24)$$

Equation 3.24 represents the least squares solution of the following equation:

$$\begin{bmatrix} \mathbf{U}_M \boldsymbol{\phi}_1 & \mathbf{U}_M \boldsymbol{\phi}_2 & \dots & \mathbf{U}_M \boldsymbol{\phi}_m \end{bmatrix} \begin{bmatrix} z_1 \\ z_2 \\ \vdots \\ z_m \end{bmatrix} = \mathbf{U}_M \mathbf{u}_{nl} \quad (3.25)$$

The coefficient of determination R^2 for eq. 3.25 can be determined to check the validity of

the approximation utilized in eq. 3.23. By varying the modal load vector by changing the coefficients a_k , the generalized load vector $\tilde{\mathbf{p}}_m$ can be determined:

$$\tilde{\mathbf{p}}_m = \tilde{\mathbf{p}}_m(\mathbf{z}_m) = \mathbf{\Phi}_m^T \mathbf{p}_m = \begin{bmatrix} \tilde{p}_1 \\ \tilde{p}_2 \\ \vdots \\ \tilde{p}_m \end{bmatrix} = \begin{bmatrix} a_1 \omega_1^2 \tilde{m}_1 \\ a_2 \omega_2^2 \tilde{m}_2 \\ \vdots \\ a_m \omega_m^2 \tilde{m}_m \end{bmatrix} \quad (3.26)$$

Then, the nonlinear generalized stiffness matrix $\tilde{\mathbf{K}}_m^t$ is obtained by taking the derivative of $\tilde{\mathbf{p}}_m$ with respect to \mathbf{z}_m :

$$\tilde{\mathbf{K}}_m^t = \frac{\partial \tilde{\mathbf{p}}_m}{\partial \mathbf{z}_m} = \begin{bmatrix} \frac{\partial \tilde{p}_1}{\partial z_1} & \frac{\partial \tilde{p}_1}{\partial z_2} & \cdots & \frac{\partial \tilde{p}_1}{\partial z_m} \\ \frac{\partial \tilde{p}_2}{\partial z_1} & \frac{\partial \tilde{p}_2}{\partial z_2} & \cdots & \frac{\partial \tilde{p}_2}{\partial z_m} \\ \vdots & \vdots & \ddots & \vdots \\ \frac{\partial \tilde{p}_m}{\partial z_1} & \frac{\partial \tilde{p}_m}{\partial z_2} & \cdots & \frac{\partial \tilde{p}_m}{\partial z_m} \end{bmatrix} \quad (3.27)$$

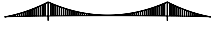






To calculate the derivatives of the stiffness matrix $\tilde{\mathbf{K}}_m^t$, a similar procedure as the one presented in section 3.2.4 is utilized when more than two modes are considered. In this case, the curved paths as shown in fig. 3.1 must be calculated for an m -dimensional grid, and the chain rule in eq. 3.20 must account for m curved coordinates.

3.3 Numerical Models of Cable-Supported Bridges

The study presented in [155] was limited to three suspension bridges having main span lengths between 1 km and 1.5 km, which is a limited range of span lengths. In this chapter, five suspension bridges with main span lengths between 1550 m and 4140 m are used in the nonlinear generalized stiffness analyses. Such a wide range for the span lengths was chosen to be able to identify a potential span length effect on the nonlinear generalized stiffness parameters. In addition to the five suspension bridges, two cable-stayed bridges with main spans close to 1 km are considered in order to compare in terms of geometric nonlinearities the two most common structural systems used for long-span bridges. Information about these bridges is presented in table 3.1. For each bridge, the table shows the type of structural system, the main span length, whether the bridge has longitudinal hydraulic buffers and an elevation view.

It should be mentioned that all the bridges considered in this study with the exception of

Table 3.1: Description of cable-supported bridges

Bridge	Type	Main span (m)	Buffers?	Elevation view
SU1	Three-span suspension Continuous girder	1550	Yes	
SU2	Three-span suspension Continuous girder	1624	Yes	
SU3a	Three-span suspension Partially continuous girder	2460	Yes	
SU3b	Three-span suspension Partially continuous girder	3300	Yes	
SU3c	Three-span suspension Partially continuous girder	4140	Yes	
CS1	Cable-stayed Rigid deck-tower connection	856	No	
CS2	Cable-stayed Continuous girder	1018	Yes	



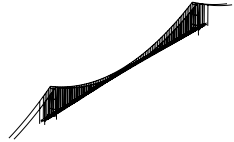



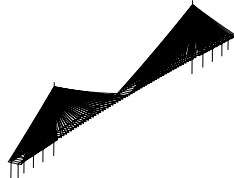
bridges SU3a and SU3c are existing structures or existing detailed designs. Bridges SU3a and SU3c are modified designs based on bridge SU3b, but with different main span lengths. They are preliminary designs for which the bridge deck properties and hanger spacing are kept the same as in bridge SU3b, but the main cables and towers were redesigned considering the new span lengths. Bridges SU3a, SU3b and SU3c have all the same sag-to-span ratio. Since the three bridges are based on the same design concept but have different span length, they provide a reliable manner to assess the span length effect. Detailed information about these bridges can be found in appendix A.

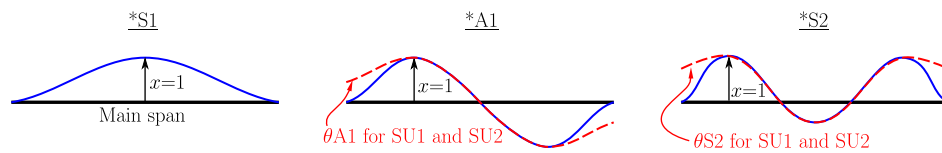
The finite element models of the bridges presented in table 3.1 were developed using the open-source finite element software *Code Aster* [180]. The procedure to calculate the nonlinear generalized stiffness parameters was automatized with a specific development within *Code Aster* using the Python programming language. Table 3.2 presents information about the finite element models of the seven cable-supported bridges used to assess the nonlinear generalized stiffness parameters. The number of elements for each model is shown as well as the natural frequencies of the mode shapes utilized in the nonlinear generalized stiffness analyses. The frequencies shown are for inactive buffers. Additionally, table 3.2 also presents typical computational times for the nonlinear generalized stiffness analyses discussed in section 3.5 when run as serial jobs on Compute Canada's cluster Graham equipped with 2.1 GHz processors.

3.3.1 Modeling Approach of Suspension Bridges

All suspension bridges for this study were modeled using the fishbone modeling approach where the deck is represented by Timoshenko beam elements connected to the cable system through rigid elements. Timoshenko beam elements are also used for the towers. Tension-

Table 3.2: Description of finite element models of cable-supported bridges (L: lateral, V: vertical, θ : torsion, S: symmetric, A: antisymmetric, 1MA: one-mode analysis, 2MA: two-mode analysis, 3MA: three-mode analysis)

Bridge	Model	Number of elements	Natural frequencies (Hz)			CPU time (min)
SU1		Truss: 410 Beam: 462	<i>Sym.</i> LS1: 0.053 VS1: 0.090 θ S1: 0.256	<i>Antisym.</i> LA1: 0.124 VA1: 0.107 θ A1: 0.274	<i>Sym.</i> LS2: 0.207 VS2: 0.133 θ S2: 0.402	1MA: 0.2 2MA: 18 3MA: 322
SU2		Truss: 432 Beam: 370	<i>Sym.</i> LS1: 0.051 VS1: 0.097 θ S1: 0.279	<i>Antisym.</i> LA1: 0.116 VA1: 0.080 θ A1: 0.358	<i>Sym.</i> LS2: 0.188 VS2: 0.131 θ S2: 0.411	1MA: 0.2 2MA: 15 3MA: 289
SU3a		Truss: 448 Beam: 1443	<i>Sym.</i> LS1: 0.037 VS1: 0.095 θ S1: 0.130	<i>Antisym.</i> LA1: 0.078 VA1: 0.065 θ A1: 0.105	<i>Sym.</i> LS2: 0.143 VS2: 0.127 θ S2: 0.170	1MA: 0.4 2MA: 34 3MA: 500
SU3b		Truss: 588 Beam: 1835	<i>Sym.</i> LS1: 0.030 VS1: 0.080 θ S1: 0.100	<i>Antisym.</i> LA1: 0.056 VA1: 0.058 θ A1: 0.081	<i>Sym.</i> LS2: 0.083 VS2: 0.107 θ S2: 0.133	1MA: 0.5 2MA: 41 3MA: 583
SU3c		Truss: 732 Beam: 2227	<i>Sym.</i> LS1: 0.027 VS1: 0.070 θ S1: 0.083	<i>Antisym.</i> LA1: 0.047 VA1: 0.052 θ A1: 0.067	<i>Sym.</i> LS2: 0.062 VS2: 0.093 θ S2: 0.109	1MA: 0.7 2MA: 50 3MA: 687
CS1		Truss: 1908 Beam: 432	<i>Sym.</i> LS1: 0.138 VS1: 0.215 θ S1: 0.693	<i>Antisym.</i> LA1: 0.338 VA1: 0.271	<i>Sym.</i> VS2: 0.361	1MA: 0.5 2MA: 31 3MA: 601
CS2		Truss: 1792 Beam: 1218	<i>Sym.</i> LS1: 0.157 VS1: 0.198 θ S1: 0.428	<i>Antisym.</i> LA1: 0.393 VA1: 0.240 θ A1: 0.587	<i>Sym.</i> VS2: 0.302	1MA: 0.5 2MA: 39 3MA: 595



only truss elements are considered for the main cables and hangers. Cable pretensions are applied using temperature loads. The suspension bridge models are analyzed considering geometric nonlinearities as mentioned previously.

3.3.2 Modeling Approach of Cable-Stayed Bridges

For the cable-stayed bridges, the modeling approach for the deck and towers is the same as described in section 3.3.1. The stay cables are subdivided into 8 to 12 tension-only truss elements. When combined to large displacement analysis, this multi-link approach for the stay cables allows the cable sag effect to be represented adequately without the need to use an effective modulus of elasticity, i.e., Ernst's modulus [181].

Two different approaches are utilized to model the cable mass. In the first approach, the mass is uniformly distributed along each stay cable. For the second approach, 50 % of the mass for each stay cable is lumped at both ends. In order to have the correct geometric stiffness for the stay cables, the cable self-weight is applied as a uniformly distributed load. Doing so, cables modes and deck-cable modes are disregarded in the second method unlike the first one, which facilitates analysis. The frequencies in table 3.2 for bridges CS1 and CS2 correspond to the lumped cable mass approach.

3.4 Reference Displacements for Nonlinear Generalized Stiffness Parameters

Before presenting the nonlinear generalized stiffness parameters for the bridges of table 3.1, reasonable displacement bounds to be used for the presentation of the results are determined. To do so, the nonlinear static response under mean wind loads are obtained for each bridge using the procedure in [19]. Mean wind loads were applied to the bridge deck, towers and cables, and the hydraulic buffers were considered to be inactive. Simulations were made for three different angles of attack. Figure 3.2 shows a typical nonlinear static response at midspan for bridge SU2 for an increasing wind speed. In fig. 3.2, a good agreement is obtained for the lateral displacement at a wind speed of 37.6 m/s when compared to the wind tunnel results (WT) and the numerical simulation made by the bridge designers (Des.).

For defining the reference displacements, the midspan displacements for a wind speed at deck height of 60 m/s are considered. They are presented for each bridge in table 3.3 for three angles of attack. The corresponding normalized quantities are also shown, i.e., the normalized lateral displacement u_y/L_{span} , the normalized vertical displacement u_z/L_{span} and

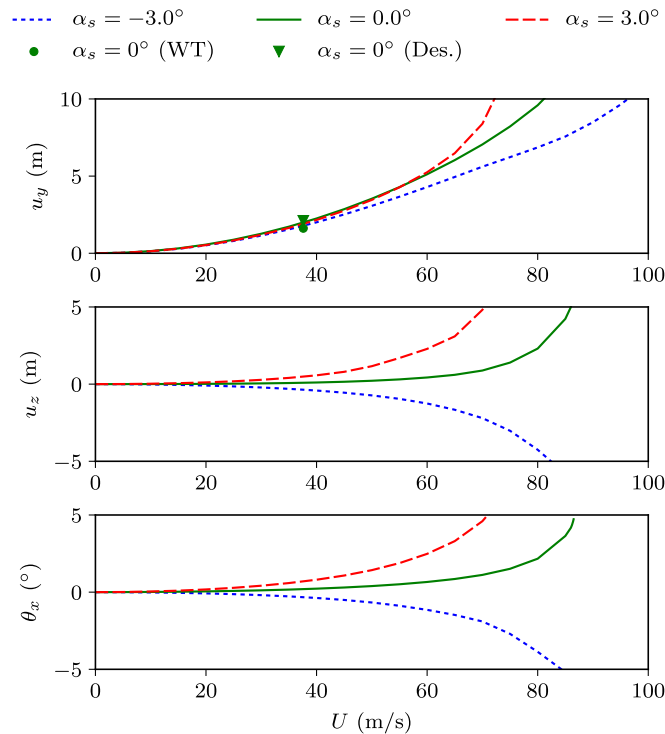


Figure 3.2: Midspan displacements under mean wind loads for bridge SU2 (U : mean wind speed, α_s : angle of attack, u_y : lateral displacement, u_z : vertical displacement, θ_x : torsional rotation)

the normalized rotation $\theta_x b_{cl}/L_{span}$ where L_{span} is the main span length and b_{cl} is half of the distance between the cables at deck level. From this table, it is clear that the bridge-deck cross section considered for bridges SU3a, SU3b and SU3c has better aerodynamic properties vertically and torsionally than those of bridges SU1 and SU2. It is reasonable to say that bridges SU3a, SU3b and SU3c would have much greater displacements if a less-aerodynamically effective bridge deck was considered. For this reason, the displacement bounds for the presentation of the results for the five suspension bridges are based on the average of the normalized displacements for bridges SU1 and SU2. Furthermore, some allowance is also included in the reference displacements for the dynamic wind effects which were estimated from wind tunnel results for full-aeroelastic or taut-strip models. A similar approach was used for the cable-stayed bridges.

Table 3.4 shows the displacement bounds that are utilized in the presentation of the nonlinear generalized stiffness parameters in section 3.5. As shown in the table, the same normalized displacements are used for all suspension bridges. For both cable-stayed bridges, the normalized displacements are also the same, but different than the ones for the suspension bridges. The corresponding physical displacements are also shown in the table. It should be

Table 3.3: Midspan displacements under mean wind loads at 60 m/s

Bridge	α_s (°)	u_y (m)	u_z (m)	θ_x (°)	u_y/L_{span} (10^{-3})	u_z/L_{span} (10^{-3})	$\theta_x b_{cl}/L_{span}$ (10^{-3})
SU1	-3	5.25	-4.16	-3.82	3.39	-2.68	-0.65
	0	5.37	-1.89	-1.09	3.46	-1.22	-0.19
	3	5.72	0.45	1.30	3.69	0.29	0.22
SU2	-3	4.29	-1.25	-1.15	2.64	-0.77	-0.17
	0	5.12	0.43	0.66	3.15	0.26	0.10
	3	5.25	2.28	2.48	3.23	1.41	0.36
SU3a	-3	10.53	-0.79	-0.38	4.28	-0.32	-0.07
	0	10.08	-0.45	-0.17	4.10	-0.18	-0.03
	3	10.96	-0.09	-0.01	4.45	-0.04	-0.00
SU3b	-3	13.64	-0.93	-0.60	4.13	-0.28	-0.08
	0	13.05	-0.54	-0.34	3.96	-0.16	-0.05
	3	14.01	-0.12	-0.17	4.25	-0.04	-0.02
SU3c	-3	15.06	-1.01	-0.61	3.64	-0.24	-0.07
	0	14.47	-0.59	-0.34	3.49	-0.14	-0.04
	3	15.40	-0.15	-0.17	3.72	-0.04	-0.02
CS1	-3	1.31	-1.41	-0.26	1.53	-1.65	-0.06
	0	1.48	-0.59	0.55	1.73	-0.69	0.12
	3	1.61	0.02	0.80	1.88	0.03	0.17
CS2	-3	0.67	-0.47	0.05	0.65	-0.46	0.02
	0	0.70	-0.13	0.24	0.69	-0.13	0.10
	3	0.73	0.16	0.43	0.71	0.16	0.18

noted that the same normalized displacements for all bridges of each structural system are considered in order to be able to compare bridges with different main span lengths.

Although the reference displacements of table 3.4 are derived from the midspan displacements, they appear to be reasonable maximums of the generalized displacements for the purpose of result presentation in section 3.5. In order to facilitate the comparison of the nonlinear generalized stiffness parameters for different modes, the same displacement bounds can be considered for fundamental and higher modes, but the results must be interpreted appropriately for higher modes as done in the following sections. This is because higher modes usually have a lesser contribution to the total dynamic response compared to the fundamental modes and consequently smaller generalized displacements. Therefore, the procedure used for determining the reference displacements is deemed sufficient in the context of comparing the nonlinear generalized stiffness parameters of different bridges.

Table 3.4: Reference displacements for the presentation of nonlinear generalized stiffness parameters

Bridge	u_y (m)	u_z (m)	θ_x (°)	u_y/L_{span} (10^{-3})	u_z/L_{span} (10^{-3})	$\theta_x b_{cl}/L_{span}$ (10^{-3})
SU1	6.20	3.10	2.95	4.00	2.00	0.50
SU2	6.50	3.25	3.45	4.00	2.00	0.50
SU3a	9.84	4.92	2.71	4.00	2.00	0.50
SU3b	13.20	6.60	3.64	4.00	2.00	0.50
SU3c	16.56	8.28	4.56	4.00	2.00	0.50
CS1	1.71	1.71	1.39	2.00	2.00	0.30
CS2	2.04	2.04	0.70	2.00	2.00	0.30

3.5 Results for Nonlinear Generalized Stiffness Analysis

In this section are presented the most important results for the nonlinear generalized stiffness analysis of the seven bridges of table 3.1. Since the same conclusions regarding the nonlinear generalized stiffness analysis can be obtained from the results of the dead-load case or the case under mean wind loads and for active or inactive buffers, the presentation is limited to the results of the dead-load configuration with inactive hydraulic buffers. This is because the mean aerodynamic loads and buffers only slightly affect the nonlinear generalized parameters as shown in sections 3.5.1 and 3.5.2 and discussed in section 3.6.1.

Even though the present discussion mainly focuses on the interaction caused by geometric nonlinearities between vertical and torsional effects, it is of interest to start with a mode-by-mode assessment in sections 3.5.3 and 3.5.4 to gain more insight. Unlike in [155] where only the vertical modes were considered, herein, vertical and torsional modes are utilized for one-mode analysis as well as lateral modes for the sake of completeness. Then, two-mode analysis results are presented in sections 3.5.5 and 3.5.6. Section 3.5.7 shows the effect of lateral modes on nonlinear structural vertical-torsional coupling.

For one-mode analysis, each nonlinear generalized stiffness curve was obtained using 81 points for which the nonlinear generalized loads are distributed uniformly. For two-mode analysis, an 81×81 uniform grid with a total of 6561 points was utilized. A grid of $41 \times 41 \times 41$, for a total of 68 921 points, was used in the calculation of nonlinear generalized-stiffness parameters for three-mode analysis. The typical computational times shown in table 3.2 correspond to these analysis parameters. The ranges of values for the load coefficients a_j (used in the load \mathbf{p}_j) were chosen such that the nonlinear behavior and nonlinear vertical-

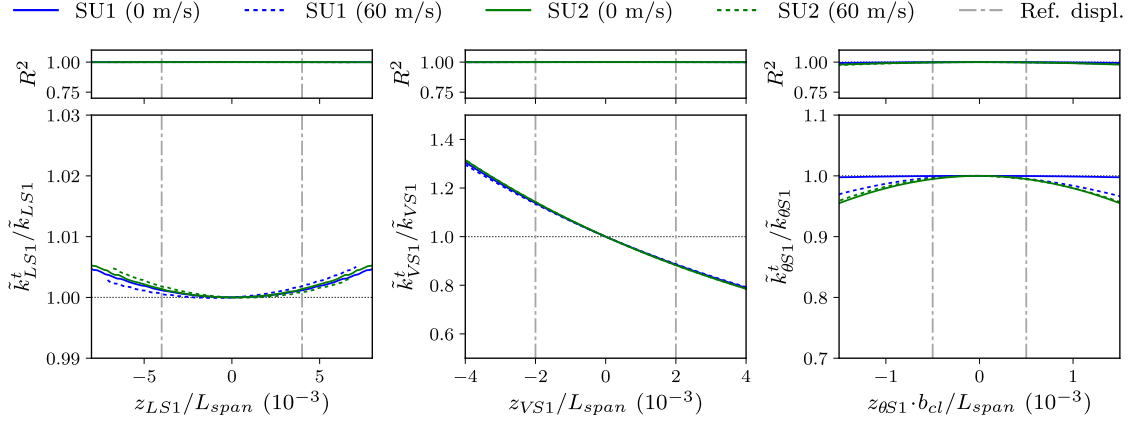


Figure 3.3: Effect of mean aerodynamic loads on one-mode nonlinear generalized stiffnesses of bridges SU1 and SU2

torsional coupling can be observed. However, the presentation of the results in the following sections are limited to the reference displacements as mentioned in section 3.4.

In order to facilitate the comparison of bridges with different span lengths, most of the results in this section are presented in a normalized form. They are presented in terms of the ratio of the nonlinear generalized stiffness to the linear generalized stiffness as a function of the normalized generalized displacements z_L / L_{span} , z_V / L_{span} or $z_{\theta} b_{cl} / L_{span}$ where L_{span} is the main span length and b_{cl} is half of the distance between the cables at deck height. Also, in the result presentation, the coefficient of determination R^2 is shown in order to judge whether the nonlinear distortions are small such that eqs. 3.6 and 3.12 are valid.

3.5.1 Effect of Mean Aerodynamic Loads

To assess the effect of the mean aerodynamic loads on the nonlinear generalized stiffnesses, the natural frequencies and mode shapes calculated considering the tangent stiffness matrix for the static response under mean wind loads at 60 m/s and an angle of attack of 0° were considered in the nonlinear generalized stiffness analysis procedure. Analyses were made from the configuration at 60 m/s. This was done for one-, two- and three-mode analysis. Since the influence is small, only selected results for one-mode analysis are presented in fig. 3.3 for bridges SU1 and SU2. This figure compares results for the dead-load scenario to the case of a mean wind speed of 60 m/s. In the figure, the dashed-dotted vertical lines correspond to the reference displacements of table 3.4. Due to fact that the effect of mean wind loads is small, the following sections refer to the dead-load configuration as mentioned previously.

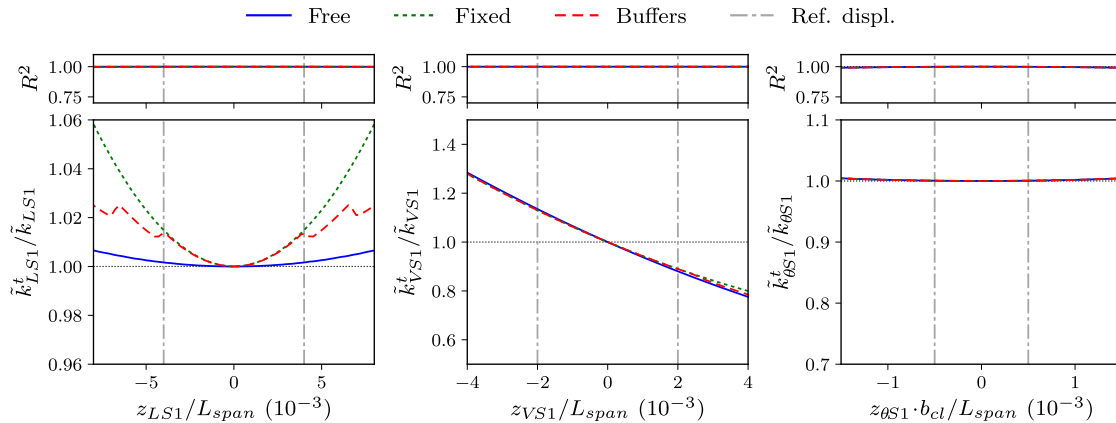


Figure 3.4: Effect of hydraulic buffers on one-mode nonlinear generalized stiffnesses of bridge SU3b

3.5.2 Effect of Hydraulic Buffers

Since all the bridges considered for this study except bridge CS1 have hydraulic buffers used to limit the longitudinal deck motions, all analyses were conducted with active and inactive buffers for comparison where applicable. It was found that buffers have a small effect on the nonlinear generalized stiffness and can be neglected. As an example, fig. 3.4 shows the effect of buffers for bridge SU3b. The first case included in the figure is for inactive buffers (free). For the second scenario (fixed), the deck is rigidly connected to the towers in the longitudinal direction. For the last scenario (buffers), the buffers are active, i.e., they are modeled as nonlinear truss elements having a bilinear material model. Due to the small influence of buffers as shown in fig. 3.4, only the results for inactive buffers are presented from now on. A more detailed discussion can be found in section 3.6.1 about the effect of buffers.

3.5.3 One-Mode Analysis of Suspension Bridges

The normalized results of the mode-by-mode procedure for the five suspension bridges are presented in fig. 3.5 for the modes of vibration corresponding to the natural frequencies shown in table 3.2. Results for lateral, vertical and torsional modes are presented.

3.5.4 One-Mode Analysis of Cable-Stayed Bridges

Similar to the suspension bridges, one-mode analyses were made for the two cable-stayed bridges in the case of the lateral, vertical and torsional modes presented in table 3.2. Figure 3.6 shows the one-mode nonlinear generalized stiffness results in normalized form for

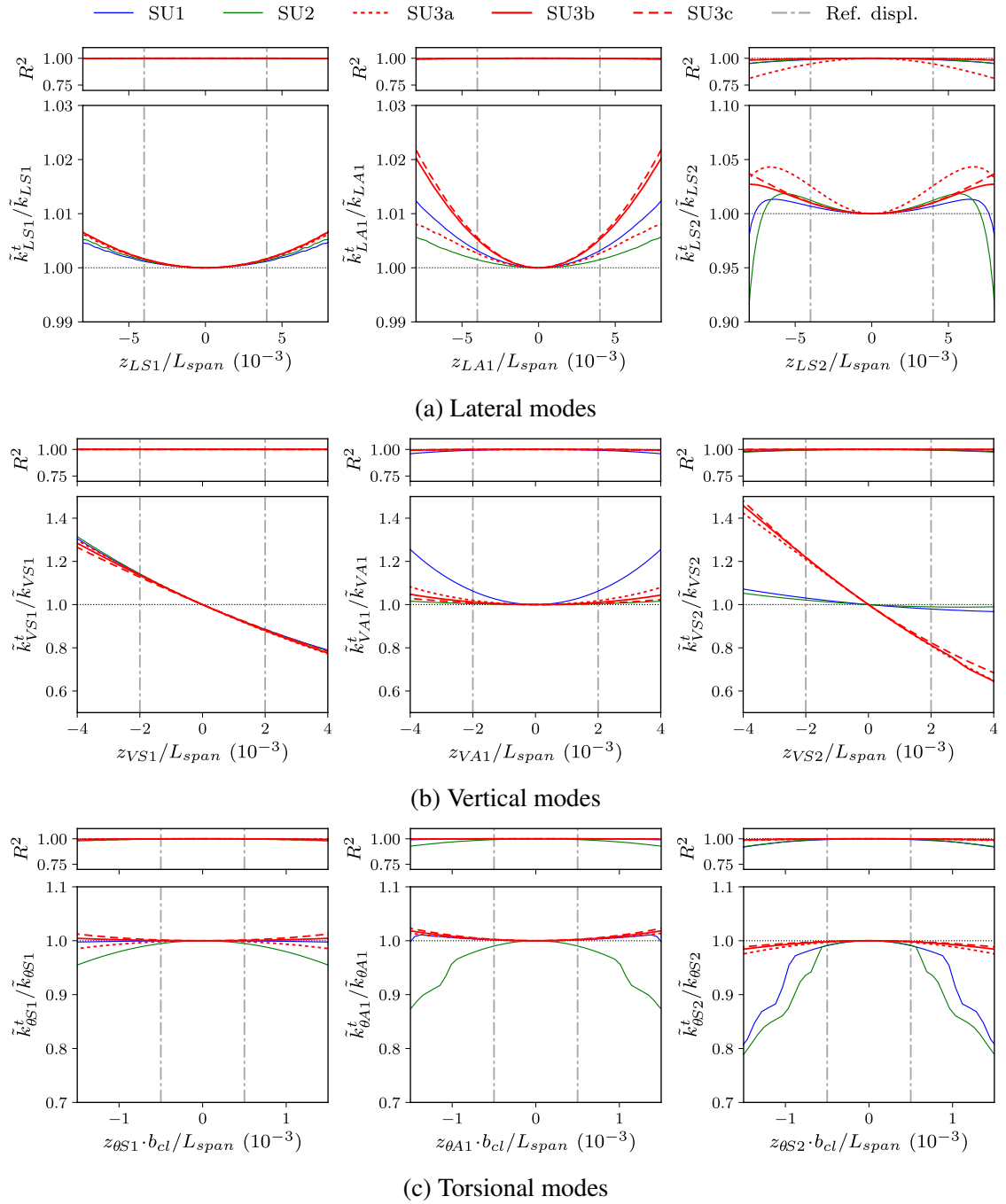


Figure 3.5: One-mode nonlinear generalized stiffness analysis of suspension bridges

both cable-stayed bridges. Both modeling approaches described in section 3.3.2, i.e., distributed cable mass (DCM) and lumped cable mass at both cable ends (LCM), are compared.

3.5.5 Two-Mode Analysis of Suspension Bridges

Then, two-mode analyses were conducted considering one vertical mode and one torsional mode having analogous shapes. The rationale of this choice is that flutter instability is caused by the coupling due to aeroelastic effects of analogous vertical and torsional modes. Hence, it is of interest to see whether similar coupling is possible due to geometric nonlinearities. This is also justified to consider analogous modes from the fact that nonlinear structural coupling is weaker for non-analogous modes in comparison to analogous modes (see appendix B).

In order to form the different pairs of vertical and torsional modes, the mode shapes are compared visually such that the vertical deck displacement of the vertical mode is similar to the torsional deck rotation of the torsional mode. As a second verification, the Modal Assurance Criterion (MAC) [182] was used to measure the similarity or correlation between vertical and torsional modes:

$$MAC_{v\theta} = \frac{(\chi_v^T \chi_\theta)^2}{(\chi_v^T \chi_v)(\chi_\theta^T \chi_\theta)} \quad (3.28)$$

where $MAC_{v\theta}$ is the modal assurance criterion varying between 0 (no correlation) and 1 (full correlation); χ_v is a vector containing the vertical displacements of the deck extracted from a vertical mode ϕ_v ; χ_θ is a vector of the torsional rotations of the deck for a torsional mode ϕ_θ . Then, by calculating the MAC for different combinations of vertical and torsional modes, it is possible to create a MAC matrix from which the pairs ϕ_v - ϕ_θ can be determined based on the largest MAC values. Using this two-step procedure, the pairs ϕ_v - ϕ_θ for the bridges of table 3.2 were obtained. In this table, each sub-column of the natural frequency column represents the mode pairings. It should be noted that the same mode pairings would have been obtained using modal integrals [183] instead of the MAC, but the MAC was preferred herein due to its independence with respect to the mode normalization, which makes its interpretation easier.

In figs. 3.7–3.9 are presented typical results of the two-mode nonlinear generalized loads and stiffnesses for bridges SU2 and SU3b. For bridge SU2, results are shown for the symmetric modal pair VS1- θ S1 whereas the symmetric modal pair VS1- θ S1 and antisymmetric modal pair VA1- θ A1 are presented for bridge SU3b. In these figures, colormaps are used to show

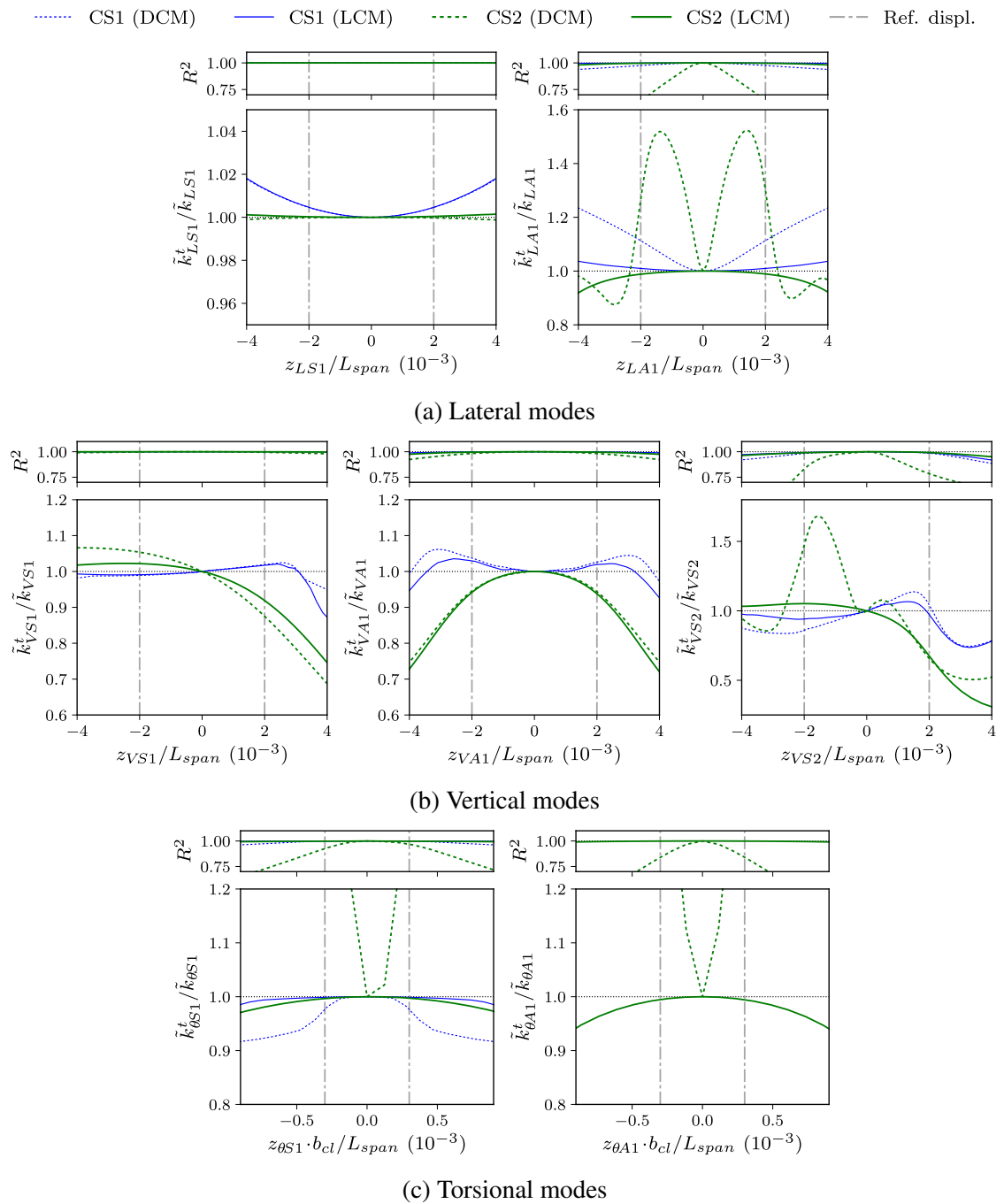


Figure 3.6: One-mode nonlinear generalized stiffness analysis of cable-stayed bridges

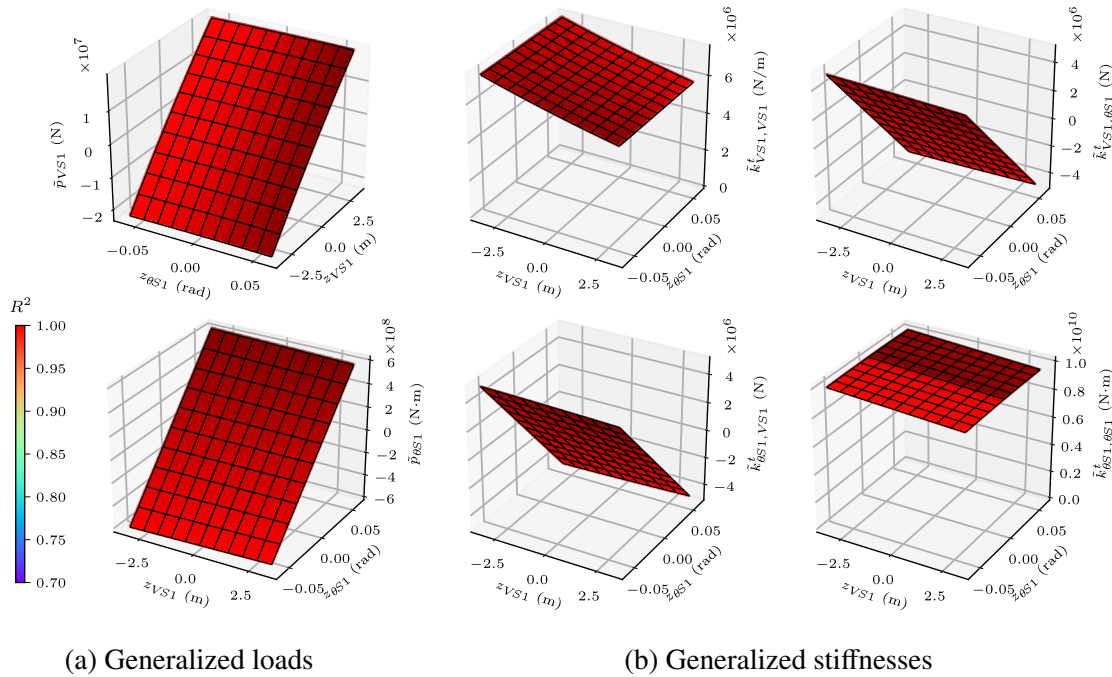


Figure 3.7: Two-mode nonlinear generalized stiffness analysis of bridge SU2 for modes VS1 and $\theta S1$

the coefficient of determination R^2 in order to judge on the validity of eq. 3.12. It should be noted that the generalized stiffnesses are not normalized in figs. 3.7–3.9. Also, the generalized displacements are limited to the values of table 3.4.

The two-mode analysis results for the five suspension bridges are compared in figs. 3.10 and 3.11. In fig. 3.10, the diagonal terms of the nonlinear generalized stiffness matrix $\tilde{\mathbf{K}}_{V\theta}^t$ are compared in normalized form in terms of the normalized generalized displacements. For the presentation of the off-diagonal terms of the nonlinear generalized stiffness matrix in fig. 3.11, the normalized quantities $(\tilde{k}_{V\theta}^t/b_{cl})/\tilde{k}_V$ and $(\tilde{k}_{\theta V}^t b_{cl})/\tilde{k}_\theta$ are used since the off-diagonal terms $\tilde{k}_{V\theta}^t$ and $\tilde{k}_{\theta V}^t$ have different units than the linear generalized stiffnesses \tilde{k}_V and \tilde{k}_θ . The quantity $\tilde{k}_{V\theta}^t/b_{cl}$ can be interpreted as a vertical generalized stiffness at the location of the cable connections to the deck. The quantity $\tilde{k}_{\theta V}^t b_{cl}$ represents an equivalent torsional generalized stiffness. For these figures, the normalized generalized displacements are limited to the values of table 3.4.

3.5.6 Two-Mode Analysis of Cable-Stayed Bridges

The two-mode nonlinear generalized stiffness parameters were obtained similarly for the cable-stayed bridges. From here, only the results for the LCM modeling approach are shown

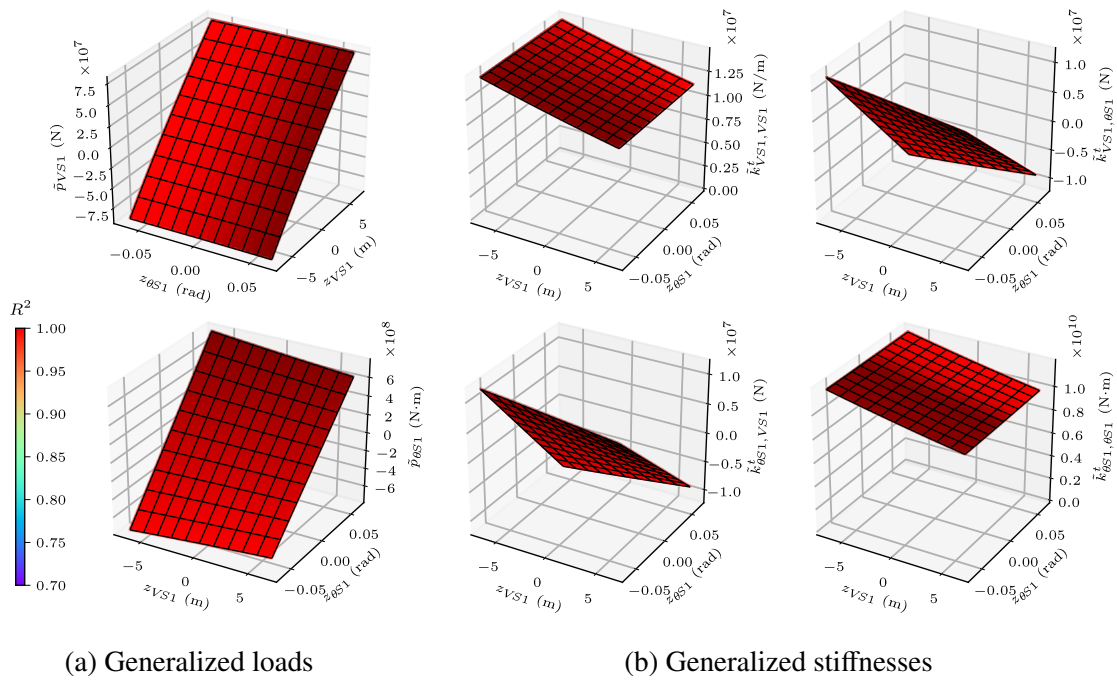


Figure 3.8: Two-mode nonlinear generalized stiffness analysis of bridge SU3b for modes VS1 and $\theta S1$

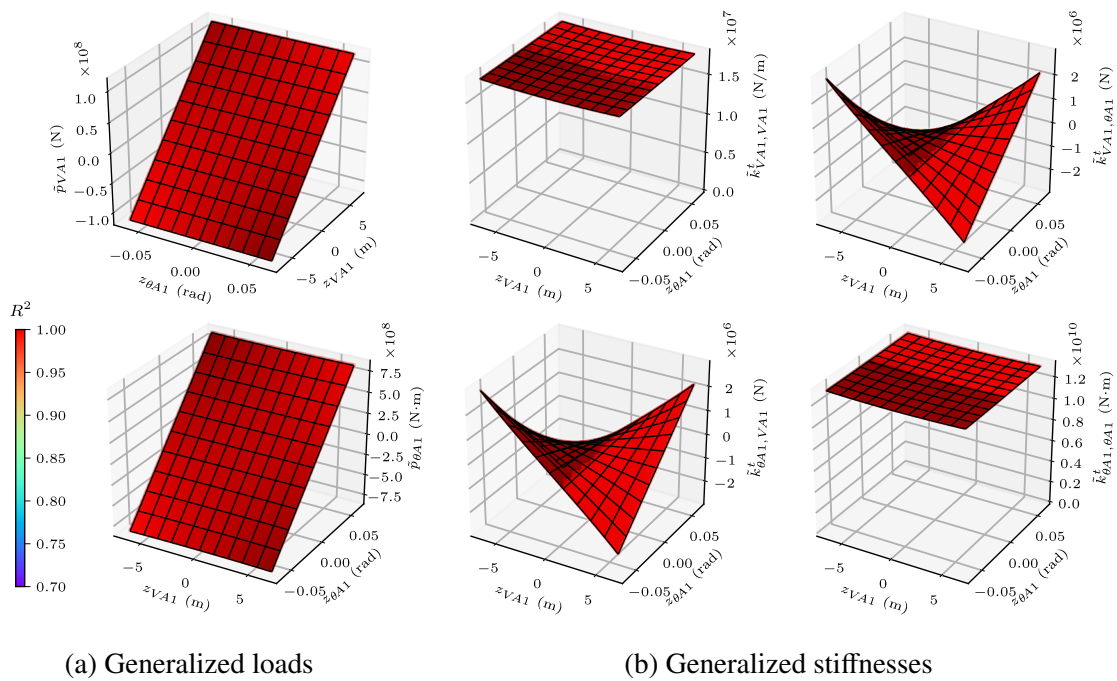


Figure 3.9: Two-mode nonlinear generalized stiffness analysis of bridge SU3b for modes VA1 and $\theta A1$

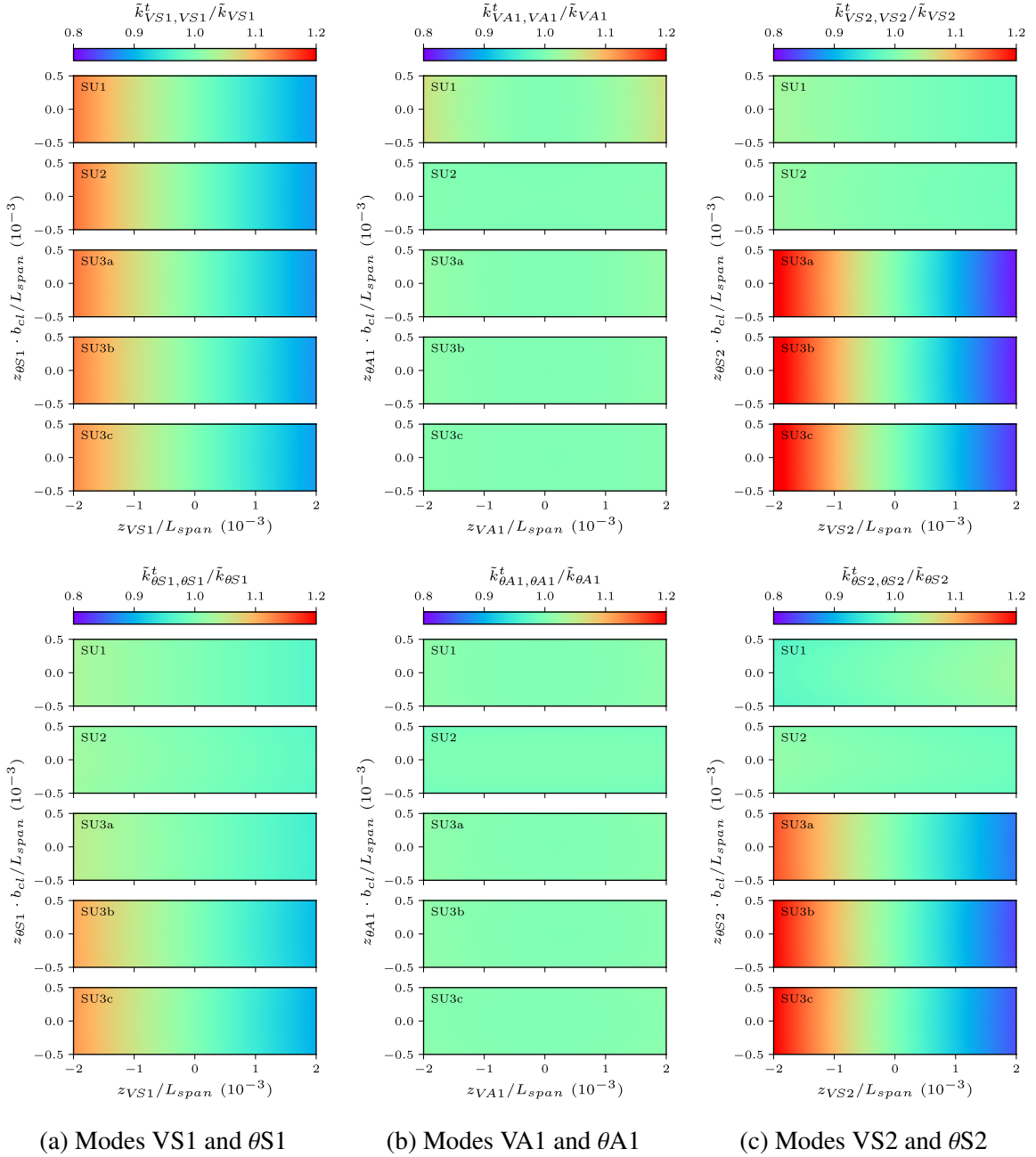


Figure 3.10: Comparison of diagonal nonlinear generalized stiffness terms for suspension bridges

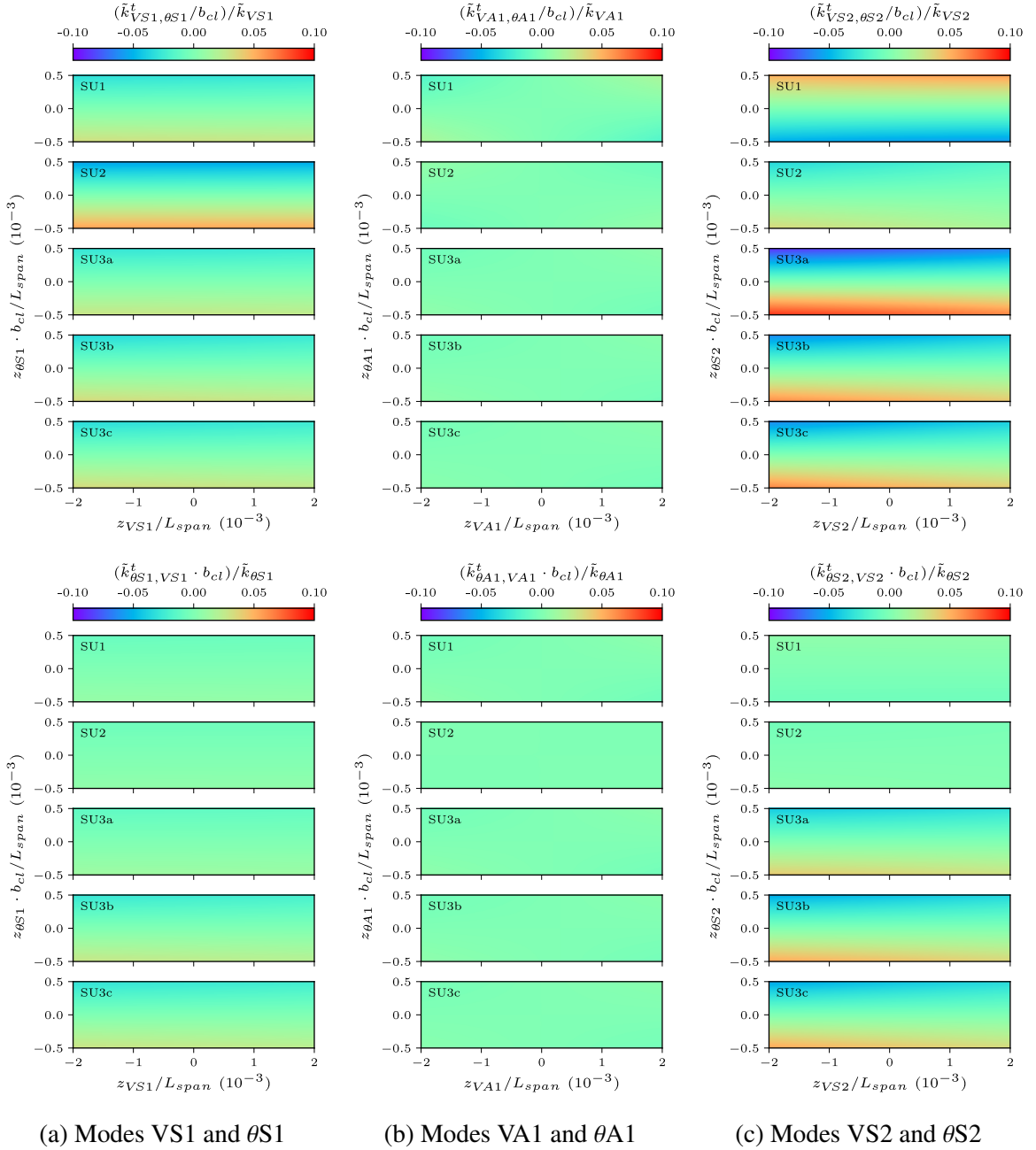


Figure 3.11: Comparison of off-diagonal nonlinear generalized stiffness terms for suspension bridges

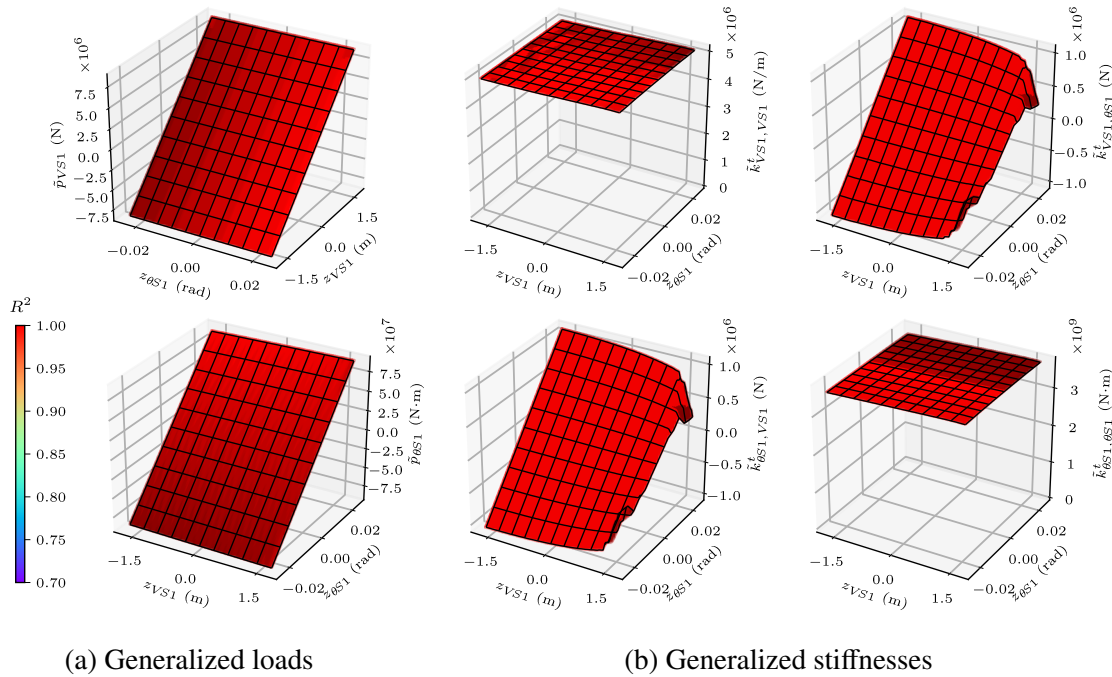


Figure 3.12: Two-mode nonlinear generalized stiffness analysis of bridge CS1 for modes VS1 and θ_{S1}

as it is more reliable as explained in section 3.6.3. Figure 3.12 illustrates typical results for bridge CS1 for the modal pair VS1- θ_{S1} , which are not normalized. A comparison of the diagonal nonlinear generalized stiffness terms for both cable-stayed bridges is made in fig. 3.13. Also, the normalized off-diagonal generalized stiffness terms are shown in fig. 3.14.

3.5.7 Effect of Lateral Modes on Vertical-Torsional Coupling

In this section, we are interested in the influence of lateral modes on the vertical-torsional coupling. Therefore, following the procedure in section 3.2.5, nonlinear generalized stiffness analyses were carried out considering three modes, i.e., one lateral mode, one vertical mode and one torsional mode having analogous shapes. The mode pairings are shown in table 3.2 as sub-columns of the natural frequency column and were determined using eq. 3.28 and visual inspection.

In fig. 3.15, the nonlinear generalized stiffnesses corresponding to the vertical and torsional modes are compared for two different values of the lateral generalized displacement. It should be noted that only one off-diagonal term is presented due to the symmetry of the nonlinear generalized stiffness matrix as discussed in sections 3.6.4 and 3.6.5. The effect

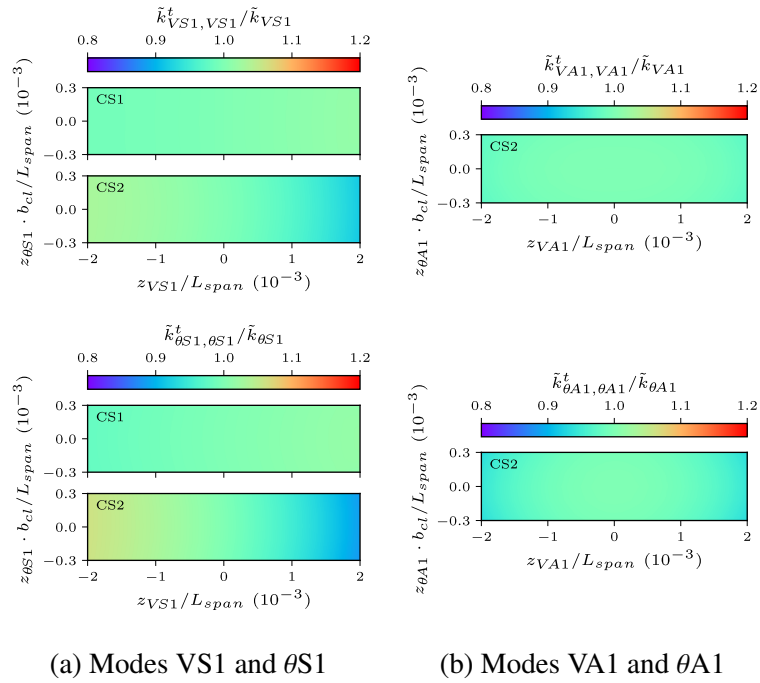


Figure 3.13: Comparison of diagonal nonlinear generalized stiffness terms for cable-stayed bridges

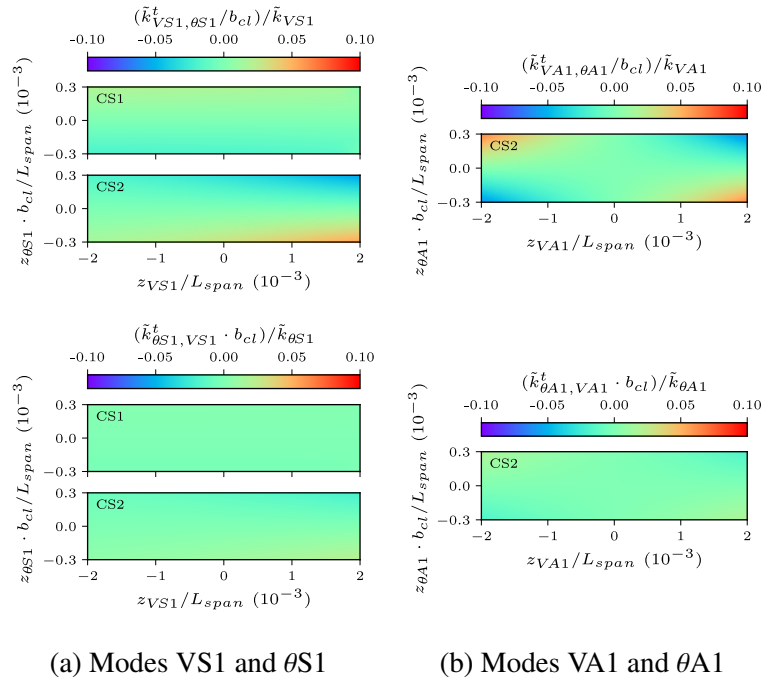


Figure 3.14: Comparison of off-diagonal nonlinear generalized stiffness terms for cable-stayed bridges

of mode LS2 on $\tilde{\mathbf{K}}_{V\theta}^t$ for the modal pair VS2- θ S2 is shown for suspension bridges SU1 and SU3b. Also, the effect of mode LS1 on $\tilde{\mathbf{K}}_{V\theta}^t$ relative to modes VS1 and θ S1 is presented for bridge CS1.

3.6 Discussion

3.6.1 Influence of Mean Aerodynamic Loads and Buffers on Nonlinear Generalized Stiffness Parameters

Theoretically, the mean aerodynamic loads could have an effect on the results of the nonlinear generalized analysis from the fact that they can modify the natural frequencies and mode shapes. However, it was observed that the modal properties at a wind speed of 60 m/s for the bridges used in this study are very close to the ones of the dead-load configuration. The variations of the natural frequencies for the modes of table 3.2 were less than 1 % with the exception of bridge SU1 with an average difference of 3 %. The greater variation for bridge SU1 could be explained by the greater static displacements at 60 m/s compared to the other bridges as shown in table 3.3. Similar observations were made in [184] about the small influence of mean wind loads on the natural frequencies since important frequency variations were only seen at the onset of aerostatic instability. This small influence on the modal parameters explains why the normalized nonlinear generalized stiffnesses for one-mode analysis in fig. 3.3 are practically the same for the dead-load configuration and for a wind speed of 60 m/s. Similar observations were made for two-mode and three-mode analysis.

Similarly, the buffers can alter the modal properties, but this effect is also small. This explains why the one-mode nonlinear generalized stiffness parameters in fig. 3.4 are not so much impacted by the buffers. The effect is slightly more pronounced for lateral modes, but this generally occurs for generalized displacements greater than the reference displacements of table 3.4. The effect of buffers was also small for two-mode and three-mode analysis.

3.6.2 One-Mode Analysis of Suspension Bridges

As it can be seen in the upper parts of the graphs in fig. 3.5 for the one-mode analysis of suspension bridges, the coefficient of determination R^2 is in general very close to 1.0 with some exceptions outside the displacement bounds that will be explained in the following paragraphs. This indicates that the nonlinear distortions are not significant in most cases for suspension bridges and that eq. 3.6 is a reasonable approximation.

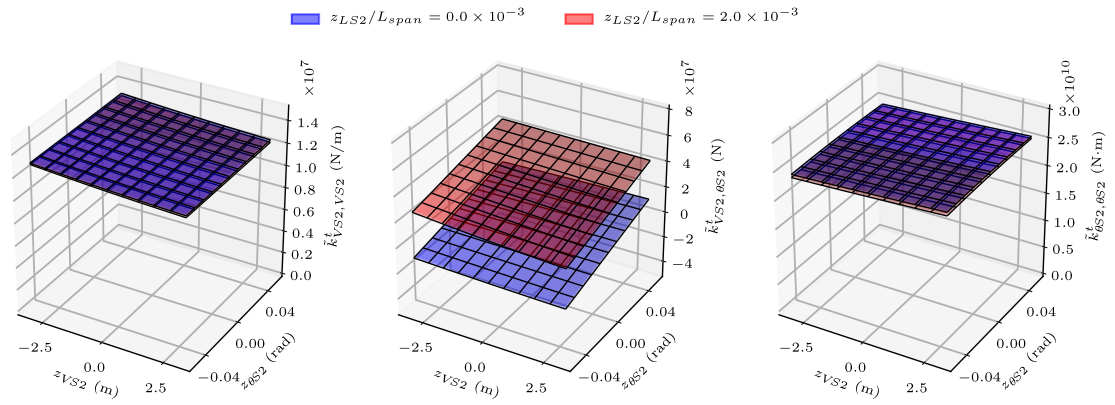
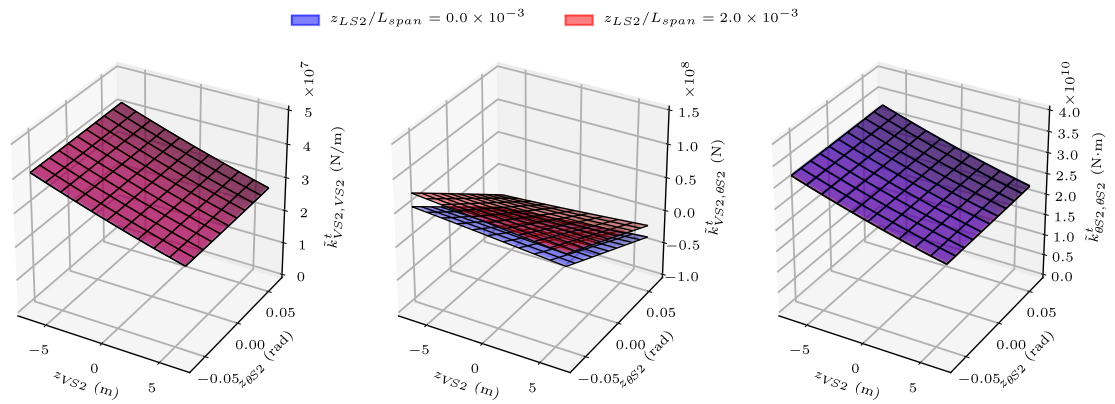
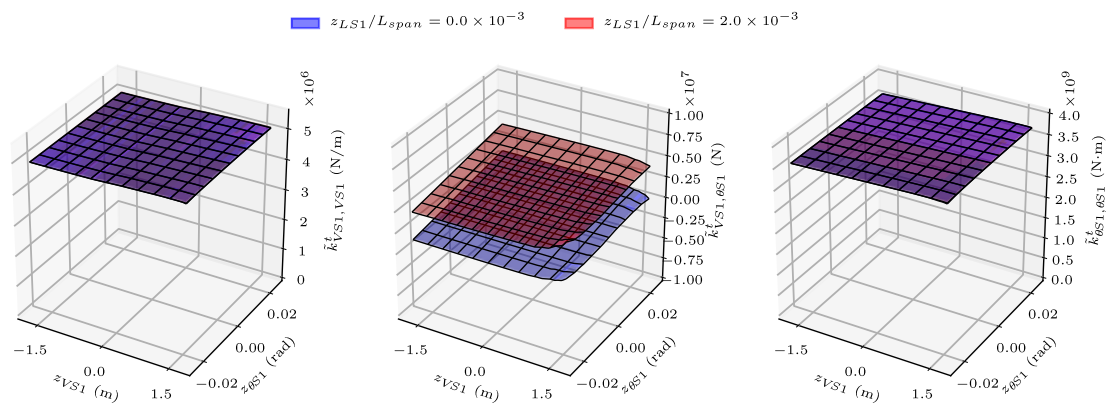
(a) Bridge SU1 for modes VS2 and θ S2(b) Bridge SU3b for modes VS2 and θ S2(c) Bridge CS1 for modes VS1 and θ S1

Figure 3.15: Effect of lateral modes on two-mode nonlinear generalized stiffnesses

Figure 3.5 shows that the one-mode nonlinear generalized stiffnesses for the suspension bridges are more nonlinear for the vertical modes. Within the reference bounds of table 3.4, there is a maximum variation of approximately $\pm 20\%$ when compared to the linear generalized stiffness. It is interesting to note that all bridges for mode VS1 follow a similar trend when presenting the results in normalized form. For \tilde{k}_{VS2}^t , bridges SU1 and SU2 have similar results. The VS2 nonlinear generalized stiffnesses for bridges SU3a, SU3b and SU3c, which have a similar behavior, are significantly more nonlinear compared to bridges SU1 and SU2. This difference between the first two bridges and the last three bridges could be attributed to the fact that bridges SU1 and SU2 have much longer side spans in comparison to bridges SU3a, SU3b and SU3c. Because of the very short side spans of the last three suspension bridges with respect to their main spans, their behavior is similar to a single-span suspension bridge. It is also possible to see that the nonlinear behavior is less important for the first antisymmetric vertical mode when compared to the symmetric modes with the exception of bridge SU1 for which symmetric and antisymmetric modes have a similar level of nonlinearities. The reason why symmetric vertical modes are more nonlinear is explained by the fact that symmetric vertical cable modes involve a change of cable tension leading to a variation of the geometric stiffness, which is a nonlinear process [185]. Therefore, a positive value (upwards) for z_{VS1} or z_{VS2} leads to a reduction in cable tension causing a softening behavior while a negative generalized displacement (downwards) for modes VS1 and VS2 causes a stiffening effect due to an increased cable tension.

For the lateral modes, except for mode LS2 for bridges SU1 and SU2, the nonlinear contribution to the generalized stiffness is only of 0% to 2% for generalized displacements within the displacement bounds. When z_{LS2} becomes very large for these bridges, there is a steep stiffness decrease that is explained by the fact that the lateral modal load for mode LS2 induces vertical displacements to the bridge deck and main cables, which activates the nonlinearities of the main cables in the vertical direction. For the same reason, R^2 values for bridge SU3a are much less than 1.0 since the nonlinear distortions cannot be represented by the linear mode of vibration. However, this occurs for generalized displacements much greater than the reference displacements.

For the results of the torsional modes, the variation of the nonlinear generalized stiffness is limited for displacements smaller than the reference displacements. Outside the displacement bounds, the stiffness degradation observed for modes $\theta A1$ and $\theta S2$ for bridges SU1 and SU2 is caused by hanger slackening near the towers as shown in figs. 3.16a–3.16c. For these bridges, hanger slackening occurs near the towers since, for modes $\theta A1$ and $\theta S2$, the torsional deck rotation is relatively large at the towers as sketched at the bottom of table 3.2.

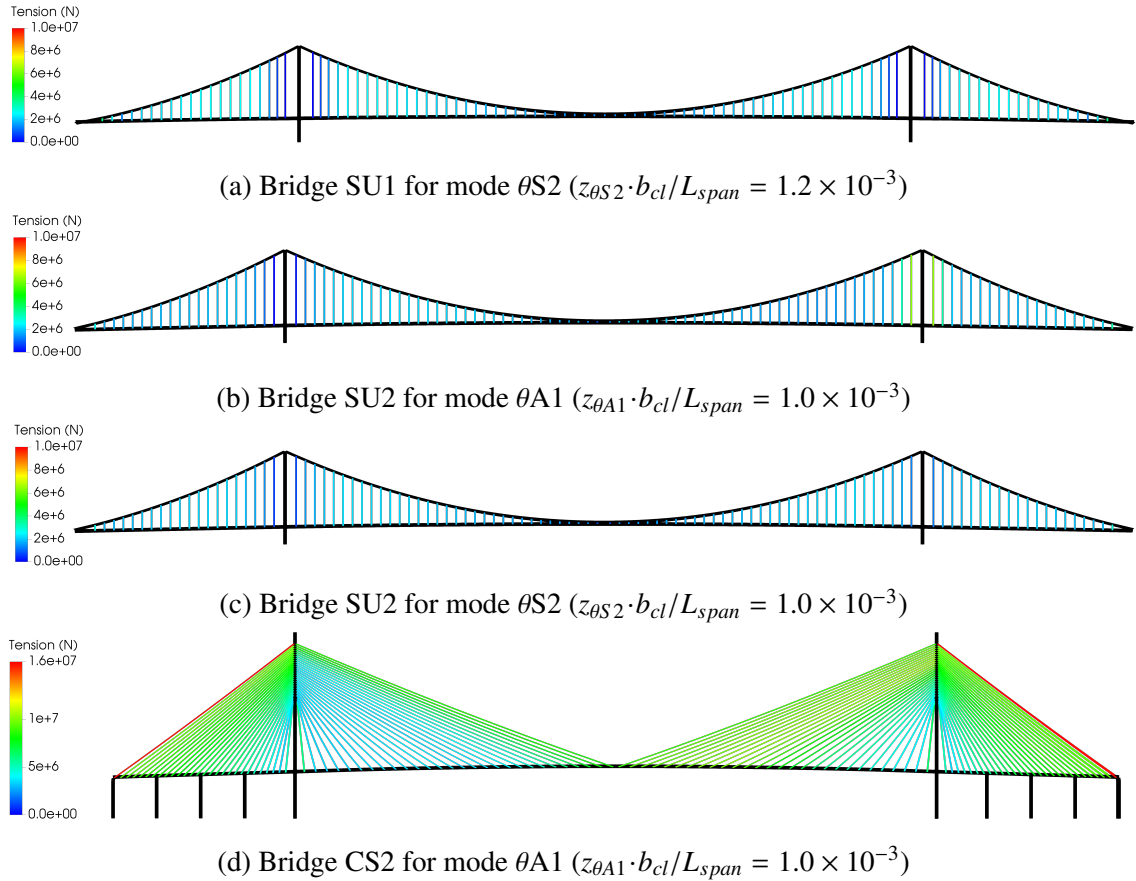


Figure 3.16: Hanger and stay cable tensions for one-mode nonlinear generalized stiffness analysis

There is a non-zero rotation at the towers because the bridge decks of bridges SU1 and SU2 are continuous and free to rotate about the longitudinal bridge axis at the towers. Hanger slackening also explains the low values of R^2 observed in these cases. Since this occurs for generalized displacements much larger than the reference displacements, such effect is unlikely to be seen on a bridge designed properly.

By comparing the different curves for bridges SU3a, SU3b and SU3c in fig. 3.5, it is possible to conclude that the span length only has a slight influence on the one-mode nonlinear generalized stiffness when the results are presented in normalized form. This result is surprising especially for the most nonlinear modes, i.e., modes VS1 and VS2 for which these bridges yield practically the same nonlinear evolution. In order to have more insight, the non-normalized results for the vertical modes for these bridges are presented in fig. 3.17. For modes VS1 and VS2, it is clear that the different curves are scaled versions of each other, confirming the observations made previously with regards to the normalized results.

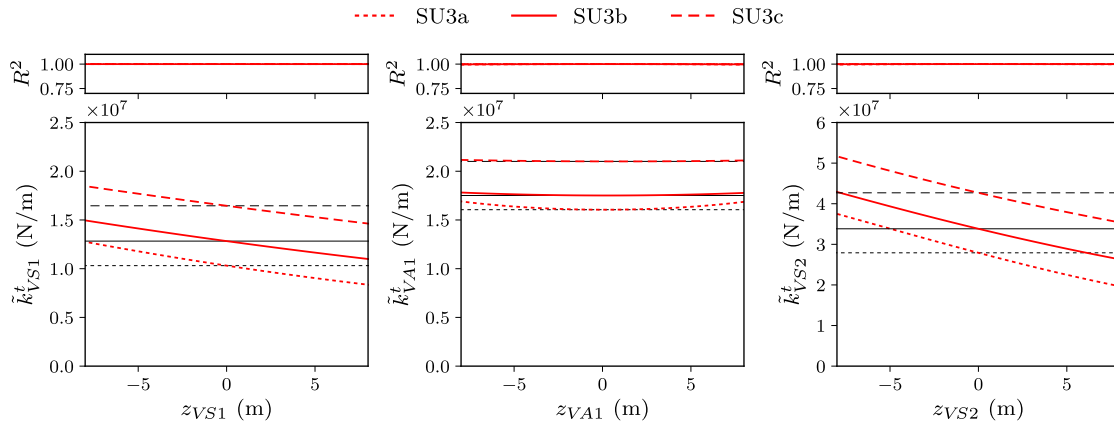


Figure 3.17: One-mode nonlinear generalized stiffness for bridges SU3a, SU3b and SU3c (vertical modes)

3.6.3 One-Mode Analysis of Cable-Stayed Bridges

According to fig. 3.6, the LCM modeling approach of cable-stayed bridges is more reliable compared to the DCM approach for calculating the nonlinear generalized stiffness parameters as demonstrated by higher values for R^2 and more uniform results. For example, R^2 values for the generalized stiffness \tilde{k}_{LA1}^t of bridge CS1 are very close to 1.0 for the LCM approach, but values less than 0.7 were obtained for the DCM technique. Since the modal load used in the nonlinear generalized stiffness analysis includes loads on the stay cables when the DCM approach is utilized, there are significant displacements of the cables which cannot be represented accurately by the linear modes of vibration because the cable displacements evolve nonlinearly. This is also the explanation why both modeling approaches yield different nonlinear generalized stiffness curves, e.g., for \tilde{k}_{LA1}^t , \tilde{k}_{VS2}^t , $\tilde{k}_{\theta S1}^t$ and $\tilde{k}_{\theta S2}^t$. Therefore, the analysis in this section focuses on the LCM results.

Within the displacement bounds, cable-stayed bridges have a stronger nonlinear behavior for the vertical modes. In fig. 3.6a for mode LS1, a slight stiffening effect is observed for bridge CS1. It is explained by the fact that the deck of bridge CS1 is not free to move longitudinally due to the rigid deck-tower connection, which causes a reduced compression in the deck due to nonlinear geometric effects. This is not observed for bridge CS2 because of a different structural system at the deck-tower junction.

For mode VS1, both cable-stayed bridges exhibit a similar behavior, i.e., a relatively constant stiffness for negative generalized displacements (downwards) and a softening for positive generalized displacements (upwards). This reduction in stiffness for mode VS1 is caused by an increased sag of the stay cables as the bridge deck moves upwards. It should be noted

that, in order to obtain a significant softening, large displacements were required. For \tilde{k}_{VA1}^t and \tilde{k}_{VS2}^t , bridges CS1 and CS2 behave differently. This could be explained by the fact that bridge CS1 has crossties that stiffen the cable system, which is not the case for bridge CS2.

Within the displacement bounds, torsional modes behave linearly, but for greater displacements, there is some nonlinear effect. They can be explained by an increased cable sag due to a decrease of the stay cable tensions as shown in fig. 3.16d.

3.6.4 Nonlinear Vertical-Torsional Coupling in Suspension Bridges

According to the colormaps in figs. 3.7–3.9, R^2 is very close to a value of 1.0 confirming the validity of eq. 3.12 for bridges SU2 and SU3b. This is also the case for the other suspension bridges and other vertical-torsional modal pairs.

As it can be observed in figs. 3.7–3.9, the non-zero off-diagonal stiffness terms of the matrix $\tilde{\mathbf{K}}_{V\theta}^t$ prove the existence of nonlinear vertical-torsional mode coupling in suspension bridges. Additionally, it can be seen that the matrix $\tilde{\mathbf{K}}_{V\theta}^t$ is symmetric since the off-diagonal stiffness terms are equal. From the different nonlinear generalized stiffness analyses of the suspension bridges, it is concluded that the nonlinear vertical-torsional coupling is stronger for the symmetric modal pairs than the antisymmetric ones. For example, this can be seen by comparing the generalized loads for symmetric and antisymmetric modes in figs. 3.7–3.9, e.g., comparing fig. 3.8a to fig. 3.9a. Furthermore, the diagonal generalized stiffness terms mostly follow the nonlinear trend obtained for the corresponding one-mode analysis, but a more pronounced effect of a second generalized displacement can be seen for the torsional diagonal stiffness terms.

Even though the coupling is mainly expressed by the existence of non-zero off-diagonal stiffness terms, the diagonal terms of $\tilde{\mathbf{K}}_{V\theta}^t$ are also affected by the application of a second generalized load. Figure 3.10 confirms that this effect is generally small for the five suspension bridges. For the diagonal terms relative to the vertical modes, the variation is less than 1 % for the nonlinear generalized stiffness when z_θ varies and z_V is kept constant. For the torsional diagonal terms of bridges SU1 and SU2, a maximum variation of 3 % is observed over the range of z_V/L_{span} considered in fig. 3.10 for a constant value of $z_\theta b_{cl}/L_{span}$. However, this effect is more pronounced for bridges SU3a, SU3b and SU3c with a maximum variation of 20 % of the torsional diagonal stiffness terms. Also, there is a span length effect of the diagonal terms for bridges SU3a, SU3b and SU3c.

In fig. 3.11, it can be observed that off-diagonal generalized stiffness terms are more important for symmetric modes than antisymmetric modes. This also shows that higher symmetric

modes have a stronger nonlinear coupling. For the same generalized displacements, there is a stronger maximum effect of about 8 % for the second symmetric mode compared to the first symmetric mode with 5 %. However, it should be kept in mind that higher modes are less excited dynamically than fundamental modes as mentioned in section 3.4. For the antisymmetric modal pair, the span length effect does not influence the nonlinear coupling. However, for the symmetric modal pairs, there is a span length effect, which is more noticeable for $\tilde{k}_{VS2,\theta S2}^t$ and $\tilde{k}_{\theta S2,VS2}^t$. Of the five suspension bridges, bridges SU3a, SU3b and SU3c have stronger nonlinear coupling.

Regarding the impact of lateral modes on the nonlinear vertical-torsional coupling of suspension bridges, it can be seen in figs. 3.15a and 3.15b that diagonal stiffness terms for modal pair VS2- θ S2 of bridges SU1 and SU3b are only slightly influenced. Similar observations were made for the three other suspension bridges and the other modal pairs. With the exception of bridges SU1 and SU2 for modes VS2 and θ S2, the off-diagonal vertical-torsional stiffness terms are lightly affected by the simultaneous application of a lateral mode (e.g. fig. 3.15b). For bridges SU1 and SU2 for modes VS2 and θ S2, the effect is more important as shown for bridge SU1 in fig. 3.15a. From these observations, it is possible to conclude that the lateral effects are in most cases negligible on the nonlinear vertical-torsional coupling of suspension bridges.

3.6.5 Nonlinear Vertical-Torsional Coupling in Cable-Stayed Bridges

Within the reference displacement bounds, values of R^2 close to 1.0 were obtained for the two-mode analysis for the cable-stayed bridges as shown in fig. 3.12 for bridge CS1. As with the suspension bridges, the matrix $\tilde{\mathbf{K}}_{V\theta}^t$ is symmetric as shown in fig. 3.12.

The influence of a second generalized displacement on the diagonal stiffness terms can be seen in fig. 3.13. For the vertical diagonal stiffness terms, there is a negligible variation when z_V is kept constant and z_θ varies. In the case of the torsional diagonal terms, a maximum variation of 10 % is observed in fig. 3.13 for a constant z_θ and a varying z_V . Figure 3.14 shows that the off-diagonal terms are generally small, but can reach values around 5 % of the diagonal terms for large generalized displacements.

Similar to the suspension bridges, the lateral modes only slightly modify the diagonal terms of the vertical-torsional stiffness matrix. This is shown in fig. 3.15c for bridge CS1. However, the off-diagonal stiffness terms are more impacted by the lateral effects.

3.6.6 Suspension Bridges vs Cable-Stayed Bridges

First, it should be mentioned that R^2 values are generally lower for cable-stayed bridges compared to suspension bridges. This is explained by the fact that the nonlinear displacement vector utilized in the nonlinear stiffness analysis is difficult to be expressed in terms of the linear modes of vibration in some cases. This is caused by the local nonlinear behavior of the stay cables. Therefore, it is concluded that nonlinear generalized stiffness analysis procedure is more adapted to suspension bridges, but it should be mentioned that it is also possible to obtain good results for cable-stayed bridges for reasonable generalized displacement values.

As discussed previously, the one-mode generalized stiffness parameters for suspension and cable-stayed bridges are more nonlinear for the vertical modes. Comparing the nonlinear generalized stiffnesses of the symmetric vertical modes in figs. 3.5 and 3.6, it is possible to say that the suspension system is more nonlinear than the cable-stayed system.

For two-mode nonlinear analyses, the relative importance of the nonlinear structural coupling is shown to be stronger for suspension bridges than cable-stayed bridges as shown in figs. 3.10, 3.11, 3.13 and 3.14. Moreover, since it is known that suspension bridges are more flexible than cable-stayed bridges, suspension bridges are more likely to have an excursion in the nonlinear range of the nonlinear generalized stiffness parameters. However, further analysis is required to confirm this.

3.6.7 Nonlinear Generalized Stiffness Parameters and Stability of Cable-Supported Bridges

Although this chapter has focused so far on assessing and comparing the level of nonlinearity and the nonlinear structural coupling in cable-supported bridge, it is relevant to discuss briefly how nonlinear generalized stiffness parameters could eventually give information on the effect of nonlinear structural coupling on the stability of bridges.

From the results of two-mode stiffness analysis, it is possible to develop an equivalent two-degree-of-freedom dynamic system representing one vertical mode and one torsional mode, especially for symmetric modal pairs as they are more nonlinear. The idea of such equivalent dynamic system is similar in principles to 2D flutter analysis except that the equivalent system is nonlinear. Including aerodynamic load models into this equivalent nonlinear system would provide preliminary information about the possibility that wind loads and nonlinear coupling lead to large torsional vibrations as demonstrated theoretically by mathematicians using very simple load models. It could be also interesting to see whether

nonlinear structural coupling could influence the flutter onset. Therefore, this approach could give information on nonlinear structural dynamic phenomena and potential structural dynamic instabilities in cable-supported bridges. Such numerical investigations are currently carried out, and experimental validations are also planned to be undertaken. For these investigations, bridges SU3a, SU3b and SU3c are of interest as they showed a stronger nonlinear behavior.

3.7 Conclusions

The nonlinear structural coupling between the modes of vibration, especially vertical-torsional coupling, could be of importance in the prediction of the dynamic response of cable-supported bridges under wind loads. Instead of using simplified models or continuum models relying on nonlinear partial differential equations as used by mathematicians, this initial investigation of vertical-torsional coupling was based on the use of pushover analysis in the context of nonlinear geometric finite element modeling. The proposed method makes use of the static application of modal loads on numerical models of long-span bridges in order to obtain nonlinear generalized stiffness parameters, which are used to quantify in a practical manner the level of nonlinearity and the nonlinear vertical-torsional coupling.

The nonlinear generalized stiffness parameters of five suspension bridges and two cable-stayed bridges were determined for one-mode, two-mode and three-mode analyses. One-mode analyses indicated that vertical modes are more nonlinear than lateral and torsional modes. For suspension bridges, symmetric vertical modes show stronger nonlinear behavior in comparison with antisymmetric vertical modes. The fact that there are non-zero off-diagonal terms in the nonlinear generalized stiffness matrix for two-mode analysis demonstrates the existence of nonlinear structural vertical-torsional coupling in suspension and cable-stayed bridges. Span length has an influence on the nonlinear vertical-torsional coupling. Three-mode analysis shows that lateral modes have in general a slight influence on the nonlinear vertical-torsional coupling with the exception of off-diagonal terms for specific bridges. In general, the nonlinear generalized stiffness procedure is more reliable for suspension bridges than cable-stayed bridges. In comparison with the cable-stayed system, the suspension bridge system exhibits a stronger level of geometric nonlinearity either for one-mode or two-mode analysis.

The method presented in this chapter is useful for providing a better understanding of nonlinear geometric phenomena in cable-supported bridges, especially nonlinear vertical-torsional coupling. Nevertheless, it is not yet possible to associate the potential occurrence

of large torsional vibrations as described by mathematicians to the level of nonlinear vertical-torsional coupling measured from nonlinear generalized stiffness analysis such that nonlinear dynamic analysis would not be required in an initial investigation. Therefore, further research is required to determine whether large torsional vibrations can be obtained using dynamic analysis. Moreover, it is still required to determine whether such coupling could influence the wind response and aeroelastic stability of long-span bridges.

Chapter 4

Theory for Nonlinear Section Model Tests

4.1 Introduction

Since the collapse of the well-known Tacoma Narrows Bridge in 1940, which is generally attributed to torsional flutter [8], a large amount of research has been carried out on the aeroelastic stability of bridges and more specifically on flutter. Since then, wind tunnel tests have been used in the design process of cable-supported bridges, and nowadays, most of their wind design can be made using analytical and numerical approaches. However, recourse to different types of wind tunnel experiments is usually made for characterizing the wind force models used in the analytical approaches and for validation purposes.

Modern wind tunnel tests for bridges as we know them today started at the University of Washington in the 1940s when Prof. F. Burt Farquharson conducted tests for the original Tacoma Narrows Bridge and its replacement [9]. He used what were to become the two most common types of wind tunnel tests, i.e., full-aeroelastic model tests and section model tests. From the fact that all the bridge elements are included in full-aeroelastic models [29], these tests give an accurate response prediction of the full bridge, but the models are expensive and complicated to fabricate. Furthermore, Froude number scaling, which has the inconvenience of limiting testing to low wind speeds, needs to be satisfied in these tests when gravity effects are important (e.g. for suspension bridges). Conversely, section model tests, where a rigid segment of the bridge deck is suspended by a springing system, are simple and affordable in comparison to full-aeroelastic model tests [30]. Compared to full-aeroelastic models, section models can be fabricated at larger scales, therefore reducing Reynolds number effects. However, dynamic section model tests are only able to simulate one vertical mode and one torsional mode at a time, although it is also possible to include a lateral mode [32, 33]. Stability can be evaluated as well as the response of the full bridge to turbulence with a specific post-processing procedure [31]. Midway between full-aeroelastic model tests and section model tests are taut-strip model tests [59]. Taut-strip models can be seen as full-aeroelastic models without towers and cables or as long flexible section models. Since the stiffness for taut-strip models is provided through taut wires or tubes, they are well suited for bridges having sinusoidal modes of vibration. More recently, a multi-supported aeroelastic model was developed to study vortex-induced vibrations [60], but only vertical modes were considered. Even real-time hybrid tests similar to what is used in structural

engineering where the aeroelastic system would be partially modeled in the lab and partially modeled in a numerical model are discussed [61, 62].

As mentioned in the previous paragraph, there have been some developments for different types of wind tunnel tests for bridges over the years, yet section model tests are by far the norm in the field because of their low cost, simplicity and versatility. They can be utilized to measure aerodynamic coefficients (e.g. static coefficients and flutter derivatives), measure the wind and motion-induced surface pressures using pressure taps and predict the dynamic response of the bridge deck. There have also been some improvements made to the procedures used in section model tests. For example, a dynamometric section model was designed [36]. An innovative section model bridge rig that can be used for free- and forced-vibration tests [33, 37] was developed. Another forced-vibration rig that can be used for arbitrary motion [40] was also created. Even though with such advancements in experimental apparatus, section model tests for bridges still rely on the same simplifications in terms of aerodynamic and structural behavior from which originate their simplicity. For example, the aerodynamic contribution of the cables is neglected. Section models can only represent one mode in each direction at a time (lateral, vertical and torsional) and assume uniform mode shapes. Additionally, the structure is assumed to behave linearly from the fact that the modes represented in the wind tunnel originate from linear structural dynamics theory.

However, it is known that cable-supported bridges can exhibit structural nonlinearities such as geometric nonlinearities [149, 150], material nonlinearities [147, 151] as well as localized nonlinearities like hydraulic buffers [12, 17, 151]. Additionally, it is worth noting that mathematicians have shown that dynamic vertical forcing can lead to large torsional oscillations due to nonlinear vertical-torsional mode coupling associated with geometric nonlinearities [166, 168–170]. In [170], these large oscillations caused by structural coupling between the modes of vibration are referred as internal parametric resonance, a structural dynamic instability. This instability is solely structural unlike flutter that is an aeroelastic phenomenon. Nonlinear vertical-torsional coupling in cable-supported bridges was assessed in chapter 3 by applying modal loads to geometrically nonlinear structures. This research showed that single-span suspension bridges have a stronger nonlinear coupling than three-span suspension bridges and cable-stayed bridges. Also, longer spans were shown to be more nonlinear due to the greater contribution of the cable system to the behavior of the bridge.

To the author's knowledge, large oscillations originating from a structural dynamic instability as described in the previous paragraph have never been demonstrated experimentally for

a bridge. Nevertheless, transition from an antisymmetric instability mode to a symmetric instability mode was observed on a full-aeroelastic model of a double-main-span suspension bridge [171]. Internal resonance caused by the aerodynamic and/or structural nonlinearities of the aeroelastic-structural system could be responsible [172, 173]. This would be different than the flutter mode transition of [174]. Such observations have led to many recent studies on nonlinear flutter and aerodynamic nonlinearities in the case of bridges [90, 96, 100, 101, 120]. However, these studies on bridges have only focused on aerodynamic nonlinearities, and structural nonlinearities have not been discussed. The only mention of structural nonlinearities in recent experimental studies for bridges refers to verifications that stiffness and damping nonlinearities of the section model test rig are small and negligible compared to aerodynamic nonlinearities [90, 102, 104]. Nevertheless, the section model test rig in [44–46] shows a slight nonlinear structural behavior for its torsional stiffness for large rotations that are greater than 15° . The nonlinear geometric behavior in torsional stiffness in [44–46] originates from the kinematics of the mechanisms utilized for the section model test rig. Consequently, it is not clear whether this nonlinear structural behavior is representative of an actual cable-supported bridge. Nonetheless, it should be noted that this rig allows for very large amplitudes of vibration, which is of interest in the study of aerodynamic nonlinearities and nonlinear flutter. In [47, 48], another experimental rig able of very large amplitudes was developed for studying aerodynamic nonlinearities, but its structural behavior is linear. In a different civil engineering application of section model tests, the swaying stiffness of a transmission line conductor is provided through a pendulum system, which makes it a geometrically nonlinear test rig [49].

In the field of aeronautics, section models of airfoils have been tested considering different types of structural nonlinearities. For example, some wind tunnel test studies have been performed considering freeplay nonlinearity in rotation [50–53]. In this case, the section model can rotate freely over a small range of rotations, and outside this range, there is a linear moment-rotation relationship. For example, this can be achieved using leaf springs for which one end is able to move freely due to a small gap in a freeplay bracket. Once the free ends of the leaf springs get in touch with the freeplay brackets, the springs provide stiffness to the system [50, 53]. A bilinear behavior has also been considered in the case of airfoils [50, 54–56]. For a hardening bilinear behavior, additional springs are incorporated to the springing system, but they are only active over a certain displacement threshold. To achieve this, leaf springs [50] or contact springs [54] can be utilized. Conversely, for a softening behavior, the additional springs lose tension for displacements over the threshold [55, 56]. Freeplay and bilinear nonlinearities are piecewise nonlinearities, but some work has also been done for continuous stiffness nonlinearities like parabolic and cubic nonlinearities [51, 57, 58].

In [57, 58], a cubic hardening stiffness was achieved using a springing system made of extension springs, cables and nonlinear cam mechanisms. These different experimental studies on airfoils have aimed at developing a better understanding of the effect of structural nonlinearities on the aeroelastic behavior of airfoils, confirming the existence of nonlinear phenomena predicted numerically as well as validating mathematical models combining nonlinear structural effects and nonlinear aeroelastic effects. It is interesting to note that Schwartz et al. [54] demonstrated with wind tunnel tests that the critical velocity for flutter of an airfoil for a hardening bilinear structural behavior is less than for the linear case. It is important to mention that the nonlinear system in [54] was weakly nonlinear as there was only a difference of 14 % between the two stiffness values of the bilinear behavior.

Therefore, considering that even weakly nonlinear systems can exhibit nonlinear dynamic phenomena [175], it appears of practical engineering value to have a better understanding of the possible interaction between structural nonlinearities and aeroelastic effects in cable-supported bridges just like it has been done for airfoils. An experimental approach based on nonlinear section model tests is believed to be the most suitable way to achieve this as the simplicity of section model tests would allow an easier interpretation of nonlinear phenomena in comparison to a full-bridge system. However, in the case of nonlinear tests for airfoils, the nonlinear structural behavior considered in previous experimental studies does not appear to have been calibrated with the nonlinear behavior of actual aircraft structural elements, rather a plausible nonlinear behavior seemed to have been used.

Consequently, this chapter presents the theoretical developments required to take into account a nonlinear structural behavior representative of a cable-supported bridge when conducting section model tests in the wind tunnel. This research is in continuity with the research presented by the author in chapter 3, which was limited to an assessment of structural nonlinearities in cable-supported bridges. Starting from the nonlinear structural behavior characterized using the numerical approach in chapter 3, it is demonstrated how this nonlinear behavior can be scaled with the purpose of conducting section model tests that consider a nonlinear structural behavior representative of a real bridge. Therefore, this examination will open the way for nonlinear section model tests of bridges. Additionally, it will eventually allow a better understanding of the interaction between structural nonlinearities and aeroelastic effects. The goal of such tests would not be to replace more advanced experimental and numerical techniques used for predicting the response of bridges subjected to wind. Instead, such new experimental tool will help develop a better understanding of structural nonlinearities in the context of the aeroelastic behavior of bridges.

At first, a method to characterize nonlinear generalized stiffnesses for cable-supported bridges

is reviewed and applied in the context of nonlinear section model tests. This technique provides a way to determine the nonlinear structural behavior to be utilized for section model tests, but it needs to be scaled properly. For this purpose, a scaling procedure of the nonlinear generalized stiffness parameters is developed by comparing the full-bridge dynamic equations to those of the section model. The assumptions utilized in the scaling procedure are validated using eleven finite element models of long-span bridges. These bridges are also utilized for testing the proposed scaling procedure.

4.2 Section Model Tests for Assessing the Effect of Structural Nonlinearities

4.2.1 Why Section Model Tests Over Other Testing Approaches?

Theoretically, as long as the Froude number scaling is satisfied, full-aeroelastic model tests are intrinsically able to represent geometric nonlinearities of the bridge structure since all bridge elements are modeled. However, the situation is more complicated because simplifications are still used. For example, even though the axial stiffness of the cables is appropriately represented due to the negligible cable stiffness in bending, it is not physically possible to have the correct scaled axial stiffness for the deck and towers at the same time as the correct scaled bending stiffness. Therefore, the standard practice is to size the structural members of the model-scale deck and towers to match the scaled bending stiffness. Consequently, the geometric stiffness for these elements is erroneous, and only the geometric stiffness originating from the cables is modeled correctly in these tests. Even if these difficulties were circumvented, it would still be difficult to perfectly match the structural behavior of the bridge prototype. This is because of a combination of model design factors, manufacturing precision factors and human factors as demonstrated by the difficulty to perfectly match the dynamic properties (natural frequencies and mode shapes) with the target ones in typical full-aeroelastic models. From these facts and the high cost of full-aeroelastic model tests, they do not appear to be the right approach for an initial experimental study of structural nonlinearities. Similarly, taut-strip models in their current form would not be able to include structural nonlinearities. This is because the taut wires or tubes used in these tests already have their own nonlinear behavior that is not representative of a cable-supported bridge. Indeed, there is stiffness softening when a cable-supported bridge moves upwards, whereas a downward displacement is associated with stiffness hardening (see chapter 3). A taut-strip model would exhibit a hardening behavior in both directions.

Consequently, it appears that section model tests could be a realistic alternative for an experimental study of the effect of structural nonlinearities on the wind response of bridges. First, they are relatively affordable as mentioned previously. They are easy to conduct, and their use is well established in the field of bridge engineering. They are versatile from the fact that it is easy to adjust the testing parameters. This is explained by the easy access to the springing system, damping devices and ballast masses at both ends of the section model. Nonlinear tests would therefore be possible by the development of a nonlinear mechanical device that will replace the springing system and from which the section model will be suspended. However, it should be recognized that only one mode in each direction can be represented in section model tests, but this is not a problem because nonlinear structural dynamic phenomena discussed by mathematicians involve specific modes. Therefore, nonlinear section model tests should focus on nonlinear vertical-torsional behavior for these critical modes. This fact is discussed in further detail in section 4.4.7.

4.2.2 Role of Section Model Tests in Bridge Design and Research

In the process of determining the wind loads to be utilized for the design of a cable-supported bridge, it is common practice to utilize an analysis procedure combining wind tunnel tests and numerical simulations. Section model tests are therefore conducted in a wind tunnel with the objectives of measuring the static coefficients for the different structural elements as well as obtaining the flutter derivatives and aerodynamic admittance functions for the bridge deck. Then, these aerodynamic properties measured experimentally are utilized in a dynamic analysis through finite element modeling to determine the flutter and buffeting responses of the bridge under consideration [34, 186–188]. Based on this analysis procedure, section model tests are typically used in the bridge engineering industry for the measurement of aerodynamic properties. Nonetheless, section model tests can also be useful for providing information about dynamic phenomena like vortex-induced vibrations and flutter as well as for easily allowing improvements to the cross section under consideration in the scenario that its stability performance is not adequate.

In research, section model tests have been used extensively in the development of different aerodynamic force models (e.g. [117]). As mentioned in section 4.1, they have also been utilized in recent studies about nonlinear flutter and aerodynamic nonlinearities [90, 96, 100, 101, 120]. Their popularity in the study of aerodynamic nonlinearities as a research tool comes from the fact that they are a simplified representation of the full-bridge aeroelastic system. Therefore, this makes it easier to analyze the effect of aerodynamic nonlinearities. With the same logic, section model tests seem to be an ideal approach for

an initial experimental assessment of the effect of structural nonlinearities on the wind stability of bridges. To achieve such tests, it is first required to determine and scale the nonlinear structural behavior representative of a full bridge, which is the subject of this chapter. It is worth noting that such nonlinear section model tests do not aim at replacing the analysis procedure currently used in the industry that combines section model tests and numerical simulations. Instead, this chapter proposes an improvement to the section model test procedure so that section model tests can be used for assessing the effect of structural nonlinearities on the stability of bridges when subjected to wind.

4.2.3 Structural Nonlinearities vs Aerodynamic Nonlinearities

Before presenting the theoretical developments required for the development of a section model testing procedure able to account for the nonlinear structural behavior of the bridge structure, it is worth briefly discussing the differences between structural nonlinearities and aerodynamic nonlinearities. As mentioned previously, cable-supported bridges can show structural nonlinearities from different origins, i.e., geometric, material and localized. For this research on nonlinear section model tests, it appears reasonable to consider inactive longitudinal hydraulic buffers since they behave as if they are inactive for the mean aerodynamic loads on the bridge deck and because they act like energy-dissipating devices for dynamic actions. Also, it is most likely that the hydraulic buffers will not be effective at high wind speeds. Additionally, material nonlinearities are unlikely to be experienced in a properly designed structure because the cable system in a cable-supported bridge, which is the main structural component, is designed elastically [149]. An analysis for a suspension bridge presented in section 4.5.1 confirms that material nonlinearities are not a concern for the wind response of properly designed bridges since the bridge deck keeps a linear material behavior even for very large displacements.

Another source of structural nonlinearity in cable-supported bridges is structural damping as it is well known that it is amplitude dependent (e.g. [189]). Damping mechanisms in cable-supported bridges are complex, and the total structural damping for these structures comes from different origins such as strain dependent damping, friction damping and foundation damping. Considering the challenge represented by the accurate characterization of nonlinear structural damping in cable-supported bridges, it is deemed sufficient for an initial development of nonlinear section model tests to consider an effective viscous damping, which is a common practice in structural engineering.

Therefore, among the different structural nonlinearities, only the geometric nonlinearities are of interest for the development of nonlinear section model tests. However, depending

on the amplitudes of motion of the bridge deck, the bridge could either behave almost linearly or have excursions in the nonlinear range. Nevertheless, it should be mentioned again that even weakly nonlinear systems can be impacted by nonlinear dynamic phenomena [54, 175]. One way to know whether a bridge can experience structural nonlinearities when subjected to wind is to conduct section model tests that account for the nonlinear geometric behavior. The advantage of using such an experimental approach is that it avoids the need to use advanced nonlinear aerodynamic force models that could be required in the case of a numerical approach.

Regarding aerodynamic nonlinearities, it is important to recognize that they represent a separate problem with respect to structural nonlinearities. They are external force nonlinearities that originate from the complex flow behavior around a bridge deck. The amplitude dependence of flutter derivatives (e.g. [90]) is an example of aerodynamic nonlinearities. Another demonstration of the nonlinear aerodynamic behavior is the hysteretic behavior of dynamic aerodynamic force coefficients (e.g. [92]). Since structural nonlinearities and aerodynamic nonlinearities are two separate problems, the occurrence of the former do not lead to the occurrence of the latter and vice versa. However, it is reasonable to say that both sources of nonlinearities would be solicited for sufficiently large amplitudes of vibration. Therefore, even though this chapter only focuses on structural nonlinearities, it should be noted that section model tests that account for a geometrically nonlinear structural behavior would automatically include aerodynamic nonlinearities.

4.3 Nonlinear Generalized Stiffness

Based on research made in aerospace engineering regarding dynamic analysis of geometrically nonlinear systems (e.g. [190]), it is possible to utilize the linear mode shapes to transform a geometrically nonlinear problem into a nonlinear problem in modal coordinates. To do so, the restoring forces in the geometrically nonlinear problem are written by separating the linear stiffness contribution and nonlinear stiffness contribution. As for the linear case, the linear contribution corresponds to the product of the linear stiffness matrix and displacement vector. The nonlinear contribution is a force vector that is a function of the displacement vector. After applying a modal transformation using the linear mode shapes, the usual generalized structural matrices (mass, damping and linear stiffness) are obtained. For the nonlinear restoring force vector, a nonlinear generalized force vector needs to be determined. Consequently, each component of the nonlinear generalized force vector can be written as a combination of parabolic and cubic stiffness terms of the generalized

displacements. Such a reduced-order modeling approach allows a significant reduction in the size of the nonlinear structural system to be solved since it was demonstrated that only a few modes need to be included to get good results [190]. However, because of the nonlinear modal coupling that exists due to the nonlinear generalized force vector, the equations of the nonlinear generalized system have to be solved simultaneously.

This idea of reducing a geometrically nonlinear dynamic system will be applied in the context of section model tests of bridges in section 4.4, but before showing how this can be done, it is suggested to utilize a different approach to characterize the nonlinear generalized stiffness. In [190], the nonlinear evolution of the nonlinear generalized restoring forces is supposed to be quadratic and cubic. However, cable-supported bridges are more complex than the structures analyzed in [190], and it is unlikely that quadratic and cubic behaviors are sufficient for such structures. Instead, the procedure developed by the author in chapter 3 will be utilized as it does not presuppose the evolution of the nonlinear generalized forces. This procedure was originally developed for an assessment of the nonlinear vertical-torsional coupling in cable-supported bridges. Unlike the approach in [190], the one in chapter 3 combines the linear and nonlinear contributions into the nonlinear generalized restoring force vector. This is shown in section 4.3.1 where the numerical procedure of chapter 3 is reviewed for the sake of completeness.

4.3.1 Overview of Numerical Approach

As shown in fig. 4.1, the dynamic system of a bridge section model considered for nonlinear tests possesses two degrees of freedom (DOF). This system can therefore move in a vertical mode and in a torsional mode. Unlike for linear tests for which the stiffness of the system in fig. 4.1 can be determined from the mass properties and natural frequencies, it is needed to determine a nonlinear force-displacement relationship representative of the full-bridge behavior in the case of nonlinear tests. As mentioned before, this is achieved by using the two-mode nonlinear generalized stiffness analysis presented in chapter 3. Nonlinear generalized stiffness analysis consists in applying static loads proportional to modes of vibration to a nonlinear finite element model of a cable-supported bridge. This allows quantifying the nonlinear behavior of the bridge in terms of dynamic properties or more specifically, selected modes of vibration. As mentioned in section 4.2.3, nonlinear generalized stiffness analysis in this study will only account for geometric nonlinearities since future nonlinear section model tests will only take them into account. The reader is referred to chapter 3 for a detailed presentation of nonlinear generalized stiffness analysis.

As for 2-DOF section model tests, one vertical mode ϕ_v and one torsional mode ϕ_θ of

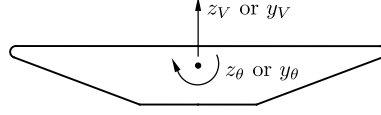


Figure 4.1: Dynamic system of a bridge section model

analogous shapes are considered for the modal load vector used in the two-mode nonlinear generalized stiffness procedure. In the approach, the following nonlinear static equation has to be solved:

$$\mathbf{f}_{SG}(\mathbf{u}_{nl}) = \mathbf{p}_{V\theta}^m \quad (4.1)$$

$$\mathbf{p}_{V\theta}^m = \mathbf{p}_V^m + \mathbf{p}_\theta^m = a_V \omega_V^2 \mathbf{M} \boldsymbol{\phi}_V + a_\theta \omega_\theta^2 \mathbf{M} \boldsymbol{\phi}_\theta \quad (4.2)$$

where $\mathbf{f}_{SG}(\mathbf{u}_{nl})$ is the internal force vector of the nonlinear geometric system; \mathbf{u}_{nl} is the nonlinear displacement vector obtained from nonlinear static analysis; \mathbf{M} is the mass matrix calculated using the finite element method; a_V and a_θ are respectively the modal load coefficients for mode $\boldsymbol{\phi}_V$ and mode $\boldsymbol{\phi}_\theta$; $\omega_V = 2\pi f_V$ and $\omega_\theta = 2\pi f_\theta$ are respectively the natural angular frequencies for mode $\boldsymbol{\phi}_V$ and mode $\boldsymbol{\phi}_\theta$; f_V and f_θ are the natural frequencies for mode $\boldsymbol{\phi}_V$ and mode $\boldsymbol{\phi}_\theta$. In eq. 4.1, the reference state of the bridge numerical model is the dead-load configuration represented by the static equilibrium after the application of the self-weight of the bridge. The natural frequencies and mode shapes in eq. 4.2 are also calculated at the dead-load configuration. To facilitate the physical interpretation of the generalized displacements, modes are normalized such that the maximum vertical displacement is unity for $\boldsymbol{\phi}_V$ and the maximum torsional rotation is unity for $\boldsymbol{\phi}_\theta$. In eq. 4.2, it should be noted that the linear natural frequencies ω_V and ω_θ are utilized in the modal load vector as scaling factors. By doing so and because of the mode normalization considered, the modal load coefficients a_V and a_θ can be interpreted as the maximum linear deck displacement or rotation. This interpretation facilitates the selection of a range of values to be considered for a_V and a_θ . This is explained in detail in chapter 3.

The nonlinear displacement vector, i.e., the solution of eq. 4.1, can be approximated using:

$$\mathbf{u}_{nl} \approx \boldsymbol{\phi}_V z_V + \boldsymbol{\phi}_\theta z_\theta = \boldsymbol{\Phi}_{V\theta} \mathbf{z}_{V\theta} \quad (4.3)$$

where $\boldsymbol{\Phi}_{V\theta} = [\boldsymbol{\phi}_V \ \boldsymbol{\phi}_\theta]$ and $\mathbf{z}_{V\theta} = [z_V \ z_\theta]^T$; z_V and z_θ are respectively the vertical mode

generalized displacement and torsional mode generalized displacement. It is possible to calculate the generalized displacements by premultiplying eq. 4.3 by $\Phi_{V\theta}^T \mathbf{M}$.

As demonstrated in chapter 3, the premultiplication of eq. 4.3 by $\Phi_{V\theta}^T \mathbf{M}$ can be seen as solving a linear least squares problem for which an uncentered coefficient of determination R^2 can be evaluated. The uncentered coefficient of determination can be used to judge whether the vector \mathbf{u}_{nl} is not too distorted in comparison to the linear combination of the modes, i.e., the linear modes of vibration are able to represent the nonlinear geometric response of the structure. The analysis performed in chapter 3 for seven different bridge structures showed that R^2 is very close to one. Consequently, the linear modes of vibration are adequate for modeling the nonlinear geometric response of bridges.

The generalized loads are calculated using the following equation:

$$\tilde{\mathbf{p}}_{V\theta}^m = \Phi_{V\theta}^T \mathbf{p}_{V\theta}^m = \begin{bmatrix} \tilde{p}_V^m \\ \tilde{p}_\theta^m \end{bmatrix} = \begin{bmatrix} a_V \omega_V^2 \tilde{m}_V \\ a_\theta \omega_\theta^2 \tilde{m}_\theta \end{bmatrix} \quad (4.4)$$

where $\tilde{m}_V = \phi_V^T \mathbf{M} \phi_V$ and $\tilde{m}_\theta = \phi_\theta^T \mathbf{M} \phi_\theta$ are the generalized masses for mode ϕ_V and mode ϕ_θ . By using eqs. 4.1 and 4.3 for different values of the modal load coefficients a_V and a_θ and calculating the corresponding generalized loads using eq. 4.4, a nonlinear generalized force-displacement relationship $\tilde{\mathbf{p}}_{V\theta}^m$ vs $\mathbf{z}_{V\theta}$ can be obtained. The two-mode tangent nonlinear generalized stiffness matrix $\tilde{\mathbf{K}}_{V\theta}^t$, which is a function of $\mathbf{z}_{V\theta}$, is then calculated as follows:

$$\tilde{\mathbf{K}}_{V\theta}^t(\mathbf{z}_{V\theta}) = \frac{\partial \tilde{\mathbf{p}}_{V\theta}^m}{\partial \mathbf{z}_{V\theta}} = \begin{bmatrix} \frac{\partial \tilde{p}_V^m}{\partial z_V} & \frac{\partial \tilde{p}_V^m}{\partial z_\theta} \\ \frac{\partial \tilde{p}_\theta^m}{\partial z_V} & \frac{\partial \tilde{p}_\theta^m}{\partial z_\theta} \end{bmatrix} \quad (4.5)$$

$\tilde{\mathbf{K}}_{V\theta}^t(\mathbf{z}_{V\theta})$ can be interpreted as the tangent stiffness matrix of an equivalent 2-DOF system (fig. 4.1) of the bridge structure which accounts for the nonlinear geometric behavior in a synthetic manner. From this fact, it is possible to define a generalized restoring force vector for this equivalent system:

$$\tilde{\mathbf{f}}_{V\theta}(\mathbf{z}_{V\theta}) = \tilde{\mathbf{p}}_{V\theta}^m = \begin{bmatrix} \tilde{f}_V(z_V, z_\theta) \\ \tilde{f}_\theta(z_V, z_\theta) \end{bmatrix} \quad (4.6)$$

By the same fact, the tangent stiffness matrix can be equivalently defined as:

$$\tilde{\mathbf{K}}_{V\theta}^t(\mathbf{z}_{V\theta}) = \frac{\partial \tilde{\mathbf{f}}_{V\theta}}{\partial \mathbf{z}_{V\theta}} = \begin{bmatrix} \frac{\partial \tilde{f}_V}{\partial z_V} & \frac{\partial \tilde{f}_V}{\partial z_\theta} \\ \frac{\partial \tilde{f}_\theta}{\partial z_V} & \frac{\partial \tilde{f}_\theta}{\partial z_\theta} \end{bmatrix} \quad (4.7)$$

Therefore, it is seen that the equivalent nonlinear system of eqs. 4.6 and 4.7 can represent the individual nonlinear vertical behavior, individual nonlinear torsional behavior and nonlinear vertical-torsional coupling for the modes under consideration. This is the information that is needed for nonlinear section model tests.


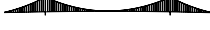









Since material nonlinearities and hydraulic buffers are not of concern in this study, only geometric nonlinearities are considered in calculating $\tilde{\mathbf{f}}_{V\theta}(\mathbf{z}_{V\theta})$ and $\tilde{\mathbf{K}}_{V\theta}^t(\mathbf{z}_{V\theta})$ as mentioned previously. This is reasonable in the context of assessing the wind behavior of cable-supported bridges. By doing so, the full bridge is therefore a conservative mechanical system and the same applies to the equivalent 2-DOF nonlinear system represented by eqs. 4.6 and 4.7. This fact will ease the design process of a nonlinear mechanical system to be utilized in the wind tunnel.

4.3.2 Numerical Models of Cable-Supported Bridges

With the objective of studying the nonlinear structural behavior of bridges using the nonlinear generalized stiffness analysis procedure of section 4.3.1 as well as developing nonlinear section model tests, numerical models of eleven cable-supported bridges were created. The eleven bridges considered in this research, which are nine suspension bridges and two cable-stayed bridges, are described in table 4.1 (see appendix A for more detail). Since it was demonstrated that single-span suspension bridges have a stronger nonlinear behavior (see chapter 3), four preliminary designs of single-span suspension bridges were developed for this study, i.e., bridges SU4a, SU4b, SU4c and SU4d. The other bridges in table 4.1 correspond to the seven long-span bridges utilized for developing nonlinear generalized stiffness analysis, and therefore, more details about them can be found in chapter 3. Information about the finite element models of the single-span suspension bridges is presented in table 4.2. This table shows the number of elements of each single-span suspension bridge as well as the natural frequencies for the dead-load configuration of the first three lateral, vertical and torsional modes for these bridges. The computational times for the nonlinear generalized stiffness analyses for these bridges are also included in table 4.2.

For the bridge decks of bridges SU4a, SU4b, SU4c and SU4d, the same steel twin-box girder was assumed considering that the same hanger spacing was used, but the cable system and towers were sized based on the different span lengths. The same sag-to-span ratio is utilized

Table 4.1: Description of cable-supported bridges

Bridge	Type	Main span (m)	Buffers?	Elevation view
SU1	Three-span suspension Continuous girder	1550	Yes	
SU2	Three-span suspension Continuous girder	1624	Yes	
SU3a	Three-span suspension Partially continuous girder	2460	Yes	
SU3b	Three-span suspension Partially continuous girder	3300	Yes	
SU3c	Three-span suspension Partially continuous girder	4140	Yes	
SU4a	Single-span suspension Girder restrained at towers	1200	Yes	
SU4b	Single-span suspension Girder restrained at towers	1800	Yes	
SU4c	Single-span suspension Girder restrained at towers	2400	Yes	
SU4d	Single-span suspension Girder restrained at towers	3000	Yes	
CS1	Cable-stayed Rigid deck-tower connection	856	No	
CS2	Cable-stayed Continuous girder	1018	Yes	


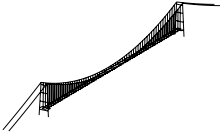
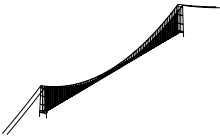
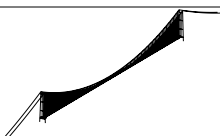
for these preliminary designs. Their designs were inspired by the design of bridge SU3b, which is an existing design of a three-span suspension bridge with very short side spans that behaves like a single-span suspension bridge.

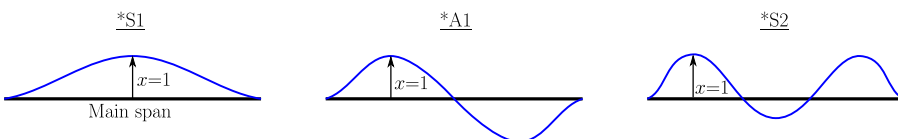
All the finite element models of the eleven bridges in table 4.1 were developed using the open-source finite element program *Code Aster* [180]. These models were validated using the commercial finite element software *SAP2000* [191]. For these numerical models, the fishbone modeling approach was utilized. The bridge deck, modeled as Timoshenko beam elements, is connected to the cable system through rigid elements. The towers are modeled as Timoshenko beam elements. Tension-only truss elements are considered for the cable system, for which the cable preloads are applied using temperature loads. For the cable-stayed bridges, the lumped cable mass approach was utilized, for which half of the mass of each stay cable is lumped at both ends. In order to account for geometric nonlinearities, all finite element analyses discussed herein are large displacement ones.

4.3.3 Results for Two-Mode Analysis of Single-Span Suspension Bridges

To put in context the nonlinear structural behavior that will have to be accounted for in nonlinear section model tests, it is relevant to present sample results for the two-mode nonlinear generalized stiffnesses of eq. 4.7. This is done for the single-span suspension bridges

Table 4.2: Description of finite element models of single-span suspension bridges (L: lateral, V: vertical, θ : torsion, S: symmetric, A: antisymmetric, 1MA: one-mode analysis, 2MA: two-mode analysis, 3MA: three-mode analysis)

Bridge	Model	Number of elements	Natural frequencies (Hz)			CPU time (min)
			Sym.	Antisym.	Sym.	
SU4a		Truss: 210 Beam: 384	LS1: 0.070	LA1: 0.203	LS2: 0.362	1MA: 0.2 2MA: 13 3MA: 199
			VS1: 0.136	VA1: 0.088	VS2: 0.182	
			θ S1: 0.244	θ A1: 0.252	θ S2: 0.384	
SU4b		Truss: 310 Beam: 504	LS1: 0.045	LA1: 0.110	LS2: 0.196	1MA: 0.2 2MA: 16 3MA: 242
			VS1: 0.109	VA1: 0.074	VS2: 0.145	
			θ S1: 0.178	θ A1: 0.168	θ S2: 0.257	
SU4c		Truss: 414 Beam: 624	LS1: 0.036	LA1: 0.075	LS2: 0.127	1MA: 0.2 2MA: 19 3MA: 275
			VS1: 0.093	VA1: 0.065	VS2: 0.124	
			θ S1: 0.140	θ A1: 0.126	θ S2: 0.194	
SU4d		Truss: 514 Beam: 744	LS1: 0.031	LA1: 0.058	LS2: 0.091	1MA: 0.3 2MA: 23 3MA: 315
			VS1: 0.083	VA1: 0.059	VS2: 0.110	
			θ S1: 0.115	θ A1: 0.100	θ S2: 0.155	



since such results for the other bridges of table 4.1 can be found in chapter 3. Therefore, the two-mode nonlinear generalized stiffnesses in a normalized form for bridges SU4a, SU4b, SU4c and SU4d are presented in fig. 4.2 for the first symmetric and antisymmetric modes. In this figure, the diagonal terms of the nonlinear generalized stiffness matrix $\tilde{\mathbf{K}}_{V\theta}^t$ are normalized with respect to the linear generalized stiffnesses \tilde{k}_V and \tilde{k}_θ . For the presentation of the off-diagonal terms, the normalized quantities $(\tilde{k}_{V\theta}^t/b_{cl})/\tilde{k}_V$ and $(\tilde{k}_{\theta V}^t/b_{cl})/\tilde{k}_\theta$ are used since the off-diagonal terms have different units than the linear generalized stiffnesses. In the expressions for the normalized off-diagonal terms, b_{cl} is half of the distance between the cables at deck height. These normalized quantities are presented in terms of the normalized generalized displacements, i.e., z_V/L_{span} and $z_\theta b_{cl}/L_{span}$ where L_{span} is the main span length. The displacement limits considered in fig. 4.2 correspond to realistic values for the wind response of cable-supported bridges (see chapter 3).

By comparing fig. 4.2a for the first symmetric modes to fig. 4.2b for the first antisymmetric modes, it is clear that the nonlinear generalized stiffness matrix $\tilde{\mathbf{K}}_{V\theta}^t$ is more nonlinear for the first symmetric modes since a linear behavior is observed for the first antisymmetric

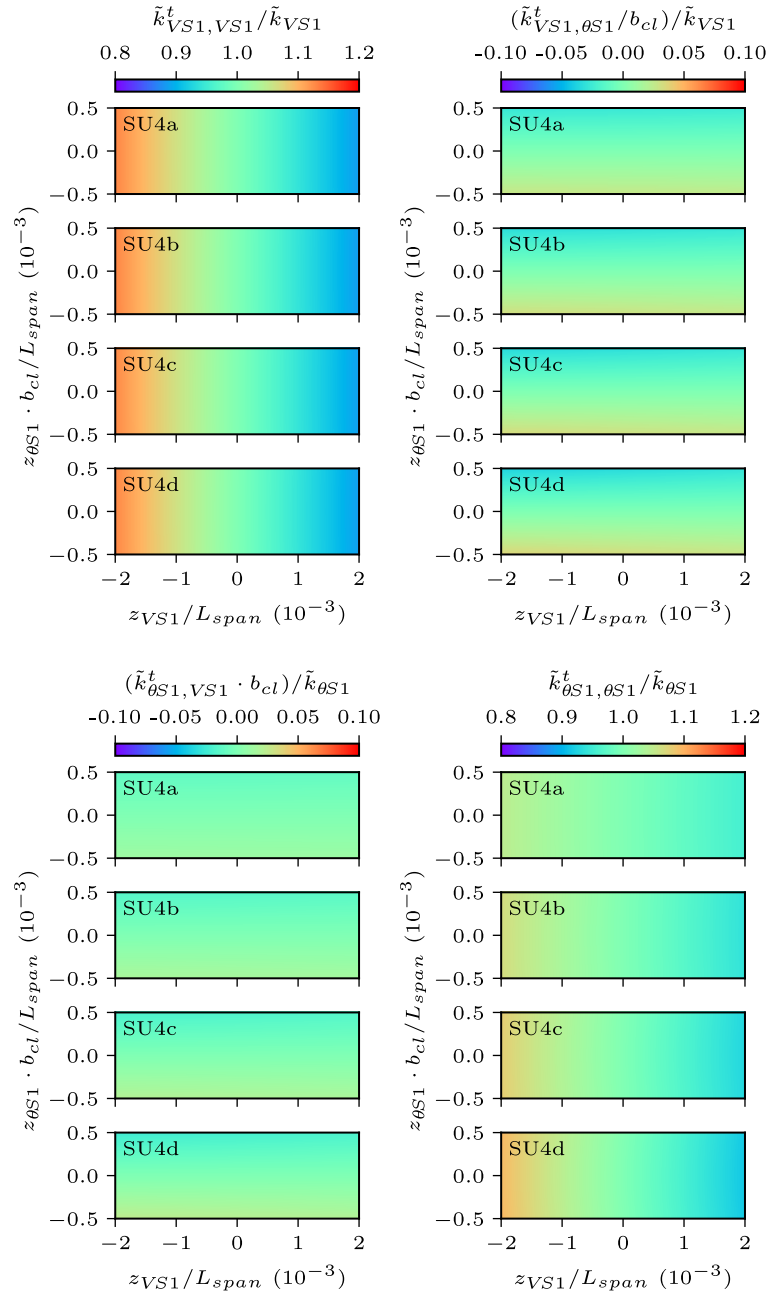
(a) Modes VS1 and $\theta S1$

Figure 4.2: Nonlinear generalized stiffness terms for single-span suspension bridges

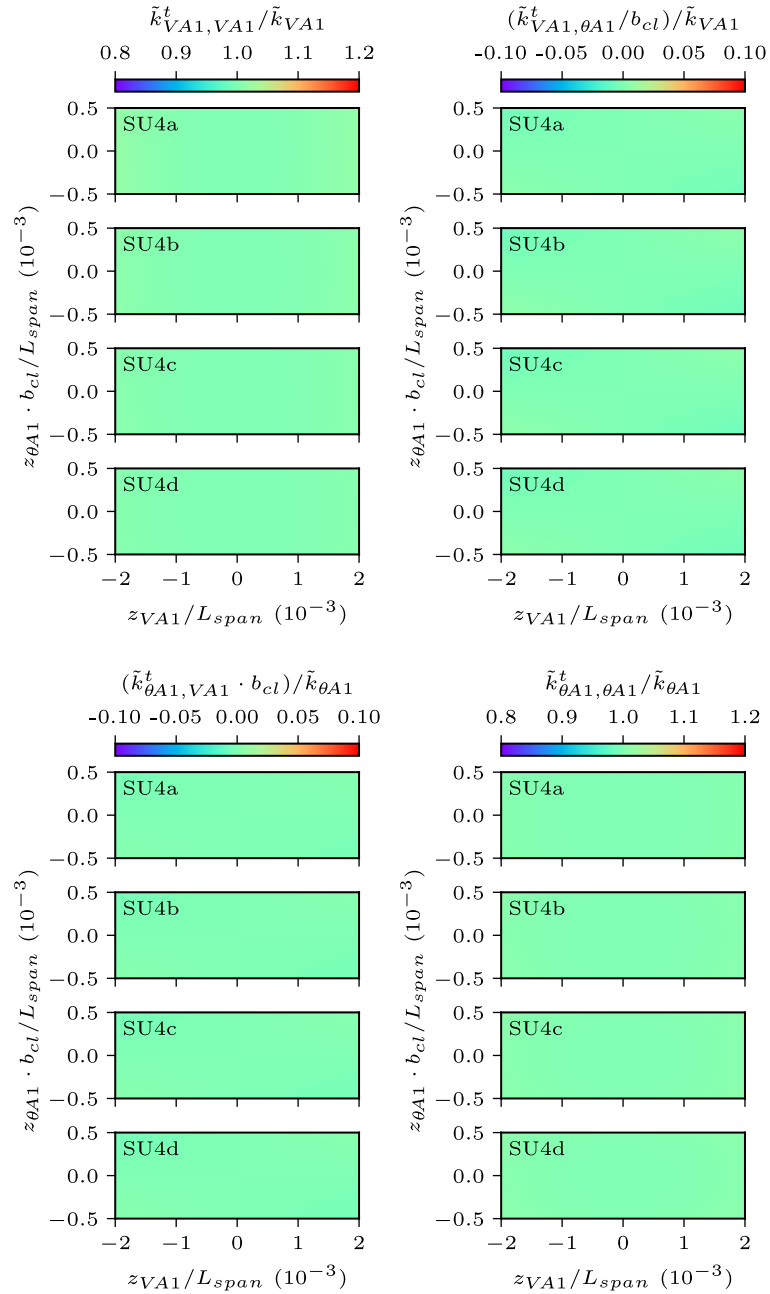
(b) Modes VA1 and $\theta A1$

Figure 4.2: Nonlinear generalized stiffness terms for single-span suspension bridges (cont.)

modal pair. Cable nonlinearity is responsible for the nonlinear behavior observed in fig. 4.2a. For the generalized displacement limits used, the nonlinear contribution to $\tilde{k}_{VS1,VS1}^t$ reaches $\pm 13\%$. For bridges SU4c and SU4d, the nonlinear contribution to $\tilde{k}_{\theta S1,\theta S1}^t$ reaches $\pm 8\%$. For the off-diagonal terms in fig. 4.2a, the maximum nonlinear contribution is about $\pm 4\%$. From this discussion, it appears that nonlinear section model tests would be relevant for the first symmetric modal pair.

4.4 Theory for Nonlinear Section Model Tests

The nonlinear structural behavior described by eqs. 4.6 and 4.7 that is obtained using the procedure summarized in section 4.3.1 will be considered for nonlinear section model tests. Consequently, as it will be discussed in what follows, the section model with a nonlinear structural behavior can be seen as a reduced-order model.

4.4.1 Modal Equations of Full Bridge

It is now required to determine how to scale the nonlinear stiffness parameters of eqs. 4.6 and 4.7 in order to be able to use them for nonlinear section model tests. This scaling procedure starts with a comparison of the full-bridge dynamic equations to those of the section model. This is done in order to determine mode correction factors to be applied to the nonlinear structural behavior given in eq. 4.6.

For line-like structures like cable-supported bridges, it is common to treat the dynamic system used for wind analysis as a continuous system [192, 193]. Therefore, the deck displacements of the full bridge can be expressed in the modal space as follows:

$$\mathbf{u}_{deck}(x, t) = \sum_{j=1}^n \boldsymbol{\psi}_j(x) z_j(t) \quad (4.8)$$

$$\mathbf{u}_{deck}(x, t) = \begin{bmatrix} p(x, t) \\ h(x, t) \\ \alpha(x, t) \end{bmatrix} \quad \boldsymbol{\psi}_j(x) = \begin{bmatrix} \psi_j^p(x) \\ \psi_j^h(x) \\ \psi_j^\alpha(x) \end{bmatrix} \quad (4.9)$$

where $\mathbf{u}_{deck}(x, t)$ is the displacement vector of the deck containing functions for the horizontal displacement $p(x, t)$, vertical displacement $h(x, t)$ and torsional rotation $\alpha(x, t)$; $\boldsymbol{\psi}_j(x)$ is a mode vector containing the functions for the modal horizontal displacement $\psi_j^p(x)$, modal

vertical displacement $\psi_j^h(x)$ and modal torsional rotation $\psi_j^\alpha(x)$; $z_j(t)$ is the generalized coordinate; x is the position along the deck; t is the time. The bridge-deck modal functions $\psi_j^p(x)$, $\psi_j^h(x)$ and $\psi_j^\alpha(x)$ can be extracted from the mode shape vector $\boldsymbol{\phi}_j$ obtained from finite element analysis.

For a modal approach for a linear structure, a system of uncoupled differential equations having the following form is utilized:

$$\tilde{m}_j \ddot{z}_j(t) + 2\xi_j \omega_j \tilde{m}_j \dot{z}_j(t) + \omega_j^2 \tilde{m}_j z_j(t) = \tilde{p}_j(t) \quad (4.10)$$

where ξ_j is the damping ratio of mode $\boldsymbol{\psi}_j(x)$; $\tilde{p}_j(t)$ is the generalized force for mode $\boldsymbol{\psi}_j(x)$. Even though only loads on the bridge deck are considered herein, it is required to account for the entire bridge when calculating the generalized mass since all the structure responds dynamically to the excitation. Therefore, the generalized mass in eq. 4.10 is defined as:

$$\tilde{m}_j = \int_{L_{br}} \boldsymbol{\psi}_j^{all}(x)^\top \mathbf{m}(x) \boldsymbol{\psi}_j^{all}(x) dx \quad (4.11)$$

where L_{br} is the length of the bridge; $\boldsymbol{\psi}_j^{all}(x) = [\psi_j^p(x) \ \psi_j^h(x) \ \psi_j^\alpha(x) \ \dots \ \psi_j^{p,cable}(x) \ \psi_j^{h,cable}(x)]^\top$ is a vector similar to $\boldsymbol{\psi}_j(x)$ in eq. 4.9 except that it accounts for all structural elements (deck, towers and cables), which means that $\boldsymbol{\psi}_j(x)$ is a subset of $\boldsymbol{\psi}_j^{all}(x)$; $\mathbf{m}(x)$ is a diagonal matrix having on its diagonal the mass functions of the different structural elements considered in $\boldsymbol{\psi}_j^{all}(x)$. For modern structural engineering practice, eq. 4.11 is impractical, and it is more practical to calculate the generalized mass using the following finite element approach:

$$\tilde{m}_j = \boldsymbol{\phi}_j^\top \mathbf{M} \boldsymbol{\phi}_j \quad (4.12)$$

Theoretically, eqs. 4.11 and 4.12 would yield the same values for \tilde{m}_j for a sufficiently discretized finite element model. From this, eq. 4.12 is preferred in this study.

The loads on the cables and towers are neglected, and only the loads applied to the deck are accounted for. Hence, the generalized force can be expressed as:

$$\tilde{p}_j(t) = \int_{L_{br}} \boldsymbol{\psi}_j(x)^\top \mathbf{p}(x, t) dx = \int_{L_{br}} [\psi_j^p(x) D(x, t) + \psi_j^h(x) L(x, t) + \psi_j^\alpha(x) M(x, t)] dx \quad (4.13)$$

where $\mathbf{p}(x, t) = [D(x, t) \ L(x, t) \ M(x, t)]^T$ is the external force vector; $D(x, t)$, $L(x, t)$ and $M(x, t)$ are respectively the lateral force, vertical force and torsional moment per unit length applied to the bridge deck.

For nonlinear section model tests, the lateral effects are not of concern and can be neglected as demonstrated by the marginal effect of lateral modes on the nonlinear generalized stiffness parameters (see chapter 3). Further simplifications are possible by recognizing that most modes of vibration for the bridges utilized in this research possess negligible bridge-deck displacement coupling. Therefore, a vertical mode $\psi_V(x)$ and a torsional mode $\psi_\theta(x)$ having analogous shapes can be simplified as follows:

$$\psi_V(x) = \begin{bmatrix} 0 \\ \psi_V^h(x) \\ 0 \end{bmatrix} \quad \psi_\theta(x) = \begin{bmatrix} 0 \\ 0 \\ \psi_\theta^\alpha(x) \end{bmatrix} \quad (4.14)$$

Hence, eq. 4.10 can be specialized for a vertical mode $\psi_V(x)$ and for a torsional mode $\psi_\theta(x)$, which are of interest for the development of nonlinear section model tests:

$$\tilde{m}_V \ddot{z}_V(t) + 2\xi_V \omega_V \tilde{m}_V \dot{z}_V(t) + \omega_V^2 \tilde{m}_V z_V(t) = \int_{L_{br}} \psi_V^h(x) L(x, t) dx \quad (4.15)$$

$$\tilde{m}_\theta \ddot{z}_\theta(t) + 2\xi_\theta \omega_\theta \tilde{m}_\theta \dot{z}_\theta(t) + \omega_\theta^2 \tilde{m}_\theta z_\theta(t) = \int_{L_{br}} \psi_\theta^\alpha(x) M(x, t) dx \quad (4.16)$$

Since it was shown that symmetric vertical-torsional modal pairs are more nonlinear than antisymmetric ones (see section 4.3.3 and chapter 3), nonlinear section model tests will focus on the first symmetric modal pair as it is likely the most critical symmetric pair for causing a structural instability or impacting aeroelastic stability. This means that linear tests are sufficient for the first antisymmetric modal pair, whereas nonlinear section model tests would be relevant for the first symmetric modal pair.

It is typically the modes with the lowest natural frequencies that are critical for flutter. For example, the first symmetric modes of the Akashi Kaikyo Bridge (main span of 1991 m) have the lowest frequencies, hence they are critical for flutter [194]. For the Messina Strait Bridge (main span of 3300 m), the first antisymmetric modes are critical as they have frequencies that are lower than the first symmetric modes [17]. A counterexample to this rule is the Izmit Bay Bridge (main span of 1550 m) for which the first antisymmetric modes and first

symmetric modes lead to practically the same flutter wind speed [174]. It is worth noting that an important factor is also the torsional-to-vertical frequency ratio, which is different for the antisymmetric modes and symmetric modes. Additionally, for bridges with very long spans, the natural frequencies are very close to each other, and it is not possible a priori to know whether the first antisymmetric modes or the first symmetric modes would be critical. This is because the antisymmetric and symmetric instabilities could have very similar critical wind speeds for flutter just like for the Izmit Bay Bridge. This is actually the case for some of the bridges in table 4.1. For example, using 2D flutter analysis in the frequency domain for bridge SU4c, it was found that the antisymmetric instability has a critical velocity of 88.3 m/s, whereas a flutter wind speed of 92.3 m/s was found for the first symmetric modes. Both critical velocities are therefore very close. Consequently, it is worth asking whether a nonlinear structural behavior could trigger the symmetric instability to happen for a lower wind speed than for the antisymmetric case. Considering the observations made in [54] on an airfoil, that could be a possibility as the nonlinear structural behavior was shown to lower the critical velocity in comparison to the linear case.

From this discussion, the theory for nonlinear section model tests would definitely be relevant for bridges having the first symmetric modes critical for flutter. In the case of bridges that are found to be critical for the first antisymmetric modes, nonlinear section model tests would still be of interest in order to check whether the nonlinear structural behavior could trigger an instability with a critical wind speed lower than what is obtained from a linear approach. Additionally, it is of interest to mention that nonlinear section model tests could be of interest for other structural systems than those considered in this research. For example, nonlinear section model tests could be interesting for double-main-span suspension bridges, such as the Maanshan Bridge in China [195] and the Chacao Bridge under construction in Chili. This is because the first antisymmetric modes in these structures would involve cable nonlinearity from the change in sag of the main cables from the modal displacements (e.g. see [195]). For these reasons, the theory for nonlinear section model tests of bridges is developed with the first symmetric modal pair in mind. Therefore, unless specifically mentioned, the modes that are considered from now on are the first symmetric ones.

4.4.2 Generalized Aerodynamic Forces

It is required to include all the different types of wind loads in this development considering that the superposition of the structural responses from the different wind effects cannot be used in the case of nonlinear analysis. Therefore, it is required to take into account of the mean aerodynamic forces, self-excited forces and buffeting forces for determining the

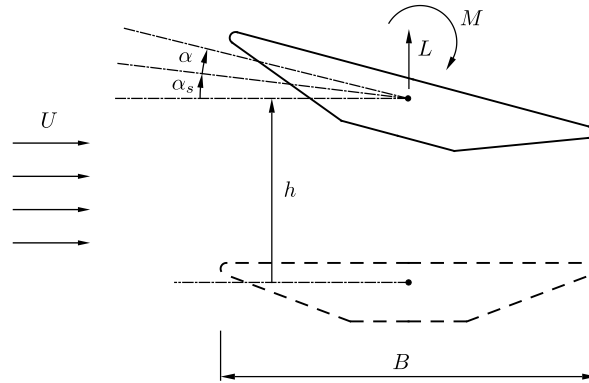


Figure 4.3: Displacements and aerodynamic forces for a bridge deck

scaling procedure to be utilized for nonlinear section model tests. As shown in fig. 4.3, only the vertical force and displacement as well as the torsional moment and rotation are considered herein. An angle of attack of 0° is also considered.

For this demonstration, we make use of linear wind load models since one of the objectives of section 4.4 is to find mode correction factors for the nonlinear structural behavior of eq. 4.6. This choice was made considering the fact that nonlinear force models would make impossible the mathematical simplifications required to determine mode correction factors. Doing so appear reasonable according to the observations made in [60] for a comparison in the case of vortex-induced vibrations between mode correction factors determined experimentally and theoretical factors obtained considering linear force models. Consequently, the mean aerodynamic forces are expressed using a linearized model accounting for the effect of the mean static rotation. With regard to the self-excited forces and buffeting forces, linear force models based on flutter derivatives and aerodynamic admittance functions are utilized due to their compact mathematical form. Another option would have been to use time-domain force models relying on convolution integrals and indicial or rational functions, but doing so has the inconvenience of making the mathematical equations longer. However, using a similar procedure in the case of the linear time-domain force models, it is easy to demonstrate that the same mode correction factors are obtained. Therefore, for the sake of finding the mode correction factors, frequency-domain models are sufficient since, just like the linear time-domain models, they assume the superposition of the aerodynamic effects. This is further discussed at the end of section 4.4.7.

The mean aerodynamic forces on the bridge deck of fig. 4.3 are expressed as follows:

$$L_s(x) = \frac{1}{2}\rho U^2 B (C_{L0} + C'_L \alpha_s(x)) = L_{s0} + L'_s \alpha_s(x) \quad (4.17)$$

$$M_s(x) = \frac{1}{2}\rho U^2 B^2 (C_{M0} + C'_M \alpha_s(x)) = M_{s0} + M'_s \alpha_s(x) \quad (4.18)$$

where $L_s(x)$ is the mean aerodynamic lift force per unit length; $M_s(x)$ is the mean aerodynamic moment per unit length; ρ is the density of air; U is the mean wind speed; B is the bridge-deck width; C_{L0} is the lift coefficient at an angle of attack of 0° ; C'_L is the slope of the lift coefficient; C_{M0} is the moment coefficient at an angle of attack of 0° ; C'_M is the slope of the moment coefficient; $\alpha_s(x)$ is the static rotation of the bridge deck.

It is also reasonable to consider that the static rotation along the bridge deck caused by the mean aerodynamic loads can be approximated as $\alpha_s(x) \approx \psi_\theta^\alpha(x) z_\theta^s$ with z_θ^s being the static generalized displacement for mode $\psi_\theta^\alpha(x)$. This is because the deck rotation of the first symmetric torsional mode $\psi_\theta^\alpha(x)$ for most cable-supported bridges has a half-sine wave shape in the main span which is similar to the static response under the mean aerodynamic loads. Thus, the following expression is obtained for the generalized mean aerodynamic lift force:

$$\tilde{p}_V^s = \int_{L_{br}} \psi_V^h(x) L_s \, dx = L_{s0} \int_{L_{br}} \psi_V^h(x) \, dx + L'_s \left(\int_{L_{br}} \psi_V^h(x) \psi_\theta^\alpha(x) \, dx \right) z_\theta^s \quad (4.19)$$

It is also reasonable to assume that $\psi_V^h(x) \approx \psi_\theta^\alpha(x)$ considering that the modes of the first symmetric vertical-torsional modal pair for the bridges considered in this study have analogous shape and that the modes are normalized such that the maximum modal displacement is unity. Consequently, eq. 4.19 becomes:

$$\tilde{p}_V^s = L_{s0} \Gamma_V^h + L'_s \Gamma_{V2}^h z_\theta^s \quad \text{with} \quad \Gamma_V^h = \int_{L_{br}} \psi_V^h(x) \, dx \quad \Gamma_{V2}^h = \int_{L_{br}} [\psi_V^h(x)]^2 \, dx \quad (4.20)$$

Similarly, the equation for the generalized mean aerodynamic moment is:

$$\tilde{p}_\theta^s = \int_{L_{br}} \psi_\theta^\alpha(x) M_s \, dx \quad (4.21)$$

$$\tilde{p}_\theta^s = M_{s0} \Gamma_\theta^\alpha + M'_s \Gamma_{\theta 2}^\alpha z_\theta^s \quad \text{with} \quad \Gamma_\theta^\alpha = \int_{L_{br}} \psi_\theta^\alpha(x) \, dx \quad \Gamma_{\theta 2}^\alpha = \int_{L_{br}} [\psi_\theta^\alpha(x)]^2 \, dx \quad (4.22)$$

For the self-excited forces, the frequency-domain model relying on flutter derivatives is used:

$$\begin{aligned} L_{se}(x, t) &= H_1 \dot{h}(x, t) + H_2 \dot{\alpha}(x, t) + H_3 \alpha(x, t) + H_4 h(x, t) \\ &= \frac{1}{2} \rho U^2 B \left(KH_1^* \frac{\dot{h}(x, t)}{U} + KH_2^* \frac{B \dot{\alpha}(x, t)}{U} + K^2 H_3^* \alpha(x, t) + K^2 H_4^* \frac{h(x, t)}{B} \right) \end{aligned} \quad (4.23)$$

$$\begin{aligned} M_{se}(x, t) &= A_1 \dot{h}(x, t) + A_2 \dot{\alpha}(x, t) + A_3 \alpha(x, t) + A_4 h(x, t) \\ &= \frac{1}{2} \rho U^2 B^2 \left(KA_1^* \frac{\dot{h}(x, t)}{U} + KA_2^* \frac{B \dot{\alpha}(x, t)}{U} + K^2 A_3^* \alpha(x, t) + K^2 A_4^* \frac{h(x, t)}{B} \right) \end{aligned} \quad (4.24)$$

where $L_{se}(x, t)$ is the self-excited lift force per unit length; $M_{se}(x, t)$ is the self-excited moment per unit length; $h(x, t)$ and $\alpha(x, t)$ are respectively the dynamic vertical displacement and the dynamic rotation; $K = \omega B/U$ is the reduced frequency; H_i^* and A_i^* ($i = 1, \dots, 4$) are the flutter derivatives, which are functions of the reduced velocity $U_R = U/(fB)$; $\omega = 2\pi f$ is the angular frequency of oscillation; the overdot denotes the time derivative. It should be noted that non-normalized flutter derivatives are utilized in the first rows of eqs. 4.23 and 4.24, whereas normalized flutter derivatives are considered in the second rows of the same equations. Equations for the non-normalized flutter derivatives are easily obtained by comparing the first and second rows of eqs. 4.23 and 4.24. For example, it is possible to find that $H_1 = 1/2 \rho U^2 B (KH_1^*/U)$. For the sake of brevity, the non-normalized formulation of the flutter derivatives is utilized in what follows.

Considering that only one mode for each direction (vertical or torsion) is usually involved in a structural dynamic instability or flutter, it appears appropriate to have $h(x, t) \approx \psi_V^h(x) z_V^d(t)$ and $\alpha(x, t) \approx \psi_\theta^\alpha(x) z_\theta^d(t)$ where $z_V^d(t)$ and $z_\theta^d(t)$ are the dynamic generalized displacements for the modal functions $\psi_V^h(x)$ and $\psi_\theta^\alpha(x)$. From this, the generalized self-excited lift force is:

$$\begin{aligned} \tilde{p}_V^{se}(t) &= \int_{L_{br}} \psi_V^h(x) L_{se}(x, t) dx \\ &= \left(\int_{L_{br}} [\psi_V^h(x)]^2 dx \right) [H_1 z_V^d(t) + H_4 z_V^d(t)] + \left(\int_{L_{br}} \psi_V^h(x) \psi_\theta^\alpha(x) dx \right) [H_2 z_\theta^d(t) + H_3 z_\theta^d(t)] \end{aligned} \quad (4.25)$$

By recognizing again that $\psi_V^h(x) \approx \psi_\theta^\alpha(x)$, the following expression is obtained for $\tilde{p}_V^{se}(t)$:

$$\tilde{p}_V^{se}(t) = \Gamma_{V2}^h \left[H_1 \dot{z}_V^d(t) + H_2 \dot{z}_\theta^d(t) + H_3 z_\theta^d(t) + H_4 z_V^d(t) \right] \quad (4.26)$$

The generalized self-excited moment is obtained in a similar manner:

$$\tilde{p}_\theta^{se}(t) = \int_{L_{br}} \psi_\theta^\alpha(x) M_{se}(x, t) dx \quad (4.27)$$

$$\tilde{p}_\theta^{se}(t) = \Gamma_{\theta 2}^\alpha \left[A_1 \dot{z}_V^d(t) + A_2 \dot{z}_\theta^d(t) + A_3 z_\theta^d(t) + A_4 z_V^d(t) \right] \quad (4.28)$$

To be able to simplify eq. 4.25 to eq. 4.26 and eq. 4.27 to eq. 4.28, it is required to assume that the values of the flutter derivatives are constant along the length of the bridge deck. However, the mean aerodynamic loads change the angle of attack of the bridge deck, which varies along the length of the bridge. This indicates that different values of flutter derivatives should be used for different locations along the bridge deck. Nevertheless, it appears reasonable to consider the values of the flutter derivatives as independent of the position along the deck for the sake of determining mode correction factors for the nonlinear structural behavior of eq. 4.6. This is discussed in more detail in section 4.5.1.

In the case of buffeting forces, the following linear force model is utilized:

$$\begin{aligned} L_b(x, t) &= L_{bu}u(x, t) + L_{bw}w(x, t) \\ &= \frac{1}{2}\rho U^2 B \left(2C_{L0}\chi_{Lu} \frac{u(x, t)}{U} + (C'_L + C_{D0})\chi_{Lw} \frac{w(x, t)}{U} \right) \end{aligned} \quad (4.29)$$

$$\begin{aligned} M_b(x, t) &= M_{bu}u(x, t) + M_{bw}w(x, t) \\ &= \frac{1}{2}\rho U^2 B^2 \left(2C_{M0}\chi_{Mu} \frac{u(x, t)}{U} + C'_M\chi_{Mw} \frac{w(x, t)}{U} \right) \end{aligned} \quad (4.30)$$

where $L_b(x, t)$ is the buffeting lift force per unit length; $M_b(x, t)$ is the buffeting moment per unit length; $u(x, t)$ and $w(x, t)$ are respectively the lateral wind fluctuations and vertical wind fluctuations; C_{D0} is the drag coefficient at an angle of attack of 0° ; χ_{Lu} , χ_{Lw} , χ_{Mu} and χ_{Mw} are the aerodynamic admittance functions.

The generalized buffeting lift force can therefore be expressed as:

$$\tilde{p}_V^b(t) = \int_{L_{br}} \psi_V^h(x) L_b(x, t) dx = \int_{L_{br}} \psi_V^h(x) [L_{bu}u(x, t) + L_{bw}w(x, t)] dx \quad (4.31)$$

In a similar manner, the generalized buffeting moment is:

$$\tilde{p}_\theta^b(t) = \int_{L_{br}} \psi_\theta^\alpha(x) M_b(x, t) dx = \int_{L_{br}} \psi_\theta^\alpha(x) [M_{bu}u(x, t) + M_{bw}w(x, t)] dx \quad (4.32)$$

4.4.3 Full-Bridge Dynamic Equations for a Nonlinear Two-Mode Aeroelastic System

By replacing $\omega_j^2 \tilde{m}_j z_j(t)$ by $\tilde{f}_j(z_V(t), z_\theta(t))$ in eqs. 4.15 and 4.16 to account for the nonlinear geometric behavior, the full-bridge aeroelastic system for the first symmetric modal pair can be written as:

$$\tilde{m}_V \ddot{z}_V(t) + 2\xi_V \omega_V \tilde{m}_V \dot{z}_V(t) + \tilde{f}_V(z_V(t), z_\theta(t)) = \tilde{p}_V^s + \tilde{p}_V^{se}(t) + \tilde{p}_V^b(t) \quad (4.33)$$

$$\tilde{m}_\theta \ddot{z}_\theta(t) + 2\xi_\theta \omega_\theta \tilde{m}_\theta \dot{z}_\theta(t) + \tilde{f}_\theta(z_V(t), z_\theta(t)) = \tilde{p}_\theta^s + \tilde{p}_\theta^{se}(t) + \tilde{p}_\theta^b(t) \quad (4.34)$$

Equations 4.33 and 4.34 can be rewritten in matrix form as:

$$\begin{bmatrix} \tilde{m}_V & 0 \\ 0 & \tilde{m}_\theta \end{bmatrix} \begin{bmatrix} \dot{z}_V^d(t) \\ \dot{z}_\theta^d(t) \end{bmatrix} + \begin{bmatrix} 2\xi_V \omega_V \tilde{m}_V - H_1 \Gamma_{V2}^h & -H_2 \Gamma_{V2}^h \\ -A_1 \Gamma_{\theta 2}^\alpha & 2\xi_\theta \omega_\theta \tilde{m}_\theta - A_2 \Gamma_{\theta 2}^\alpha \end{bmatrix} \begin{bmatrix} z_V^d(t) \\ z_\theta^d(t) \end{bmatrix} + \begin{bmatrix} \tilde{f}_V(z_V(t), z_\theta(t)) \\ \tilde{f}_\theta(z_V(t), z_\theta(t)) \end{bmatrix} \\ + \begin{bmatrix} -H_4 \Gamma_{V2}^h & -H_3 \Gamma_{V2}^h \\ -A_4 \Gamma_{\theta 2}^\alpha & -A_3 \Gamma_{\theta 2}^\alpha \end{bmatrix} \begin{bmatrix} z_V^s(t) \\ z_\theta^s(t) \end{bmatrix} = \begin{bmatrix} L_{s0} \Gamma_V^h + L_s' \Gamma_{V2}^h z_\theta^s \\ M_{s0} \Gamma_\theta^\alpha + M_s' \Gamma_{\theta 2}^\alpha z_\theta^s \end{bmatrix} + \begin{bmatrix} \int_{L_{br}} \psi_V^h(x) [L_{bu}u(x, t) + L_{bw}w(x, t)] dx \\ \int_{L_{br}} \psi_\theta^\alpha(x) [M_{bu}u(x, t) + M_{bw}w(x, t)] dx \end{bmatrix} \quad (4.35)$$

In eq. 4.35, the following equations for the the generalized displacements were used:

$$z_V(t) = z_V^s + z_V^d(t) \quad z_\theta(t) = z_\theta^s + z_\theta^d(t) \quad (4.36)$$

where z_V^s and $z_V^d(t)$ are respectively the static generalized displacement and dynamic generalized displacement for the first symmetric vertical mode; z_θ^s and $z_\theta^d(t)$ are respectively the static generalized displacement and dynamic generalized displacement for the first symmetric

torsional mode.

Before continuing, it is worth demonstrating that the restoring forces in eqs. 4.33 and 4.34 or eq. 4.35 can be developed for a linear structure to give the restoring force terms of eqs. 4.15 and 4.16. For example, linearizing the vertical nonlinear restoring force leads to the following:

$$\begin{aligned}\tilde{k}_V z_V(t) &= \frac{\partial \tilde{f}_V}{\partial z_V} z_V(t) = \omega_V^2 \tilde{m}_V \frac{\partial a_V}{\partial z_V} z_V(t) \\ &= \omega_V^2 \tilde{m}_V z_V(t)\end{aligned}\quad (4.37)$$

where \tilde{k}_V is the vertical generalized stiffness. In eq. 4.37, it is recognized that $\partial a_V / \partial z_\theta = 1$ for a linear structure because $\partial a_V / \partial z_\theta$ is the ratio of the linear generalized displacement to the nonlinear generalized displacement (see chapter 3). A similar demonstration can be made in the case of the torsional restoring force.

4.4.4 Nonlinear Dynamic Equations of Full-Scale Section Model

In a similar manner, it is possible to write the equations of motion for a 2-DOF section model at full-scale (fig. 4.3). In this case, the vertical displacement $y_V(t)$ and rotation $y_\theta(t)$ of the full-scale section model are defined as:

$$y_V(t) = y_V^s + y_V^d(t) \quad y_\theta(t) = y_\theta^s + y_\theta^d(t) \quad (4.38)$$

where y_V^s and $y_V^d(t)$ are the static and dynamic contributions to the vertical displacement; y_θ^s and $y_\theta^d(t)$ are the static and dynamic contributions to the rotation. The dynamic equation of the section model is presented in the following equation:

$$\begin{aligned}\begin{bmatrix} \bar{m}_V & 0 \\ 0 & \bar{m}_\theta \end{bmatrix} \begin{bmatrix} \ddot{y}_V^d(t) \\ \ddot{y}_\theta^d(t) \end{bmatrix} + \begin{bmatrix} 2\xi_V \omega_V \bar{m}_V - H_1 & -H_2 \\ -A_1 & 2\xi_\theta \omega_\theta \bar{m}_\theta - A_2 \end{bmatrix} \begin{bmatrix} \dot{y}_V^d(t) \\ \dot{y}_\theta^d(t) \end{bmatrix} + \begin{bmatrix} \bar{f}_V(y_V(t), y_\theta(t)) \\ \bar{f}_\theta(y_V(t), y_\theta(t)) \end{bmatrix} \\ + \begin{bmatrix} -H_4 & -H_3 \\ -A_4 & -A_3 \end{bmatrix} \begin{bmatrix} y_V^d(t) \\ y_\theta^d(t) \end{bmatrix} = \begin{bmatrix} L_{s0} + L'_s y_\theta^s \\ M_{s0} + M'_s y_\theta^s \end{bmatrix} + \begin{bmatrix} \frac{\int_{L_{mp}} [L_{bu} u(x,t) + L_{bw} w(x,t)] dx}{L_{mp}} \\ \frac{\int_{L_{mp}} [M_{bu} u(x,t) + M_{bw} w(x,t)] dx}{L_{mp}} \end{bmatrix}\end{aligned}\quad (4.39)$$

It should be noted that this equation is expressed per unit length of the section model. In eq. 4.39, \bar{m}_V and \bar{m}_θ are respectively the mass per unit length and mass moment of inertia

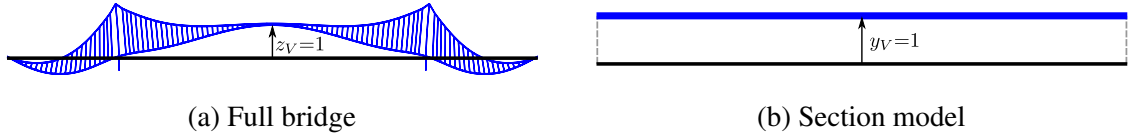


Figure 4.4: Comparison of typical mode shapes for a full bridge and a section model

per unit length of the section model; $\bar{f}_V(y_V(t), y_\theta(t))$ and $\bar{f}_\theta(y_V(t), y_\theta(t))$ are functions to be determined for the nonlinear restoring vertical force per unit length and nonlinear restoring moment per unit length; L_{mp} is the length of the section model at full scale.

Equations to calculate \bar{m}_V , \bar{m}_θ , $\bar{f}_V(y_V(t), y_\theta(t))$ and $\bar{f}_\theta(y_V(t), y_\theta(t))$, which are required for designing nonlinear section model experiments, are to be obtained by comparing the full-bridge equations (eq. 4.35) and the section-model equations (eq. 4.39).

4.4.5 Effective Distributed Mass

As illustrated in fig. 4.4a, the entire bridge reacts dynamically when only the bridge deck is subjected to wind loads. Consequently, since the section model only includes the bridge deck (fig. 4.4b), it is needed to account for a contribution from the cable system and towers to the mass and mass moment of inertia considered for the section model. When responding dynamically, the section model would consequently have the same effect in terms of inertial effects and kinetic energy as the full bridge.

Similarly, it is important to recognize that the energy dissipation from structural and aerodynamic origins must be in the same proportion for the full bridge and the section model. This means that the ratio between the structural damping forces and aerodynamic damping forces must be the same for both systems. Theoretically, this will guarantee that instabilities caused by aeroelastic effects like galloping and flutter occur at the same critical wind speed for the full bridge and the section model. Such a ratio can be calculated from the coefficients of the effective damping matrices in eqs. 4.35 and 4.39. As an example, the diagonal coefficient for the vertical mode is considered, which yields the following equality for the ratio of the structural damping coefficient to the aerodynamic damping coefficient:

$$\frac{2\xi_V\omega_V\tilde{m}_V}{H_1\Gamma_{V2}^h} = \frac{2\xi_V\omega_V\bar{m}_V}{H_1} \quad (4.40)$$

Since the same damping ratio ξ_V is utilized for the full bridge and the section model, the following equation can be obtained:

$$\bar{m}_V = \frac{\tilde{m}_V}{\Gamma_{V2}^h} = \frac{\tilde{m}_V}{\int_{L_{br}} [\psi_V^h(x)]^2 dx} \quad (4.41)$$

Equation 4.41 indicates that the effective mass per unit length for the first symmetric vertical mode to be used for the section model has to be calculated from the generalized mass and its corresponding mode in order to ensure a realistic prediction of aeroelastic instabilities. In a similar manner, the effective mass moment of inertia per unit length for the first symmetric torsional mode is:

$$\bar{m}_\theta = \frac{\tilde{m}_\theta}{\Gamma_{\theta 2}^\alpha} = \frac{\tilde{m}_\theta}{\int_{L_{br}} [\psi_\theta^\alpha(x)]^2 dx} \quad (4.42)$$

Since \tilde{m}_V and \tilde{m}_θ are to be calculated using eq. 4.12, the effective distributed mass properties in eqs. 4.41 and 4.42 therefore account for the mass contributions of all structural elements including the cable system and towers. It should be noted that effective mass properties like in eqs. 4.41 and 4.42 have been used in previous section model test research [196, 197]. From eqs. 4.41 and 4.42, we have that $\tilde{m}_V = \bar{m}_V \Gamma_{V2}^h$ and $\tilde{m}_\theta = \bar{m}_\theta \Gamma_{\theta 2}^\alpha$, which can be substituted into eq. 4.35 to give the following equation after dividing the first row by Γ_{V2}^h and the second row by $\Gamma_{\theta 2}^\alpha$:

$$\begin{aligned} & \begin{bmatrix} \bar{m}_V & 0 \\ 0 & \bar{m}_\theta \end{bmatrix} \begin{bmatrix} \ddot{z}_V^d(t) \\ \ddot{z}_\theta^d(t) \end{bmatrix} + \begin{bmatrix} 2\xi_V \omega_V \bar{m}_V - H_1 & -H_2 \\ -A_1 & 2\xi_\theta \omega_\theta \bar{m}_\theta - A_2 \end{bmatrix} \begin{bmatrix} \dot{z}_V^d(t) \\ \dot{z}_\theta^d(t) \end{bmatrix} + \begin{bmatrix} \frac{\tilde{f}_V(z_V(t), z_\theta(t))}{\Gamma_{V2}^h} \\ \frac{\tilde{f}_\theta(z_V(t), z_\theta(t))}{\Gamma_{\theta 2}^\alpha} \end{bmatrix} \\ & + \begin{bmatrix} -H_4 & -H_3 \\ -A_4 & -A_3 \end{bmatrix} \begin{bmatrix} \dot{z}_V^d(t) \\ \dot{z}_\theta^d(t) \end{bmatrix} = \begin{bmatrix} L_{s0} \frac{\Gamma_V^h}{\Gamma_{V2}^h} + L'_s z_\theta^s \\ M_{s0} \frac{\Gamma_\theta^\alpha}{\Gamma_{\theta 2}^\alpha} + M'_s z_\theta^s \end{bmatrix} + \begin{bmatrix} \frac{\int_{L_{br}} \psi_V^h(x) [L_{bu}u(x,t) + L_{bw}w(x,t)] dx}{\Gamma_{V2}^h} \\ \frac{\int_{L_{br}} \psi_\theta^\alpha(x) [M_{bu}u(x,t) + M_{bw}w(x,t)] dx}{\Gamma_{\theta 2}^\alpha} \end{bmatrix} \end{aligned} \quad (4.43)$$

4.4.6 Different Mode Normalization for Full-Bridge Dynamic Equations

When comparing eqs. 4.39 and 4.43, it is possible to notice additional factors for the constant term of the mean aerodynamic loads in the case of the full-bridge equation. For the vertical force, the factor is $\Gamma_V^h / \Gamma_{V2}^h$, and the factor $\Gamma_\theta^\alpha / \Gamma_{\theta 2}^\alpha$ is the moment one. From this fact, it is interesting to consider a different mode normalization and its corresponding modal integrals for the full-bridge equations of motion:

$$\begin{aligned}
\bar{\psi}_V^h(x) &= \beta_V \psi_V^h(x) & \bar{\psi}_\theta(x) &= \beta_\theta \psi_\theta^\alpha(x) \\
\bar{\Gamma}_V^h &= \int_{L_{br}} \bar{\psi}_V^h(x) dx & \bar{\Gamma}_{V2}^h &= \int_{L_{br}} [\bar{\psi}_V^h(x)]^2 dx \\
\bar{\Gamma}_\theta^\alpha &= \int_{L_{br}} \bar{\psi}_\theta^\alpha(x) dx & \bar{\Gamma}_{\theta2}^\alpha &= \int_{L_{br}} [\bar{\psi}_\theta^\alpha(x)]^2 dx
\end{aligned} \tag{4.44}$$

where $\psi_V^h(x)$ and $\psi_\theta^\alpha(x)$ are modes normalized such that their maximums are unity; $\bar{\psi}_V^h(x)$ is the first symmetric vertical mode normalized such that $\bar{\Gamma}_V^h/\bar{\Gamma}_{V2}^h = 1$; $\bar{\psi}_\theta^\alpha(x)$ is the first symmetric torsional mode normalized such that $\bar{\Gamma}_\theta^\alpha/\bar{\Gamma}_{\theta2}^\alpha = 1$.

Integrating both sides of the first equation in eq. 4.44 then dividing by $\bar{\Gamma}_{V2}^h$ allows determining the expression for β_V . A similar procedure leads to the expression of β_θ . Therefore, the expressions for β_V and β_θ are:

$$\beta_V = \frac{\Gamma_V^h}{\Gamma_{V2}^h} = \frac{\int_{L_{br}} \psi_V^h(x) dx}{\int_{L_{br}} [\psi_V^h(x)]^2 dx} \tag{4.45}$$

$$\beta_\theta = \frac{\Gamma_\theta^\alpha}{\Gamma_{\theta2}^\alpha} = \frac{\int_{L_{br}} \psi_\theta^\alpha(x) dx}{\int_{L_{br}} [\psi_\theta^\alpha(x)]^2 dx} \tag{4.46}$$

For the full bridge, the vertical displacement of the deck can be expressed as $h(x, t) = \psi_V^h(x)z_V(t)$ and $h(x, t) = \bar{\psi}_V^h(x)y_V(t) = \beta_V\psi_V^h(x)y_V(t)$. Similarly, the torsional rotation of the deck can be obtained using $\alpha(x, t) = \psi_\theta^\alpha(x)z_\theta(t)$ and $\alpha(x, t) = \bar{\psi}_\theta^\alpha(x)y_\theta(t) = \beta_\theta\psi_\theta^\alpha(x)y_\theta(t)$. From this, we have that:

$$z_V(t) = \beta_V y_V(t) \quad z_\theta(t) = \beta_\theta y_\theta(t) \tag{4.47}$$

Thus, the following equation can be obtained by substituting eq. 4.47 into eq. 4.43 and making use of eqs. 4.45 and 4.46:

$$\begin{aligned}
& \begin{bmatrix} \bar{m}_V & 0 \\ 0 & \bar{m}_\theta \end{bmatrix} \begin{bmatrix} \beta_V \ddot{y}_V^d(t) \\ \beta_\theta \ddot{y}_\theta^d(t) \end{bmatrix} + \begin{bmatrix} 2\xi_V \omega_V \bar{m}_V - H_1 & -H_2 \\ -A_1 & 2\xi_\theta \omega_\theta \bar{m}_\theta - A_2 \end{bmatrix} \begin{bmatrix} \beta_V \dot{y}_V^d(t) \\ \beta_\theta \dot{y}_\theta^d(t) \end{bmatrix} + \begin{bmatrix} \bar{f}_V(\beta_V y_V(t), \beta_\theta y_\theta(t)) \\ \bar{f}_\theta(\beta_V y_V(t), \beta_\theta y_\theta(t)) \end{bmatrix} \\
& + \begin{bmatrix} -H_4 & -H_3 \\ -A_4 & -A_3 \end{bmatrix} \begin{bmatrix} \beta_V y_V^d(t) \\ \beta_\theta y_\theta^d(t) \end{bmatrix} = \begin{bmatrix} \beta_V L_{s0} + L'_s \beta_\theta y_\theta^s \\ \beta_\theta M_{s0} + M'_s \beta_V y_V^s \end{bmatrix} + \begin{bmatrix} \frac{\int_{L_{br}} \psi_V^h(x) [L_{bu} u(x,t) + L_{bw} w(x,t)] dx}{\Gamma_{V2}^h} \\ \frac{\int_{L_{br}} \psi_\theta^\alpha(x) [M_{bu} u(x,t) + M_{bw} w(x,t)] dx}{\Gamma_{\theta 2}^\alpha} \end{bmatrix} \quad (4.48)
\end{aligned}$$

Considering that $\psi_V^h(x) \approx \psi_\theta^\alpha(x)$ for the first symmetric modal pair, it is reasonable to assume that $\beta_V \approx \beta_\theta$. Therefore, dividing the first row by β_V and the second row by β_θ in eq. 4.48 gives:

$$\begin{aligned}
& \begin{bmatrix} \bar{m}_V & 0 \\ 0 & \bar{m}_\theta \end{bmatrix} \begin{bmatrix} \dot{y}_V^d(t) \\ \dot{y}_\theta^d(t) \end{bmatrix} + \begin{bmatrix} 2\xi_V \omega_V \bar{m}_V - H_1 & -H_2 \\ -A_1 & 2\xi_\theta \omega_\theta \bar{m}_\theta - A_2 \end{bmatrix} \begin{bmatrix} \dot{y}_V^d(t) \\ \dot{y}_\theta^d(t) \end{bmatrix} + \begin{bmatrix} \bar{f}_V(\beta_V y_V(t), \beta_\theta y_\theta(t)) \\ \bar{f}_\theta(\beta_V y_V(t), \beta_\theta y_\theta(t)) \end{bmatrix} \\
& + \begin{bmatrix} -H_4 & -H_3 \\ -A_4 & -A_3 \end{bmatrix} \begin{bmatrix} y_V^d(t) \\ y_\theta^d(t) \end{bmatrix} = \begin{bmatrix} L_{s0} + L'_s y_\theta^s \\ M_{s0} + M'_s y_V^s \end{bmatrix} + \begin{bmatrix} \frac{\int_{L_{br}} \psi_V^h(x) [L_{bu} u(x,t) + L_{bw} w(x,t)] dx}{\int_{L_{br}} \psi_V^h(x) dx} \\ \frac{\int_{L_{br}} \psi_\theta^\alpha(x) [M_{bu} u(x,t) + M_{bw} w(x,t)] dx}{\int_{L_{br}} \psi_\theta^\alpha(x) dx} \end{bmatrix} \quad (4.49)
\end{aligned}$$

By comparing eq. 4.39 for the full-scale section model and eq. 4.49 for the full bridge, it is possible to notice that they are the same with the exception of the restoring force vector and buffeting force vector. The buffeting force vectors in eqs. 4.39 and 4.49 are different due to the correlation of the buffeting loads along the bridge deck making further simplifications not possible in eq. 4.49. However, it is believed that the buffeting load vectors for the section model and full bridge are reasonably similar. Considering that the components of the buffeting force vector have expressions similar to joint acceptance functions, this seems like a reasonable assumption because the section model and full bridge have similar joint acceptance functions for the first symmetric modes [31]. This assumption is validated in section 4.5.5.

From eqs. 4.39 and 4.49, it is therefore possible to conclude that the restoring forces per unit length $\bar{f}_V(y_V, y_\theta)$ and $\bar{f}_\theta(y_V, y_\theta)$ to be modeled in nonlinear section model tests are expressed as:

$$\bar{f}_V(y_V, y_\theta) = \frac{\tilde{f}_V(\beta_V y_V, \beta_\theta y_\theta)}{\Gamma_V^h} = \frac{\tilde{f}_V(\beta_V y_V, \beta_\theta y_\theta)}{\int_{L_{br}} \psi_V^h(x) dx} \quad (4.50)$$

$$\bar{f}_\theta(y_V, y_\theta) = \frac{\tilde{f}_\theta(\beta_V y_V, \beta_\theta y_\theta)}{\Gamma_\theta^\alpha} = \frac{\tilde{f}_\theta(\beta_V y_V, \beta_\theta y_\theta)}{\int_{L_{br}} \psi_\theta^\alpha(x) dx} \quad (4.51)$$

In eqs. 4.50 and 4.51, the parameters β_V , β_θ , Γ_V^h and Γ_θ^α can be interpreted as mode correction factors for the restoring forces. This is because the section model has uniform mode shapes, whereas it is not the case for the full bridge as shown in fig. 4.4.

Additionally, it is worth noting that the mode factors β_V and β_θ are utilized to calculate the generalized displacements of the full bridge from the section model displacements as shown in eq. 4.47. Due to the unity-based normalization used for the modes, eq. 4.47 gives the maximum displacements of the full bridge directly. It is interesting to note that the expressions for β_V and β_θ given in eqs. 4.45 and 4.46 are equivalent to the displacement correction factors of [60, 197] in the case of linear aerodynamic force models.

4.4.7 Discussion on Nonlinear Modal Dynamic Problem

Before showing how to scale eqs. 4.50 and 4.51, it is appropriate to discuss eq. 4.39 for the section model and eq. 4.49 for the full bridge. Firstly, these equations account only for one vertical mode and one torsional mode, i.e., the first symmetric modes since they are of interest for nonlinear section model tests. This is sufficient in the study of vertical-torsional dynamic instabilities and flutter since these phenomena involve specific modes as already mentioned in section 4.2.1.

Secondly, eqs. 4.50 and 4.51 use the idea from [190] for which the dynamic system of a geometrically nonlinear structure, herein a cable-supported bridge, is represented in the modal space considering a nonlinear generalized stiffness behavior. Therefore, the nonlinear modal dynamic systems of eqs. 4.39 and 4.49 can be seen as nonlinear reduced-order models. This was discussed previously in section 4.3. The assumption that the nonlinear geometric response of a structure can be represented appropriately using the linear modes of vibration was validated in [190]. Furthermore, this was also confirmed in chapter 3 for modal loads similar to those in eq. 4.2 as discussed in section 4.3.1.

It is also worth mentioning again that linear frequency-domain force models were considered in the development of eqs. 4.39 and 4.49. This choice was made due to their mathematical

elegance that makes possible an easier interpretation of the different aerodynamic effects. Doing so also makes it possible to determine mode correction factors for the nonlinear generalized stiffness as mentioned in section 4.4.2. However, it should be mentioned that eqs. 4.39 and 4.49 cannot be solved numerically because of the frequency-domain force models and the nonlinear structural behavior. One option to solve numerically the nonlinear modal dynamic problem would be to use the time-domain counterparts of the frequency-domain force models, which rely on convolution integrals and assume a linear aerodynamic behavior. In order to account for the aerodynamic nonlinearities, it would be needed to utilize nonlinear aerodynamic models, which are more difficult to use. Nevertheless, using nonlinear section model tests in the wind tunnel, aerodynamic nonlinearities will be considered automatically just like the structural nonlinearities.

4.4.8 Scaling of Nonlinear Generalized Stiffness Parameters

It is now needed to determine the scaled parameters for the nonlinear section model tests. For the mass properties, damping ratios and displacements, the usual scaling equations can be utilized [193, 198]:

$$\bar{m}_{vm} = \lambda_L^2 \bar{m}_{vp} \quad \bar{m}_{\theta m} = \lambda_L^4 \bar{m}_{\theta p} \quad (4.52)$$

$$\xi_{vm} = \xi_{vp} \quad \xi_{\theta m} = \xi_{\theta p} \quad (4.53)$$

$$y_{vm} = \lambda_L y_{vp} \quad y_{\theta m} = y_{\theta p} \quad (4.54)$$

where $\lambda_L = L_m/L_p$ is the geometric scale; subscript m refers to the model; subscript p refers to the prototype or full-scale bridge.

However, it is not possible to directly use the frequency scale for nonlinear tests like it is the case for linear tests, for which the frequency scale is utilized to determine the scaled stiffness. Instead for the nonlinear tests, the restoring forces $\bar{f}_v(y_v, y_\theta)$ and $\bar{f}_\theta(y_v, y_\theta)$ need to be scaled. Since the restoring forces are caused by displacements due to external forces from aerodynamic origins, they can be scaled as follows:

$$\bar{f}_{V_m}(y_{V_m}, y_{\theta_m}) = \lambda_U^2 \lambda_L \bar{f}_{V_p}(y_{V_p}, y_{\theta_p}) = \lambda_U^2 \lambda_L \bar{f}_{V_p} \left(\frac{y_{V_m}}{\lambda_L}, y_{\theta_m} \right) \quad (4.55)$$

$$\bar{f}_{\theta_m}(y_{V_m}, y_{\theta_m}) = \lambda_U^2 \lambda_L^2 \bar{f}_{\theta_p}(y_{V_p}, y_{\theta_p}) = \lambda_U^2 \lambda_L^2 \bar{f}_{\theta_p} \left(\frac{y_{V_m}}{\lambda_L}, y_{\theta_m} \right) \quad (4.56)$$

where $\lambda_U = U_m/U_p$ is the velocity scale. By combining eqs. 4.50 and 4.55 as well as eqs. 4.51 and 4.56, it is possible to obtain the equations to convert the restoring forces obtained from nonlinear generalized stiffness analysis for the full bridge into stiffness parameters to be used for the scaled section model:

$$\bar{f}_{V_m}(y_{V_m}, y_{\theta_m}) = \frac{\lambda_U^2 \lambda_L}{\Gamma_V^h} \tilde{f}_{V_p} \left(\frac{\beta_V}{\lambda_L} y_{V_m}, \beta_\theta y_{\theta_m} \right) \quad (4.57)$$

$$\bar{f}_{\theta_m}(y_{V_m}, y_{\theta_m}) = \frac{\lambda_U^2 \lambda_L^2}{\Gamma_\theta^\alpha} \tilde{f}_{\theta_p} \left(\frac{\beta_V}{\lambda_L} y_{V_m}, \beta_\theta y_{\theta_m} \right) \quad (4.58)$$

It should be noted that after some experiments, it was found that the modal integrals Γ_V^h and Γ_θ^α should be calculated using the absolute values of $\psi_V^h(x)$ and $\psi_\theta^\alpha(x)$. This is also applicable to the numerators of the expressions for β_V and β_θ . This is because negative values can occur for $\psi_V^h(x)$ and $\psi_\theta^\alpha(x)$ in some cases. Therefore, it appears more conservative to use the absolute values. Furthermore, not using the absolute values in Γ_V^h , Γ_θ^α , β_V and β_θ could lead to values of zero for these parameters in the case of antisymmetric modes. This would mean that the generalized displacements are also zero because of eq. 4.47, and this is not realistic since antisymmetric modes can also be dynamically excited in cable-supported bridges. Therefore, even though this research focuses on the first symmetric modal pair, the absolute values are considered herein to be consistent with the antisymmetric case. This was similarly done in [60, 197].

In the case of small displacements, it is interesting to demonstrate that eqs. 4.57 and 4.58 lead to the usual stiffness equations based on the frequency scale. For small displacements, the off-diagonal stiffness terms are zero, and the model-scale vertical stiffness per unit length \bar{k}_{V_m} can be obtained as follows from eq. 4.57:

$$\bar{k}_{V_m} = \frac{\partial \bar{f}_{V_m}}{\partial y_{V_m}} = \frac{\lambda_U^2 \lambda_L}{\Gamma_V^h} \frac{\partial \tilde{f}_{V_p}}{\partial z_{V_p}} \frac{dz_{V_p}}{dy_{V_m}} \quad (4.59)$$

From the second equation in eq. 4.37, we have that $\partial \tilde{f}_{vp} / \partial z_{vp} = \omega_{vp}^2 \tilde{m}_{vp}$ when the generalized displacements are small. From eqs. 4.47 and 4.54, it is easy to demonstrate that $dz_{vp} / dy_{vm} = \beta_V / \lambda_L = \Gamma_V^h / (\Gamma_{V2}^h \lambda_L)$. Using these expressions in eq. 4.59 yields:

$$\bar{k}_{vm} = \lambda_U^2 \omega_{vp}^2 \frac{\tilde{m}_{vp}}{\Gamma_{V2}^h} = \left(\frac{\lambda_U}{\lambda_L} \omega_{vp} \right)^2 \bar{m}_{vm} \quad (4.60)$$

The right-hand side of eq. 4.60 is obtained using $\tilde{m}_{vp} / \Gamma_{V2}^h = \bar{m}_{vp} = \bar{m}_{vm} / \lambda_L^2$, which is obtained from eqs. 4.41 and 4.52. It is easy to see that the right-hand side of eq. 4.60 corresponds to the usual vertical stiffness equation for linear section model tests relying on the frequency scale $\lambda_f = \lambda_U / \lambda_L$. A similar demonstration can be made for the torsional stiffness.

4.5 Validation of Assumptions Used in the Theory for Nonlinear Section Model Tests

It is now needed to verify the assumptions utilized in the scaling procedure of the nonlinear generalized behavior. In the following subsections, the analysis of five simplifications used in the theory presented in section 4.4 is made. Firstly, the full-bridge mean wind responses of the different bridges are analyzed to check whether the static rotation of the bridge deck is small. Secondly, an analysis is made for the effective distributed mass properties to be considered for section model tests. The shape similarity between vertical and torsional modes is also discussed. Then, it is verified that the mean wind response can be approximated from section model tests. Lastly, a comparison between the buffeting forces for the full bridge and the section model is presented.

4.5.1 Full-Bridge Mean Wind Response

Since the flutter derivatives for most of the bridges in table 4.1 are only available for an angle of attack of 0° , it is not possible to use 3D flutter analysis that accounts for the variation of the flutter derivatives to assess the effect of such variation. Measuring the flutter derivatives for these bridges at different angles of attack is out the scope of this chapter, which is to present the theoretical developments required to account for structural nonlinearities in the section model testing procedure. Instead, an analysis of the full-bridge mean wind responses is considered with the objective of checking the magnitude of the maximum static rotation of the bridge deck. This provides an indirect approach to judge whether it is reasonable to use

Table 4.3: Midspan displacements under mean aerodynamic loads at high wind speed for an angle of attack of 0° (u_y : lateral displacement, u_z : vertical displacement, θ_x : torsional rotation)

Bridge	U (m/s)	u_y (m)	u_z (m)	θ_x ($^\circ$)
SU1	82.0	11.47	-8.57	-7.03
SU2	74.2	8.03	1.31	1.45
SU3a	100.0	27.03	-0.67	-0.52
SU3b	100.0	35.18	-0.87	-1.06
SU3c	100.0	39.29	-1.06	-1.04
SU4a	100.0	5.55	-1.19	0.60
SU4b	100.0	13.70	-0.14	1.67
SU4c	88.3	15.06	-0.25	1.62
SU4d	74.0	13.37	-0.85	0.93
CS1	100.0	4.14	-0.42	2.09
CS2	100.0	1.98	-0.01	0.80

the flutter derivatives for the same angle of attack along the bridge deck in the development of the equations for the nonlinear structural behavior to be used for nonlinear section model tests.

For this verification, the nonlinear static response under the mean aerodynamic loads are calculated for each bridge using the procedure in [19]. Mean aerodynamic loads were applied to the bridge deck, towers and cables, and the hydraulic buffers were inactive. The analyses were conducted by gradually increasing the wind speed until an aerostatic instability was reached. For each bridge, table 4.3 presents the maximum deck displacements at midspan for an angle of attack of 0° at what is considered to be high wind speeds. For bridges SU1, SU2, SU4c and SU4d, the results are shown for their flutter wind speeds determined from experiments or 2D flutter analysis. For the other bridges, it was not possible to use their flutter wind speeds since they are greater than what is achievable in dynamic tests and flutter derivative tests in a wind tunnel. In this case, the displacements in table 4.3 for these bridges are presented for a high wind speed of 100 m/s, which is deemed sufficient for the sake of this demonstration. Additionally, since the results in this table come from a finite element model, a different notation than previously is used for the deck displacements to avoid confusion with the nonlinear modal system discussed in section 4.4.

In table 4.3, the maximum static rotation of the deck has a maximum value of approximately 2° with the exception of bridge SU1, which has a maximum static rotation at the flutter wind speed of just over -7° . For bridge SU1, the large rotation is explained by the fact

that the flutter wind speed is close to the critical wind speed for an aerostatic instability. Therefore, for almost all these bridges, we have that the rotation along the bridge deck varies between 0° at the deck supports and a maximum value of 2° at midspan. A variation of 2° of the angle of attack does not have a significant effect on the flutter derivatives based on the studies in [139, 195, 199, 200], but it can be more pronounced for other deck cross sections as in [36]. When this effect is limited, the predicted flutter wind speed is not significantly impacted as shown in [139], but it is worth mentioning that this is case specific since the effect of the angle of attack on the flutter derivatives could be more significant for a different bridge. Nevertheless, from this discussion, it appears reasonable to consider the flutter derivatives as constant in order to allow simplifications leading to eqs. 4.26 and 4.28. This makes possible the developments required to find mode correction factors for the nonlinear structural behavior required for nonlinear section model tests.

It is also of interest to utilize nonlinear static analysis for the mean aerodynamic forces to confirm that material nonlinearities are not a concern and that only geometric nonlinearities are relevant for nonlinear section model tests as mentioned in section 4.2.3. This is done by comparing the nonlinear aerostatic response of bridge SU2 with and without considering the material nonlinearities. For the finite element model of bridge SU2 with material nonlinearities, multifiber beam elements with an elastoplastic behavior are considered for the steel box-girder deck. In this model, the towers and cables are assumed to have an elastic behavior just like in the model with geometric nonlinearities as it was confirmed that these elements stay within their elastic limit. In fig. 4.5, the midspan displacements under the mean aerodynamic loads for an increasing wind speed are presented. Results are shown for the geometrically nonlinear model (LD) and the geometrically nonlinear model with material nonlinearities (LDNL). Three angles of attack are considered for the wind. Also, the vertical line in this figure corresponds to the flutter wind speed for an initial angle of attack of 0° . As it can be observed in fig. 4.5, both models lead to the same mean wind response, which confirms that material nonlinearities are not of interest for nonlinear section model tests.

4.5.2 Comparison for Effective Distributed Mass

The effective distributed mass \bar{m}_V and the effective distributed mass moment of inertia \bar{m}_θ to be considered for section model tests can be calculated using eqs. 4.41 and 4.42. However, it is of interest to compare this approach to the intuitive approach given by the following equations:

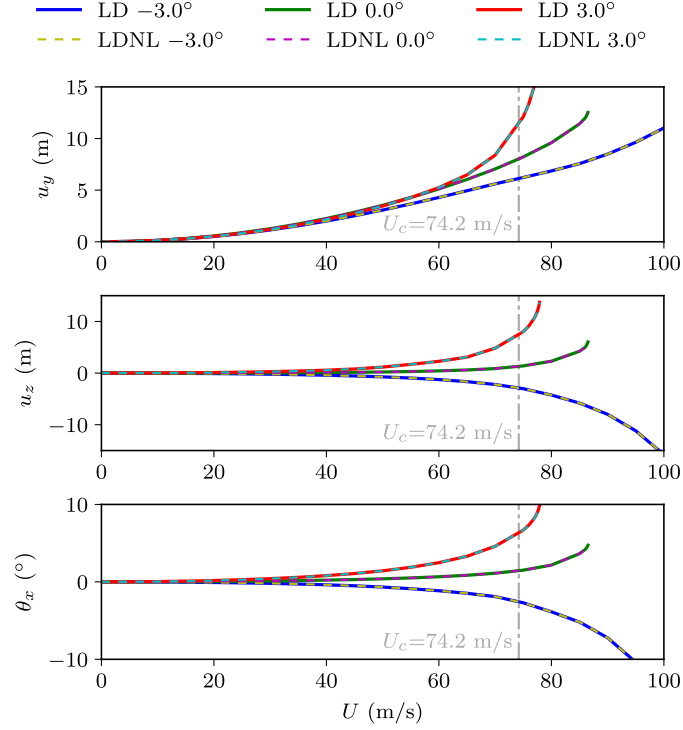


Figure 4.5: Midspan displacements under mean aerodynamic loads for bridge SU2 (u_y : lateral displacement, u_z : vertical displacement, θ_x : torsional rotation, U_c : flutter wind speed)

$$\bar{m}_V = \bar{m}_{deck} + 2\bar{m}_{cable} \quad (4.61)$$

$$\bar{m}_\theta = \overline{MMI}_{deck} + 2(\bar{m}_{cable} b_{cl}^2) \quad (4.62)$$

where \bar{m}_{deck} is the mass per unit length of the bridge deck; \overline{MMI}_{deck} is the mass moment of inertia per unit length of the bridge deck; \bar{m}_{cable} is the mass per unit length for a main cable; b_{cl} is half of the main cable spacing. When used for cable-stayed bridges, \bar{m}_{cable} corresponds to 25 % of the total mass of the stay cables divided by the length of the bridge covered by stays. One quarter is considered because half the cable mass is assumed to move with the bridge deck with this mass divided in two for each side of the bridge when there are two planes of stay cables. The distance b_{cl} between the bridge center line and the cable plane is measured at the deck level in the case of cable-stayed bridges.

In what follows, the approach of eqs. 4.61 and 4.62 is referred as method A. Method B corresponds to the procedure of eqs. 4.41 and 4.42, which relies on a modal approach. During the initial testing of method B for symmetric and antisymmetric modes, it was found

Table 4.4: Comparison of effective distributed mass properties (first symmetric vertical-torsional modal pair)

Bridge	Method A		Method B		Method B*	
	\bar{m}_V (10^3 kg/m)	\bar{m}_θ (10^6 kg · m ² /m)	\bar{m}_V (10^3 kg/m)	\bar{m}_θ (10^6 kg · m ² /m)	\bar{m}_V^* (10^3 kg/m)	\bar{m}_θ^* (10^6 kg · m ² /m)
SU1	24.17	2.920	23.99	2.885	23.65	2.880
SU2	23.06	2.423	23.76	4.406	22.96	2.410
SU3a	45.54	20.098	44.67	34.312	44.04	19.852
SU3b	56.76	27.850	56.78	29.707	55.60	27.902
SU3c	73.54	39.299	74.53	40.037	73.20	39.979
SU4a	30.26	8.703	30.27	8.132	30.07	8.113
SU4b	33.81	10.622	33.94	10.116	33.63	10.104
SU4c	38.05	12.911	38.33	12.554	37.90	12.542
SU4d	44.52	16.392	45.13	16.367	44.49	16.356
CS1	14.66	0.672	14.78	0.677	14.44	0.627
CS2	38.97	12.736	37.89	11.541	37.03	11.118

that it gives results much higher than method A in some cases. For the vertical modes, this is because some of these modes have some longitudinal displacements (mainly antisymmetric modes), which is explained by the inactive longitudinal hydraulic buffers. It was also found that, for some bridges, the torsional modes possess some lateral displacements. Therefore, the following equations are also tested for the calculation of the effective distributed mass properties:

$$\bar{m}_V^* = \frac{\tilde{m}_V^*}{\int_{L_{br}} [\psi_V^h(x)]^2 dx} \quad \bar{m}_\theta^* = \frac{\tilde{m}_\theta^*}{\int_{L_{br}} [\psi_\theta^\alpha(x)]^2 dx} \quad (4.63)$$

where $\tilde{m}_V^* = \phi_V^{*\top} \mathbf{M} \phi_V^*$; ϕ_V^* is a vertical mode shape for which the components corresponding to the longitudinal degrees of freedom are set to zero; $\tilde{m}_\theta^* = \phi_\theta^{*\top} \mathbf{M} \phi_\theta^*$; ϕ_θ^* is a torsional mode shape for which the components corresponding to the lateral degrees of freedom are set to zero. The approach of eq. 4.63 is referred as method B*. The results of the three different methods for calculating the effective distributed mass properties are presented in table 4.4 for the eleven bridges of table 4.1. In this table, the values correspond to full-scale ones. For the sake of brevity, only the values for the first symmetric vertical mode and the first symmetric torsional mode are shown.

As it can be observed in table 4.4, there is a very good agreement for \bar{m}_V between methods A, B and B*. Similar values are obtained for methods B and B* because the first symmetric vertical modes do not involve significant longitudinal displacements. However, with inactive hydraulic buffers, the first antisymmetric vertical modes can have non-negligible longitudinal displacements. In this case, methods B and B* give significantly different results. For example, considering the first antisymmetric vertical mode of bridge SU1, method B gives

40.21×10^3 kg/m, whereas method B* yields 23.73×10^3 kg/m. In this case, method B* gives results closer to method A, which has a value of 24.17×10^3 kg/m. For the mass moment of inertia \bar{m}_θ , a very good agreement is obtained between the three methods except for bridges SU2 and SU3a, for which method B yields much higher values compared to the two other methods. This is explained by the fact that the first symmetric torsional modes for these bridges possess non-negligible lateral displacements.

From this analysis, methods A and B* should be preferred over method B since it overestimates the mass values to be used for section model tests in specific cases. With inactive hydraulic buffers, the longitudinal modal displacements for the bridge deck are not restrained, which can lead to greater values of \bar{m}_V with method B. However, even if they are inactive, hydraulic buffers can provide some sort of dynamic restraint in the longitudinal direction through nonlinear energy dissipation. Consequently, it seems reasonable not to include the longitudinal degrees of freedom when calculating the effective distributed mass, i.e., using method B*. For the torsional modes, the lateral modal displacements, when existent, can also lead to an overestimation of \bar{m}_θ . As lateral effects associated with torsional modes are difficult to represent in section model tests, it appears reasonable not to account for them and use method B* for calculating the effective mass moment of inertia per unit length.

However, since the nonlinear structural behavior of eqs. 4.50 and 4.51 was obtained in relation to \bar{m}_V and \bar{m}_θ based on method B, it is needed to account for mass correction factors in eqs. 4.50 and 4.51 when methods A or B* are used. For being more practical than the intuitive approach of method A, especially for cable-stayed bridges, method B* is the approach preferred for this research. Therefore, eqs. 4.50 and 4.51 need to be modified as follows:

$$\bar{f}_V^*(y_V, y_\theta) = \frac{\bar{m}_V^*}{\bar{m}_V} \cdot \frac{\tilde{f}_V(\beta_V y_V, \beta_\theta y_\theta)}{\Gamma_V^h} \quad (4.64)$$

$$\bar{f}_\theta^*(y_V, y_\theta) = \frac{\bar{m}_\theta^*}{\bar{m}_\theta} \cdot \frac{\tilde{f}_\theta(\beta_V y_V, \beta_\theta y_\theta)}{\Gamma_\theta^\alpha} \quad (4.65)$$

where $\bar{f}_V^*(y_V, y_\theta)$ and $\bar{f}_\theta^*(y_V, y_\theta)$ are the mass-corrected restoring forces per unit length; \bar{m}_V and \bar{m}_θ are the mass properties per unit length from method B; \bar{m}_V^* and \bar{m}_θ^* are the mass properties per unit length from method B*. The mass correction factors \bar{m}_V^*/\bar{m}_V and $\bar{m}_\theta^*/\bar{m}_\theta$ in eqs. 4.64 and 4.65 are required in order to obtain the correct natural frequencies when \bar{m}_V^* and \bar{m}_θ^* are considered for the mass properties of the section model.

4.5.3 Shape Similarity for Vertical and Torsional Modes

In the theory developed in section 4.4, some simplifications made are only possible when the first symmetric vertical mode $\psi_V^h(x)$ and the first symmetric torsional mode $\psi_\theta^\alpha(x)$ are similar in shape. This is to guarantee that the correction factors for these modes have similar values. Therefore, this section presents a comparison of the mode correction factors as well as an analysis of the shape similarity of the modes.

Table 4.5 shows the mode correction factors for the first symmetric vertical-torsional modal pair. As mentioned in section 4.4.8 and shown in eqs. 4.66 and 4.67, the correction factors Γ_V^h , Γ_θ^α , β_V and β_θ are calculated using the absolute values of the modal functions. For the sake of completeness, the factors Γ_{V2}^h and $\Gamma_{\theta2}^\alpha$ are also presented in table 4.5, which are defined below:

$$\Gamma_V^h = \int_{L_{br}} |\psi_V^h(x)| dx \quad \Gamma_\theta^\alpha = \int_{L_{br}} |\psi_\theta^\alpha(x)| dx \quad (4.66)$$

$$\beta_V = \frac{\int_{L_{br}} |\psi_V^h(x)| dx}{\int_{L_{br}} [\psi_V^h(x)]^2 dx} \quad \beta_\theta = \frac{\int_{L_{br}} |\psi_\theta^\alpha(x)| dx}{\int_{L_{br}} [\psi_\theta^\alpha(x)]^2 dx} \quad (4.67)$$

In table 4.5, the relative deviations between the mode correction factors as defined in the following equations are also included:

$$\Delta\Gamma_{V\theta} = \frac{|\Gamma_V^h - \Gamma_\theta^\alpha|}{\max(\Gamma_V^h, \Gamma_\theta^\alpha)} \quad \Delta\Gamma_{V\theta2} = \frac{|\Gamma_{V2}^h - \Gamma_{\theta2}^\alpha|}{\max(\Gamma_{V2}^h, \Gamma_{\theta2}^\alpha)} \quad \Delta\beta_{V\theta} = \frac{|\beta_V - \beta_\theta|}{\max(\beta_V, \beta_\theta)} \quad (4.68)$$

Further to comparing the mode correction factors, the shape similarity of the modes is verified using the Modal Assurance Criterion (MAC) [182]. Since modal functions are considered herein, the modal assurance criterion $MAC_{V\theta}$ for $\psi_V^h(x)$ and $\psi_\theta^\alpha(x)$ is calculated as per eq. 4.69. The MAC varies from 0 to 1, and a MAC value closer to 1 indicates a better shape similarity. The values of $MAC_{V\theta}$ for the eleven bridges are also presented in table 4.5, which were calculated using the following equation:

$$MAC_{V\theta} = \frac{\left(\int_{L_{br}} \psi_V^h(x) \psi_\theta^\alpha(x) dx \right)^2}{\left(\int_{L_{br}} [\psi_V^h(x)]^2 dx \right) \left(\int_{L_{br}} [\psi_\theta^\alpha(x)]^2 dx \right)} \quad (4.69)$$

Table 4.5: Comparison of mode correction factors (first symmetric vertical-torsional modal pair)

Bridge	Γ_V^h (m)	Γ_θ^α (m)	$\Delta\Gamma_{V\theta}$ (%)	Γ_{V2}^h (m)	$\Gamma_{\theta2}^\alpha$ (m)	$\Delta\Gamma_{V\theta2}$ (%)	β_V (m)	β_θ (m)	$\Delta\beta_{V\theta}$ (%)	$MAC_{V\theta}$
SU1	1279.1	1023.2	20.0	845.0	710.0	16.0	1.514	1.441	4.8	0.7910
SU2	1133.4	994.2	12.3	730.6	724.8	0.8	1.551	1.372	11.6	0.7093
SU3a	988.7	1004.9	1.6	650.3	706.4	7.9	1.520	1.423	6.4	0.9665
SU3b	1318.0	1321.7	0.3	886.9	914.2	3.0	1.486	1.446	2.7	0.9917
SU3c	1651.0	1654.2	0.2	1142.7	1145.0	0.2	1.445	1.445	0.0	0.9997
SU4a	472.5	622.7	24.1	315.0	466.5	32.5	1.500	1.335	11.0	0.7524
SU4b	712.4	840.9	15.3	474.9	630.9	24.7	1.500	1.333	11.2	0.8269
SU4c	948.9	1049.1	9.5	639.0	784.6	18.6	1.485	1.337	10.0	0.8939
SU4d	1186.9	1247.8	4.9	803.2	919.8	12.7	1.478	1.357	8.2	0.9417
CS1	280.0	387.8	27.8	186.6	284.2	34.3	1.500	1.365	9.0	0.9404
CS2	329.3	356.3	7.6	218.1	249.4	12.6	1.510	1.429	5.4	0.9925

From table 4.5, it is possible to observe that bridges SU3a, SU3b, SU3c, SU4c and SU4d have small values for the deviations of the mode correction factors $\Delta\Gamma_{V\theta}$ and $\Delta\beta_{V\theta}$. Additionally, the values of $MAC_{V\theta}$ for these bridges are generally greater than 0.9. For the suspension bridges SU1, SU2, SU4a and SU4b, the mode correction factor deviations $\Delta\Gamma_{V\theta}$ and $\Delta\beta_{V\theta}$ are slightly more important, especially for $\Delta\Gamma_{V\theta}$ for SU1 and SU4a. It is also worth noting that the values for $MAC_{V\theta}$ are less than 0.9 unlike the other suspension bridges. A potential explanation is that bridges SU1, SU2, SU4a and SU4b have main spans shorter than the other suspension bridges, which means that they have a greater relative contribution from their bridge deck to the bridge dynamic behavior due to smaller main cables. Additionally, the contribution from the bridge deck in terms of dynamic behavior is relatively greater for the torsional modes than the vertical modes as demonstrated by larger natural frequencies for the torsional modes than for the vertical ones. For example, the torsional-to-vertical frequency ratios for bridges SU4a, SU4b, SU4c and SU4d are respectively 1.79, 1.63, 1.51 and 1.39. Therefore, this ratio decreases with an increasing span length. The fact that shorter bridges have larger frequency ratios indicate that their bridge deck contributes more to the dynamic torsional behavior of the bridge in comparison to the vertical dynamic behavior. This means that the modal shape function $\psi_\theta^\alpha(x)$ is affected differently by the bridge deck than the vertical function $\psi_V^h(x)$. All of this leads to slightly different mode correction factors and smaller values of $MAC_{V\theta}$ in the case of suspension bridges with shorter span lengths. For the cable-stayed bridges CS1 and CS2, values for $MAC_{V\theta}$ are greater than 0.9. The mode correction factor deviations $\Delta\Gamma_{V\theta}$ and $\Delta\beta_{V\theta}$ are acceptable except for $\Delta\Gamma_{V\theta}$ for bridge CS1, for which the deviation is more than 20%. For all the bridges, it is also observed that the deviations $\Delta\Gamma_{V\theta2}$ are greater than the deviations $\Delta\Gamma_{V\theta}$. However, since Γ_{V2}^h and $\Gamma_{\theta2}^\alpha$ do not intervene directly in the mode correction of the nonlinear restoring forces, this is not

problematic. From all the previous observations and considering that suspension bridges with very long spans are more interesting for this research on structural nonlinearities, the approximations made in section 4.4 that assume that $\psi_V^h(x) \approx \psi_\theta^\alpha(x)$ and $\beta_V \approx \beta_\theta$ seem reasonable.

4.5.4 Mean Wind Response from Section Model Tests

In the case of nonlinear tests, the static displacements must also be considered as it influences the restoring forces and the nonlinear dynamic behavior as demonstrated by eq. 4.49. Therefore, this section verifies that the mean wind response can be approximated with a sufficient level of accuracy from section model tests. This is done by comparing the nonlinear aerostatic response of the full bridge as per [19] to the solution of the following equation for the section-model case:

$$\begin{bmatrix} \overline{f}_V^*(y_V^s, y_\theta^s) \\ \overline{f}_\theta^*(y_V^s, y_\theta^s) \end{bmatrix} = \begin{bmatrix} L_{s0} + L'_s y_\theta^s \\ M_{s0} + M'_s y_\theta^s \end{bmatrix} \quad (4.70)$$

Equation 4.70 is obtained by setting the dynamic displacements to zero in eq. 4.39 and considering only the mean aerodynamic loads. It should be noted that in eq. 4.70 the restoring force vector accounts for the mass correction factors of eqs. 4.64 and 4.65. The static displacements of the section model y_V^s and y_θ^s are calculated by solving eq. 4.70 using the Newton-Raphson method. From these, eq. 4.47 is utilized to give the generalized displacements of the full bridge that are used to calculate an approximation of the full-bridge mean wind response using $h_s(x) \approx \psi_V^h(x)z_h^s$ and $\alpha_s(x) \approx \psi_\theta^\alpha(x)z_\theta^s$. This procedure was utilized for the eleven cable-supported bridges in the case of the first symmetric modal pair. An initial angle of attack of 0° was also considered.

In what follows, selected results are presented for a comparison between the full-bridge mean wind response from nonlinear aerostatic analysis and the section-model results obtained using the procedure described in the previous paragraph. Figure 4.6 compares the maximum bridge-deck displacements at midspan obtained from section-model analysis and full-bridge analysis for an increasing wind speed. Results for bridges SU2, SU3b and SU4d are shown. In fig. 4.7, the static displacements along the bridge deck from section-model analysis and full-bridge analysis are compared for a mean wind speed of 60 m/s. The vertical dotted lines in fig. 4.7 shows the tower locations. Since bridge SU4d is a single-span suspension bridge, the tower locations are not illustrated in fig. 4.7c.

As it can be observed in fig. 4.6, the section-model approach provides a better evaluation of

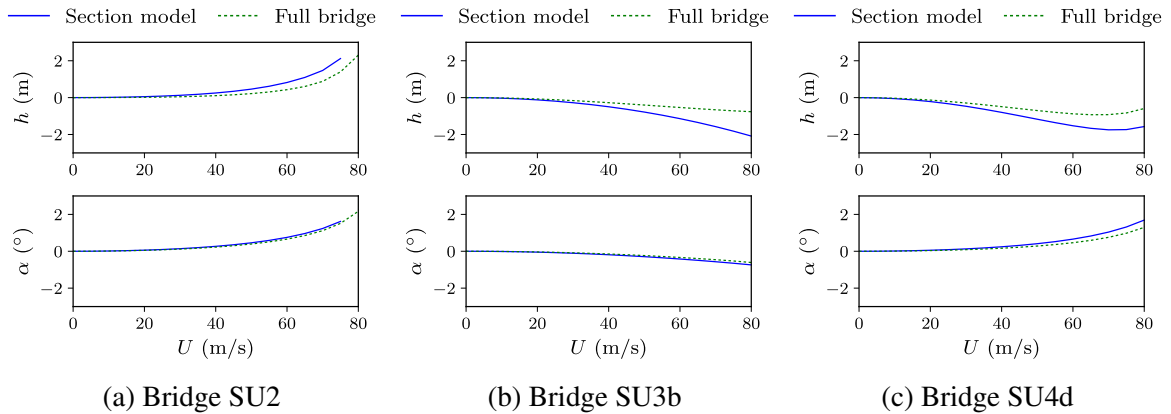


Figure 4.6: Maximum bridge-deck displacements under mean aerodynamic loads

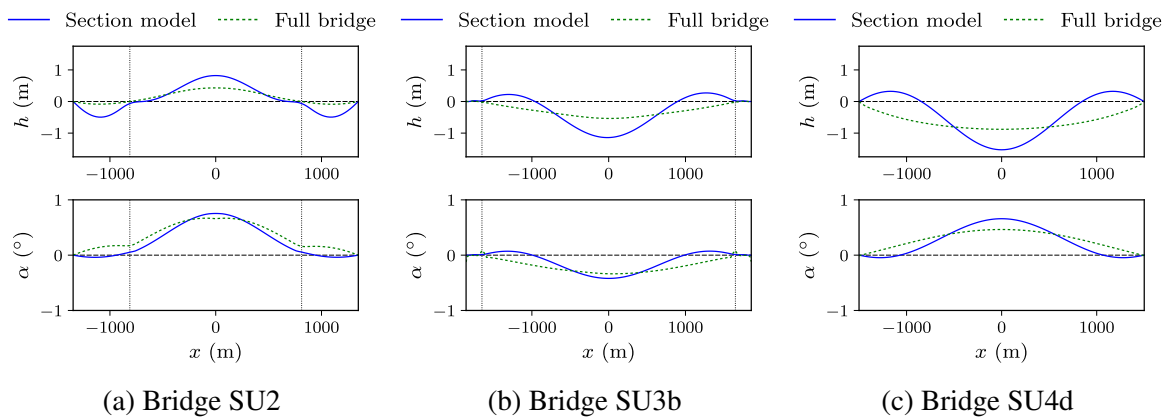


Figure 4.7: Bridge-deck displacement profile for mean aerodynamic loads at 60 m/s

the maximum torsional rotation in comparison to the vertical displacement. This is because, compared to the rotation, the displacement profile obtained from the vertical mode shape for the section-model results demonstrates larger differences than the profile obtained for the full bridge. This can be seen in fig. 4.7. Similar results were obtained for the other bridges. Consequently, even though the vertical displacements are not approximated as well as for the torsional rotations in the section model approach, there is only a noticeable difference for wind speeds over about 60 m/s. As nonlinear section model tests mainly aim at assessing the nonlinear dynamic behavior of bridges under wind loads, it appears that the static response is approximated with a sufficient degree of accuracy in section model tests. Also, because of the relatively small rotations of the bridge deck along its length, it is reasonable to assume that the same flutter derivatives can be used everywhere along the bridge deck as considered in section 4.4.2.

4.5.5 Buffeting Force Vector

The buffeting force vector in eq. 4.39 for the section model and the one in eq. 4.49 obtained from the full-bridge modal equations have analogous expressions. For the section-model case, the effective buffeting force per unit length $\overline{f}_{V,mp}^b(t)$ and effective buffeting moment per unit length $\overline{f}_{\theta,mp}^b(t)$ are:

$$\overline{f}_{V,mp}^b(t) = \frac{\int_{L_{mp}} L_b(x, t) dx}{L_{mp}} \quad (4.71)$$

$$\overline{f}_{\theta,mp}^b(t) = \frac{\int_{L_{mp}} M_b(x, t) dx}{L_{mp}} \quad (4.72)$$

For the full-bridge case, the following equations give respectively the expression for the effective buffeting force per unit length $\overline{f}_{V,br}^b(t)$ and the effective moment per unit length $\overline{f}_{\theta,br}^b(t)$:

$$\overline{f}_{V,br}^b(t) = \frac{\int_{L_{br}} |\psi_V^h(x)| L_b(x, t) dx}{\int_{L_{br}} |\psi_V^h(x)| dx} \quad (4.73)$$

$$\overline{f}_{\theta,br}^b(t) = \frac{\int_{L_{br}} |\psi_\theta^\alpha(x)| M_b(x, t) dx}{\int_{L_{br}} |\psi_\theta^\alpha(x)| dx} \quad (4.74)$$

To be consistent with the discussion in section 4.4.8 and to avoid a division by zero in the hypothetical case of antisymmetric modes, the absolute values of the modal functions are considered in eqs. 4.73 and 4.74.

In order to check whether section model tests can approximate in a satisfactory manner the buffeting response for the first symmetric modal pair, it is relevant to compare eqs. 4.71 and 4.72 to eqs. 4.73 and 4.74 in the case of a numerically simulated wind field. The numerical wind time histories were generated using the ergodic spectral representation method [201] and assuming the spectral representation by Solari and Piccardo [202]. The simulated wind field was generated every 30 m along the bridge deck for a mean wind speed of 60 m/s. Longitudinal and vertical turbulence intensities are respectively 10 % and 5 %.

Previously, the buffeting forces were expressed using a frequency-domain model, but for this

demonstration, a time-domain approach is preferred. This is because the nonlinear behavior considered for section model tests also evolves in the time domain. Therefore, the buffeting force and moment in eqs. 4.71–4.74 are expressed as follows considering the dimensionless time $s = Ut/B$ [203, 204]:

$$L_b(x, s) = \frac{1}{2}\rho U^2 B \int_0^s \left(2C_{L0} \phi'_{Lu}(s - \sigma) \frac{u(x, \sigma)}{U} + (C'_L + C_{D0}) \phi'_{Lw}(s - \sigma) \frac{w(x, \sigma)}{U} \right) d\sigma \quad (4.75)$$

$$M_b(x, s) = \frac{1}{2}\rho U^2 B^2 \int_0^s \left(2C_{M0} \phi'_{Mu}(s - \sigma) \frac{u(x, \sigma)}{U} + C'_M \phi'_{Mw}(s - \sigma) \frac{w(x, \sigma)}{U} \right) d\sigma \quad (4.76)$$

where the prime denotes the derivative with respect to the dimensionless time s ; ϕ_{Lu} , ϕ_{Lw} , ϕ_{Mu} and ϕ_{Mw} are the buffeting indicial functions. For the sake of this demonstration, it is sufficient to use the Küssner function in place of the indicial functions. The Küssner function and its derivative are given below [203]:

$$\phi(s) = 1 - 0.500e^{-0.130s} - 0.500e^{-s} \quad (4.77)$$

$$\phi'(s) = 0.065e^{-0.130s} + 0.500e^{-s} \quad (4.78)$$

where $\phi(s)$ and $\phi'(s)$ are the Küssner function and its derivatives. For the sake of brevity, the terms for the initial conditions in eqs. 4.75 and 4.76 are omitted since $\phi(0) = 0$. It should be noted that the quasi-steady approach has often been utilized for calculating the buffeting forces, but the inclusion of the frequency dependence through aerodynamic admittance functions has become common practice in frequency-domain buffeting analysis (e.g. see [34, 188, 205]). When the admittance functions for the lift and moment are not available, the Sears function has often been considered in lieu of experimentally measured admittance functions. This is why herein the Küssner function is utilized as it is the time-domain counterpart of the Sears function. This was similarly done in [82] to account for the time lag effect in an approximate manner.

Figure 4.8 presents a comparison of the time histories of the effective buffeting forces of bridges SU4a, SU4d and CS1 for the full-scale section model and the full bridge. A length of 160 m is considered for the section model, which corresponds to the full-scale length of a 1/75 model of typical length tested at the Boundary Layer Wind Tunnel Laboratory at the University of Western Ontario (BLWTL). In fig. 4.9, the power spectral densities (PSD)

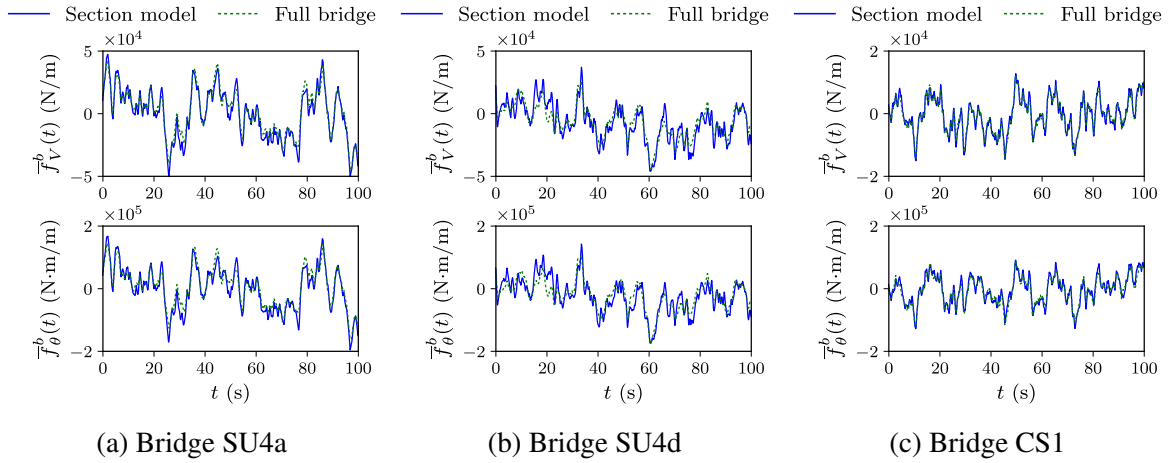


Figure 4.8: Time histories of effective buffeting forces per unit length

$\bar{S}_{f_V}^b$ and $\bar{S}_{f_\theta}^b$ of the effective buffeting force per unit length $\bar{f}_V^b(t)$ and effective buffeting moment per unit length $\bar{f}_\theta^b(t)$ are compared for the section model and the full bridge. To obtain the results presented in these figures, a wind field was generated along the bridge deck. Then, the buffeting forces were calculated at different locations along the bridge deck using eqs. 4.75 and 4.76. Afterwards, the effective buffeting forces are obtained from eqs. 4.73 and 4.74 for the full bridge. The same wind field is considered for the section model, but the integration over the length of the section model in eqs. 4.71 and 4.72 is done using the wind field around the middle of the bridge. This is justified by the fact that section model tests aim at predicting the generalized displacements of specific modes, which are related to the maximum modal displacements occurring in the middle of the bridge for the first symmetric modes. Therefore, either for the full bridge or the section model, a time integration at different locations along the bridge deck is utilized to obtain the buffeting forces at these locations. Then, a span-wise integration is performed to obtain the effective buffeting forces per unit length.

As it can be seen in fig. 4.8, there is a very good agreement between the section model and the full bridge for the time histories of the effective buffeting forces. Similarly, the PSDs agree well in fig. 4.9. It is worth noting that there is a slightly larger discrepancy for bridge SU4d in fig. 4.9b in comparison to figs. 4.9a and 4.9c. This is explained by the longer span length of 3000 m in comparison to bridges SU4a and CS1 with span lengths of 1200 m and 856 m respectively. It should be noted that the results for the other bridges in table 4.1 also agree well.

It is worth noting that the low-frequency content of the wind spectra cannot be modeled correctly in section model tests when grid-generated turbulence is used. However, the grid-

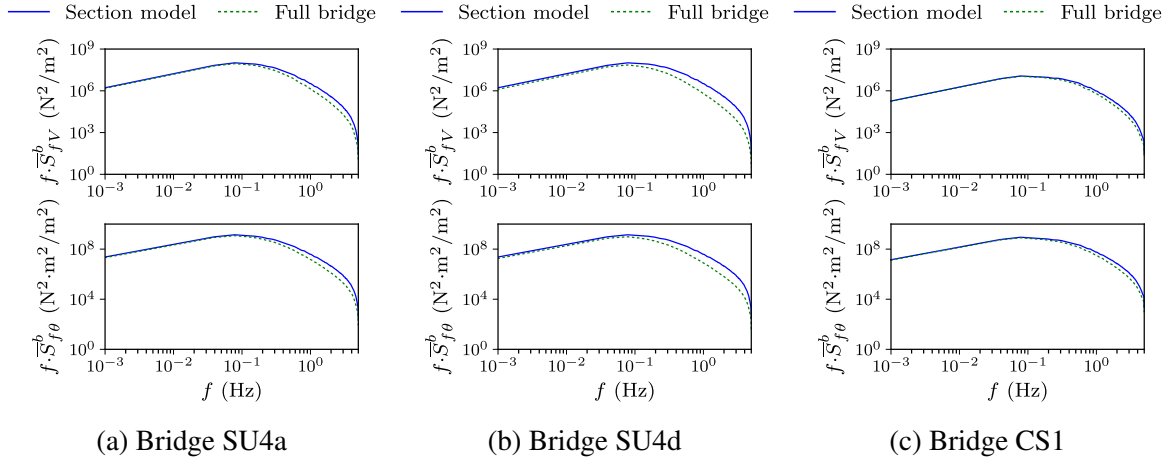


Figure 4.9: Power spectral density of effective buffeting forces per unit length

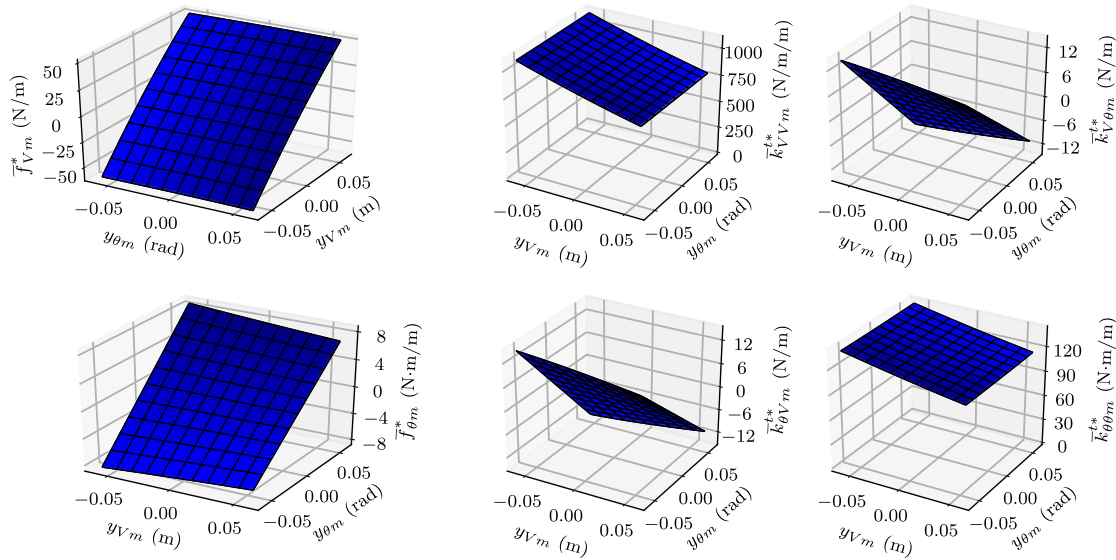
generated turbulence in the frequency range of the natural frequencies of the first symmetric modal pair is believed to be sufficiently accurate for the sake of this research. From this demonstration and discussion, it is possible to conclude that the buffeting effects can be considered in a satisfactory manner to see whether buffeting effects can trigger a nonlinear dynamic instability in nonlinear section model tests.

4.6 Example and Discussion on Scaled Nonlinear Generalized Behavior

4.6.1 Example of Scaled Nonlinear Generalized Behavior for Bridge SU4c

The discussion in section 4.5 confirms the validity of the assumptions utilized in the scaling procedure of section 4.4 for nonlinear section model tests. Therefore, it is now of interest to calculate the scaled nonlinear generalized behavior corresponding to the first symmetric modal pair for the bridges of table 4.1. After calculating the nonlinear generalized stiffness parameters using the procedure described in section 4.3, they were scaled using eqs. 4.57 and 4.58. As method B* is considered in this research to calculate the mass properties of the section models, mass correction factors were applied to the scaled nonlinear generalized behavior as shown in eqs. 4.64 and 4.65.

For the sake of brevity and from the fact that similar results are obtained for the different bridges, scaled nonlinear generalized stiffness parameters are shown in fig. 4.10 only for bridge SU4c. For this specific case, the scaling factors used are $\lambda_L = 1/75$ and $\lambda_U = 1/3.75$,



(a) Generalized restoring forces

(b) Generalized stiffnesses

Figure 4.10: Scaled nonlinear generalized behavior for bridge SU4c ($\lambda_L = 1/75$ and $\lambda_U = 1/3.75$)

which are realistic values for the BLWTL. The scaled generalized restoring forces per unit length \bar{f}_{jm}^* and the scaled generalized stiffnesses per unit length \bar{k}_{jkm}^{t*} are presented in this figure. The nonlinear stiffness behavior can be seen for the diagonal terms. Also, the non-zero off-diagonal terms in fig. 4.10b confirms the nonlinear coupling between vertical and torsional modes.

4.6.2 Comparison Between Linear and Nonlinear Cases for Bridge SU4c

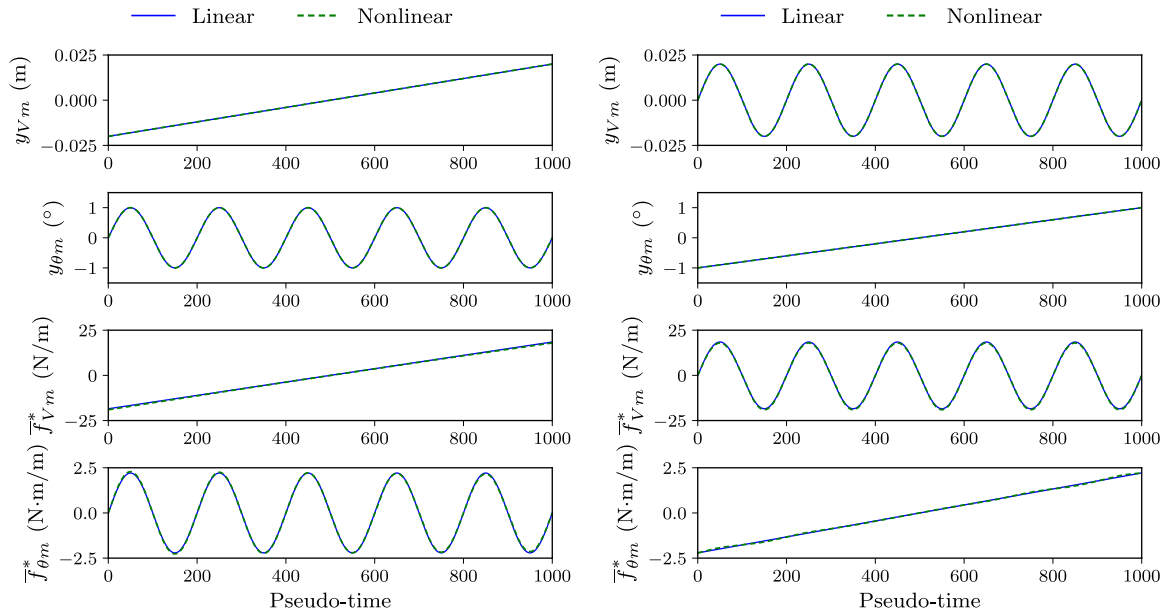
In order to better understand the impact of considering a nonlinear structural behavior as shown in fig. 4.10 on section model tests, it is of interest to make a comparison between the linear case and the nonlinear case. To do so, the forces per unit length are calculated using the linear and nonlinear procedures for four different displacement scenarios. The results of this analysis are presented in fig. 4.11 for bridge SU4c with $\lambda_L = 1/75$ and $\lambda_U = 1/3.75$. The first scenario is for small displacements of the section model that vary between ± 0.02 m and $\pm 1^\circ$. Additionally, for the first displacement scenario, the vertical displacements are considered to vary linearly with respect to a pseudo-time, whereas the torsional rotations vary in a sinusoidal manner with respect to the pseudo-time. The results for the first displacement scenario are shown in fig. 4.11a. Similarly, fig. 4.11b presents the results for the second

displacement scenario, which considers the same displacement limits as for the first case, but y_{Vm} varies sinusoidally and $y_{\theta m}$ varies linearly in this case. For the third and fourth displacement cases shown in figs. 4.11c and 4.11d, large displacements varying between ± 0.1 m and $\pm 5^\circ$ are utilized. For the third scenario, y_{Vm} and $y_{\theta m}$ are respectively linear and sinusoidal (fig. 4.11c). For the fourth scenario in fig. 4.11d, the vertical displacements are sinusoidal with respect to the pseudo-time, and the torsional rotations are linear. In each subfigure of fig. 4.11, the two top graphs are the displacements, and the two bottom graphs correspond to the vertical force and torsional moment per unit length. In fig. 4.11, the solid line corresponds to the linear case based on the natural frequencies and mass properties, whereas the dashed line refers to the nonlinear case based on the approach of section 4.4.

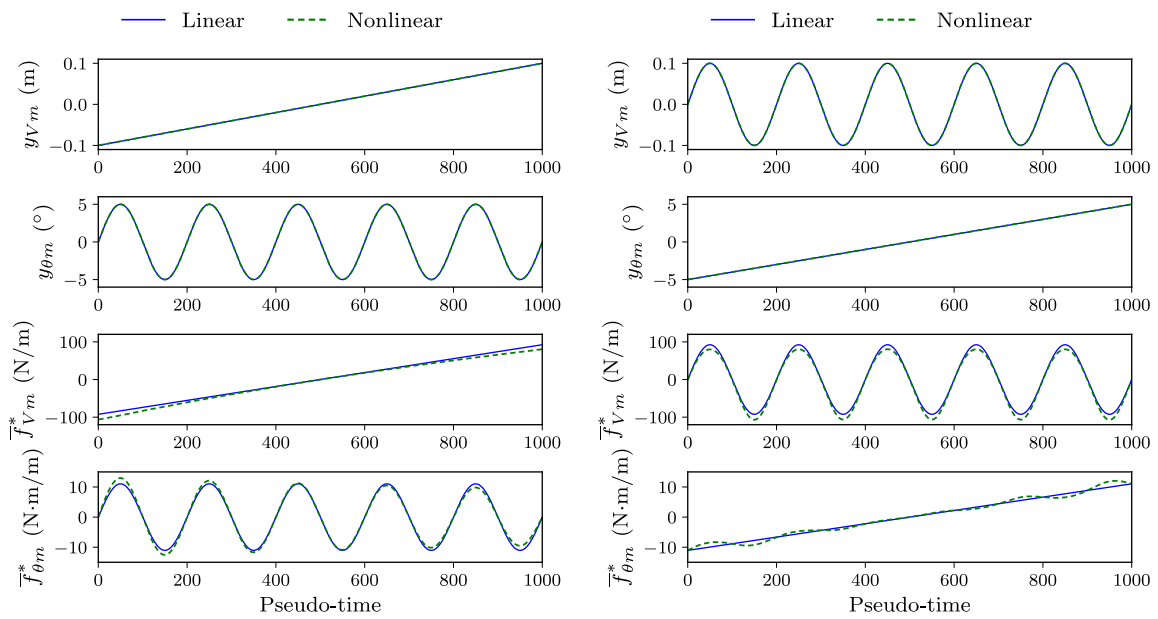
Firstly, in figs. 4.11a and 4.11b, it is interesting to note that for small displacements, the nonlinear approach gives the same results as for the linear approach that considers the linear stiffness behavior given by $\bar{k}_{Vm}^* = \omega_{Vm}^2 \bar{m}_{Vm}^*$ and $\bar{k}_{\theta m}^* = \omega_{\theta m}^2 \bar{m}_{\theta m}^*$. This observation therefore confirms the validity of the nonlinear approach as it reduces to a linear behavior for small displacements. It also confirms the demonstration made in eq. 4.60. However, in the case of large displacements, there are discrepancies between the linear and nonlinear approaches as shown in figs. 4.11c and 4.11d. These subfigures show that the nonlinear behavior is more important for the vertical force. It is also possible to see the nonlinear vertical-torsional coupling in these figures. For example, in fig. 4.11c, the maximum values of the torsional moment per unit length $\bar{f}_{\theta m}^*$ are greater for a pseudo-time from 0 to 200 than for a pseudo-time from 800 to 1000. The nonlinear vertical-torsional coupling is also demonstrated by the sinusoidal variation of $\bar{f}_{\theta m}^*$ around the linear case in fig. 4.11d. From this analysis, the effect of structural nonlinearities seems to be negligible for small displacements, but for larger displacements they are more apparent. It therefore seems of interest to use an experimental approach to see whether they could have an effect on the aeroelastic stability of bridges.

4.6.3 Implications of Nonlinear Structural Behavior on Testing Procedure

Typical experimental rigs for section model tests use vertical springs connected to a torsion arm as described in [30]. Such an experimental setup has vertical and torsional stiffnesses that are constant irrespective of the amplitude of vibration, which means that such rig behaves linearly [104]. Consequently, using a setup consisting of vertical springs, it is not possible to represent a nonlinear structural behavior similar to the one presented in fig. 4.10. Therefore, it will be required to use a different experimental approach in order to conduct nonlinear section model tests for bridges.



(a) Small displacements (y_{Vm} : linear, $y_{\theta m}$: sinusoidal) (b) Small displacements (y_{Vm} : sinusoidal, $y_{\theta m}$: linear)



(c) Large displacements (y_{Vm} : linear, $y_{\theta m}$: sinusoidal) (d) Large displacements (y_{Vm} : sinusoidal, $y_{\theta m}$: linear)

Figure 4.11: Analysis of nonlinear behavior for the scaled section model of bridge SU4c ($\lambda_L = 1/75$ and $\lambda_U = 1/3.75$)

To simulate a nonlinear behavior similar to fig. 4.10 in the wind tunnel, it would be possible to utilize an active control experimental test rig like the one proposed in [62], which allows real-time hybrid tests. In such real-time hybrid tests, the aerodynamic forces applied to the section model are measured from wind tunnel tests. Then, the measured aerodynamic forces are applied to a numerical model of the dynamic system that accounts for the nonlinear structural behavior. By solving numerically the dynamic system, the corresponding displacements of the section model are obtained, which are then imposed to the section model using electric motors, for example. Such an experimental procedure requires a very sophisticated experimental apparatus composed of a data acquisition system, electric motors, a control system for the motors and a computer. The difficulty of such a procedure is undoubtedly its real-time aspect.

Considering that conducting real-time hybrid wind tunnel tests at the BLWTL would require substantial developments and investments, it appears that developing a nonlinear mechanical device would be more reasonable for an initial experimental investigation of the effect of structural nonlinearities on the aeroelastic stability of bridges. Such a nonlinear device needs to be able to simulate with sufficient accuracy a nonlinear structural behavior similar to fig. 4.10. Based on the research in [57], it appears feasible to design a nonlinear mechanical device for nonlinear section model tests. Currently, different options are being studied for a nonlinear springing system that can be utilized for nonlinear section model tests of bridges. This includes springs with varying pitch or diameter, contact springs, inclined springs and nonlinear cam mechanisms.

4.7 Conclusions

As spans are getting longer in cable-supported bridges, it seems appropriate to develop a better understanding of the incidence of structural nonlinearities on the aeroelastic and dynamic stability of these bridges. This is validated by the observations made by mathematicians regarding large oscillations in suspension bridges due to nonlinear dynamic phenomena associated with geometric nonlinearities of the bridge structure. It is believed that an experimental approach would be an effective way to study the wind response of bridges when structural nonlinearities are considered. Therefore, in order to eventually assess the effect of structural nonlinearities on the stability of bridges, the idea of accounting for geometric nonlinearities when conducting section model tests for bridges is proposed in this chapter.

After revisiting two-mode nonlinear generalized stiffness analysis of bridges for one vertical

mode of vibration and one analogous torsional mode, the nonlinear dynamic equations in the modal space for the full bridge and the section-model equations were derived. Because of the different shapes of the modes of vibration for the full bridge and the section model, it was needed to develop expressions for mode correction factors to be applied to the two-mode nonlinear generalized restoring forces of the full bridge. This was accomplished by comparing the full-bridge dynamic equations to the section-model equations. It was also shown how to convert, from full scale to model scale, the mode-corrected two-mode nonlinear generalized behavior, which is to be used for nonlinear section model tests.

Then, it was required to validate the assumptions made in the development of the theoretical equations for nonlinear section model tests. Eleven finite element models of cable-supported bridges were utilized for this purpose. The full-bridge mean wind responses of the different bridges were analyzed to see whether the static rotation of the bridge deck is small. An analysis of the effective distributed mass properties to be considered for section model tests was included. The shape similarity between analogous vertical and torsional modes was checked, and it was concluded that they have a very good similarity for most of the eleven bridges. It was verified that the mean wind response of the bridge can be approximated with a sufficient level of accuracy using section model tests when the first symmetric vertical-torsional modal pair is considered for the section model. The buffeting forces for the full bridge and the section model were also compared. A good agreement was found, but it is important to keep in mind the limitations of the grid-generated turbulence typically utilized for section model tests. Finally, the scaling procedure of the nonlinear generalized behavior was tested.

An experimental rig for such nonlinear section model tests is currently being designed, and wind tunnel tests are expected to be conducted in the near future. The findings and results of such nonlinear tests will be reported in future publications. Eventually, this research will allow a better understanding of the interaction between structural nonlinearities and aeroelastic effects for long span cable-supported bridges.

Chapter 5

Design of Test Rig for Nonlinear Section Model Tests

5.1 Introduction

Even though the use of computational fluid dynamics (CFD) has been more common in the field of bridge engineering in the past years (e.g. [64]), wind tunnel tests are still today the norm for assessing the safety of cable-supported bridges under wind loads. The two most common types of wind tunnel tests are full-aeroelastic model tests and section model tests. Considering that all structural elements are included in full-aeroelastic model tests, they provide an accurate prediction of the full-bridge response [29]. However, these tests are complicated and expensive due to the size and intricacy required for full-aeroelastic models. Compared to full-aeroelastic model tests, section model tests, where a rigid segment of a bridge deck is suspended by a springing system, are affordable and relatively straightforward [30]. In general, section model tests can represent one vertical mode and one torsional mode, but a lateral mode has also been included in some cases [32]. Some interesting developments have been made for experimental apparatuses utilized for section model tests that have expanded their usefulness. For example, a dynamometric section model of the Messina Strait Bridge was developed [36]. In [37], an innovative section model test rig that can be utilized for free- and forced-vibration tests was designed. Another example is the development of a forced-vibration test rig that can be used for arbitrary motion [40]. With the idea of increasing the number of modes represented in section model tests while keeping the simplicity of such tests, taut-strip model tests were developed [59]. These tests are suitable for bridges having sinusoidal modes of vibration since the model stiffness is provided through taut wire or tubes. Hence, a taut-strip model can be seen as a long flexible section model. More recently, a multi-supported aeroelastic model was used, but only vertical modes were considered since the research in [60] focused on vortex-induced vibrations in the vertical direction. Moreover, similar to what is used in structural engineering, real-time hybrid tests where the aeroelastic system would be partially modeled in the lab and partially represented in a numerical model are discussed [61, 62].

Even though there are so many options when it comes to choosing an experimental approach for testing bridges in a wind tunnel, bridge engineers have often chosen section model

tests due to their simplicity, versatility and cost effectiveness. Even with the advancements made over many decades in experimental apparatus, the same simplifications in terms of aerodynamic and structural behaviors are still used for section model tests in the case of bridges. For example, these tests neglect the aerodynamic contribution of the cable system. Only one mode in each direction can be represented at a time in section model tests, which is assumed to be uniform along the length of the section model. Additionally, since the modes represented in the wind tunnel originate from linear structural dynamics theory, the bridge structure is therefore assumed to behave linearly.

However, cable-supported bridges can exhibit structural nonlinearities such as geometric nonlinearities [149, 150], material nonlinearities [147, 151] as well as localized nonlinearities like hydraulic buffers [12, 17, 151]. Furthermore, using advanced mathematical approaches, it was shown that dynamic vertical forcing can lead to large torsional oscillations due to nonlinear vertical-torsional mode coupling associated with geometric nonlinearities [168–170]. Internal parametric resonance, a structural dynamic instability caused by the nonlinear structural coupling between modes of vibration, would be responsible for such large oscillations [170]. This instability has a structural origin unlike flutter, which is an aeroelastic phenomenon. In order to have a better understanding of nonlinear vertical-torsional coupling in cable-supported bridges, modal loads were applied to geometrically nonlinear structures, which allowed quantifying the level of nonlinear coupling (see chapter 3). It was shown that single-span suspension bridges have a stronger nonlinear coupling than three-span suspension bridges and cable-stayed bridges. The longer spans were also shown to be more nonlinear due to the greater contribution of the cable system to the bridge structural behavior.

To the author's knowledge, large oscillations caused by a structural dynamic instability as described in the previous paragraph has never been seen on an actual structure. Nevertheless, for a full-aeroelastic model of a double-main-span suspension bridge, a transition from an antisymmetric instability mode to a symmetric instability mode was observed [171]. What was observed for this full-aeroelastic bridge model would be caused by internal resonance associated with the nonlinearities of the aeroelastic system [172, 173]. This phenomenon is different than the flutter mode transition of [174] associated with two flutter instability modes having the same critical wind speed. These observations have led to numerous recent studies on nonlinear flutter and aerodynamic nonlinearities [90, 96, 100, 101, 120]. These studies have only focused on aerodynamic nonlinearities, and in recent experimental studies for bridges, structural nonlinearities are only discussed in the assessment of stiffness and damping nonlinearities of the section model test rig [90, 102, 104]. Nonetheless, the section model test apparatus of [45] demonstrates a weak nonlinear structural behavior

in torsion for rotations greater than 15° . This nonlinear behavior is caused by the fact that the test rig in [45] uses a different mechanism than vertical springs to allow for large amplitudes of motion of the section model. Therefore, it appears unlikely that the nonlinear torsional behavior in [45] is representative of an actual cable-supported bridge. However, the experimental rig in [45] is interesting for studying aerodynamic nonlinearities as it allows for large displacements. Another example of test rig able of large displacements is discussed in [47], but this rig is only of interest for aerodynamic nonlinearities since it has a linear structural behavior. In aeronautics, section model tests on airfoils have been conducted considering different types of structural nonlinearities, including freeplay, bilinear, parabolic and cubic nonlinearities (e.g. [50, 52, 54, 57]). It is worth mentioning that in the case of an airfoil with a bilinear behavior, it was observed that the critical velocity is less than in the case of a linear structural behavior [54]. The nonlinear system in [54] was weakly nonlinear with a difference of 14 % between the two stiffnesses of the bilinear system.

Considering that even weakly nonlinear systems can exhibit nonlinear dynamic phenomena [175], it appears appropriate to have a better understanding of the possible interaction between structural nonlinearities and aeroelastic effects. An appropriate way to achieve this would be to use an experimental approach. Consequently, this chapter presents the design of an experimental apparatus for section model tests of bridges able to account for the effect of structural nonlinearities. At first, a procedure to characterize and scale the target nonlinear generalized structural behavior of a cable-supported bridge in the context of nonlinear section model tests is reviewed. Then, a mechanical system able to model the nonlinear structural behavior for section model tests is discussed as well as a numerical approach used to calibrate the parameters of the mechanical system. Using four single-span suspension bridges with main spans ranging from 1.2 km to 3.0 km as case studies, this calibration procedure is tested to ensure its practicality. After discussing the characteristics needed for a nonlinear section model test rig, the design of such a test rig is briefly presented.

5.2 Scaled Nonlinear Generalized Structural Behavior

Between full-aeroelastic model tests, section model tests and taut-strip model tests, it is believed that the section model testing procedure is well suited for an experimental study of the effect of structural geometric nonlinearities on the stability of bridges when subjected to wind. This is because, even though full-aeroelastic models are in theory able to account for geometric nonlinearities, there is still the limitation that only either the bending stiffness or axial stiffness of a specific structural element of a bridge can be properly scaled. For

structural elements where both effects are important, their geometric stiffness would be erroneous in a full-aeroelastic model. This would be the case for the deck of a cable-stayed bridge that is rigidly connected to the towers like in the case of the *Pont de Normandie* in France. Additionally, full-aeroelastic model tests are very expensive, and therefore, they do not appear to be the right approach for an initial experimental study of structural nonlinearities. In the case of taut-strip models, the taut wires or tubes used in such models would not be able to represent the nonlinear behavior of a cable-supported bridge. For a bridge, an upward displacement leads to stiffness softening and a downward displacement is associated with stiffness hardening (see chapter 3), whereas a taut-strip model has a hardening behavior in both directions.

Even though section model tests are only able to account for one mode in each direction, their affordability and ease of use make them interesting for an assessment of the influence of structural nonlinearities on the wind response of bridges. The fact that only one mode in each direction can be represented can be circumvented by recognizing that nonlinear dynamic instability phenomena involve specific modes. Consequently, nonlinear section model tests should pay attention to the modes that are more critical for dynamic instabilities. Additionally, section model tests are versatile due to the easy access to the springing system, damping devices and ballast masses at both ends of the section model. Because of their versatility and the fact they represent a simplified representation of the bridge aeroelastic system, they have become popular in research for the study of the wind behavior of bridges. They also allow an easier interpretation of the studied phenomenon. Replacing the springing system by a nonlinear device representing the nonlinear behavior of a bridge and from which a section model will be suspended will allow nonlinear tests.

In the case of this research, the effect of structural nonlinearities on the wind stability of bridges is of interest, more specially stiffness nonlinearities. Due to the difficulty to characterize nonlinear structural damping in cable-supported bridges, an effective viscous damping is sufficient for an initial development of nonlinear section model tests. The procedure discussed herein for nonlinear section model tests of bridges does not aim at replacing the wind analysis procedure used in the industry that combines section model tests and numerical simulations. This research aims at improving the section model test procedure so that section model tests can be used for assessing the effect of structural nonlinearities on the aeroelastic stability of bridges. This research solely focuses on structural nonlinearities, but it should be recognized that aerodynamic nonlinearities are automatically considered when conducting section model tests.

Before discussing a mechanical device for such nonlinear tests, it is relevant to review the

theoretical developments for nonlinear section model tests of bridges. For more details about the theory, the reader is referred to chapters 3 and 4.

5.2.1 Nonlinear Generalized Stiffness

For nonlinear section model tests, it is assumed that only geometric nonlinearities are of concern. This appears to be a reasonable assumption since the cable system of a properly designed cable-supported bridge is the main structural component and it is also designed elastically [149]. A detailed discussion about the fact that only geometric nonlinearities are relevant for nonlinear section model tests can be found in chapter 4. Therefore, the calculation of nonlinear generalized structural behavior for nonlinear tests that is reviewed in this section will only account for geometric nonlinearities. Longitudinal hydraulic buffers are also considered as inactive when determining the nonlinear generalized stiffness behavior of a bridge.

As for typical section model tests, two degrees of freedom (DOF) are considered in the case of nonlinear tests, which are a vertical displacement y_V and a torsional rotation y_θ . Consequently, as shown in fig. 5.1, one vertical mode and one analogous torsional mode can be represented. However, in the case of nonlinear tests, the stiffness properties of the system cannot be calculated from the mass properties and natural frequencies. Instead, it is needed to determine a nonlinear force-displacement relationship representative of the full-bridge behavior. This is done by considering two-mode nonlinear generalized stiffness analysis as discussed in chapter 3. By applying static loads proportional to modes of vibration to a nonlinear finite element model of a cable-supported bridge, it is possible to quantify the nonlinear behavior of the bridge in terms of selected modes of vibration, which are intrinsic dynamic properties.

Two-mode nonlinear generalized stiffness analysis begins by solving the following nonlinear static equation:

$$\mathbf{f}_{SG}(\mathbf{u}_{nl}) = \mathbf{p}_{V\theta}^m \quad (5.1)$$

$$\mathbf{p}_{V\theta}^m = \mathbf{p}_V^m + \mathbf{p}_\theta^m = a_V \omega_V^2 \mathbf{M} \boldsymbol{\phi}_V + a_\theta \omega_\theta^2 \mathbf{M} \boldsymbol{\phi}_\theta \quad (5.2)$$

where $\mathbf{f}_{SG}(\mathbf{u}_{nl})$ is the internal force vector of the nonlinear geometric system of a bridge with inactive hydraulic buffers; \mathbf{u}_{nl} is the nonlinear displacement vector obtained from nonlinear static analysis; \mathbf{M} is the mass matrix calculated using the finite element method; a_V and

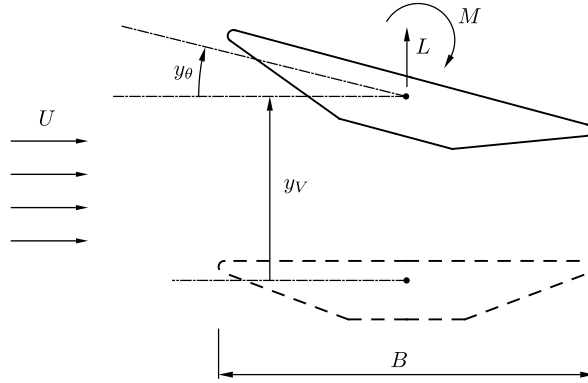


Figure 5.1: Dynamic system of a bridge section model (y_V : vertical displacement, y_θ : torsional rotation, B : bridge-deck width, U : mean wind speed, L : vertical force, M : torsional moment)

a_θ are respectively the modal load coefficients for mode ϕ_V and mode ϕ_θ ; $\omega_V = 2\pi f_V$ and $\omega_\theta = 2\pi f_\theta$ are respectively the natural angular frequencies for mode ϕ_V and mode ϕ_θ ; f_V and f_θ are the natural frequencies for mode ϕ_V and mode ϕ_θ . In eq. 5.1, the dead-load configuration is utilized as the reference state of the bridge numerical model. The natural frequencies and mode shapes are also for the dead-load configuration. Modes are normalized such that the maximum vertical displacement is unity for ϕ_V , and the maximum torsional rotation is unity for ϕ_θ . Doing so facilitates the physical interpretation of the generalized displacements.

By solving eq. 5.1 considering different values of the modal coefficients a_V and a_θ , it is possible to obtain a nonlinear generalized force-displacement relationship that can be expressed as follows (see chapters 3 and 4):

$$\tilde{\mathbf{f}}_{V\theta}(\mathbf{z}_{V\theta}) = \begin{bmatrix} \tilde{f}_V(z_V, z_\theta) \\ \tilde{f}_\theta(z_V, z_\theta) \end{bmatrix} \quad (5.3)$$

where $\tilde{\mathbf{f}}_{V\theta}(\mathbf{z}_{V\theta})$ is the generalized restoring force vector associated with modes ϕ_V and mode ϕ_θ ; $\mathbf{z}_{V\theta} = [z_V \ z_\theta]^T$; z_V and z_θ are respectively the vertical mode generalized displacement and torsional mode generalized displacement, which are calculated by applying a modal transformation to \mathbf{u}_{nl} . From the nonlinear force-displacement relationship of eq. 5.3, a nonlinear generalized stiffness matrix can be obtained using the following equation:

$$\tilde{\mathbf{K}}_{V\theta}^t(\mathbf{z}_{V\theta}) = \frac{\partial \tilde{\mathbf{f}}_{V\theta}}{\partial \mathbf{z}_{V\theta}} = \begin{bmatrix} \frac{\partial \tilde{f}_V}{\partial z_V} & \frac{\partial \tilde{f}_V}{\partial z_\theta} \\ \frac{\partial \tilde{f}_\theta}{\partial z_V} & \frac{\partial \tilde{f}_\theta}{\partial z_\theta} \end{bmatrix} \quad (5.4)$$

where $\tilde{\mathbf{K}}_{V\theta}^t(\mathbf{z}_{V\theta})$ is the two-mode tangent nonlinear generalized stiffness matrix, which is a function of the generalized displacement vector $\mathbf{z}_{V\theta}$. Since only geometric nonlinearities are accounted for in the process of calculating $\tilde{\mathbf{f}}_{V\theta}(\mathbf{z}_{V\theta})$ and $\tilde{\mathbf{K}}_{V\theta}^t(\mathbf{z}_{V\theta})$, the two-DOF nonlinear generalized system represented by eqs. 5.3 and 5.4 is therefore a conservative system.

As discussed in chapter 4, eq. 5.3 represents the restoring forces of a reduced-order model based on linear modes of vibration that accounts for the nonlinear geometric structural behavior. This is similar in principle to the approach of [190] utilized in aerospace engineering. For the reduced-modeling approach of [190], it was shown that a significant reduction in the size of the geometrically nonlinear dynamic system can be achieved since only a few modes are required in order to get good results. The dynamic response of a reduced-order model is solved numerically as shown in [190], but herein, the nonlinear structural behavior given by eq. 5.3 will be modeled mechanically and the dynamic response of the nonlinear generalized system will be obtained from section model tests in the wind tunnel. It is possible to see that eqs. 5.3 and 5.4 can represent the information needed for nonlinear section model tests, i.e., the individual nonlinear vertical behavior, the individual nonlinear torsional behavior and the nonlinear vertical-torsional coupling.

It is also worth noting that nonlinear generalized stiffness analysis as discussed in this section in the context of nonlinear section model tests is more relevant for the first symmetric vertical mode and the first symmetric torsional mode, i.e., the first symmetric modal pair. This is because symmetric vertical-torsional modal pairs were shown to be more nonlinear than antisymmetric ones (see chapter 3). Consequently, unless specifically mentioned, modes ϕ_V and ϕ_θ from now refer to the first symmetric ones. This indicates that linear tests can be utilized for the first antisymmetric modal pair, whereas nonlinear tests would be utilized for the first symmetric modal pair. Even though the first antisymmetric modal pair is typically critical with regard to flutter for very long suspension bridges, the critical velocities for the antisymmetric modes and symmetric modes can be similar as observed in [174]. Considering that, it would be interesting to see whether the nonlinear structural behavior could trigger the symmetric instability to happen for a lower wind speed than for the antisymmetric case. This could be possible considering that the nonlinear structural behavior was shown to lower the critical velocity for an airfoil in [54].

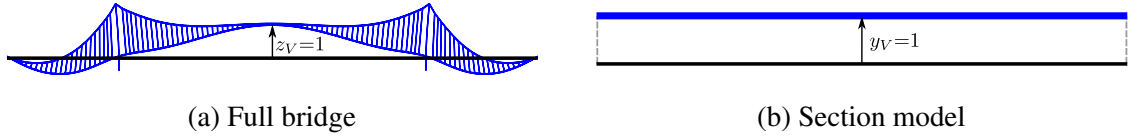


Figure 5.2: Comparison of typical mode shapes for a full bridge and a section model

5.2.2 Mode Correction Factors for Nonlinear Generalized Stiffness

As exemplified in fig. 5.2, a full-scale bridge has modal displacements that vary along the length of the bridge; this is unlike the section model for which mode shapes are uniform. Therefore, by comparing the modal dynamic equations of the full bridge to those of the section model case, it can be demonstrated that the force-displacement relationship of eq. 5.3 has to be modified with mode correction factors (see chapter 4). These correction factors are calculated using the following modal integrals:

$$\Gamma_V^h = \int_{L_{br}} |\psi_V^h(x)| dx \quad \Gamma_\theta^\alpha = \int_{L_{br}} |\psi_\theta^\alpha(x)| dx \quad (5.5)$$

where Γ_V^h are Γ_θ^α are the mode correction factors for the generalized restoring forces; $\psi_V^h(x)$ is a function for the vertical displacements along the bridge deck of the first symmetric vertical mode; $\psi_\theta^\alpha(x)$ is a function for the torsional rotations along the bridge deck of the first symmetric torsional mode; x is the position along the deck; L_{br} is the length of the bridge. The modal functions $\psi_V^h(x)$ and $\psi_\theta^\alpha(x)$ can be obtained from the mode vectors ϕ_V and ϕ_θ respectively. Also, it is worth noting that the absolute values of $\psi_V^h(x)$ and $\psi_\theta^\alpha(x)$ are utilized in eq. 5.5 since the modal displacement functions can have negative values.

Similarly, the generalized displacements also need a mode correction. To do so, the following modal integrals need to be calculated first:

$$\Gamma_{V2}^h = \int_{L_{br}} [\psi_V^h(x)]^2 dx \quad \Gamma_{\theta2}^\alpha = \int_{L_{br}} [\psi_\theta^\alpha(x)]^2 dx \quad (5.6)$$

Then, the mode correction factors β_V and β_θ for the generalized displacements can be obtained using the following equations:

$$\beta_V = \frac{\Gamma_V^h}{\Gamma_{V2}^h} = \frac{\int_{L_{br}} |\psi_V^h(x)| dx}{\int_{L_{br}} [\psi_V^h(x)]^2 dx} \quad (5.7)$$

$$\beta_\theta = \frac{\Gamma_\theta^\alpha}{\Gamma_{\theta2}^\alpha} = \frac{\int_{L_{br}} |\psi_\theta^\alpha(x)| dx}{\int_{L_{br}} [\psi_\theta^\alpha(x)]^2 dx} \quad (5.8)$$

The mode correction factors of eqs. 5.7 and 5.8 can be used to relate the vertical displacement y_V and torsional rotation y_θ of the section model to the generalized displacements z_V and z_θ . This is done using the following equations:

$$z_V = \beta_V y_V \quad z_\theta = \beta_\theta y_\theta \quad (5.9)$$

This equation directly gives the maximum displacements of the full bridge because of the unity-based normalization used for the modes. By dividing the generalized restoring forces $\tilde{f}_V(z_V, z_\theta)$ and $\tilde{f}_\theta(z_V, z_\theta)$ by the modal integrals of eq. 5.5 and substituting the generalized displacements z_V and z_θ by the expressions of eq. 5.9, the following equations can be obtained for the mode-corrected generalized restoring forces per unit length $\bar{f}_V(y_V, y_\theta)$ and $\bar{f}_\theta(y_V, y_\theta)$, which are the quantities required for nonlinear section model tests:

$$\bar{f}_V(y_V, y_\theta) = \frac{\tilde{f}_V(\beta_V y_V, \beta_\theta y_\theta)}{\Gamma_V^h} = \frac{\tilde{f}_V(\beta_V y_V, \beta_\theta y_\theta)}{\int_{L_{br}} \psi_V^h(x) dx} \quad (5.10)$$

$$\bar{f}_\theta(y_V, y_\theta) = \frac{\tilde{f}_\theta(\beta_V y_V, \beta_\theta y_\theta)}{\Gamma_\theta^\alpha} = \frac{\tilde{f}_\theta(\beta_V y_V, \beta_\theta y_\theta)}{\int_{L_{br}} \psi_\theta^\alpha(x) dx} \quad (5.11)$$

5.2.3 Effective Distributed Mass

After showing how to convert the generalized restoring forces into restoring forces per unit length, it is worth discussing how to convert the generalized masses into the effective mass and mass moment of inertia per unit length that will be considered for section model tests. This can be done by dividing the generalized masses by the modal integrals of eq. 5.6:

$$\bar{m}_V = \frac{\tilde{m}_V}{\Gamma_{V2}^h} = \frac{\tilde{m}_V}{\int_{L_{br}} [\psi_V^h(x)]^2 dx} \quad (5.12)$$

$$\bar{m}_\theta = \frac{\tilde{m}_\theta}{\Gamma_{\theta 2}^\alpha} = \frac{\tilde{m}_\theta}{\int_{L_{br}} [\psi_\theta^\alpha(x)]^2 dx} \quad (5.13)$$

where \bar{m}_V is the effective mass per unit length for the first symmetric vertical mode ϕ_V ; \bar{m}_θ is the effective mass moment of inertia per unit length for the first symmetric torsional mode ϕ_θ ; $\tilde{m}_V = \phi_V^T \mathbf{M} \phi_V$ and $\tilde{m}_\theta = \phi_\theta^T \mathbf{M} \phi_\theta$ are the generalized masses for mode ϕ_V and mode ϕ_θ . In chapter 4, it was shown that eqs. 5.12 and 5.13 overestimate the effective mass parameters in specific cases. Consequently, the following equations were suggested for the effective distributed mass properties:

$$\bar{m}_V^* = \frac{\tilde{m}_V^*}{\int_{L_{br}} [\psi_V^h(x)]^2 dx} \quad \bar{m}_\theta^* = \frac{\tilde{m}_\theta^*}{\int_{L_{br}} [\psi_\theta^\alpha(x)]^2 dx} \quad (5.14)$$

where $\tilde{m}_V^* = \phi_V^{*T} \mathbf{M} \phi_V^*$ with ϕ_V^* being a vertical mode shape for which the components corresponding to the longitudinal degrees of freedom are set to zero; $\tilde{m}_\theta^* = \phi_\theta^{*T} \mathbf{M} \phi_\theta^*$ with ϕ_θ^* being a torsional mode shape for which the components corresponding to the lateral degrees of freedom are set to zero.

5.2.4 Scaling of Nonlinear Generalized Stiffness

The quantities discussed above have referred to a full-scale bridge. These quantities need to be scaled in order to be utilized for section model tests. The mass properties, damping ratios and displacements can be scaled using the usual approach as shown below:

$$\bar{m}_{Vm} = \lambda_L^2 \bar{m}_{Vp} \quad \bar{m}_{\theta m} = \lambda_L^4 \bar{m}_{\theta p} \quad (5.15)$$

$$\xi_{Vm} = \xi_{Vp} \quad \xi_{\theta m} = \xi_{\theta p} \quad (5.16)$$

$$y_{Vm} = \lambda_L y_{Vp} \quad y_{\theta m} = y_{\theta p} \quad (5.17)$$

where $\lambda_L = L_m/L_p$ is the geometric scale; subscript m refers to the model; subscript p refers to the prototype or full-scale bridge; ξ_V and ξ_θ are the damping ratios. The nonlinear force-displacement relationship to be considered for nonlinear section model tests that corresponds

to the generalized restoring forces per unit length $\bar{f}_V(y_V, y_\theta)$ and $\bar{f}_\theta(y_V, y_\theta)$ needs to be scaled as follows:

$$\bar{f}_{V_m}(y_{V_m}, y_{\theta_m}) = \lambda_U^2 \lambda_L \bar{f}_{V_p}(y_{V_p}, y_{\theta_p}) = \lambda_U^2 \lambda_L \bar{f}_{V_p} \left(\frac{y_{V_m}}{\lambda_L}, y_{\theta_m} \right) \quad (5.18)$$

$$\bar{f}_{\theta_m}(y_{V_m}, y_{\theta_m}) = \lambda_U^2 \lambda_L^2 \bar{f}_{\theta_p}(y_{V_p}, y_{\theta_p}) = \lambda_U^2 \lambda_L^2 \bar{f}_{\theta_p} \left(\frac{y_{V_m}}{\lambda_L}, y_{\theta_m} \right) \quad (5.19)$$

where $\lambda_U = U_m/U_p$ is the velocity scale. By combining eqs. 5.10 and 5.11 with eqs. 5.18 and 5.19, it is possible to obtain the restoring force parameters to be used for the scaled section model:

$$\bar{f}_{V_m}(y_{V_m}, y_{\theta_m}) = \frac{\lambda_U^2 \lambda_L}{\Gamma_V^h} \tilde{f}_{V_p} \left(\frac{\beta_V}{\lambda_L} y_{V_m}, \beta_\theta y_{\theta_m} \right) \quad (5.20)$$

$$\bar{f}_{\theta_m}(y_{V_m}, y_{\theta_m}) = \frac{\lambda_U^2 \lambda_L^2}{\Gamma_\theta^\alpha} \tilde{f}_{\theta_p} \left(\frac{\beta_V}{\lambda_L} y_{V_m}, \beta_\theta y_{\theta_m} \right) \quad (5.21)$$

5.3 Springing System for Nonlinear Section Model Tests

It is now required to conceptualize a mechanical device able to represent the scaled nonlinear structural behavior of eqs. 5.20 and 5.21, which is needed for nonlinear section model tests. Equations 5.20 and 5.21 represent a conservative mechanical system since only the geometric nonlinearities are considered when calculating the nonlinear generalized stiffness parameters. Therefore, the structural system to be represented in the wind tunnel is path independent, depends only on the loads applied on it and does not dissipate energy through hysteresis loops. After trying different solutions, it was found that a mechanical device for nonlinear section model tests can be the system of inclined springs shown in fig. 5.3. In this system, it is considered that the inclined springs have a linear behavior and that their lengths and inclinations can be adjusted.

5.3.1 Target Scaled Properties for Inclined Spring System

Before determining a procedure to determine the stiffnesses as well the lengths and inclinations of the springs, the equations for calculating the mass properties and nonlinear restoring forces for a scaled section model of length L_{mm} are presented. As mentioned in section 5.2.3,

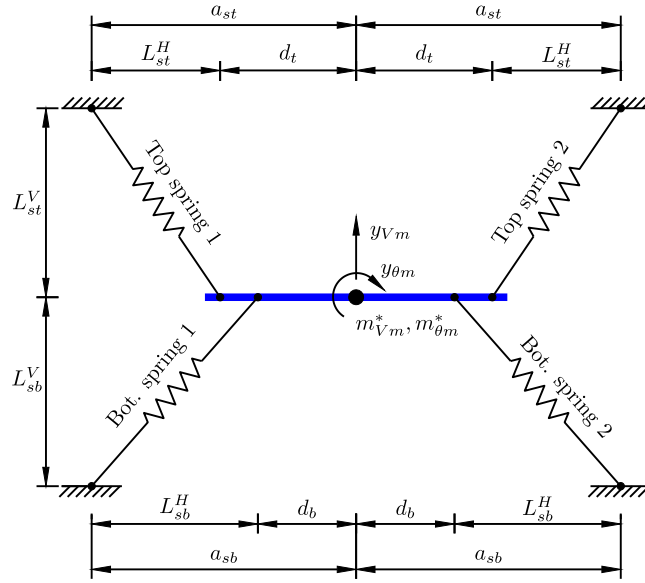


Figure 5.3: Spring configuration for nonlinear section model tests

the mass properties given in eq. 5.14 are utilized in this research, which leads to the following equations for the mass properties of the scaled section model:

$$m_{Vm}^* = \bar{m}_{Vm}^* L_{mm} \quad m_{\theta m}^* = \bar{m}_{\theta m}^* L_{mm} \quad (5.22)$$

where m_{Vm}^* and $m_{\theta m}^*$ are respectively the mass and mass moment of inertia of the scaled section model; \bar{m}_{Vm}^* and $\bar{m}_{\theta m}^*$ are the mass and mass moment of inertia per unit length of the scaled section model. To obtain the restoring forces for a section model having the mass properties shown in eq. 5.22, eqs. 5.20 and 5.21 have to be multiplied by the length of the section model L_{mm} :

$$f_{Vm}^*(y_{Vm}, y_{\theta m}) = L_{mm} \frac{\bar{m}_V^* \lambda_U^2 \lambda_L}{\bar{m}_V \Gamma_V^h} \cdot \tilde{f}_{Vp} \left(\frac{\beta_V}{\lambda_L} y_{Vm}, \beta_\theta y_{\theta m} \right) \quad (5.23)$$

$$f_{\theta m}^*(y_{Vm}, y_{\theta m}) = L_{mm} \frac{\bar{m}_\theta^* \lambda_U^2 \lambda_L^2}{\bar{m}_\theta \Gamma_\theta^\alpha} \cdot \tilde{f}_{\theta p} \left(\frac{\beta_V}{\lambda_L} y_{Vm}, \beta_\theta y_{\theta m} \right) \quad (5.24)$$

where $f_{Vm}^*(y_{Vm}, y_{\theta m})$ and $f_{\theta m}^*(y_{Vm}, y_{\theta m})$ are the scaled mass-corrected restoring vertical force and moment. In eqs. 5.23 and 5.24, the mass-correction factors \bar{m}_V^*/\bar{m}_V and $\bar{m}_\theta^*/\bar{m}_\theta$ need to be used when the full-scale mass properties from eq. 5.14 are utilized. This is to ensure the

correct natural frequencies when \bar{m}_v^* and \bar{m}_θ^* are considered for the mass properties of the section model.

5.3.2 Resultant Forces for Inclined Spring System

To determine a spring configuration able to represent the nonlinear restoring forces of eqs. 5.23 and 5.24, it is first needed to write the nonlinear equations for the resultant forces caused by the springs in fig. 5.3. In fig. 5.3, the lever arms d_t and d_b on the torsion arm of the top springs and bottom springs are solely considered as positive quantities. This also applies to the vertical distances L_{st}^V and L_{sb}^V for the springs. However, the horizontal distances L_{st}^H , L_{sb}^H , a_{st} and a_{sb} can have positive or negative values. For positive values of L_{st}^H and L_{sb}^H , the springs are inclined outwards as illustrated in fig. 5.3, whereas negative values indicate inwardly inclined springs. It is also important to mention that both top springs have the same stiffness, length and inclination; the same applies to the bottom springs. Additionally, the springs in fig. 5.3 account for the stiffness at each end of the section model. This means that half of the calculated spring stiffnesses should be utilized at each end of the model in the wind tunnel. From the geometry in fig. 5.3, the horizontal distances for the springs are:

$$L_{st}^H = a_{st} - d_t \quad (5.25)$$

$$L_{sb}^H = a_{sb} - d_b \quad (5.26)$$

The first step in developing the equations for the spring resultant forces is to derive equations for the spring elongations. The spring elongations ΔL_{st1} and ΔL_{st2} for top spring 1 and top spring 2 are:

$$\Delta L_{st1} = L_{st1} - L_{st} + \Delta L_{st}^p \quad (5.27)$$

$$\Delta L_{st2} = L_{st2} - L_{st} + \Delta L_{st}^p \quad (5.28)$$

where L_{st} is the initial length of the top springs; L_{st1} is the final length of top spring 1; L_{st2} is the final length of top spring 2; ΔL_{st}^p is the displacement prestress of the top springs. It is required to account for the prestress since nonlinear equations for the springs are developed herein. The expressions for L_{st} , L_{st1} and L_{st2} are:

$$L_{st} = \sqrt{(L_{st}^H)^2 + (L_{st}^V)^2} \quad (5.29)$$

$$L_{st1} = \sqrt{(L_{st1}^H)^2 + (L_{st1}^V)^2} \quad \text{with} \quad L_{st1}^H = L_{st}^H + d_t - d_t \cos y_{\theta m} \quad L_{st1}^V = L_{st}^V - y_{Vm} - d_t \sin y_{\theta m} \quad (5.30)$$

$$L_{st2} = \sqrt{(L_{st2}^H)^2 + (L_{st2}^V)^2} \quad \text{with} \quad L_{st2}^H = L_{st}^H + d_t - d_t \cos y_{\theta m} \quad L_{st2}^V = L_{st}^V - y_{Vm} + d_t \sin y_{\theta m} \quad (5.31)$$

Similarly, the spring elongations for the bottom springs ΔL_{sb1} and ΔL_{sb2} are:

$$\Delta L_{sb1} = L_{sb1} - L_{sb} + \Delta L_{sb}^p \quad (5.32)$$

$$\Delta L_{sb2} = L_{sb2} - L_{sb} + \Delta L_{sb}^p \quad (5.33)$$

$$L_{sb} = \sqrt{(L_{sb}^H)^2 + (L_{sb}^V)^2} \quad (5.34)$$

$$L_{sb1} = \sqrt{(L_{sb1}^H)^2 + (L_{sb1}^V)^2} \quad \text{with} \quad L_{sb1}^H = L_{sb}^H + d_b - d_b \cos y_{\theta m} \quad L_{sb1}^V = L_{sb}^V + y_{Vm} + d_b \sin y_{\theta m} \quad (5.35)$$

$$L_{sb2} = \sqrt{(L_{sb2}^H)^2 + (L_{sb2}^V)^2} \quad \text{with} \quad L_{sb2}^H = L_{sb}^H + d_b - d_b \cos y_{\theta m} \quad L_{sb2}^V = L_{sb}^V + y_{Vm} - d_b \sin y_{\theta m} \quad (5.36)$$

where L_{sb} is the initial length of the bottom springs; L_{sb1} and L_{sb2} are the final lengths of bottom spring 1 and bottom spring 2; ΔL_{sb}^p is the displacement prestress of the bottom springs. As mentioned previously, the springs have a linear behavior:

$$F_{st}(\Delta L) = k_{st} \Delta L \quad F_{sb}(\Delta L) = k_{sb} \Delta L \quad (5.37)$$

where $F_{st}(\Delta L)$ and $F_{sb}(\Delta L)$ are the forces in the top springs and bottom springs respectively; k_{st} and k_{sb} are the stiffnesses of the top springs and bottom springs. Using the free-body diagram for the torsion arm shown in fig. 5.4 and from equilibrium, the resultant forces for the nonlinear springing system are:

$$F_H(y_{Vm}, y_{\theta m}) = \frac{L_{st1}^H}{L_{st1}} F_{st}(\Delta L_{st1}) - \frac{L_{st2}^H}{L_{st2}} F_{st}(\Delta L_{st2}) + \frac{L_{sb1}^H}{L_{sb1}} F_{sb}(\Delta L_{sb1}) - \frac{L_{sb2}^H}{L_{sb2}} F_{sb}(\Delta L_{sb2}) \quad (5.38)$$

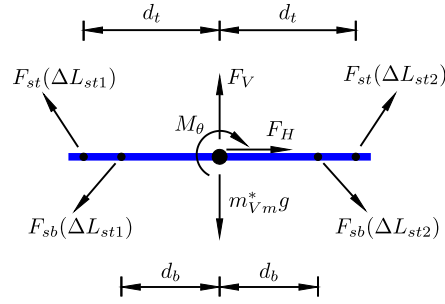


Figure 5.4: Free-body diagram of the nonlinear springing system

$$F_V(y_{Vm}, y_{\theta m}) = -\frac{L_{st1}^V}{L_{st1}} F_{st}(\Delta L_{st1}) - \frac{L_{st2}^V}{L_{st2}} F_{st}(\Delta L_{st2}) + \frac{L_{sb1}^V}{L_{sb1}} F_{sb}(\Delta L_{sb1}) + \frac{L_{sb2}^V}{L_{sb2}} F_{sb}(\Delta L_{sb2}) + m_{Vm}^* g \quad (5.39)$$

$$M_\theta(y_{Vm}, y_{\theta m}) = \frac{L_{st1}^H}{L_{st1}} F_{st}(\Delta L_{st1}) d_t \sin y_{\theta m} - \frac{L_{st1}^V}{L_{st1}} F_{st}(\Delta L_{st1}) d_t \cos y_{\theta m} + \frac{L_{st2}^H}{L_{st2}} F_{st}(\Delta L_{st2}) d_t \sin y_{\theta m} + \frac{L_{st2}^V}{L_{st2}} F_{st}(\Delta L_{st2}) d_t \cos y_{\theta m} + \frac{L_{sb1}^H}{L_{sb1}} F_{sb}(\Delta L_{sb1}) d_b \sin y_{\theta m} + \frac{L_{sb1}^V}{L_{sb1}} F_{sb}(\Delta L_{sb1}) d_b \cos y_{\theta m} + \frac{L_{sb2}^H}{L_{sb2}} F_{sb}(\Delta L_{sb2}) d_b \sin y_{\theta m} - \frac{L_{sb2}^V}{L_{sb2}} F_{sb}(\Delta L_{sb2}) d_b \cos y_{\theta m} \quad (5.40)$$

where $F_H(y_{Vm}, y_{\theta m})$ is the horizontal resultant force of the springing system; $F_V(y_{Vm}, y_{\theta m})$ is the vertical resultant force of the springing system; $M_\theta(y_{Vm}, y_{\theta m})$ is the resultant moment of the springing system; g is the gravitational acceleration. The spring resultant forces in eqs. 5.38–5.40 are geometrically nonlinear because of the nonlinear equations for the spring lengths and elongations (eqs. 5.27–5.36). The equations for the force resultants of the system in fig. 5.3 were validated using large-displacement analysis using the finite element software *SAP2000* [191]. It is also worth noting that, due to the inclined springs, there is a non-zero horizontal resultant force as shown in fig. 5.4 when the rotation y_θ is not zero. This force has to be resisted by the experimental rig used for nonlinear section model tests as discussed in section 5.6.

5.3.3 Prestressing of Inclined Spring System

To determine an equation for the prestress displacements, the equality $F_V(0, 0) = 0$ is used. When $y_{Vm} = 0$ and $y_{\theta m} = 0$, eqs. 5.27 and 5.28 become $\Delta L_{st1} = \Delta L_{st2} = \Delta L_{st}^p$, and eqs. 5.32

and 5.33 are simplified to $\Delta L_{sb1} = \Delta L_{sb2} = \Delta L_{sb}^p$. Therefore, by setting eq. 5.39 to zero and rearranging it, it is found that the prestress displacement for the top springs can be written as follows:

$$\Delta L_{st}^p = \frac{L_{st} L_{sb}^V k_{sb}}{L_{st}^V L_{sb} k_{st}} \Delta L_{sb}^p + \frac{L_{st}}{2L_{st}^V k_{st}} m_V^* g \quad (5.41)$$

As it can be seen in eq. 5.41, the top spring prestress is dependent on the bottom spring prestress and the gravity load. It is therefore concluded that the bottom spring prestress ΔL_{sb}^p is a parameter to be decided depending on how large the displacements are expected to be such that the bottom springs are under tension at all times.

5.3.4 Fitting Procedure for Nonlinear Spring Configuration

In order to determine the parameters of the spring configuration shown in fig. 5.3, a nonlinear least-squares procedure is utilized. The target values are the scaled nonlinear generalized restoring forces of eqs. 5.23 and 5.24. Consequently, the following error function needs to be minimized:

$$J_{V\theta} = \sum_{i=1}^N \left\{ [f_{Vm}^*(y_{Vmi}, y_{\theta mi}) - F_V(y_{Vmi}, y_{\theta mi})]^2 + \left[\frac{f_{\theta m}^*(y_{Vmi}, y_{\theta mi})}{b_{clm}} - \frac{M_{\theta}(y_{Vmi}, y_{\theta mi})}{b_{clm}} \right]^2 \right\} \quad (5.42)$$

where b_{clm} is half of the cable spacing at model scale; N is the number of samples of the nonlinear generalized restoring forces used in the calculation of $J_{V\theta}$. In eq. 5.42, the moment contribution is divided by b_{clm} such that the error $J_{V\theta}$ has consistent units, i.e., force units. By using half of the cable spacing, this means that the sum of both forces of an equivalent couple representing the moment is taken into account for the moment contribution to $J_{V\theta}$. Additionally, half of the cable spacing was preferred to half of the bridge deck width since the cables provide a large proportion of the torsional stiffness of a cable-supported bridge.

Equation 5.42 is optimized by varying the parameters a_{st} , L_{st}^V , d_t , k_{st} , a_{sb} , L_{sb}^V , d_b and k_{sb} . The constant parameters to be provided as inputs are ΔL_{sb}^p , m_{Vm}^* and b_{clm} . This nonlinear least-squares problem is a constrained-optimization problem because of the physical limitations of the section model experimental rig. Except a_{st} , k_{st} , a_{sb} and k_{sb} , all the varying parameters are bounded from zero to the maximum positive values that the experimental rig can accommodate. The parameters a_{st} and a_{sb} are bounded by the maximum positive and

negative values possible for the section model test rig. The spring stiffnesses k_{st} and k_{sb} are bounded by a minimum positive value and maximum positive value chosen from experience of solving this nonlinear least-squares problem.

It was found that annealing optimization and differential evolution optimization are effective at finding an optimized solution to eq. 5.42, but the differential evolution method was mostly utilized for this study. Since the problem in eq. 5.42 is a nonlinear least-squares problem, there are many local minimums. Therefore, due to the stochastic nature of these optimization methods, the optimization process is run many times in order to find the global minimum for the constrained minimization problem of eq. 5.42.

In order to evaluate the goodness of the fit and because the coefficient of determination is not valid for nonlinear least-squares problems, the standard error of the regression $\sigma_{V\theta}$ is utilized, which is defined as:

$$\sigma_{V\theta} = \sqrt{\frac{J_{V\theta}}{2N}} \quad (5.43)$$

The lower the standard error of the regression is, the better is the fit. To the denominator of eq. 5.43, $2N$ is used because of the contributions from the vertical force and moment to the error function $J_{V\theta}$. The standard error of the regression indicates how wrong the spring model is on average in terms of the response units, i.e., force units. A lower value for $\sigma_{V\theta}$ is better.

5.4 Steps for Determining Test Parameters for Nonlinear Section Model Tests





It seems appropriate to summarize the steps to calculate the parameters of the nonlinear springing system that will allow conducting nonlinear section model tests for a specific bridge. This nine-step procedure is described below.

1. It is first required to develop a fishbone finite element model of the cable-supported bridge under consideration. After calculating the static equilibrium for the cable preloads and dead loads using large displacement analysis, the natural frequencies and modes of vibration for the dead-load configuration can be calculated.
2. Following the procedure for nonlinear generalized stiffness analysis described in section 5.2.1, the nonlinear evolution of the nonlinear generalized restoring forces

$\tilde{f}_V(z_V, z_\theta)$ for the first symmetric vertical mode and $\tilde{f}_\theta(z_V, z_\theta)$ for the first symmetric torsional mode is obtained.

3. The mode correction factors Γ_V^h and Γ_θ^α for the first vertical-torsional modal pair can be calculated using eq. 5.5. Similarly, eqs. 5.7 and 5.8 are utilized to calculate the mode correction factors β_V and β_θ for the first symmetric modes.
4. After calculating the factors Γ_{V2}^h and $\Gamma_{\theta2}^\alpha$ given in eq. 5.6, the effective mass properties per unit length can be calculated using eqs. 5.12 and 5.13 for \bar{m}_V and \bar{m}_θ . If the modified effective distributed mass properties \bar{m}_V^* and \bar{m}_θ^* are considered as it is the case in this research, they can be obtained from eq. 5.14. In this case, it is also needed to evaluate the mass ratios \bar{m}_V^*/\bar{m}_V and $\bar{m}_\theta^*/\bar{m}_\theta$.
5. Then, the geometric scale factor λ_L and velocity scale factor λ_U have to be chosen based on the capabilities of the wind tunnel that is utilized.
6. After choosing the scale factors, the scaled mass properties per unit length are obtained from eq. 5.15, which are used to obtain the mass and mass moment of inertia of a model-scale section model of length L_{mm} using eq. 5.22.
7. Using eqs. 5.23 and 5.24, it is now possible to scale the nonlinear evolution of the nonlinear generalized restoring forces calculated from nonlinear generalized stiffness analysis in order to obtain the nonlinear force-displacement relationships $f_{V_m}^*(y_{V_m}, y_{\theta_m})$ and $f_{\theta_m}^*(y_{V_m}, y_{\theta_m})$. These are for a scaled model of length L_{mm} . This is achieved by applying the mode correction factors Γ_V^h , Γ_θ^α , β_V and β_θ as well as the mass correction ratios \bar{m}_V^*/\bar{m}_V and $\bar{m}_\theta^*/\bar{m}_\theta$ if applicable.
8. Once $f_{V_m}^*(y_{V_m}, y_{\theta_m})$ and $f_{\theta_m}^*(y_{V_m}, y_{\theta_m})$ are determined, it is needed to choose the displacement prestress ΔL_{sb}^p to be utilized for the bottom springs of the springing system shown in fig. 5.3. The prestress value is selected based on what is achievable for the section model test rig as well as based on the maximum expected displacements for the section model so that the bottom springs stay under tension.
9. Through nonlinear least-squares analysis, the parameters a_{st} , L_{st}^V , d_t , k_{st} , a_{sb} , L_{sb}^V , d_b and k_{sb} of the nonlinear springing system are determined. This is done by minimizing eq. 5.42 using the differential evolution optimization method. The goodness of the fit between the nonlinear spring configuration and $f_{V_m}^*(y_{V_m}, y_{\theta_m})$ and $f_{\theta_m}^*(y_{V_m}, y_{\theta_m})$ can be assessed using eq. 5.43.

Table 5.1: Description of cable-supported bridges

Bridge	Type	Main span (m)	Buffers?	Elevation view
SU4a	Single-span suspension Girder restrained at towers	1200	Yes	
SU4b	Single-span suspension Girder restrained at towers	1800	Yes	
SU4c	Single-span suspension Girder restrained at towers	2400	Yes	
SU4d	Single-span suspension Girder restrained at towers	3000	Yes	

5.5 Nonlinear Spring Configurations for Single-Span Suspension Bridges

Based on the observations made in chapter 3, it was decided to focus on single-span suspension bridges in this study since this structural system has a stronger nonlinear behavior. Therefore, the step-by-step procedure of section 5.4 was utilized to determine the nonlinear spring configurations for the four single-span suspension bridges described in table 5.1. These bridges are preliminary designs of suspension bridges with main spans ranging from 1.2 km to 3.0 km. They were inspired by existing bridge designs, and detailed information about them can be found in chapter 4. The procedure of section 5.4 was utilized for the bridges of table 5.1 for the first vertical-torsional modal pair.

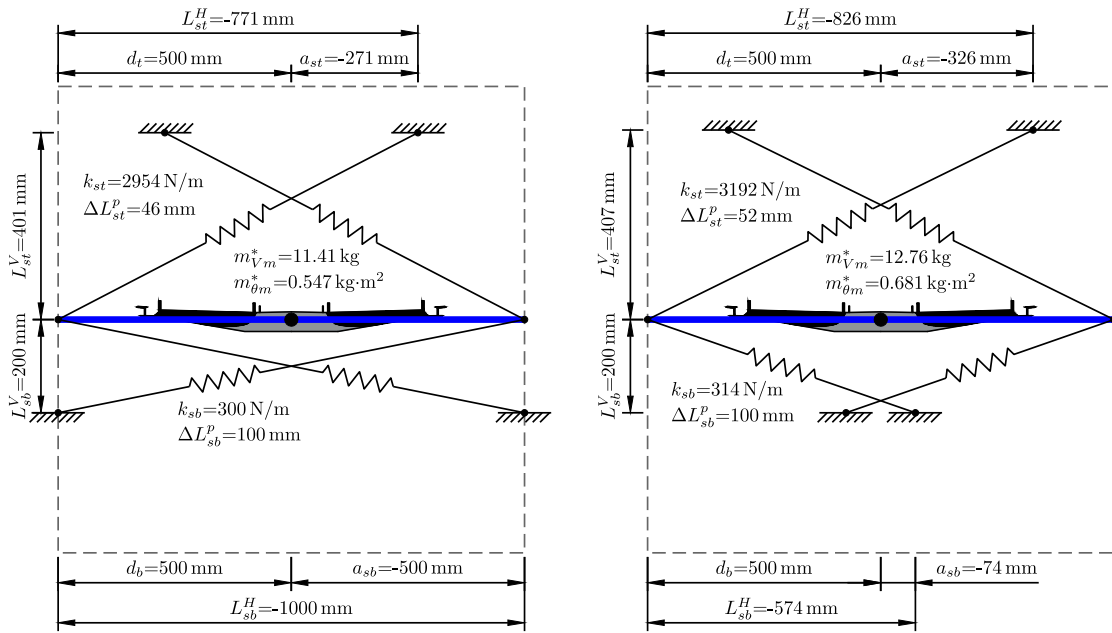
The main purpose of obtaining these nonlinear spring configurations is to assess the feasibility of using such spring configurations at the Boundary Layer Wind Tunnel Laboratory (BLWTL) of the University of Western Ontario. Therefore, in determining these initial spring arrangements, it is considered that the spring attachment points and torsion arm must be located within a square of 1000 mm, which corresponds to the size of the openings in the streamlined walls in which the springing system is mounted at the BLWTL. Therefore, when solving the nonlinear least-squares problem described in eq. 5.42, the dimensions a_{st} and a_{sb} were constrained between -500 mm and 500 mm. Values for d_t and d_b ranges from 0 mm to 500 mm. In order to have sufficient clearance for the vertical motion of the bridge model, L_{st}^V and L_{sb}^V were constrained between 200 mm and 500 mm. For these bridges, it was found that good results were obtained when constraining the spring stiffness k_{st} between 500 N/m and 5000 N/m as well as constraining the spring stiffness k_{sb} between 300 N/m and 2000 N/m. For the bottom spring prestress, it was assumed that $\Delta L_{sb}^P = 100$ mm.

Following this procedure for bridges SU4a, SU4b, SU4c and SU4d, the spring configurations presented in fig. 5.5 were obtained. In the fitting process for each bridge, 6561 points were

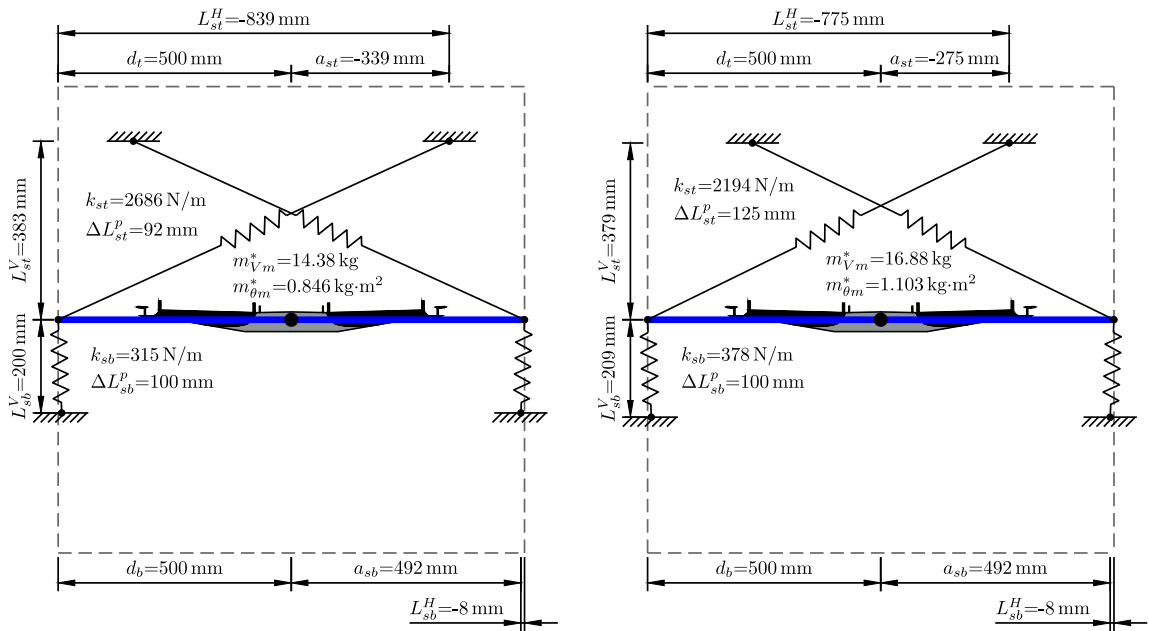
considered, i.e., $N = 6561$. The differential evolution optimization method was run 10 times to find the spring configurations giving the lowest standard error of the regression. A model length L_{mm} of 2.134 m was considered as it corresponds to the typical model length used at the BLWTL. Also, the velocity scales were chosen such that an instability can be observed in the wind tunnel. The spring stiffnesses shown in fig. 5.5 represent the total stiffness provided to the section model. Consequently, the stiffnesses to be used in the wind tunnel should be half of those in fig. 5.5 due to the two springing systems used at the ends of the section model. Also, it should be noted that the dashed grey lines in fig. 5.5 represent the usable space for the springs in the case of the BLWTL section model setup (1000 mm by 1000 mm).

In figs. 5.6 and 5.7, bridges SU4c and SU4d are taken as examples for the comparison between the target scaled nonlinear behavior and the one modeled using a springing system with inclined springs. In order to facilitate the interpretation of these figures, only every three points of the target nonlinear generalized results are presented. Figures 5.6a and 5.7a present the scaled nonlinear generalized restoring forces, whereas figs. 5.6b and 5.7b show the scaled nonlinear generalized stiffnesses k_{jkm}^{t*} . For obtaining the scaled nonlinear generalized stiffnesses in these figures, the scaled results for the nonlinear generalized restoring forces were differentiated as per eq. 5.4. In figs. 5.6 and 5.7, the results are limited within displacement bounds of ± 0.06 m for y_{vm} and ± 0.06 rad for $y_{\theta m}$, which corresponds to $\pm 3.44^\circ$. These limits are seen as reasonable maximum displacements to be encountered during section model tests. For these displacement values, the inclined springs are always under tension. These displacement limits were only used for visualization purposes since the fitting procedure was run using results for displacements three times larger than these limits.

As it can be seen in figs. 5.6 and 5.7, there is a good agreement between the target nonlinear behavior and the behavior modeled using inclined springs. There are reasonable discrepancies in figs. 5.6b and 5.7b for the off-diagonal terms. Similar observations were made for bridges SU4a and SU4b. The good fit of the inclined spring setup with the target nonlinear behavior is confirmed by the small values of the standard error of the regression shown in fig. 5.5 in comparison to the magnitude of the forces in figs. 5.6a and 5.7a. Therefore, based on the visual inspection of figs. 5.6 and 5.7 and the small values for the standard error of the regression, it is concluded that a springing system with inclined springs is suitable for nonlinear section model tests. This is also confirmed by the fact that the spring configurations are physically realistic because they fit within a square of 1000 mm as shown in fig. 5.5.



(a) Bridge SU4a ($\lambda_L = 1/75$, $\lambda_U = 1/5.5$ and $\sigma_{V\theta} = 1.54$ N) (b) Bridge SU4b ($\lambda_L = 1/75$, $\lambda_U = 1/4.5$ and $\sigma_{V\theta} = 0.85$ N)



(c) Bridge SU4c ($\lambda_L = 1/75$, $\lambda_U = 1/3.75$ and $\sigma_{V\theta} = 1.06$ N) (d) Bridge SU4d ($\lambda_L = 1/75$, $\lambda_U = 1/3.5$ and $\sigma_{V\theta} = 1.36$ N)

Figure 5.5: Nonlinear spring configurations for the single-span suspension bridges

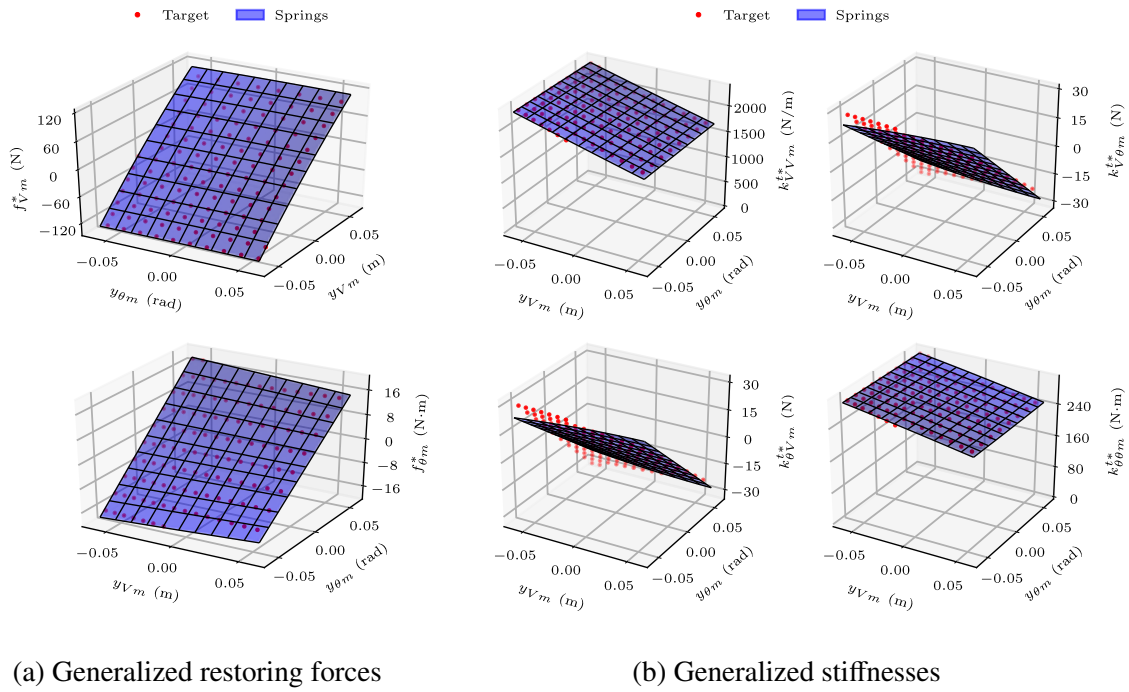


Figure 5.6: Comparison between target and spring-modeled scaled nonlinear generalized behavior for bridge SU4c

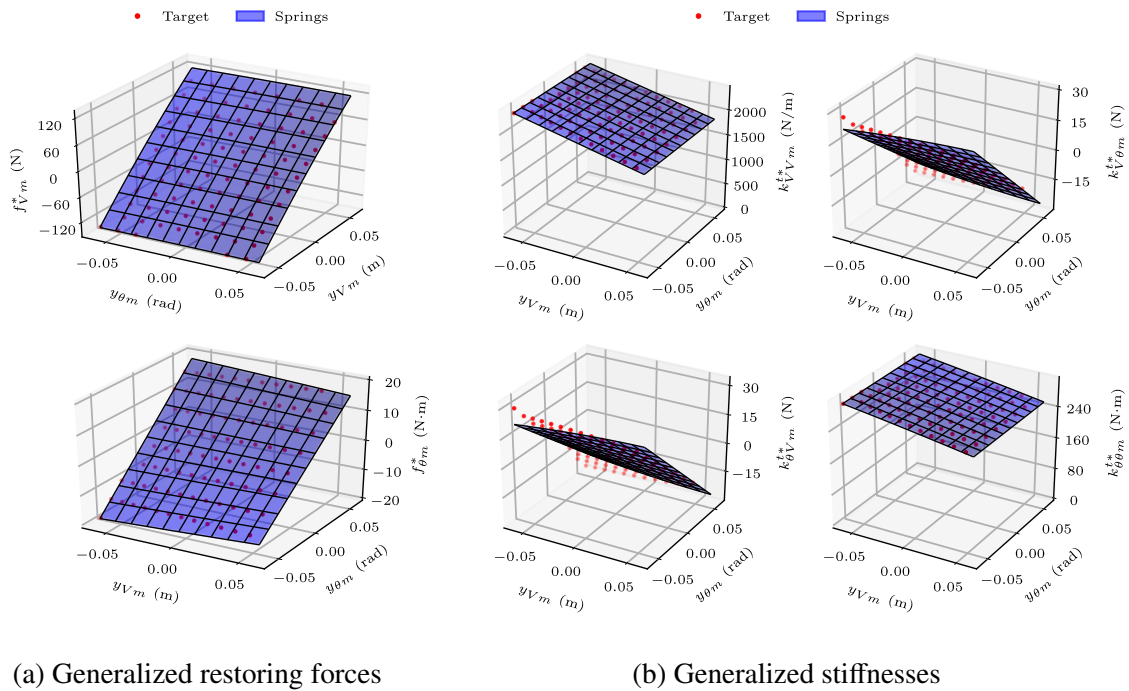


Figure 5.7: Comparison between target and spring-modeled scaled nonlinear generalized behavior for bridge SU4d

5.6 Discussion on Requirements Needed for a Nonlinear Section Model Test Rig

In order to achieve nonlinear spring configurations like those of section 5.5, a new dynamic test rig for section model tests is required. Consequently, the next step in this research was to design an experimental apparatus able to be utilized for nonlinear section model tests. It is therefore relevant to discuss briefly the desirable characteristics for such a test rig.

A bridge rig for nonlinear tests is required to be easy to adjust. Indeed, it needs to have an efficient and fast way to change the vertical and horizontal positions of the attachment points for the inclined springs. This will facilitate the adjustments of the inclinations of the springs. Furthermore, the nonlinear rig must have the capability to have intersecting springs as shown in fig. 5.5. This can be achieved by having the possibility to arrange the springs on two different vertical planes. Additionally, the adjustment of the springs includes their pretensioning. Therefore, it would be practical for the rig to be equipped with load cells in order to measure the spring pretension forces.

Such a rig needs to be able to represent the structural coupling between the vertical and torsional behaviors as expressed in eqs. 5.23 and 5.24 as well as exemplified in figs. 5.6 and 5.7. This is achieved by utilizing the same springs to provide the vertical stiffness and torsional stiffness as it is the case for the inclined spring configuration in fig. 5.3. Due to the inclination of the springs, there is a non-zero horizontal resultant force given by eq. 5.38 and shown in fig. 5.4. Consequently, a rig for nonlinear tests must be able to resist this force while allowing the bridge model to move vertically and in rotation. As for typical section model tests, the drag force on the section model must also be withstood by the bridge rig.

The nonlinear rig must be designed in a way that facilitates the adjustment of mass and damping properties. Damping should also be as linear as possible, i.e., it should be as close as realistically achievable to viscous damping. This is to ensure that only the effect of structural nonlinearities will be assessed when comparing linear section model tests to nonlinear tests. It is also worth noting that a nonlinear section model test rig should be easily utilized for conducting linear section model tests. This is because nonlinear tests are of interest in the study of the dynamic response and stability, but linear tests are also relevant for the extraction of flutter derivatives or for bridges that behave linearly.

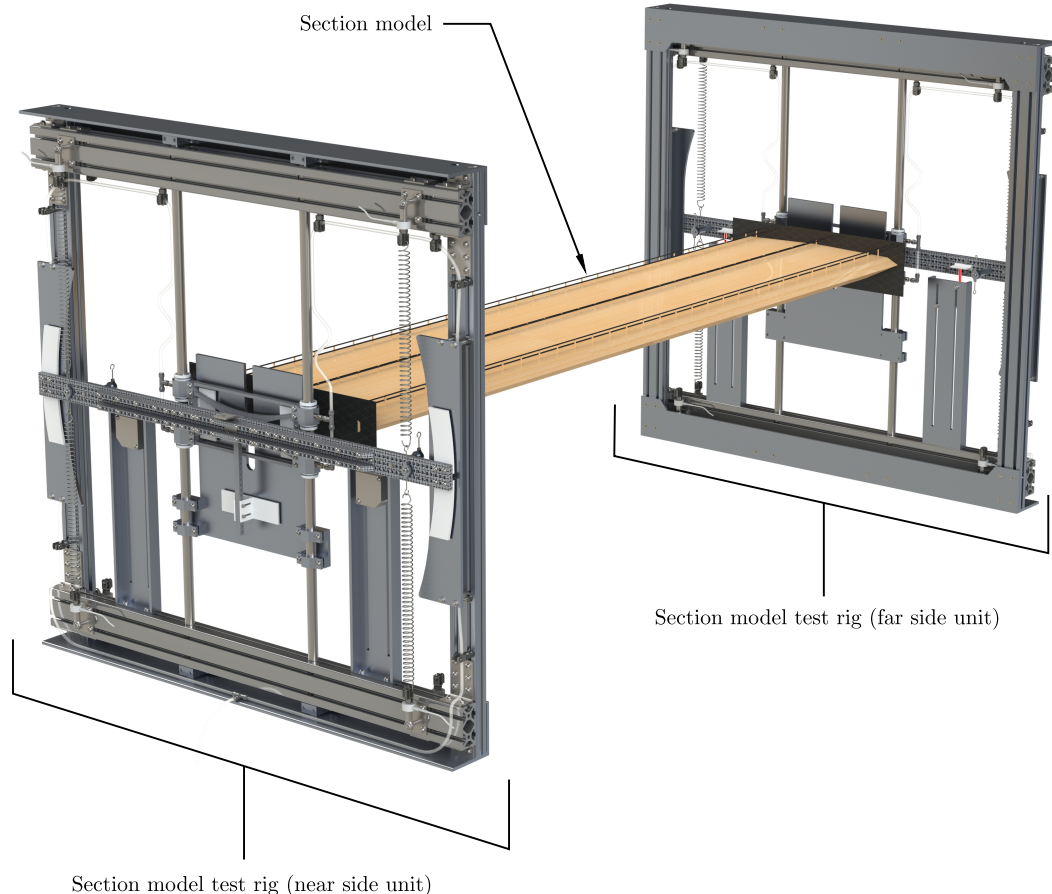


Figure 5.8: Three-dimensional model of new section model test rig

5.7 Design of New Section Model Test Rig

Based on the requirements discussed in the previous section for a nonlinear section model test rig, a design for a new section model test apparatus was developed. The design was elaborated considering that future nonlinear section model tests will be conducted at the BLWTL of the University of Western Ontario. The three-dimensional model of the new bridge rig is shown in fig. 5.8. Since the existing streamlined walls used at the BLWTL for section model tests can also be utilized in combination with the new bridge rig, fig. 5.8 only shows the two units of the bridge rig to which the section model is attached. Each unit of the rig has to be inserted into the openings of the streamlined walls. It should also be noted that, for the sake of clarity, the figures in this section show the new section model test rig in a linear test configuration, i.e., with vertical springs.

As shown in fig. 5.8, the bridge rig consists of two identical units located at both ends of the section model. A detailed description of a typical unit is presented in fig. 5.9. Both units of the nonlinear section model test rig are 1065 mm wide and 1065 mm high. Each unit consists of an external aluminum frame made of two horizontal angles and two vertical T-slot extrusions. Two additional horizontal T-slot aluminum extrusions are fastened to the vertical extrusions of the external aluminum frame, one near the top of the frame and the other near the bottom. The springs, which support a moving cart, are attached to these horizontal extrusions. In order to have more flexibility, it is possible to attach springs on both side of the horizontal extrusions, i.e., it is possible to have springs on two different vertical planes. This will allow intersecting springs in the case of nonlinear tests as discussed in section 5.6. For this purpose, the front spring attachment pivots and back spring attachment pivots need to be utilized. Each unit also includes a magnetic damping system. Additionally, laser displacement sensors will be utilized for measuring the motion of the section model, and each spring connects to a load cell in order to measure the spring forces.

As illustrated in fig. 5.10, the vertical positions of the horizontal T-slot aluminum extrusions can be adjusted, which is done by untightening T-slot bolts. Similarly, the spring mounts on the front and rear faces of the horizontal extrusions can be moved horizontally along the extrusions. This ability to move the spring attachment points is essential in order to be able to obtain the appropriate spring lengths and inclinations in the case of nonlinear tests. Due to the inclination of the springs in nonlinear tests, the spring mounts on the horizontal extrusions and torsion arm are free to rotate from the usage of bearings. This is why they are referred as the spring attachment pivots. Their free rotation is essential because, with inclined springs, a vertical displacement of the bridge model leads to a change in the spring inclinations, which requires a free rotation of the ends of the springs. In fig. 5.10, it is also worth noting that the laser displacement sensors can be moved horizontally and vertically. This is useful as the ballast masses added to the torsion arm could interfere with the laser sensors in specific cases and having the possibility to move them would resolve such interference. Figure 5.10 also illustrates how the displacements are measured using laser displacements sensors and laser targets.

As shown in fig. 5.11, the moving parts of the bridge rig allowing the bridge model to move vertically and torsionally consist of a torsion arm (fig. 5.12) and a moving cart (fig. 5.13). These components of the rig are mainly made out of carbon fiber composite in order to be light and stiff. By using a ball bearing located at the center of the moving cart, the torsion arm can rotate about the aluminum shaft located at the middle of the arm. A self-aligning ball bearing is considered to avoid the transfer of a bending moment to the vertically moving

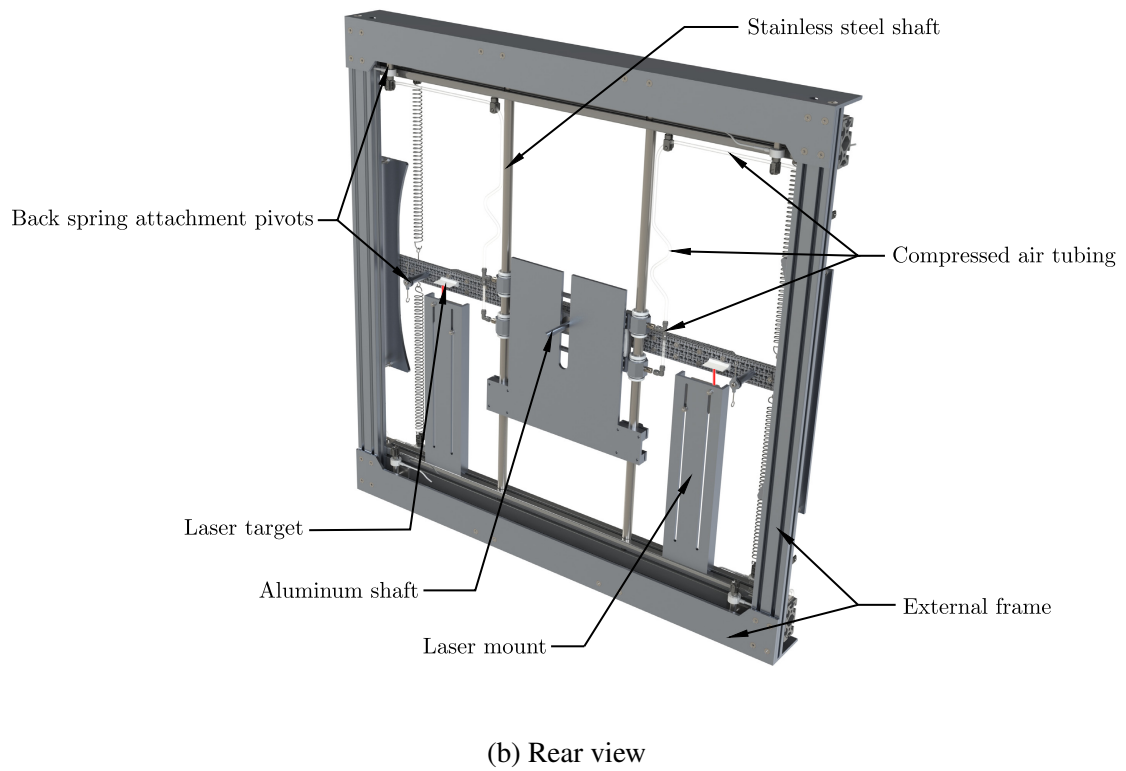
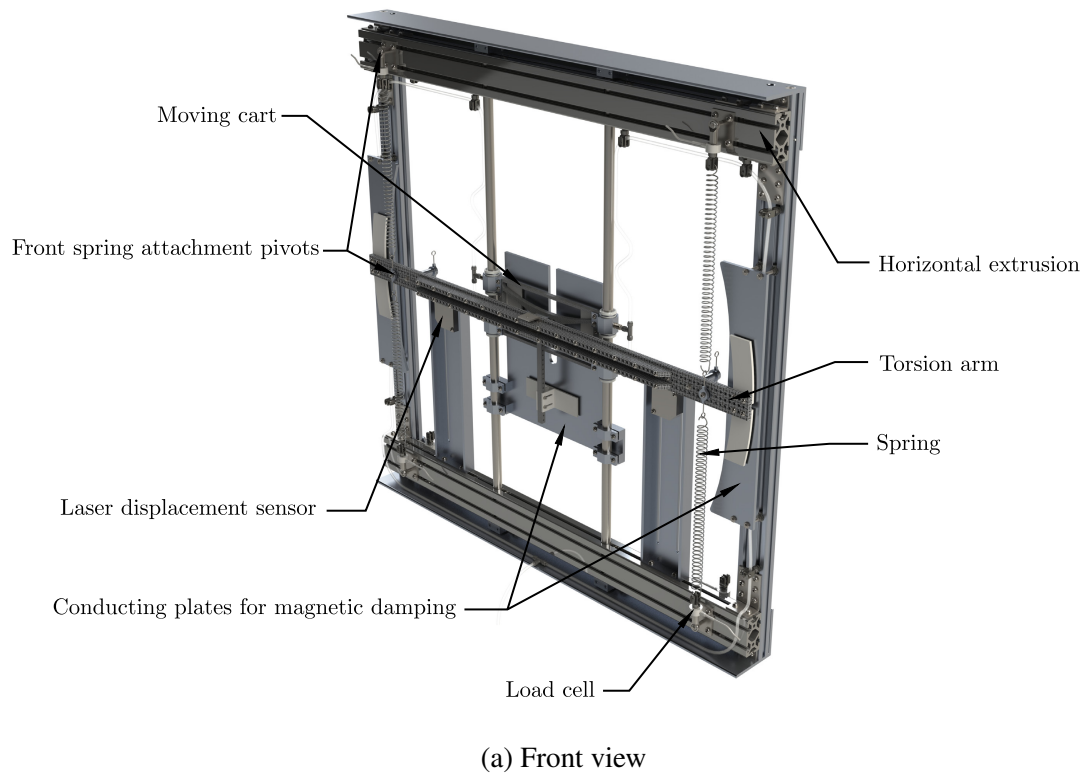


Figure 5.9: Description of new section model test rig

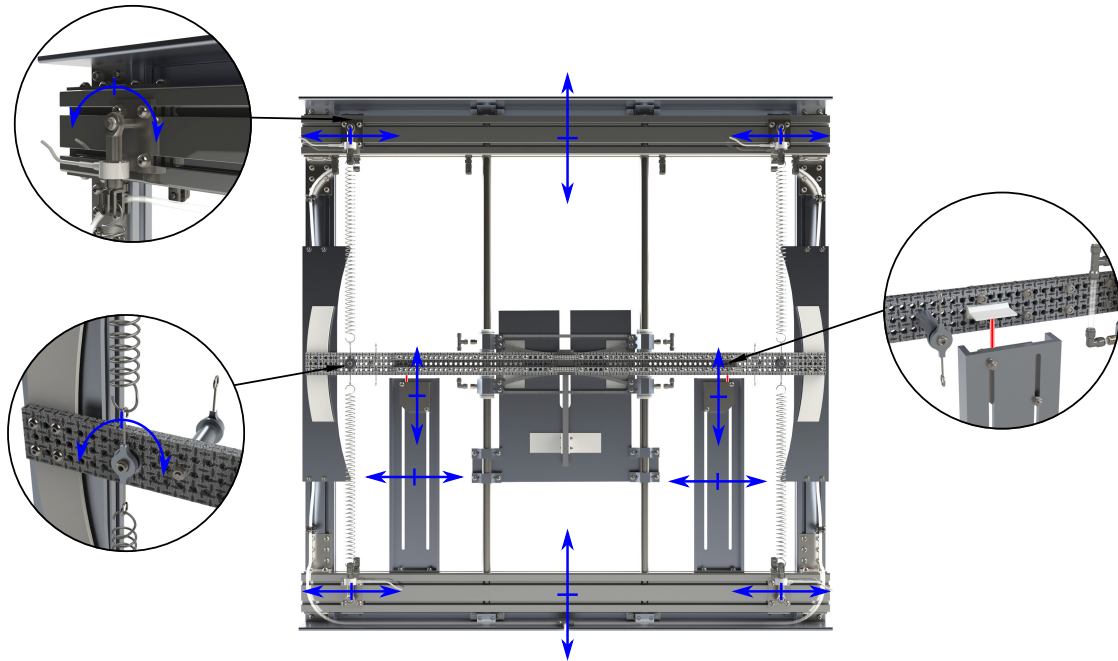


Figure 5.10: Possible adjustments for the new section model test rig

cart. This is important to avoid exceeding the capacity of the air bushings shown in fig. 5.13 that are used for the vertical motion of the cart. This is also at the end of this aluminum shaft that the section model is mounted.

As illustrated in fig. 5.11, the air bushing cart slides along stainless steel shafts. To provide dry compressed air to the air bushings, the tubing system identified in fig. 5.9 is required. An air bushing system was considered because the horizontal resultant force caused by the inclined springs has to be resisted while allowing the section model to move vertically. The bushings also have to resist the drag force coming from the section model. The size of the air bushings considered was chosen such that the specified maximum radial load can withstand the horizontal resultant force from the inclined springs and the drag force.

For the new bridge rig, a magnetic damping system is utilized. The two main components of this system are magnets and conducting plates. When a magnet that is close to a conducting plate moves in a plane parallel to the plate, electromagnetic forces are exerted on the magnet due to eddy currents occurring in the plate. These forces can be used to dampen a bridge model as they occur to be theoretically proportional to the velocity, i.e., they behave like viscous damping forces. To have a system that is light, it was decided to consider permanent rare-earth magnets made of neodymium due to their strongness and lightness. As shown in figs. 5.12 and 5.13, the prismatic neodymium magnets are placed in 3D-printed magnet trays.

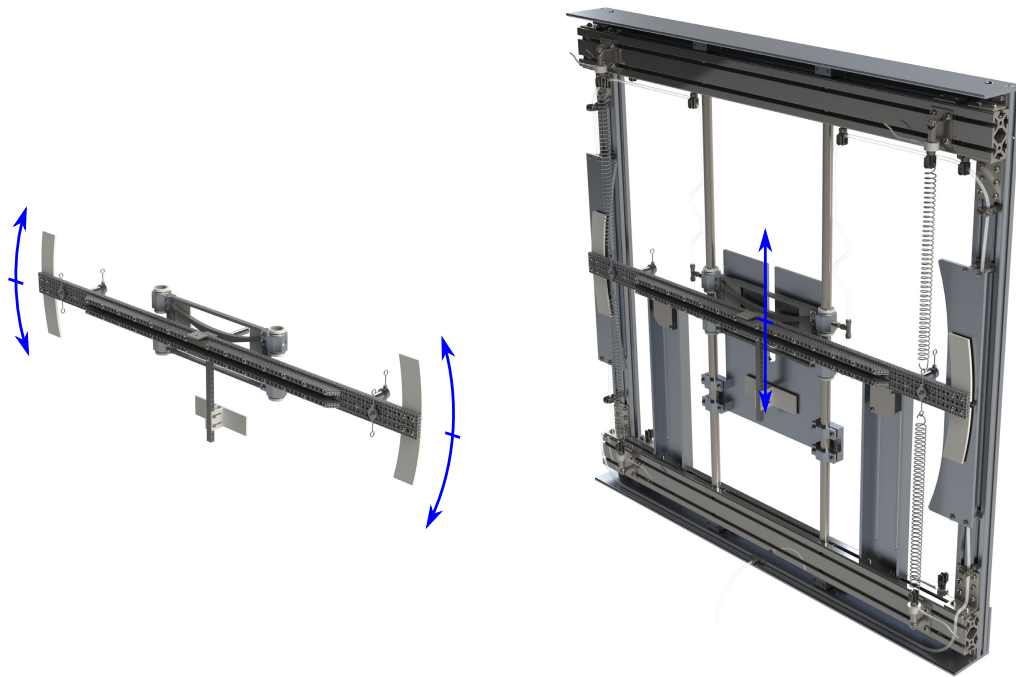


Figure 5.11: Mechanism of new section model test rig

The number of magnets utilized can be easily adjusted by adding or removing magnets. For the conducting plates, aluminum is considered due to its good electrical conductivity. The damping subsystem located at the ends of the torsion bar mainly provides damping for the torsional mode, but also contributes to the vertical damping in a limited manner. The vertical damping can then be adjusted using the magnet trays of the air bushing cart (fig. 5.13) and the conducting plate located between the stainless steel shafts. If needed, it will be possible to add more magnets using the damping tray attached to the small arm that is perpendicular to the torsion arm.

The next step in this research is to fabricate this new section model test rig that can be used for nonlinear tests as well as linear tests. By comparing the linear test results to the nonlinear ones, it will be possible to know whether geometric nonlinearities can have an adverse effect on the stability and dynamic performance of long-span bridges.

5.8 Conclusions

For very long cable-supported bridges, especially suspension bridges, it appears that a better understanding of the interaction between structural nonlinearities and aerodynamic effects

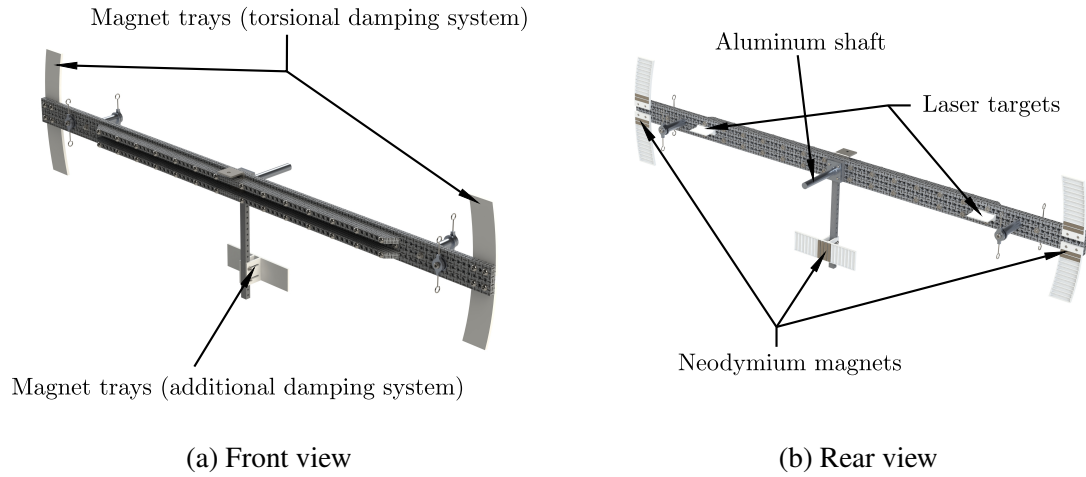


Figure 5.12: Torsion arm of new section model test rig

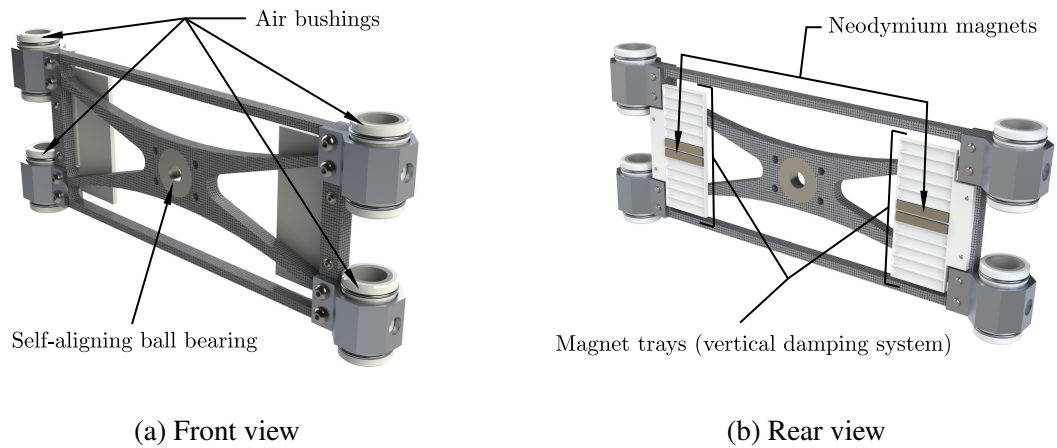


Figure 5.13: Air bushing cart of new section model test rig

is needed. In this chapter, an experimental technique relying on section model tests was proposed to study such interaction. This approach will make possible the inclusion of geometric nonlinearities when conducting section model tests for bridges.

Starting from the scaled nonlinear generalized structural behavior of a cable-supported bridge, it was found that a springing system consisting of inclined springs can represent this nonlinear behavior. It was demonstrated that the inclined spring configuration can be obtained by solving a nonlinear least-squares problem for which the target values correspond to the scaled nonlinear generalized structural behavior. To determine the spring parameters, stochastic optimization methods are used in the fitting procedure. The annealing optimization method and differential evolution optimization method were shown to be effective at determining the optimal inclined spring configuration. In order to validate the practicality of using inclined springs for section model tests, the procedure was tested for four single-span suspension bridges having main spans of 1.2 km, 1.8 km, 2.4 km and 3.0 km. Good agreement was observed between the structural behavior modeled using inclined springs and the target results. It was also demonstrated that the inclined spring configurations for these bridges are physically realistic for the wind tunnel at the University of Western Ontario.

A design was developed for a new bridge rig suitable for nonlinear section model tests. For the proposed bridge rig, it would be easy to make adjustments to the inclined spring configuration. This new bridge rig relies on air bushings and magnetic damping. This bridge rig for nonlinear section model tests is currently being fabricated, and nonlinear section model tests are planned for the near future. The findings and results of a comparison between linear and nonlinear section model tests will be reported in future publications. It is expected that this research will lead to a better understanding of the interaction between structural nonlinearities and aeroelastic effects for very long cable-supported bridges.

Chapter 6

Nonlinear Section Model Tests

6.1 Introduction

Considering the computational resources available today and the advancement made in the field of computational fluid dynamics (CFD), virtual wind tunnel tests (e.g. [64]) have been more common in the field of bridge engineering. This is because CFD can easily provide initial information about the aerodynamic behavior of a bridge. This is especially interesting in the early stages of a bridge design project. Nevertheless, wind tunnel tests are still the preferred method when it comes to assessing the behavior and safety of cable-supported bridges subjected to wind. The two most common wind tunnel testing techniques utilized in the industry are full-aeroelastic model tests and section model tests.

Full-aeroelastic model tests [29] are useful in the determination of the full-bridge response under wind loads since a scale replica of a bridge that include all important structural elements is utilized. However, they are complicated and expensive due to the size and the level of detail required for full-aeroelastic models. In comparison, a rigid segment of a bridge deck is suspended by a springing system in the case of section model tests [30]. This makes section model tests more affordable and less complicated. Even though a lateral mode has sometimes been considered (e.g. [32]), section model tests typically account for one vertical mode and one torsional mode. The practicality of section model tests has been extended by some interesting developments in terms of experimental apparatuses. Examples of such developments include a dynamometric section model for the Messina Strait Bridge [36]. Also, the development of an innovative section model test rig that can be utilized for free- and forced-vibration tests is discussed in [37]. In [40], another test rig for forced-vibration tests is mentioned, but this one can also be used for arbitrary motion.

With the objective of including more modes of vibration in section model tests without having the added complexity of full-aeroelastic model tests, taut-strip model tests were elaborated [59]. Considering that the model stiffness is provided through taut wires or tubes, this testing procedure is well adapted to bridges exhibiting sinusoidal modes of vibration. More recently, a multi-supported aeroelastic model was developed for the assessment of vortex-induced vibrations in bridges [60]. This modeling technique is limited to the study of the dynamic vertical response as only vertical modes can be properly represented. Even

frameworks for real-time hybrid tests are discussed in [61, 62]. Similar to the procedure utilized in structural engineering, the aeroelastic system of a cable-supported bridge would be partially modeled in the lab and partially represented in a numerical model.

Although there are many options when it comes to wind tunnel testing of bridges, section model tests have become the standard approach in the field of bridge engineering. This is mainly explained by their versatility as they can be utilized to measure aerodynamic coefficients, measure aerodynamic pressures as well as determine bridge-deck dynamic responses. Another advantage of section model tests is their simplicity; but from it arises some limitations and assumptions regarding the aerodynamic and structural behaviors. One of them is that the aerodynamic contribution of the cable system is typically neglected. For the structural behavior, the modes of vibration are assumed as uniform, and only one mode in each direction can be accounted for. It is also worth mentioning that section model tests assume a linear structural behavior of the bridge since the modes represented in such tests and their corresponding modal properties originate from linear structural dynamics theory.

However, cable-supported bridges can exhibit structural nonlinearities from different origins. This includes geometric nonlinearities [149, 150], material nonlinearities [147, 151] and localized nonlinearities like those caused by hydraulic buffers [12, 17, 151]. For suspension bridges, mathematicians and engineers [168–170] have also demonstrated that dynamic vertical forcing can lead to large torsional oscillations as a result of structural nonlinearities, i.e., there is nonlinear vertical-torsional coupling due to the geometric nonlinearities. The phenomenon at cause would be internal parametric resonance, a structural dynamic instability [170]. Compared to flutter which is caused by the coupling between the air-flow and the structure, this instability arises from a nonlinear structural coupling between modes of vibration. A practical approach to assess nonlinear vertical-torsional coupling in cable-supported bridges was proposed in chapter 3. It relies on applying modal loads to geometrically nonlinear bridge structures. Using this approach, it was demonstrated that single-span suspension bridges have a stronger nonlinear coupling when compared to three-span suspension bridges and cable-stayed bridges. Since the cable system contributes more to the bridge structural behavior for longer spans, it was found that the bridges with greater spans are more nonlinear.

To the author's knowledge, the structural instability described in the previous paragraph has never been witnessed on an actual bridge. Nevertheless, a transition from an antisymmetric instability mode to a symmetric instability mode was experienced on a full-aeroelastic model of a double-main-span suspension bridge [172, 173]. It appears that it would not be caused by a flutter mode transition as observed in [174], which occurs between flutter instability

modes having the same critical wind speed. Instead, internal resonance associated with the nonlinearities of the aeroelastic system would be responsible. This has led to many recent experimental studies on nonlinear flutter and aerodynamic nonlinearities for bridge decks [90, 96, 100, 101, 120]. However, in these studies on bridges, the effect of structural nonlinearities was not assessed experimentally. In these experimental investigations, structural nonlinearities have only been discussed with regard to the intrinsic nonlinear behavior in stiffness and damping of the experimental apparatus used for section model tests [90, 102, 104]. This was done to ensure that these effects are small compared to aerodynamic nonlinearities, which is the subject of interest of these studies.

Nevertheless, the section model test rig used to test bridges in [45] shows a slight nonlinear structural behavior in torsion for large rotations greater than 15° due to the kinematics of the rig mechanism. Considering that the research in [45] aims at assessing aerodynamic nonlinearities at large amplitudes of vibration, it is unlikely that this nonlinear torsional behavior is representative of the nonlinear structural behavior of a cable-supported bridge. The experimental apparatus utilized in [47] is also capable of large displacements as it is used to study aerodynamic nonlinearities, but its structural behavior is linear. In the case of section model tests for airfoils, different experimental studies have been conducted considering a nonlinear structural behavior in stiffness such as freeplay, bilinear, parabolic and cubic nonlinearities [50, 52, 54, 57]. It is worth noting that the flutter wind speed of an airfoil with a slight bilinear behavior was shown to be less than the linear flutter wind speed [54]. Therefore, it seems that supplemental investigations are required in order to understand the influence of structural nonlinearities on the aeroelastic stability of cable-supported bridges. This appears of practical engineering value considering that even weakly nonlinear systems can experience nonlinear dynamic phenomena [175].

Consequently, this chapter presents an experimental assessment of the effect of structural nonlinearities on the aeroelastic stability and wind response of cable-supported bridges. To achieve this, a new experimental procedure for wind tunnel tests of bridges is utilized. Indeed, the section model test procedure is modified so that the nonlinear structural behavior of cable-supported bridges can be modeled. First, the theoretical developments required for such nonlinear section model tests of bridges are briefly reviewed. This is followed by a description of the experimental apparatus utilized for nonlinear section model tests, which was specifically developed for this purpose. The calibration procedure for the mechanical device required for nonlinear tests is also briefly discussed. This testing procedure was tested for three suspension bridges having main spans of 1624 m, 2400 m and 3000 m. The first one is a single-box girder bridge, whereas the two others are suspension bridges with twin-box

girders. A comparison between the results for linear tests and those for nonlinear tests is made in order to understand the effect of structural nonlinearities on the wind behavior of bridges.

6.2 Overview of Theory for Nonlinear Section Model Tests

For this study on the effect of structural nonlinearities on flutter, full-aeroelastic model tests are not considered due to their cost and the fact that the scaled axial and bending stiffnesses cannot be simultaneously taken into account for the different structural elements in these tests. In their current form, taut-strip models are also not of interest for this research as the taut wires or tubes utilized for these tests already possess their own nonlinear behavior, which is not representative of a cable-supported bridge. Instead, section model tests are considered herein because of the flexibility they offer since it is easy to adjust the structural parameters at the ends of the section model. Hence, a nonlinear device representative of the nonlinear structural behavior can be utilized in place of a typical springing system; this will allow nonlinear section model tests. This represents an improvement of the section model test procedure in comparison to the standard linear approach. The fact that section model tests allow an easier interpretation of the studied phenomenon is also an interesting aspect of these tests. Additionally, the fact that one mode in each direction can be represented in section model tests is not problematic since this study mostly focuses on flutter, an instability that typically involves one vertical mode and one torsional mode.

Nonlinear section model tests for bridges do not intend to replace the analysis procedure utilized in the industry combining section model tests and numerical analysis. It is rather a supplemental tool to understand the effect of structural nonlinearities on the aeroelastic behavior of bridges. In this initial development of nonlinear section model tests, we are only interested in stiffness nonlinearities due to the difficulty to characterize nonlinear structural damping in cable-supported bridges. Even though structural nonlinearities are the focus of such experimental approach, it is worth mentioning that aerodynamic nonlinearities are automatically accounted for when section model tests are utilized. The first step to conduct section model tests accounting for the effect of structural nonlinearities is to determine the scaled nonlinear structural behavior to be utilized for such experiments. For the sake of completeness, this procedure is briefly reviewed in this section, but the reader is referred to chapters 3 and 4 to find more information about it.

6.2.1 Nonlinear Generalized Stiffness

The nonlinear structural behavior in stiffness to be utilized for nonlinear section model tests is determined from nonlinear finite element analysis. This is achieved by applying loads that are proportional to modes of vibration onto a geometrically nonlinear numerical model of a cable-supported bridge. In this method, only geometric nonlinearities are of concern as the structures of interest in this research are cable-supported bridges. Longitudinal hydraulic buffers are also inactive. The reader can find a detailed presentation of nonlinear generalized stiffness analysis in the context of cable-supported bridges in chapter 3. This idea of using linear modes of vibration in the context of geometrically nonlinear structures has been used before in civil engineering [155] and in the field of aerospace engineering (e.g. [190]).

By following this numerical procedure for the first symmetric vertical mode and first symmetric torsional mode of a bridge, the nonlinear generalized restoring force $\tilde{f}_V(z_V, z_\theta)$ and nonlinear generalized restoring moment $\tilde{f}_\theta(z_V, z_\theta)$ relative to these modes are obtained. Since a nonlinear structure is considered, both are functions of the generalized vertical displacement z_V and generalized rotation z_θ . By using matrix notation for the nonlinear generalized restoring forces in eq. 6.1, it is possible to calculate a two-mode tangent nonlinear generalized stiffness matrix as shown in eq. 6.2:

$$\tilde{\mathbf{f}}_{V\theta}(\mathbf{z}_{V\theta}) = \begin{bmatrix} \tilde{f}_V(z_V, z_\theta) \\ \tilde{f}_\theta(z_V, z_\theta) \end{bmatrix} \quad (6.1)$$

$$\tilde{\mathbf{K}}_{V\theta}^t(\mathbf{z}_{V\theta}) = \frac{\partial \tilde{\mathbf{f}}_{V\theta}}{\partial \mathbf{z}_{V\theta}} = \begin{bmatrix} \frac{\partial \tilde{f}_V}{\partial z_V} & \frac{\partial \tilde{f}_V}{\partial z_\theta} \\ \frac{\partial \tilde{f}_\theta}{\partial z_V} & \frac{\partial \tilde{f}_\theta}{\partial z_\theta} \end{bmatrix} \quad (6.2)$$

where $\mathbf{z}_{V\theta} = [z_V \ z_\theta]^\top$; $\tilde{\mathbf{K}}_{V\theta}^t(\mathbf{z}_{V\theta})$ is the two-mode tangent nonlinear generalized stiffness matrix. It is worth noting that each term of the tangent nonlinear generalized stiffness matrix is also a function of both generalized displacements, i.e., z_V and z_θ . The non-zero off-diagonal terms in $\tilde{\mathbf{K}}_{V\theta}^t$ and the fact that the matrix entries are functions of both generalized displacements demonstrate the nonlinear structural vertical-torsional coupling in cable-supported bridges.

For this research, nonlinear generalized stiffness analysis is utilized to characterize the nonlinear structural behavior to be considered for nonlinear section model tests. In the nonlinear generalized stiffness approach, it is worth mentioning that the modes used for the modal loads are normalized such that the maximum vertical displacement or maximum rotation of

the deck are unity. Additionally, compared to antisymmetric modal pairs, symmetric modal pairs show a more nonlinear evolution of the generalized restoring forces (see chapter 3). Therefore, nonlinear section model tests are relevant for symmetric modal pairs, and linear tests are sufficient for antisymmetric modal pairs. Considering that the natural frequencies of the different modes in very long cable-supported bridges are very close to each other, the flutter wind speeds for the first antisymmetric modal pair and the first symmetric modal pair can also be close. Therefore, it is of interest to see whether the nonlinear structural behavior could trigger the symmetric instability to happen before the antisymmetric instability.

6.2.2 Mode Correction Factors

Mode correction factors are required for the nonlinear generalized restoring forces since the modal displacements for a specific mode vary along a bridge whereas a section model has uniform modes of vibration. This is why the generalized restoring forces need to be divided by the correction factors given in eq. 6.3. For the same reason, the generalized masses have to be divided by the factors in eq. 6.4, and the generalized displacements need to be modified by eq. 6.5.

$$\Gamma_V^h = \int_{L_{br}} |\psi_V^h(x)| dx \quad \Gamma_\theta^\alpha = \int_{L_{br}} |\psi_\theta^\alpha(x)| dx \quad (6.3)$$

$$\Gamma_{V2}^h = \int_{L_{br}} [\psi_V^h(x)]^2 dx \quad \Gamma_{\theta2}^\alpha = \int_{L_{br}} [\psi_\theta^\alpha(x)]^2 dx \quad (6.4)$$

$$\beta_V = \frac{\Gamma_V^h}{\Gamma_{V2}^h} \quad \beta_\theta = \frac{\Gamma_\theta^\alpha}{\Gamma_{\theta2}^\alpha} \quad (6.5)$$

In eqs. 6.3–6.5, $\psi_V^h(x)$ is a function for the vertical displacements along the bridge deck of the first symmetric vertical mode; $\psi_\theta^\alpha(x)$ is a function for the torsional rotations along the bridge deck of the first symmetric torsional mode. The functions $\psi_V^h(x)$ and $\psi_\theta^\alpha(x)$ are normalized such that the maximum vertical displacement or maximum rotation are unity. The generalized displacements, which also correspond to the maximum deck displacements due to the normalization utilized for the modes, are given by $z_V = \beta_V y_V$ and $z_\theta = \beta_\theta y_\theta$ with y_V and y_θ being respectively the vertical displacement and rotation of the section model at full scale.

6.2.3 Effective Distributed Mass Properties

Using the correction factors in eq. 6.4 onto the generalized masses \tilde{m}_V and \tilde{m}_θ leads to the calculation of the mass per unit length \bar{m}_V and mass moment of inertia per unit length \bar{m}_θ that will be utilized for section model tests:

$$\bar{m}_V = \frac{\tilde{m}_V}{\Gamma_{V2}^h} \quad \bar{m}_\theta = \frac{\tilde{m}_\theta}{\Gamma_{\theta 2}^\alpha} \quad (6.6)$$

Since eq. 6.6 can sometimes overestimate the mass parameters to be used for a section model (see chapter 4), the following equations were therefore considered in this research:

$$\bar{m}_V^* = \frac{\tilde{m}_V^*}{\Gamma_{V2}^h} \quad \bar{m}_\theta^* = \frac{\tilde{m}_\theta^*}{\Gamma_{\theta 2}^\alpha} \quad (6.7)$$

where $\tilde{m}_V^* = \boldsymbol{\phi}_V^{*\top} \mathbf{M} \boldsymbol{\phi}_V^*$ with $\boldsymbol{\phi}_V^*$ being a vertical mode shape for which the components corresponding to the longitudinal degrees of freedom are set to zero; $\tilde{m}_\theta^* = \boldsymbol{\phi}_\theta^{*\top} \mathbf{M} \boldsymbol{\phi}_\theta^*$ with $\boldsymbol{\phi}_\theta^*$ being a torsional mode shape for which the components corresponding to the lateral degrees of freedom are set to zero; \mathbf{M} is the mass matrix calculated using the finite element method.

6.2.4 Scaled Nonlinear Generalized Stiffness Behavior

The nonlinear generalized stiffness behavior discussed in section 6.2.1 corresponds to a full-scale bridge, and it therefore needs to be scaled. For this purpose, the geometric scale λ_L and velocity scale λ_U are utilized. For nonlinear tests, the mass parameters are scaled as for linear section model tests, i.e., $\bar{m}_{Vm}^* = \lambda_L^2 \bar{m}_{Vp}^*$ and $\bar{m}_{\theta m}^* = \lambda_L^4 \bar{m}_{\theta p}^*$ where subscripts m and p refer to the model and the prototype bridge respectively. For the damping ratios, we have that $\xi_{Vm} = \xi_{Vp}$ and $\xi_{\theta m} = \xi_{\theta p}$. The displacements and rotations are obtained using the usual approach, i.e., $y_{Vm} = \lambda_L y_{Vp}$ and $y_{\theta m} = y_{\theta p}$. For a model-scale section model of length L_{mm} , the mass of the model is $m_{Vm}^* = \bar{m}_{Vm}^* L_{mm}$, and the mass moment of inertia is $m_{\theta m}^* = \bar{m}_{\theta m}^* L_{mm}$. Therefore, a section model having m_{Vm}^* and $m_{\theta m}^*$ as its scaled mass properties must have the following scaled nonlinear stiffness behavior:

$$f_{Vm}^*(y_{Vm}, y_{\theta m}) = L_{mm} \frac{\bar{m}_V^* \lambda_U^2 \lambda_L}{\bar{m}_V \Gamma_V^h} \cdot \tilde{f}_{Vp} \left(\frac{\beta_V}{\lambda_L} y_{Vm}, \beta_{\theta} y_{\theta m} \right) \quad (6.8)$$

$$f_{\theta m}^*(y_{Vm}, y_{\theta m}) = L_{mm} \frac{\bar{m}_{\theta}^* \lambda_U^2 \lambda_L^2}{\bar{m}_{\theta} \Gamma_{\theta}^{\alpha}} \cdot \tilde{f}_{\theta p} \left(\frac{\beta_V}{\lambda_L} y_{Vm}, \beta_{\theta} y_{\theta m} \right) \quad (6.9)$$

where $f_{Vm}^*(y_{Vm}, y_{\theta m})$ and $f_{\theta m}^*(y_{Vm}, y_{\theta m})$ are the scaled mass-corrected restoring vertical force and moment. In converting the nonlinear generalized restoring forces, eqs. 6.8 and 6.9 account for the mode correction factors and scaling factors. Additionally, the mass-correction factors \bar{m}_V^*/\bar{m}_V and $\bar{m}_{\theta}^*/\bar{m}_{\theta}$ are utilized to ensure the correct natural frequencies when \bar{m}_V^* and \bar{m}_{θ}^* are considered for the mass properties per unit length of the section model.

6.3 Experimental Apparatus for Nonlinear Section Model Tests

As discussed in chapter 5, the nonlinear springing system that is considered for nonlinear section model tests of bridges requires an arrangement of inclined springs similar to the one illustrated in fig. 6.1. For such a spring configuration, it is considered that each spring behaves linearly since the nonlinear behavior is provided by the nonlinear geometric effects due to the inclination of the springs. In order to be able to conduct section model tests using the springing system of fig. 6.1, it is required to use a calibration procedure to determine the spring parameters that satisfy the nonlinear generalized stiffness behavior of eqs. 6.8 and 6.9. In chapter 5, it was also found that an experimental rig specifically designed for nonlinear section model tests is required for this research. These two elements are discussed in the following subsections.

6.3.1 Calibration Procedure for Nonlinear Spring Configuration

The spring parameters and stiffnesses shown in fig. 6.1 are determined using a nonlinear least-squares procedure. Therefore, the following error function needs to be minimized so that the inclined spring system matches as well as possible the scaled nonlinear generalized restoring forces of eqs. 6.8 and 6.9:

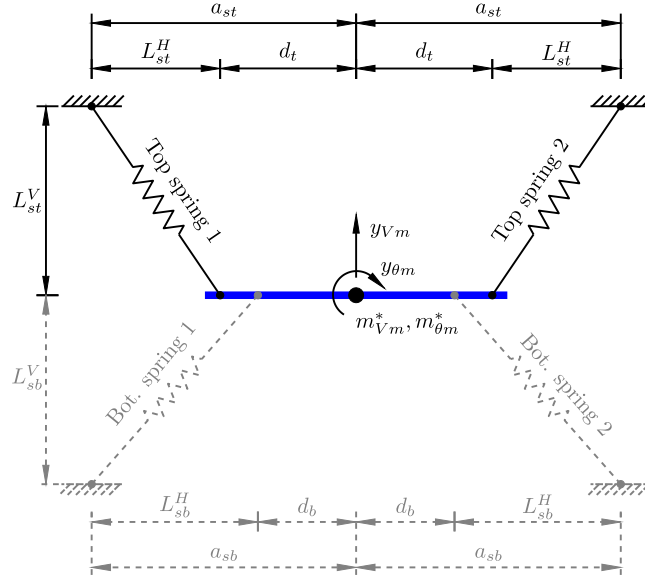


Figure 6.1: Spring configuration for nonlinear section model tests

$$J_{V\theta} = \sum_{i=1}^N \left\{ [f_{Vm}^*(y_{Vmi}, y_{\theta mi}) - F_V(y_{Vmi}, y_{\theta mi})]^2 + \left[\frac{f_{\theta m}^*(y_{Vmi}, y_{\theta mi})}{b_{clm}} - \frac{M_{\theta}(y_{Vmi}, y_{\theta mi})}{b_{clm}} \right]^2 \right\} \quad (6.10)$$

where b_{clm} is half of the cable spacing at model scale; N is the number of samples of the nonlinear generalized restoring forces used in the calculation of $J_{V\theta}$; $F_V(y_{Vmi}, y_{\theta mi})$ is the vertical resultant force of the springing system; $M_{\theta}(y_{Vmi}, y_{\theta mi})$ is the resultant moment of the springing system. It is worth noting that all the top springs have the same stiffness; the same applies to the bottom springs.

The goodness of the fit for the springing system is evaluated using the standard error of the regression $\sigma_{V\theta}$, which is defined as follows:

$$\sigma_{V\theta} = \sqrt{\frac{J_{V\theta}}{2N}} \quad (6.11)$$

A lower value for the standard error of the regression indicates a better fit. Additionally, it should be noted that $2N$ is utilized in eq. 6.11 because of the contributions from both the vertical force and moment to $J_{V\theta}$. The differential evolution optimization method is utilized for the minimization of eq. 6.10. More information can be found about this calibration

procedure in chapter 5.

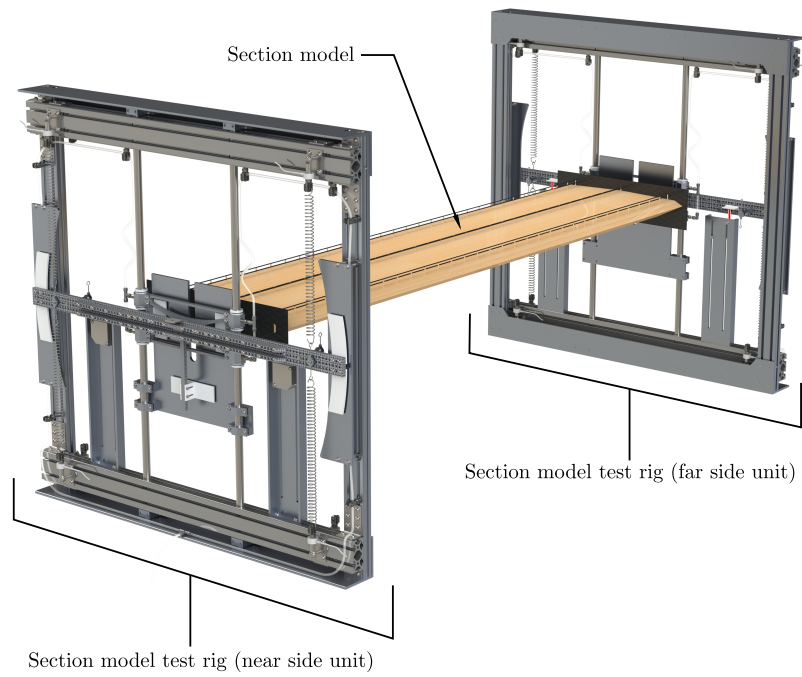
Using this calibration procedure for single-span suspension bridges in chapter 5, it was found that intersecting springs are required. Even though the experimental rig presented in section 6.3.2 is capable of intersecting springs, it is possible to have a fit as good by only using non-intersecting top springs for the bridges considered in this research. This means there are no bottom springs. In this case, the springs depicted as dashed lines in fig. 6.1 are omitted in the nonlinear least-squares procedure by setting their stiffnesses to zero.

6.3.2 Description of Nonlinear Section Model Test Rig

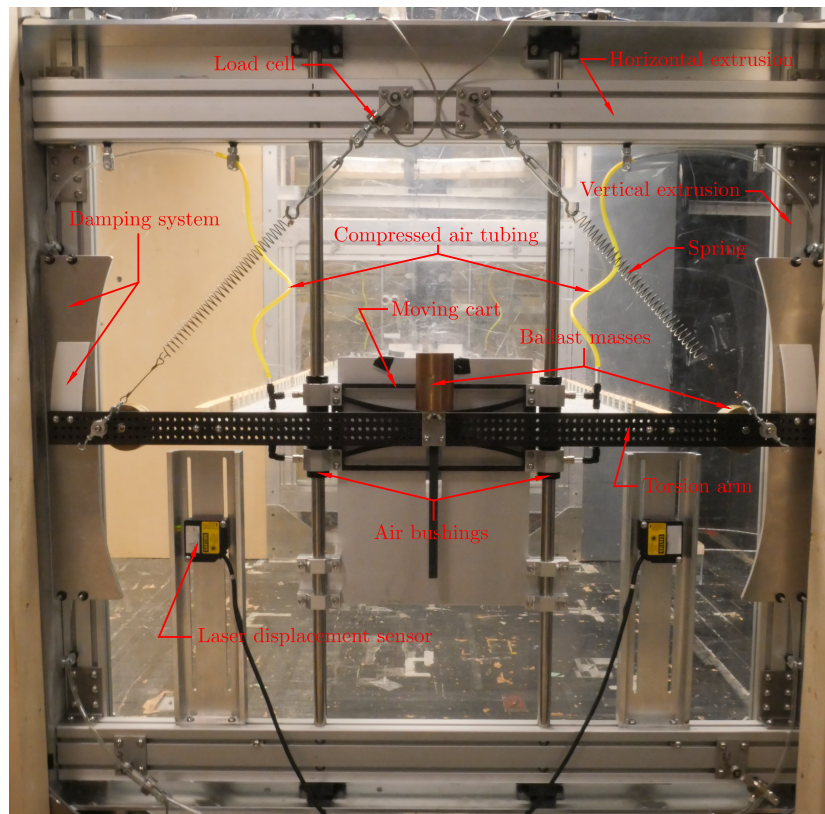
In order to be able to easily adjust the vertical and horizontal positions of the attachment points of the inclined springs required for nonlinear tests, a new section model test rig was developed, which was discussed in chapter 5. This nonlinear section model test rig is shown in fig. 6.2. As it can be seen in the 3D rendering of fig. 6.2a, the experimental rig is made of two units that are located at the ends of the bridge model. A typical unit as fabricated is illustrated in fig. 6.2b. Each unit is inserted into streamlined walls that are installed in the wind tunnel (see fig. 6.3). Both units of the nonlinear section model test rig are 1065 mm wide and 1065 mm high. This new experimental rig for section model tests of bridges can be utilized with vertical springs in the case of linear tests (fig. 6.2a) as well as with inclined springs for nonlinear tests (fig. 6.2b).

To have the correct spring lengths and inclinations in the case of nonlinear tests, each unit has vertical and horizontal aluminum extrusions allowing an easy adjustment of the spring attachment points. Suspended to the springs, there is a moving cart mounted on air bushings that allow the section model to move in the vertical direction. A torsion arm is mounted on a ball bearing in the middle of the moving cart so that the section model can also rotate. Therefore, only the vertical and torsional degrees of freedom are considered for nonlinear section model tests since the lateral mode was shown to have an insignificant effect on the nonlinear generalized stiffness behavior (see chapter 3). The moving cart and torsion arm are made out of carbon fiber composite so that these elements are light and stiff.

For the adjustment of the structural damping, a magnetic damping system, consisting of neodymium magnets and conducting plates in aluminum, is utilized. Also, the mass properties of the section model can be adjusted using ballast masses as shown in fig. 6.2b. The motion of the section model is measured using laser displacement sensors. Load cells are also utilized for the measurement of the individual spring forces.



(a) Three-dimensional model



(b) Typical unit

Figure 6.2: New section model test rig

6.4 Experimental Program




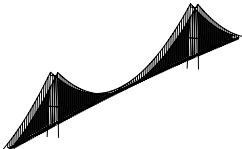
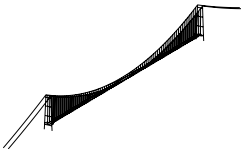
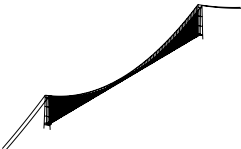
6.4.1 Boundary Layer Wind Tunnel Laboratory at the University of Western Ontario

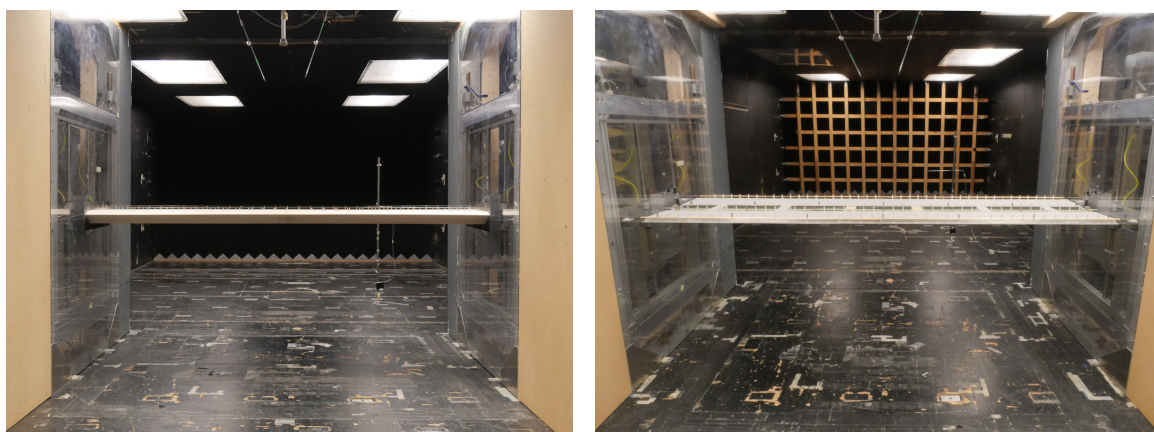
Wind tunnel tests for the experimental rig presented in section 6.3.2 were conducted at the Boundary Layer Wind Tunnel Laboratory (BLWTL) of the University of Western Ontario. More specifically, wind tunnel tests were carried out in the high-speed test section of BLWT 2 as shown in fig. 6.3. For section model tests of bridges conducted in BLWT 2, the bridge model is positioned between two streamlined walls, which are typically positioned such that there is a distance of 2.15 m between them. As mentioned previously, the units of the section model test rig are located inside these walls. Additionally, the test section where bridge section models are tested is 1.77 m high, and a maximum wind speed of 30 m/s can be reached at this location. The mean wind speed is measured using two Pitot tubes positioned above the bridge model, which are shown in fig. 6.3. Under smooth flow conditions, turbulence intensities are less than 0.5 %. For the grid shown in fig. 6.3b that is placed at the entrance of the high-speed test section, the turbulent flow measured at the location of the section model has a longitudinal turbulence intensity of 4.8 % and a vertical turbulence intensity of 4.4 %.

6.4.2 Bridge Section Models

Of the eleven cable-supported bridges that have been analyzed for the purpose of this research (see chapters 3–5), single-span suspension bridges are of interest for nonlinear section model tests since they are more nonlinear in comparison to three-span suspension bridges and cable-stayed bridges. Single-span suspension bridges with longer spans are particularly interesting because they have a stronger nonlinear vertical-torsional coupling. With reference to the bridge names used in chapters 3–5, bridges SU4c and SU4d therefore appear of interest as they are single-span suspension bridges with main spans of 2400 m and 3000 m respectively. For the sake of comparison, bridge SU2, a three-span suspension bridge with a main span of 1624 m, is also included in this study. The deck of bridge SU2 is a single-box girder. For the decks of bridges SU4c and SU4d, the same twin-box girder is considered. A description of these bridges is presented in table 6.1, but further information about them can be found in chapters 3–5. Consequently, section model tests were conducted for bridges SU2, SU4c and SU4d at the BLWTL as shown in fig. 6.3. The section model of bridge SU2 has a geometric scale of 1/70 for a model width of 443 mm. This model is

Table 6.1: Description of cable-supported bridges

Bridge	SU2	SU4c	SU4d
Type	Three-span suspension	Single-span suspension	Single-span suspension
Bridge deck	Single-box girder	Twin-box girder	Twin-box girder
Spans (m)	536 + 1624 + 536	2400	3000
Bridge-deck width (m)	31.0	46.4	46.4
Bridge-deck cross section			
Finite element model			



(a) Bridge SU2

(b) Bridges SU4c and SU4d

Figure 6.3: Bridge models utilized for nonlinear section model tests

also 1806 mm long. For bridges SU4c and SU4d, the 2134 mm-long section model has a geometric scale of 1/75 for a model width of 619 mm.

6.4.3 Validation of Nonlinear Section Model Test Rig

Before conducting nonlinear section model tests using the new bridge rig, it was required to validate its accuracy and reliability for dynamic tests. For this purpose, the section model of bridge SU2 was considered since it had been previously tested in the main wind tunnel of the *Université de Sherbrooke*. At first, it was decided to measure the mean aerodynamic force coefficients using the static test rig of the BLWTL in order to compare them to those from the *Université de Sherbrooke*. This aimed at ensuring that the section model of bridge SU2 was not altered in its transportation between the two wind tunnel laboratories. Then, the flutter derivatives and linear dynamic responses for bridge SU2 measured using the new

bridge rig were compared to those measured using the existing bridge rig at the BLWTL and those obtained in the main wind tunnel of the *Université de Sherbrooke*. This second step of the validation procedure allows to confirm the adequacy of the new bridge rig for dynamic section model tests. With the exception of the flutter derivative tests at the BLWTL for which only a smooth flow was used, all the wind tunnel results for this validation were measured using smooth and turbulent flow conditions, either at the *Université de Sherbrooke* or the BLWTL. The reader is referred to appendix C in order to find more information about the validation procedure of the new bridge rig.

6.4.4 Linear Section Model Tests

In order to have a basis of comparison for the nonlinear section model tests, linear section model tests were first carried out for the suspension bridges of table 6.1. These tests correspond to standard dynamic tests where vertical springs are utilized to suspend the bridge section model. The new bridge rig of the BLWTL was utilized for these wind tunnel tests. The experimental rig was set up in a similar manner to what is illustrated in fig. 6.2a.

The full-scale test parameters utilized for these dynamic tests are presented in table 6.2. With the exception of bridge SU2, linear dynamic tests were performed for the first symmetric modal pair as well as the first antisymmetric modal pair. This was done because the frequencies for the first symmetric modal pair (f_{VS1} and $f_{\theta S1}$) and the frequencies for the first antisymmetric modal pair (f_{VA1} and $f_{\theta A1}$) are close to each other. Therefore, it is not a priori clear which modal pair is critical for flutter. For bridge SU2, it was only possible to do tests for the first symmetric modal pair since the torsional-to-vertical frequency ratio required in the case of the first antisymmetric modal pair cannot be achieved with the experimental rigs of the BLWTL. This was not problematic because 2D flutter analysis relying on complex eigenvalue analysis for bridge SU2 indicated that the first symmetric modal pair was critical for flutter since the first antisymmetric modal pair has a much higher critical wind speed.

Due to the fact that most bridges are tested for the first symmetric and antisymmetric modal pairs, the mass per unit length \bar{m}_V^* and mass moment of inertia per unit length \bar{m}_θ^* that are shown in table 6.2 correspond to the average values given by eq. 6.7 for the first symmetric modes and first antisymmetric modes. It is also worth mentioning that the experimental mass properties were within 5 % of the full-scale target values that are presented in table 6.2. Similarly, the experimental natural frequencies were in good agreement with the target natural frequencies in table 6.2. Regarding the damping ratios, the values presented in table 6.2 correspond to the experimental ones. In the case of the first symmetric modes for bridges SU4c and SU4d, the damping ratios used during the linear tests (see values

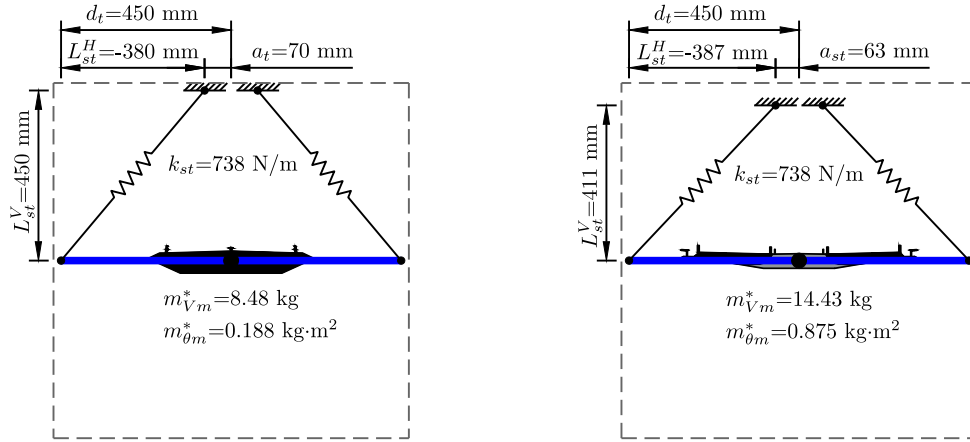
Table 6.2: Full-scale test parameters for section model tests (\overline{m}_V^* : mass per unit length, \overline{m}_θ^* : mass moment of inertia per unit length, f_{VS1} : natural frequency of first symmetric vertical mode, ξ_{VS1} : damping ratio of first symmetric vertical mode, $f_{\theta S1}$: natural frequency of first symmetric torsional mode, $\xi_{\theta S1}$: damping ratio of first symmetric torsional mode, f_{VA1} : natural frequency of first antisymmetric vertical mode, ξ_{VA1} : damping ratio of first antisymmetric vertical mode, $f_{\theta A1}$: natural frequency of first antisymmetric torsional mode, $\xi_{\theta A1}$: damping ratio of first antisymmetric torsional mode, α_s : angle of attack)

Bridge	SU2	SU4c	SU4d
\overline{m}_V^* (10^3 kg/m)	23.01	38.03	44.56
\overline{m}_θ^* (10^6 kg · m ² /m)	2.505	12.977	16.889
f_{VS1} (Hz)	0.097	0.093	0.083
ξ_{VS1} (%)	L: 0.40, NL: 0.40	L: 0.58, NL: 0.63	L: 0.55, NL: 0.58
$f_{\theta S1}$ (Hz)	0.279	0.140	0.115
$\xi_{\theta S1}$ (%)	L: 0.28, NL: 0.38	L: 0.72, NL: 0.71	L: 0.61, NL: 0.61
f_{VA1} (Hz)	-	0.065	0.059
ξ_{VA1} (%)	-	L: 0.44	L: 0.39
$f_{\theta A1}$ (Hz)	-	0.126	0.100
$\xi_{\theta A1}$ (%)	-	L: 0.27	L: 0.36
α_s (°)	0.0	0.0	0.0

for L) were set to match those for the nonlinear tests. This is discussed in more detail in section 6.4.5. Additionally, it is worth noting that linear dynamic tests were conducted for smooth and turbulent flows and for an angle of attack of 0°.

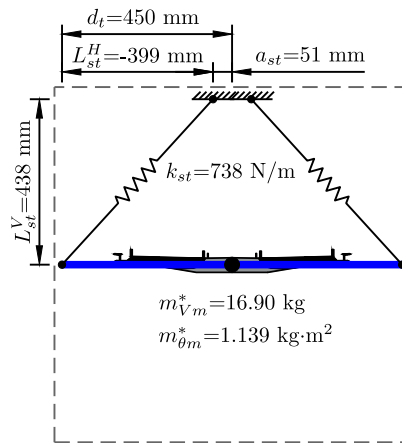
6.4.5 Nonlinear Section Model Tests

As mentioned in section 6.2.1, linear section model tests are sufficient for the first antisymmetric modal pairs, and nonlinear section model tests are therefore only relevant for the first symmetric modal pairs in this study. By following the procedure presented in sections 6.2 and 6.3.1, the nonlinear structural behavior and inclined spring configurations were determined for the first symmetric modal pairs of the bridges in table 6.1. Figure 6.4 presents the spring configurations utilized for the nonlinear section model tests, which were obtained considering the mass properties of table 6.2 and scaling parameters given in fig. 6.4. Also, in this figure, the dashed grey lines represent the usable space inside the units of the new bridge rig for the springs and moving parts. The spring stiffnesses in this figure correspond to the individual spring stiffness of each spring shown in the figure. However, since two springing systems are used in the wind tunnel, i.e., one at each end of the section model, the springs utilized in the wind tunnel have a stiffness that is half of the values given in fig. 6.4. As shown in this figure, it was decided to use the same springs for the nonlinear tests of the three bridges. Consequently, the velocity scale was changed for the different bridges instead



(a) Bridge SU2 ($\lambda_L = 1/70$, $\lambda_U = 1/4.18$, $L_{mm} = 1806$ mm, $\Gamma_V^h = 1133.4$, $\Gamma_\theta^\alpha = 994.2$, $\beta_V = 1.551$, $\beta_\theta = 1.372$, $\bar{m}_V^*/\bar{m}_V = 0.968$, $\bar{m}_\theta^*/\bar{m}_\theta = 0.569$)

(b) Bridge SU4c ($\lambda_L = 1/75$, $\lambda_U = 1/5.17$, $L_{mm} = 2134$ mm, $\Gamma_V^h = 948.9$, $\Gamma_\theta^\alpha = 1049.1$, $\beta_V = 1.485$, $\beta_\theta = 1.337$, $\bar{m}_V^*/\bar{m}_V = 0.992$, $\bar{m}_\theta^*/\bar{m}_\theta = 1.034$)



(c) Bridge SU4d ($\lambda_L = 1/75$, $\lambda_U = 1/4.96$, $L_{mm} = 2134$ mm, $\Gamma_V^h = 1186.9$, $\Gamma_\theta^\alpha = 1247.8$, $\beta_V = 1.478$, $\beta_\theta = 1.357$, $\bar{m}_V^*/\bar{m}_V = 0.987$, $\bar{m}_\theta^*/\bar{m}_\theta = 1.032$)

Figure 6.4: Nonlinear spring configurations for the first symmetric modal pairs of the suspension bridges

of using springs with different stiffness values. Doing so made easier the adjustment of the section model test rig when switching between the different nonlinear spring configurations. The individual stiffness of each spring was measured so that the average spring stiffness can be considered in the calibration process of section 6.3.1 (twice the average due to the two springing systems). This was done by suspending weights to the springs and measuring the corresponding displacements using a laser displacement sensor. Additionally, as it is shown

in fig. 6.2b, turnbuckles are utilized to adjust the distance between the spring attachment points of the horizontal extrusion and torsion arm.

Since only the top springs are used in the spring configurations of fig. 6.4, the spring prestressing is therefore only provided by the weight of the section model. For this reason, it was decided to use extension springs without initial pretension. By doing so, the weight of the section model provides a maximum spring extension, ensuring that the springs stay under tension at all times even when the section model moves. To avoid the vibration of the inclined springs, light springs with a relatively small wire diameter were utilized as shown in fig. 6.2b. It is also worth mentioning that top-spring-only setups were utilized for the linear tests with vertical springs of bridges SU4c and SU4d.

Just like in the case of linear tests, standard procedures can be utilized in the case of nonlinear section model tests for the measurement of the natural frequencies, mass, mass moment of inertia and damping ratios as long the amplitudes of vibration are small so that the behavior is quasilinear. However, in the case of inclined spring configurations, the added mass technique cannot be used to calculate the mass and mass moment of inertia, but these quantities can be calculated from the frequencies and stiffness of the system. With the inclined spring configurations, it is also required to check the nonlinear structural behavior of the system by applying known vertical forces and torsional moments and by measuring the corresponding displacements. This is to make sure that the nonlinear stiffness provided by the inclined springs matches the target nonlinear structural behavior. From the measurement of the nonlinear structural behavior, the tangent stiffnesses when y_V and y_θ are close to zero can be obtained for the purpose of calculating the experimental mass and mass moment of inertia. Additionally, it is worth mentioning that the measured frequencies in the case of the nonlinear tests for small amplitudes of vibration were very close to the target linear frequencies presented in table 6.2. With regard to the mass and mass moment of inertia, the experimental values were within 5 % of the full-scale target values shown in table 6.2.

Once the bridge rig is set up for nonlinear section model tests, its usage for dynamic tests is the same as for typical linear tests where the dynamic response of a bridge is obtained by gradually increasing the wind speed in the wind tunnel. However, it was found that the inherent mechanical damping of the new bridge rig was higher when set up for nonlinear tests in the case of bridges SU4c and SU4d. Indeed, it was not possible for the nonlinear tests to have damping ratios around 0.3 % for these bridges, which was the value that was initially intended to be considered in the dynamic section model tests. Instead, damping ratios around 0.6 % were obtained for the nonlinear tests as shown in table 6.2 in the case of the first symmetric modal pair (see values for NL). The additional inherent damping observed for the

nonlinear tests is possibly explained by the fact that there are greater rotational amplitudes of the bearings located on the top spring attachment points in the case of inclined springs in comparison to a vertical spring configuration. Consequently, the linear tests for the first symmetric modal pairs were carried out again for a damping ratio close to 0.6 % in order to be able to make a direct result comparison with the nonlinear test results. As shown in table 6.2, the damping ratios for the linear and nonlinear cases are similar for each of the three bridges in the case of the first symmetric modal pair.

6.5 Results

6.5.1 Static Aerodynamic Coefficients

Before conducting dynamic section model tests, the static aerodynamic coefficients were measured for the bridge section models utilized in this research. For the single-box girder model of bridge SU2, static tests were conducted just prior to the dynamic tests. The section model for bridges SU4c and SU4d was tested for the static coefficients during a previous wind tunnel test campaign at the BLWTL. For the presentation of the static coefficients, the following formulation is considered for the mean aerodynamic forces:

$$D_s = \frac{1}{2}\rho U^2 B C_D(\alpha_s) \quad L_s = \frac{1}{2}\rho U^2 B C_L(\alpha_s) \quad M_s = \frac{1}{2}\rho U^2 B^2 C_M(\alpha_s) \quad (6.12)$$

where D_s , L_s and M_s are the mean aerodynamic drag force, mean aerodynamic lift force and mean aerodynamic moment per unit length; ρ is the density of air; U is the mean wind speed; B is the bridge-deck width; C_D , C_L and C_M are respectively the drag coefficient, lift coefficient and moment coefficient; α_s is the angle of attack. The sign convention that is utilized for the aerodynamic forces in this chapter is shown in fig. 6.5.

The static coefficients of the section model of bridge SU2 as well as the static coefficients of the section model for bridges SU4c and SU4d are presented in fig. 6.6. For the sake of brevity, only the results for a turbulent flow are included in this section. These results were measured for a Reynolds number of approximately 3.3×10^5 for bridge SU2, whereas the section model of bridges SU4c and SU4d was tested for a Reynolds number of approximately 5.6×10^5 . The Reynolds number is calculated with respect to the bridge-deck width. Additionally, the static coefficients were measured for angles of attack varying between -10° and 10° with increments of 1° .

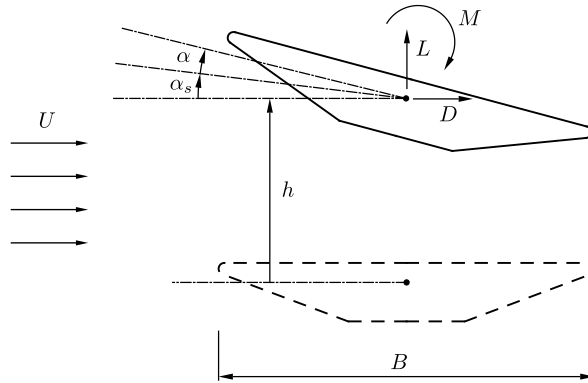


Figure 6.5: Sign convention for displacements and forces

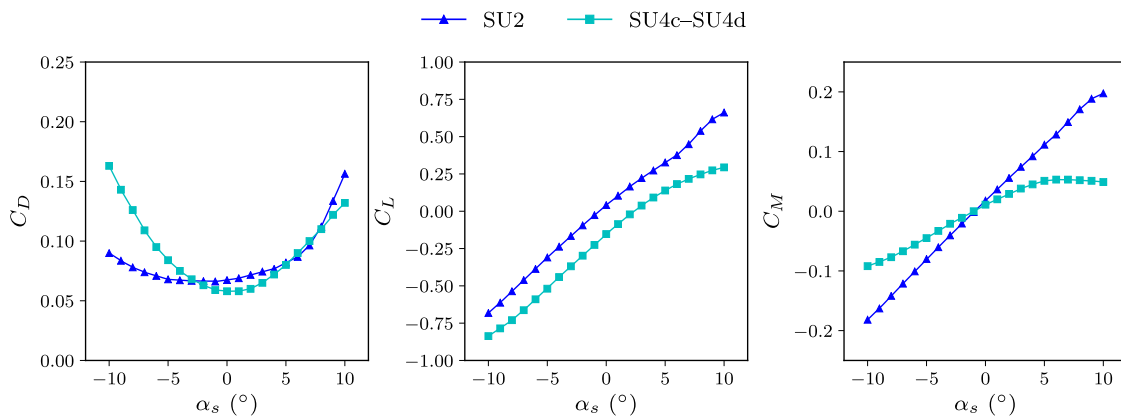


Figure 6.6: Static aerodynamic coefficients (turbulent flow)

6.5.2 Old Bridge Rig vs New Bridge Rig for Linear Tests

Following the measurements of the static coefficients, linear section model tests for the same section model were performed using the old bridge rig of the BLWTL as well as the new BLWTL bridge rig. As mentioned previously, this was done in order to validate the new bridge rig. The first verification consisted in comparing the flutter derivatives for both section model test rigs measured using the free-vibration test approach. For this purpose, the self-excited forces and flutter derivatives are defined as shown in the following equations:

$$L_{se}(t) = \frac{1}{2}\rho U^2 B \left(KH_1^* \frac{\dot{h}}{U} + KH_2^* \frac{B\dot{\alpha}}{U} + K^2 H_3^* \alpha + K^2 H_4^* \frac{h}{B} \right) \quad (6.13)$$

$$M_{se}(t) = \frac{1}{2}\rho U^2 B^2 \left(KA_1^* \frac{\dot{h}}{U} + KA_2^* \frac{B\dot{\alpha}}{U} + K^2 A_3^* \alpha + K^2 A_4^* \frac{h}{B} \right) \quad (6.14)$$

where $L_{se}(t)$ and $M_{se}(t)$ are the self-excited lift force and self-excited moment per unit length; t is the time; $h = h(t)$ and $\alpha = \alpha(t)$ are respectively the dynamic vertical displacement and dynamic rotation; $K = \omega B/U$ is the reduced frequency; $\omega = 2\pi f$ is the angular frequency of oscillation; H_i^* and A_i^* ($i = 1, \dots, 4$) are the flutter derivatives, which are functions of the reduced velocity $U_R = U/(fB)$; f is the frequency of oscillation; the overdot denotes the time derivative. The sign convention considered for the forces and displacements is shown in fig. 6.5.

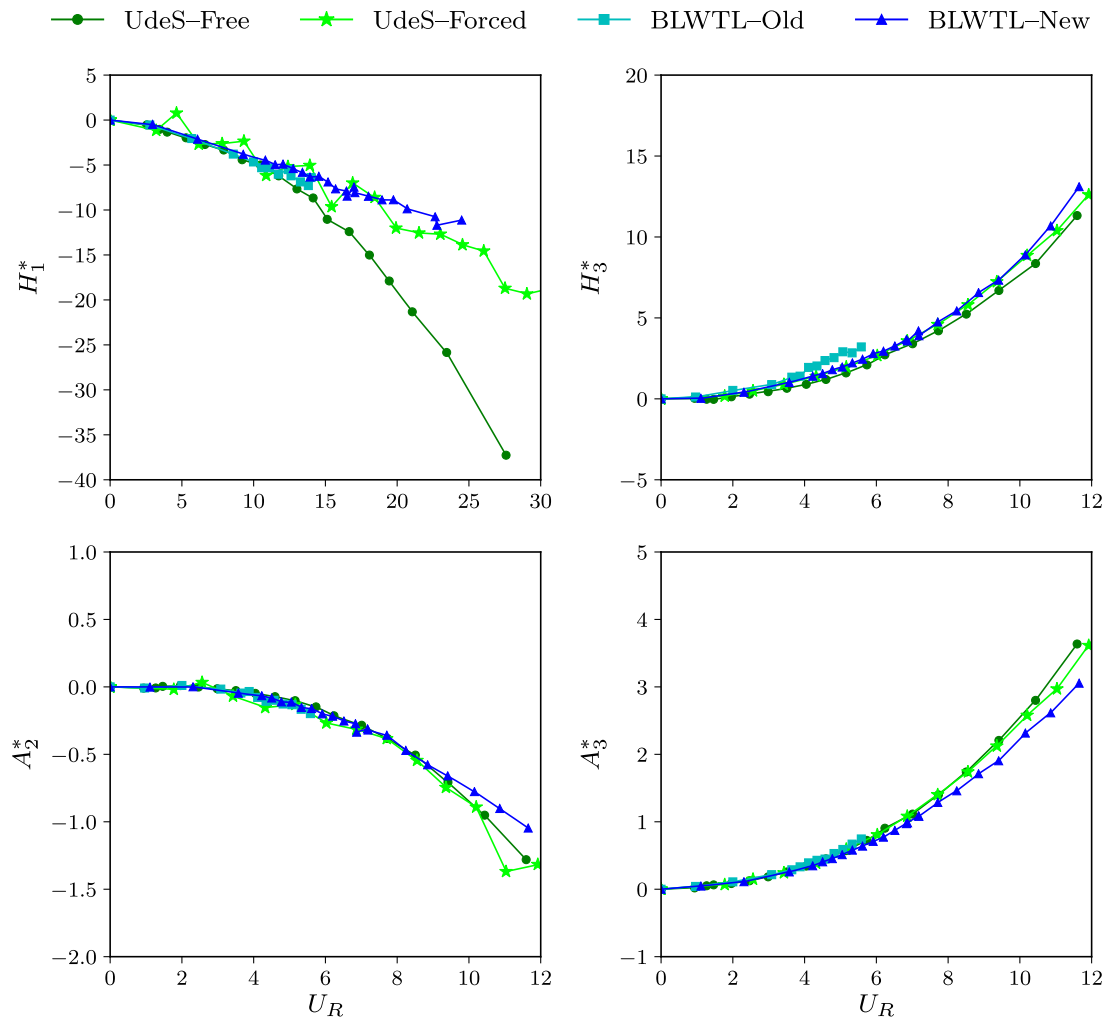


Figure 6.7: Flutter derivatives of bridge SU2 (smooth flow)

Figure 6.7 presents a comparison between the flutter derivatives for the section model of bridge SU2 measured using the old bridge rig (BLWTL-Old) and the new bridge rig (BLWTL-New). For the sake of brevity, only selected flutter derivatives are presented, and the reader is referred to appendix C for the detailed presentation of this analysis. The

Modified Unifying Least-Squares (MULS) method [27] was utilized for the calculation of the flutter derivatives from the free-vibration test results. In addition to the flutter derivatives measured at the BLWTL, fig. 6.7 also includes the flutter derivatives of bridge SU2 measured in the main wind tunnel of the *Université de Sherbrooke*. At the *Université de Sherbrooke*, the flutter derivatives were measured using the free-vibration procedure (UdeS-Free) as well as the forced-vibration approach (UdeS-Forced). For the forced-vibration technique, the flutter derivatives were calculated from the experimental results using a linear least-squares approach. The results in fig. 6.7 are for smooth flow conditions and an angle attack of 0° .

The second verification undertaken to validate the new bridge rig consisted in comparing the dynamic responses of the sprung model of bridge SU2 measured using the old and new bridge rigs. These linear dynamic tests were carried out considering the dynamic properties for the first symmetric modal pair. The dynamic response measured for bridge SU2 at the *Université de Sherbrooke* was also included in this comparison. However, due to limitations of the experimental apparatus at the *Université de Sherbrooke*, damping ratios were just over 0.9% for the *Université de Sherbrooke* results. Samples results of this analysis for a smooth flow are presented in fig. 6.8. Results for a turbulent flow can be found in appendix C. Figures 6.8a and 6.8b show respectively the mean displacements and peak displacements of the linear dynamic responses for bridge SU2 measured using the different experimental rigs.

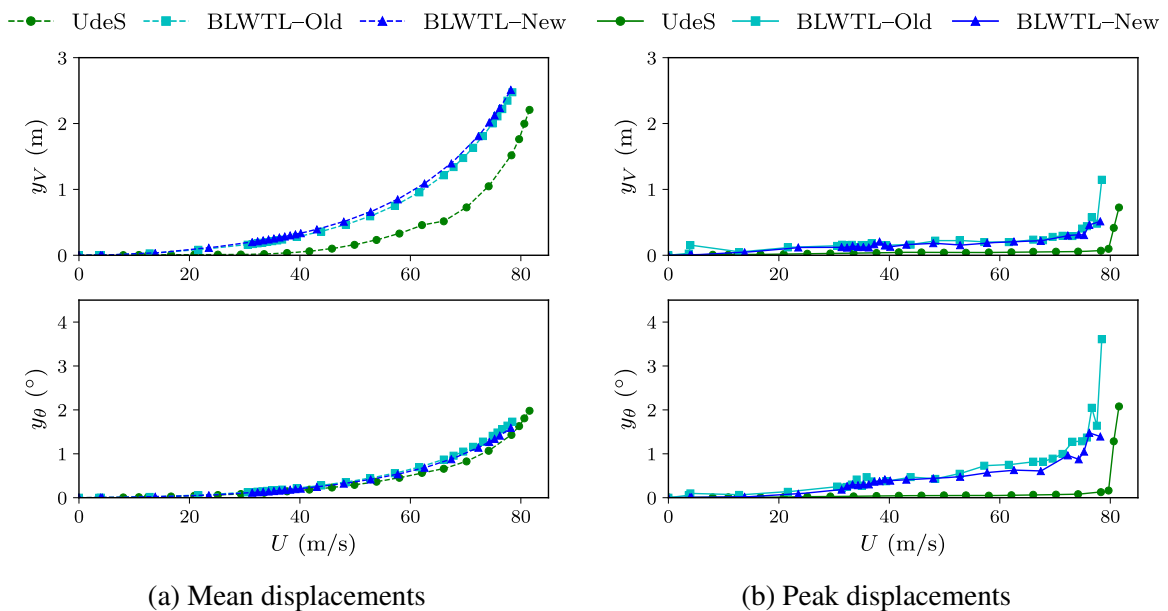


Figure 6.8: Linear dynamic response of bridge SU2 for modes VS1 and TS1 and a smooth flow (full scale)

6.5.3 Structural Behavior for Nonlinear Section Model Tests

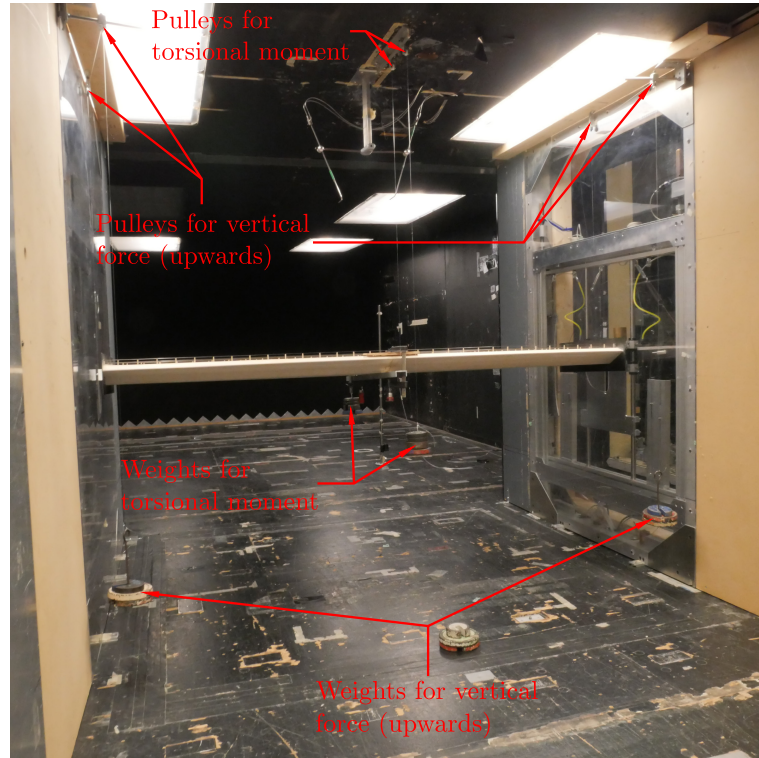
Supplemental to the measurements of the mass, mass moment of inertia, natural frequencies and damping ratios, it is also required to check the nonlinear stiffness behavior in the case of nonlinear tests, which was briefly discussed in section 6.4.5. As illustrated in fig. 6.9, this was done by applying known vertical forces and torsional moments to the bridge model using weights, pulleys and wires. The corresponding displacements were measured using laser displacement sensors as shown in fig. 6.9b. For bridge SU2, six different amplitudes for the vertical force and seven different values for the torsional moment were considered, which lead to a total of 42 combinations. In the case of bridges SU4c and SU4d, 49 force-moment combinations for seven values for the vertical force and torsional moment were utilized to verify the nonlinear stiffness behavior.

In fig. 6.10, the experimental nonlinear stiffness behaviors measured using the approach described in the previous paragraph are compared to the target nonlinear behaviors for bridges SU2, SU4c and SU4d. The target behaviors, shown as surfaces in this figure, correspond to the scaled nonlinear behavior of eqs. 6.8 and 6.9, calculated following the procedure of section 6.2 for each bridge. The experimental results are shown as colored circles in this figure. The coloring that is used for the circles shows the error between the experimental results and the target numerical values. The error for the vertical force $|\Delta f_{V_m}^*|$ and the error for the torsional moment $|\Delta f_{\theta_m}^*|$ are calculated as per eq. 6.15. In fig. 6.10, the standard errors for the experimental results are also shown, which were calculated using the following equations:

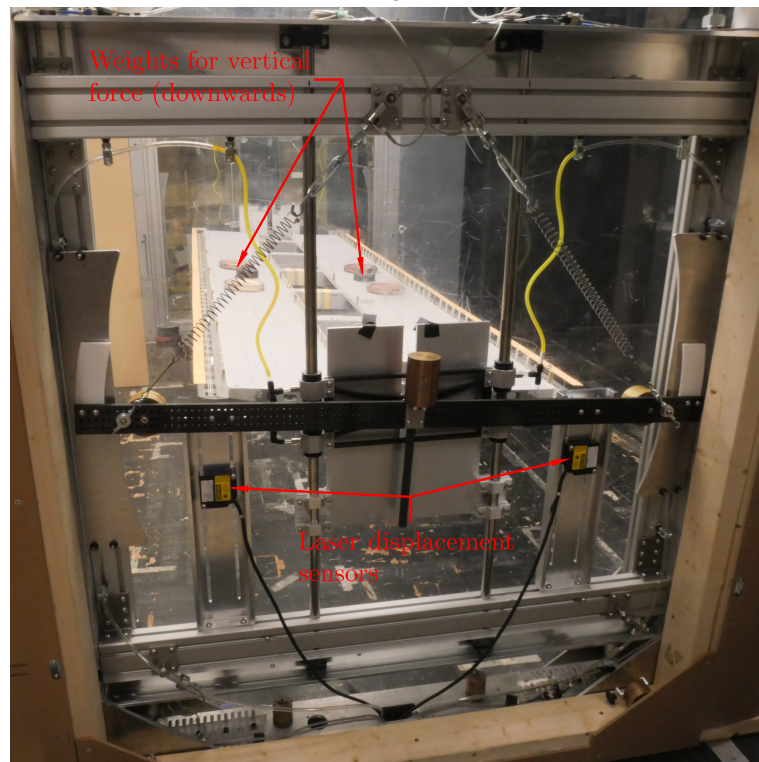
$$|\Delta f_{V_m}^*| = |f_{V_m}^* - F_V| \quad |\Delta f_{\theta_m}^*| = |f_{\theta_m}^* - F_\theta| \quad (6.15)$$

6.5.4 Mean and Peak Displacements for Dynamic Tests

In this section, the main results of the dynamic section model tests are included. The linear test results and nonlinear test results are presented for each bridge of table 6.1 considering the dynamic properties shown in table 6.2. More specifically, the mean and peak displacements measured using the new bridge rig for an increasing wind speed are shown in this section. These results correspond to the full-scale displacements of the section model. The main and peak displacements for bridge SU2 for a smooth flow and a turbulent flow are respectively found in figs. 6.11 and 6.12. Figures 6.13 and 6.14 present the dynamic test results of bridge SU4c for smooth and turbulent flow conditions. In the case of bridge SU4d, the dynamic test



(a) Bridge SU2



(b) Bridges SU4c and SU4d

Figure 6.9: Setup for measuring nonlinear structural behavior

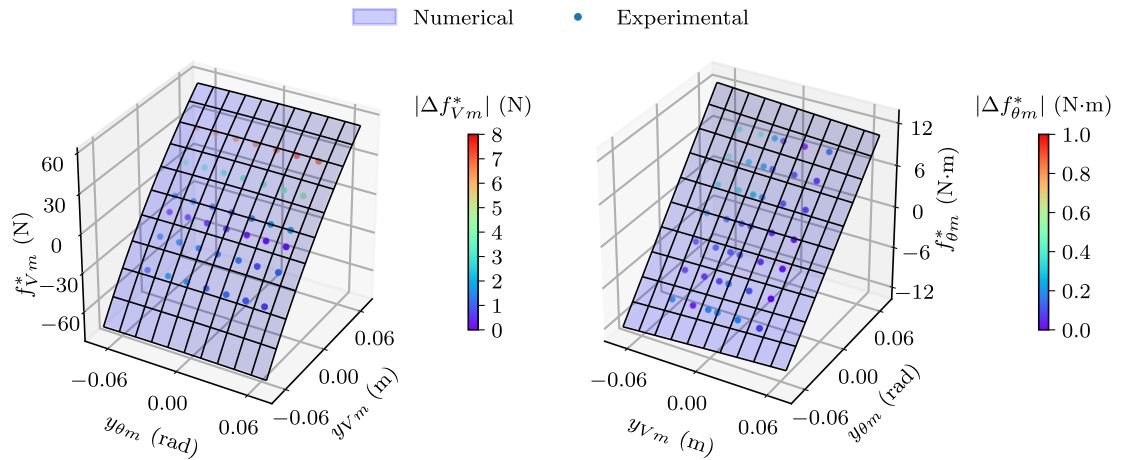
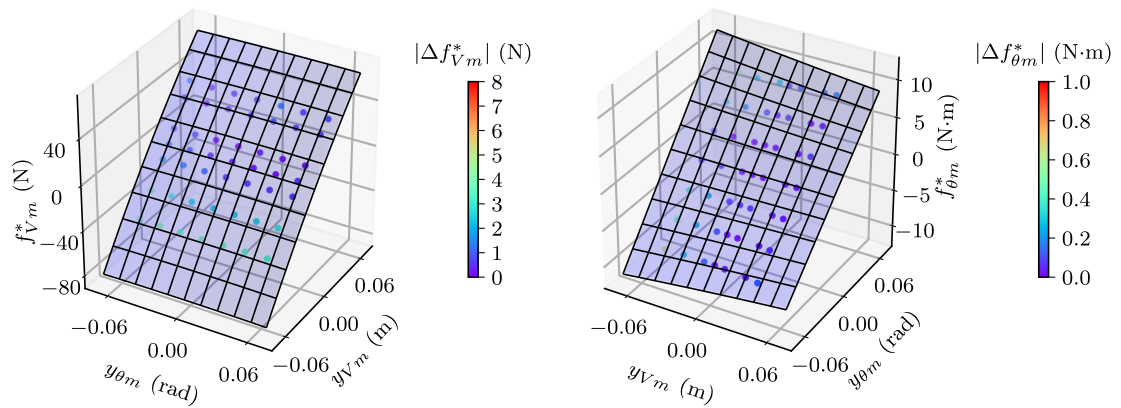
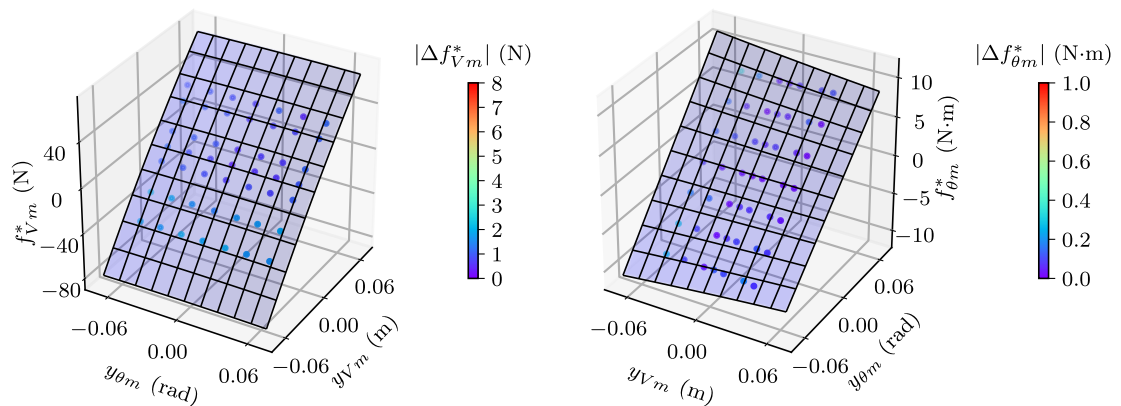
(a) Bridge SU2 ($\sigma_{V\theta} = 2.41$ N)(b) Bridge SU4c ($\sigma_{V\theta} = 1.47$ N)(c) Bridge SU4d ($\sigma_{V\theta} = 0.97$ N)

Figure 6.10: Comparison between target nonlinear behavior and experimental nonlinear behavior

Table 6.3: Flutter wind speeds for linear and nonlinear tests (full scale)

Bridge	U_{cr} for smooth flow (m/s)			U_{cr} for turb. flow (m/s)		
	A1L	S1L	S1NL	A1L	S1L	S1NL
SU2	-	78.2	74.9	-	78.9	77.6
SU4c	70.0	76.5	82.3	77.1	77.1	>93.5
SU4d	60.1	69.4	75.0	61.0	64.7	>90.1

results for a smooth flow and a turbulent flow are shown in figs. 6.15 and 6.16. For bridge SU2, the results for the first symmetric modal pair are presented for the linear case (S1L) and nonlinear case (S1NL). Supplemental to the linear and nonlinear results for the first symmetric modal pair, the linear dynamic test results for the first antisymmetric modal pair (A1L) are also included in these figures in the case of bridges SU4c and SU4d.

From the peak displacement results obtained for the different bridges, the flutter wind speeds were determined, which are presented in table 6.3. In this table, the flutter wind speed is defined as the wind speed at which the peak rotation reaches a value of 1.5° . It is worthy to note that in some cases it was not possible to measure the displacements for a peak rotation greater than 1.5° since the displacements would suddenly become very large and the wind tunnel had to be stopped. In this case, the wind speed for which the last point that was recorded for the peak displacement results was considered as the flutter wind speed.

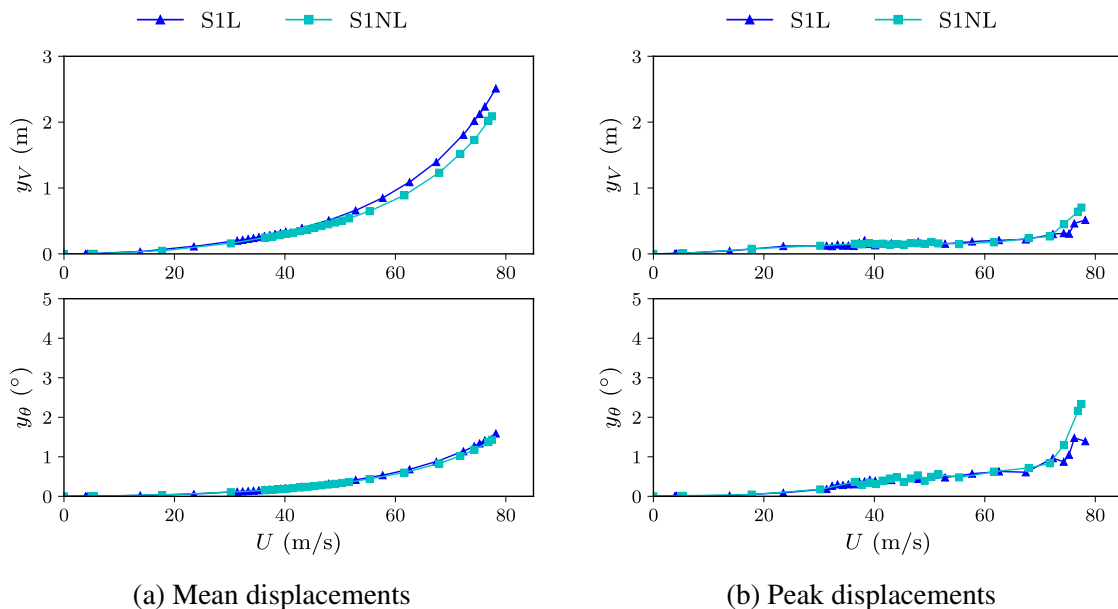


Figure 6.11: Linear and nonlinear dynamic responses of bridge SU2 for a smooth flow

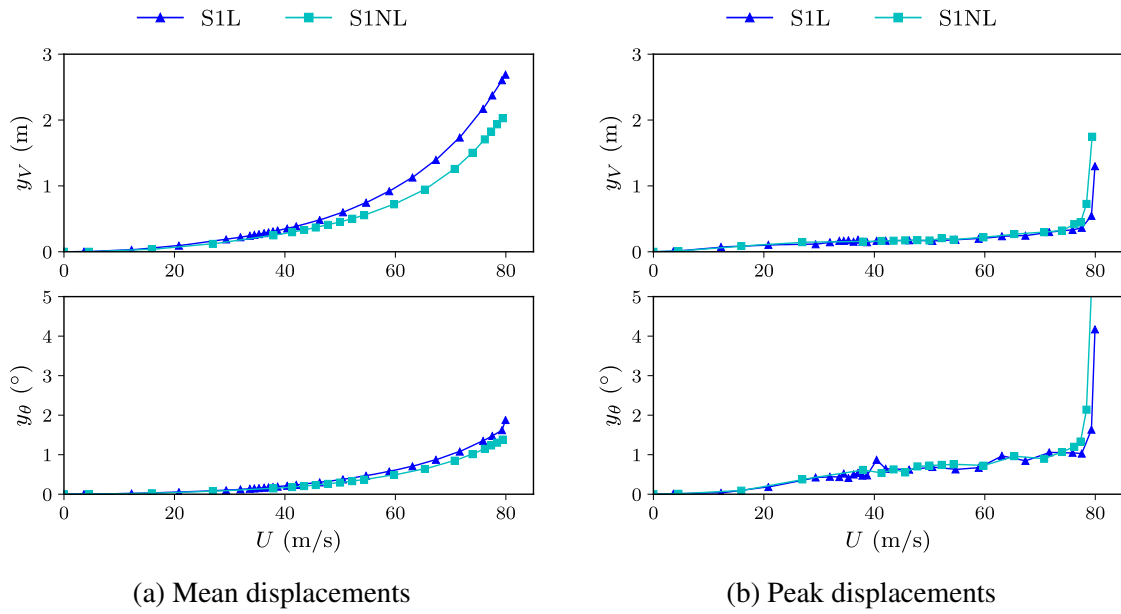


Figure 6.12: Linear and nonlinear dynamic responses of bridge SU2 for a turbulent flow

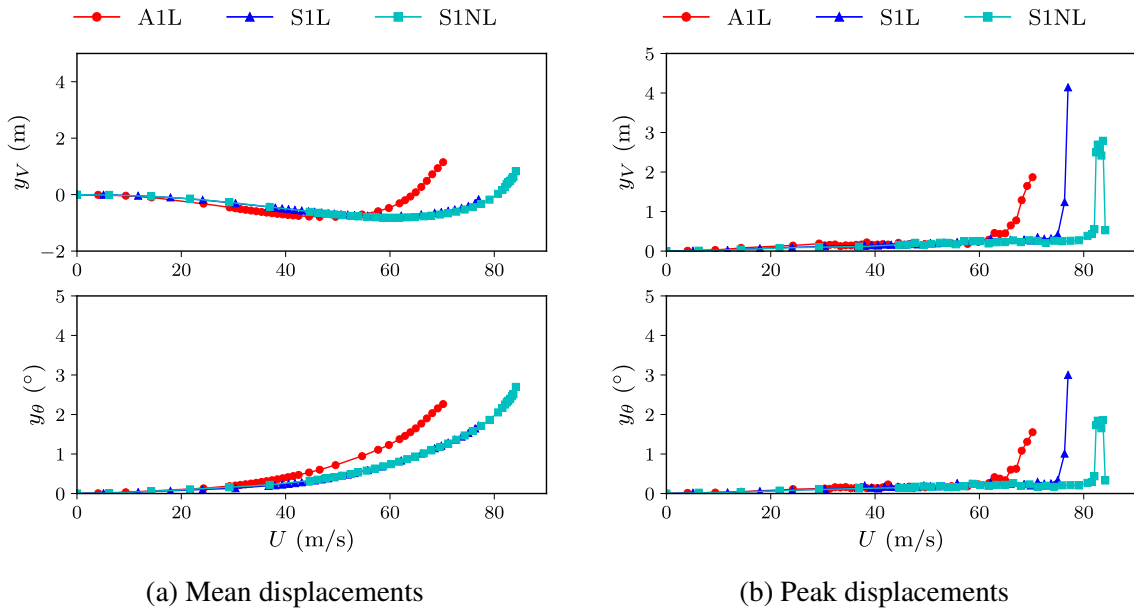


Figure 6.13: Linear and nonlinear dynamic responses of bridge SU4c for a smooth flow

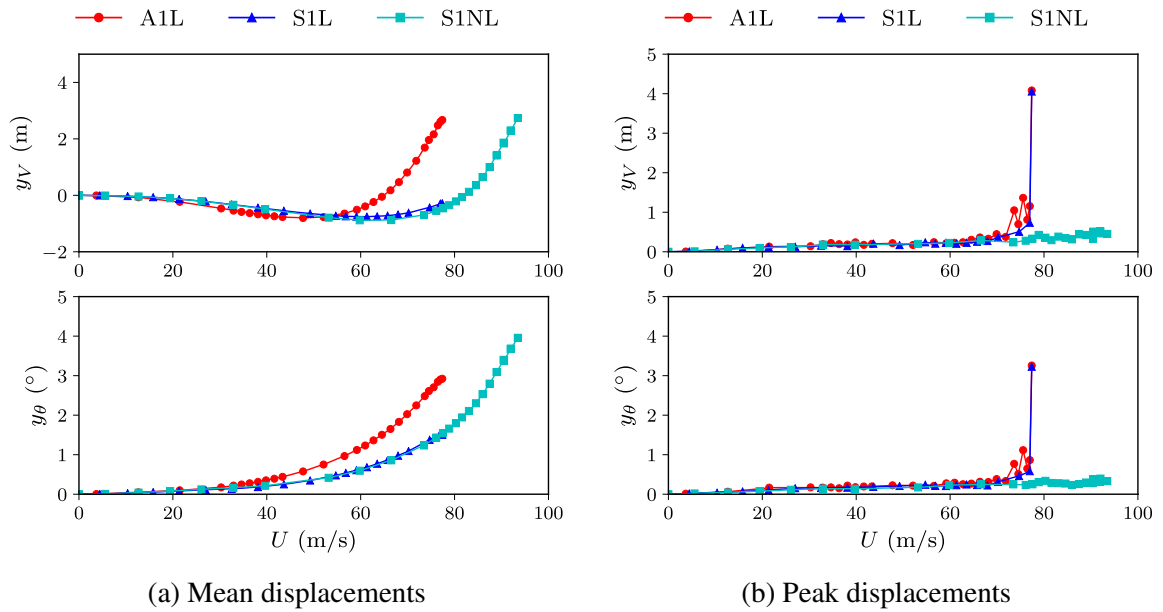


Figure 6.14: Linear and nonlinear dynamic responses of bridge SU4c for a turbulent flow

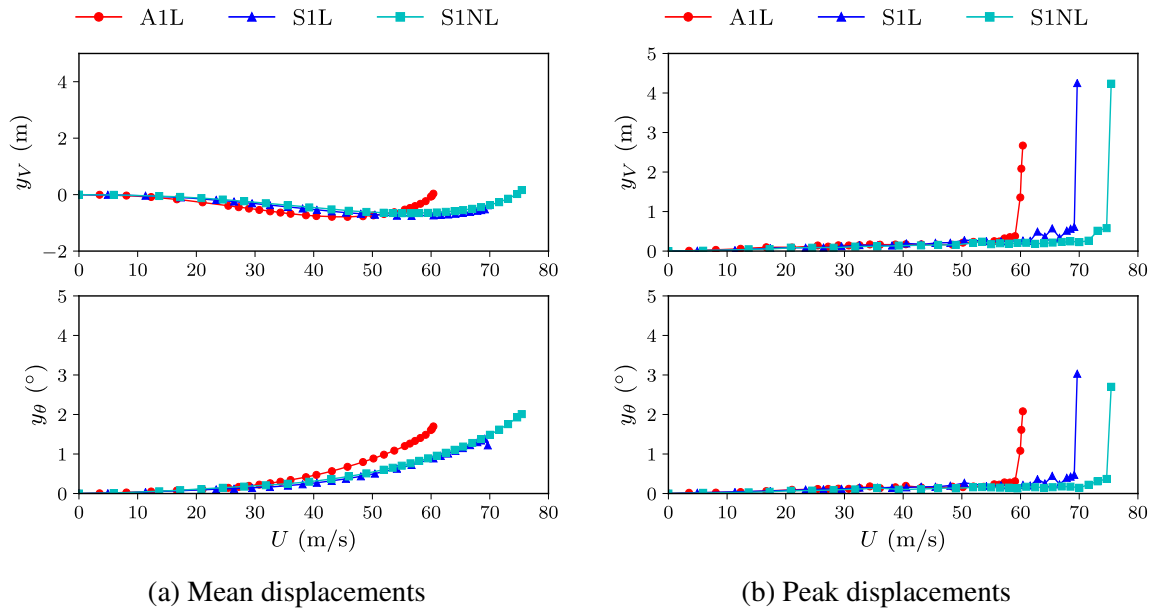


Figure 6.15: Linear and nonlinear dynamic responses of bridge SU4d for a smooth flow

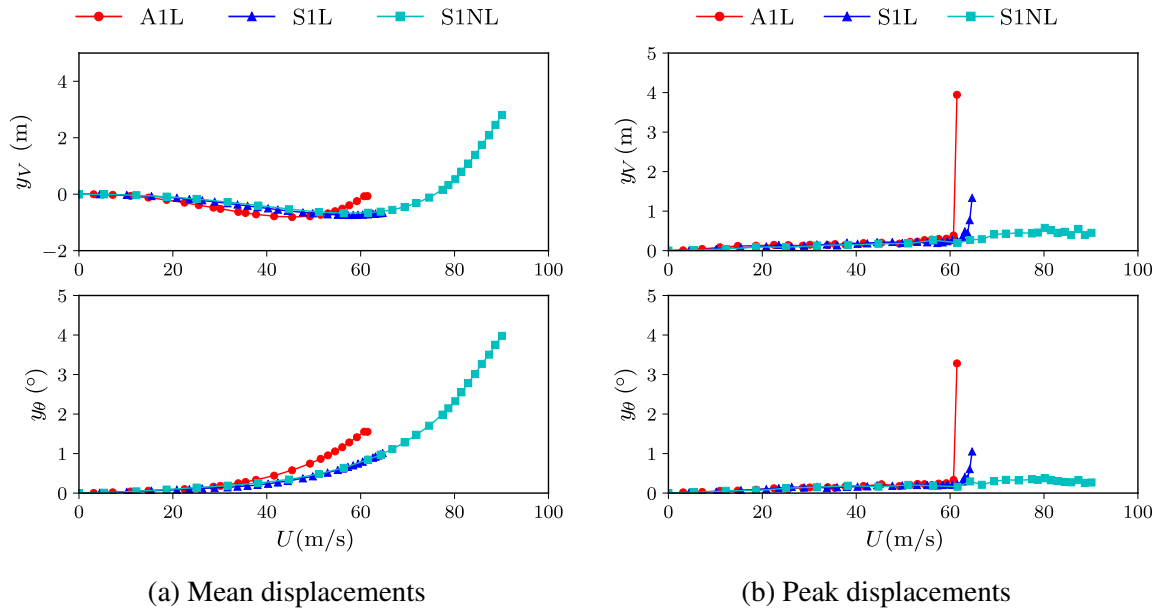


Figure 6.16: Linear and nonlinear dynamic responses of bridge SU4d for a turbulent flow

6.5.5 Linear and Nonlinear Dynamic Responses When Flutter Is Reached

For the dynamic tests of bridges SU2, SU4c and SU4d, it is also interesting to analyze the linear and nonlinear dynamic responses when flutter is reached. For this purpose, it is relevant to present the displacement time histories of the flutter instability of each bridge. A comparison of the power spectral densities (PSD) of the displacements for the linear and nonlinear tests is also included. The time histories and PSDs presented in this section are for the full-scale displacements of the section model. The displacement time histories and PSDs for bridges SU2, SU4c and SU4d are presented in figs. 6.17–6.19. To make it easier to compare the PSDs of the displacements, they are presented in a normalized format. The vertical displacement PSD (S_{yV}) is divided by the variance of the vertical displacement (σ_{yV}^2), whereas the torsional rotation PSD ($S_{y\theta}$) is normalized with respect to the variance of the torsional rotation ($\sigma_{y\theta}^2$). In figs. 6.17–6.19, the results of the linear and nonlinear tests are presented for the first symmetric modal pair (S1L and S1NL). The time histories and PSDs for the antisymmetric modal pair (A1L) are also included in figs. 6.18 and 6.19.

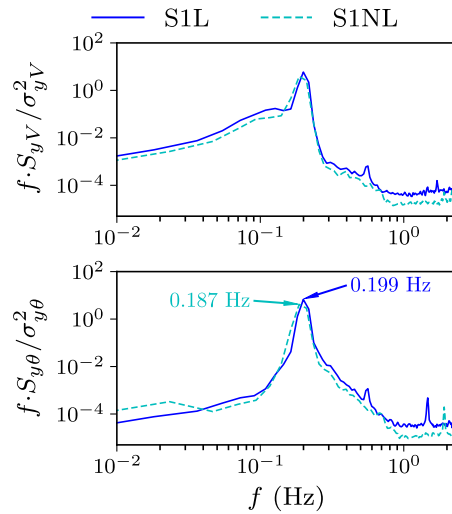
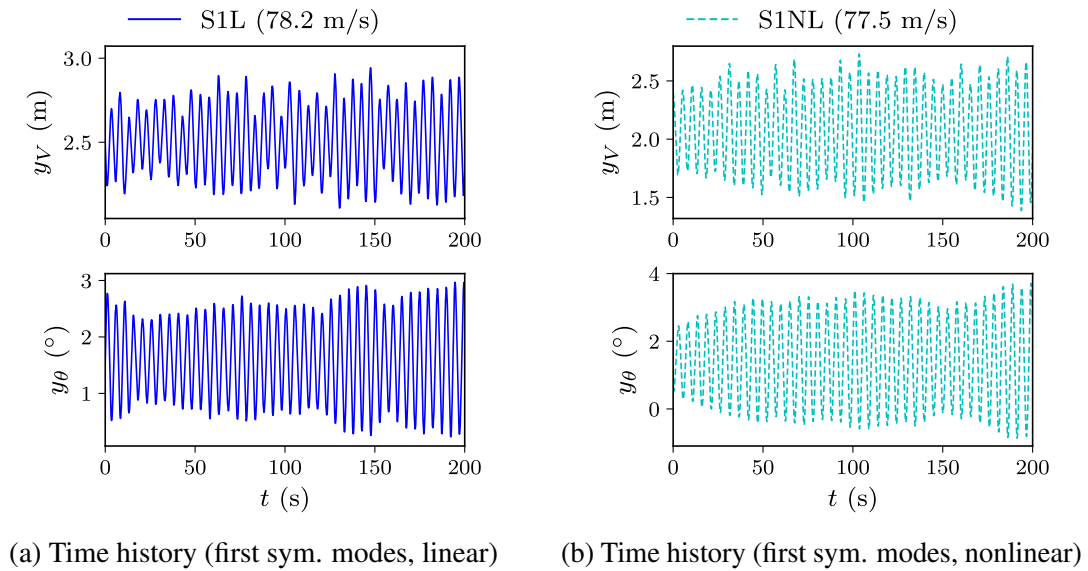
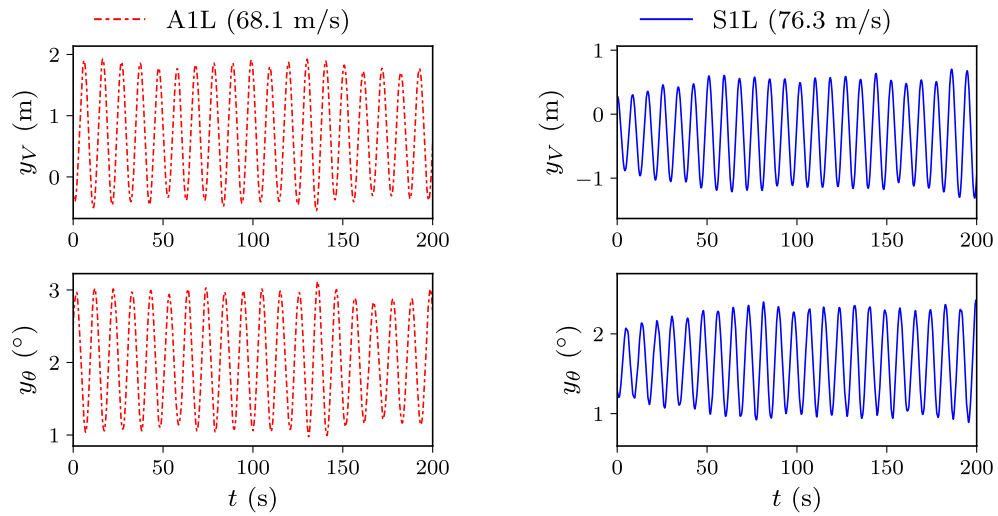
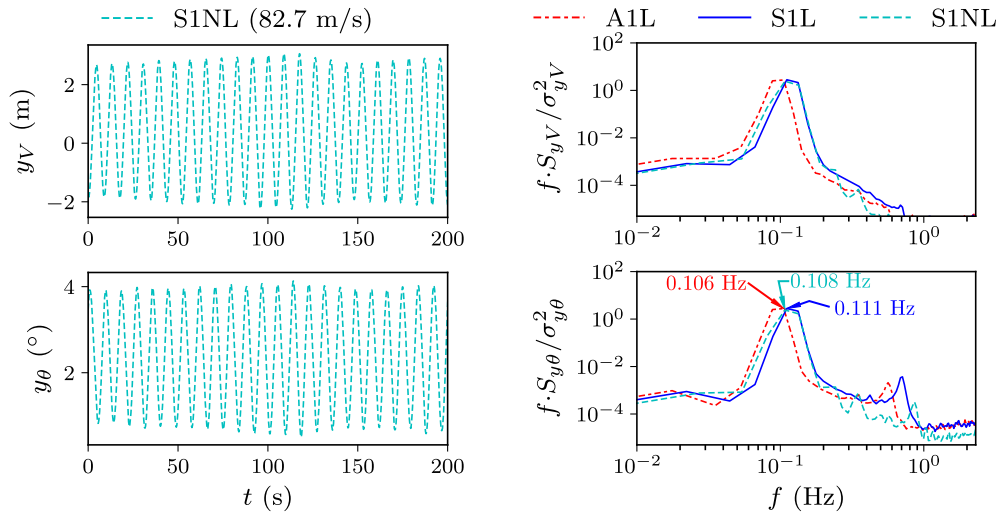


Figure 6.17: Flutter dynamic response of bridge SU2 for a smooth flow

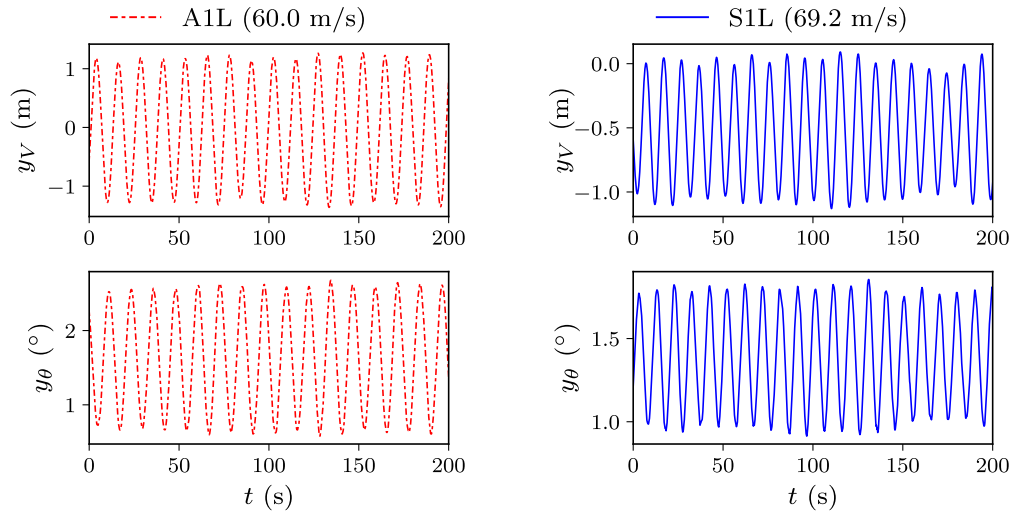


(a) Time history (first antisym. modes, linear) (b) Time history (first sym. modes, linear)

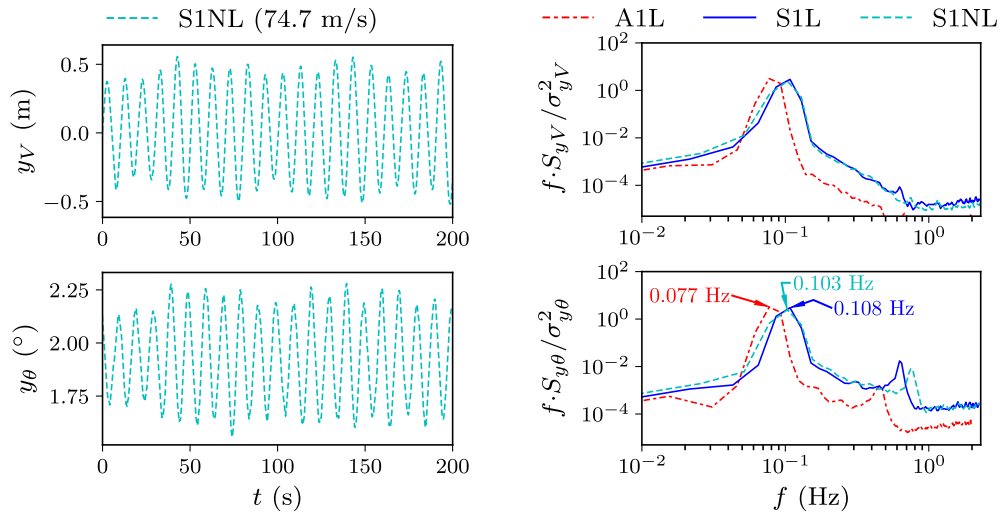


(c) Time history (first sym. modes, nonlinear) (d) Power spectral density

Figure 6.18: Flutter dynamic response of bridge SU4c for a smooth flow



(a) Time history (first antisym. modes, linear) (b) Time history (first sym. modes, linear)



(c) Time history (first sym. modes, nonlinear) (d) Power spectral density

Figure 6.19: Flutter dynamic response of bridge SU4d for a smooth flow

6.6 Discussion

6.6.1 Static Aerodynamic Coefficients of Bridge Section Models

In the case of the single-box girder of bridge SU2, the measurements of the static coefficients were made at the *Université de Sherbrooke* and at the BLWTL in order to confirm that the section model was not damaged during its storage and transportation between the *Université de Sherbrooke* and the BLWTL. As discussed in appendix C, a good agreement was obtained between the static coefficients measured at the different wind tunnels, confirming that the section model for bridge SU2 was not altered during its transportation.

From the analysis of fig. 6.6, it is of interest to notice that there is a change of slope for the moment coefficient of the section model used for bridges SU4c and SU4c. This occurs at an angle of attack just over 4° . In comparison, the moment coefficient for bridge SU2 is practically linear over the range of angles of attack tested. To a lesser extent, the lift coefficient for bridges SU4c and SU4d also shows a change of slope at an angle of attack around 4° , whereas the lift coefficient is still linear for bridge SU2. The change of slope observed for the twin-box girder model of bridges SU4c and SU4d is likely attributed to the fact that the airflow passes through the gap in the middle of the bridge deck when the angle of attack is greater than 4° . This could be confirmed using CFD, but this was deemed out of the scope of this research on structural nonlinearities. For the drag coefficient, the minimum values for both section models are obtained for angles of attack close to 0° as it is typically the case.

6.6.2 Validity of the New Section Model Test Rig

As discussed in section 6.4.3, the first step of the validation procedure of the new bridge rig consisted in measuring the flutter derivatives for bridge SU2. Figure 6.7 shows that there is a good agreement between the flutter derivatives obtained with the different experimental rigs. Regarding the dynamic responses of bridge SU2 measured with the three different section model test rigs, there is an excellent agreement between the old and new bridge rigs of the BLWTL as shown in fig. 6.8. The peak displacements obtained at the *Université de Sherbrooke* are less than those for the two BLWTL rigs since higher damping ratios of around 0.9 % were utilized due to experimental limitations. Nevertheless, from this analysis of the flutter derivatives and dynamic responses for bridge SU2, it is possible to confirm the adequacy of the new section model test rig. A detailed presentation of the results and discussions about this analysis can be found in appendix C.

6.6.3 Process of Conducting Nonlinear Section Model Tests

It was found that it is easier to first perform the linear section model tests before the nonlinear tests. Doing so facilitates the calibration of the mass and mass moment of inertia since the added mass technique can be utilized for the linear tests. After conducting the linear tests, the springs are arranged according to the nonlinear configurations illustrated in fig. 6.4, and the ballast masses used to adjust the mass properties are kept the same as for in the linear tests. Nonetheless, the mass and mass moment of inertia are checked again for the nonlinear test configurations. In this case, the mass properties are calculated using the natural frequencies and tangent stiffnesses of the nonlinear system as explained in section 6.4.5. It was found that the mass properties for the nonlinear tests were practically the same as those for the linear tests.

As for the linear tests, the experimental natural frequencies and damping ratios were also measured. In addition to that, the nonlinear behavior in stiffness was measured by applying known forces and moments to the section model (see sections 6.4.5 and 6.5.3). This was found to be a lengthy procedure due to the numerous force-moment combinations required to obtain the graphs that are shown in fig. 6.10. According to fig. 6.10, it is possible to say that the experimental nonlinear behavior in stiffness matches quite well the target numerical nonlinear behavior. This is demonstrated by the small values for the standard error $\sigma_{V\theta}$ that is around 1 N to 2 N. In fig. 6.10a, there are more noticeable differences in the case of the vertical force of bridge SU2 for large displacements. Nevertheless, the average values for the errors $|\Delta f_{Vm}^*|$ and $|\Delta f_{\theta m}^*|$ for bridge SU2 are 2.48 N and 0.15 Nm, which are small values with respect to the forces and moments in fig. 6.10. The average errors for bridges SU4c and SU4d are even smaller. For bridge SU4c, the average errors are 1.28 N and 0.10 Nm, whereas average errors of 1.08 N and 0.07 Nm are obtained for bridge SU4d. From this analysis, it is concluded that the inclined spring configurations utilized for the nonlinear section model tests represent in a satisfactory manner the target nonlinear stiffness behavior.

6.6.4 Linear Dynamic Tests vs Nonlinear Dynamic Tests

When looking at the results of the dynamic responses for bridge SU2 in figs. 6.11 and 6.12, it is possible to see that the critical velocity for flutter is only slightly impacted by the nonlinear structural behavior. According to table 6.3, the nonlinear behavior reduces the flutter wind speed by 4.2 % and 1.7 % for a smooth flow and a turbulent flow. This is explained by the fact that bridge SU2 was found to be the least nonlinear of the three bridges used in this research (according to fig. 6.10 and nonlinear generalized stiffness analysis results presented

in appendix B). Even though the flutter wind speed was not significantly impacted by the nonlinear structural behavior for bridge SU2, it is possible to see that the evolution of the flutter peak displacements in the case of a smooth flow is more gradual for the nonlinear behavior compared to the linear behavior (see figs. 6.8 and 6.11). For a linear behavior, the displacements become suddenly very large (see fig. 6.8). It is interesting to note that the gradual evolution of the peak displacements for wind speeds in the vicinity of flutter was not observed for a turbulent flow as shown in fig. 6.12. According to table 6.3, it appears that turbulence does not have a significant influence on the critical velocity for flutter in the case of bridge SU2. Regarding the mean displacements, slightly smaller vertical displacements are observed for the nonlinear tests of bridge SU2.

For bridges SU4c and SU4d for smooth flow conditions, figs. 6.13 and 6.15 show that the nonlinear structural behavior increases the flutter critical velocity by 7.6 % and 8.2 % based on table 6.3. It appears that the greater nonlinear structural behaviors for bridges SU4c and SU4d lead to a more significant impact on the flutter wind speeds compared to bridge SU2. In fig. 6.13, it is also interesting to note that, once flutter is reached, the peak displacements stabilize over a small range of wind speeds until the bridge becomes stable again. It is believed that this is related to the change of slope observed for the moment coefficient in fig. 6.6 in the case of the twin-box girder deck for bridges SU4c and SU4d. For the first symmetric modal pair, the nonlinear structural behavior delays the onset of flutter in comparison to the linear case, which allow the bridge model to have a greater mean rotation close to 3° as shown in fig. 6.13a. Including the dynamic response, this means that the rotation of the model can reach more than 5° . This is within the range of angles for which a nonlinear evolution of the moment coefficient is observed in fig. 6.6. The nonlinear variation of C_M leads to the peculiar instability shown in fig. 6.13 since the flutter derivatives A_3^* , which is important for coupled flutter, is related to the slope of C_M according to quasi-steady theory. Therefore, it seems that there is a combined effect of structural nonlinearities and aerodynamic nonlinearities that caused the instability of fig. 6.13. As shown in fig. 6.15, this peculiar instability was not observed for bridge SU4d. It is believed that the mean rotation was not sufficient to trigger it as the flutter occurred for a lower wind speed in the case of bridge SU4d compared to bridge SU4c. Also, figs. 6.14 and 6.16 show that the combined effect of structural nonlinearities and turbulence is sufficient to prevent flutter over the range of wind speeds achievable in the wind tunnel with the new bridge rig. This is surprising considering that an instability was experienced for a linear behavior and a turbulent flow. For this reason, the nonlinear results for a turbulent flow were remeasured in order to confirm them.

When looking at the time histories of the flutter responses for the first symmetric modes in figs. 6.17–6.19, it is not possible to see noticeable differences between the linear or nonlinear responses. The same applies to the PSDs of the flutter responses presented in figs. 6.17c, 6.18d and 6.19d since the linear and nonlinear results for the first symmetric modes show similar trends. More specifically, the PSD peaks around 0.2 Hz for bridge SU2 and around 0.1 Hz for bridge SU4c and SU4d, associated with coupled flutter, are practically the same for the linear and nonlinear cases for the first symmetric modes. Figures 6.17c, 6.18d and 6.19d also show other peaks close to 1 Hz. These peaks are attributed to vibrations of the section model, but they do not detract from the conclusion regarding the PSD peaks corresponding to flutter.

For bridges SU4c and SU4d, linear dynamic section model tests were also conducted for the first antisymmetric modes as shown in figs. 6.13–6.16 and table 6.3. In general, the flutter wind speeds for the first antisymmetric modes are less than those obtained in the dynamic tests for the first symmetric modes, either linear or nonlinear. However, it seems that antisymmetric flutter is delayed by a turbulent flow when comparing fig. 6.13 and fig. 6.14. In fig. 6.14, it appears that the antisymmetric and symmetric instabilities occur for the same wind speed, which is of 77.1 m/s according to table 6.3. Regarding the flutter response PSD of bridge SU4c for a smooth flow presented in fig. 6.18, it is possible to notice that the frequency of the antisymmetric instability is very close to the one for the symmetric instability. For bridge SU4d, there is a more significant difference between the flutter frequencies for the first antisymmetric and symmetric modes, with the antisymmetric case having the lowest frequency (see fig. 6.19).

From the analysis of the results of this initial experimental investigation of the effect of structural nonlinearities on the aeroelastic stability of cable-supported bridges, it appears that a nonlinear stiffness behavior mostly have an effect on the critical flutter wind speed since nonlinear dynamic phenomena of structural origins were not observed. Further research would be required in order to understand why the flutter wind speed can be impacted by a nonlinear structural behavior. It will be worth studying whether this could be caused by a slight variation of the natural frequencies because of the varying stiffness or by a combination of nonlinear structural effects and nonlinear aerodynamic effects. Therefore, it is recommended to conduct more nonlinear section model tests for this purpose. It would also be of interest to perform wind tunnel tests in the case of other structural systems. Since simple suspension bridges, often used as pedestrian bridges, are nonlinear structures [42, 43], it would be relevant to include this structural system in future experimental work. Double-main-span suspension bridges would be of interest as well. Additionally, it would

be interesting to compare experimental results of nonlinear section model tests to numerical simulations. In future research efforts, it would be interesting to see whether the symmetric instability could be triggered for a wind speed lesser than the critical wind speed for the antisymmetric instability.

6.7 Conclusions

Cable-supported bridges are intrinsically geometrically nonlinear due to the cable systems utilized in these structures. Since the cable systems contribute more to the total stiffness of longer bridges, this intrinsic nonlinear behavior could be of importance for the dynamic behavior of long cable-supported bridges. This could especially be the case with regard to the dynamic response of bridges subjected to wind actions like flutter. This is why this chapter aimed at studying the effect of structural nonlinearities on the aeroelastic stability of cable-supported bridges. More specifically, an innovative wind tunnel test approach for bridges based on section model tests able to account for the nonlinear structural behavior was utilized to see whether a nonlinear structural behavior can impact the stability of bridges. The focus of this study was on geometric nonlinearities, which are of concern for cable-supported bridges.

The theory for nonlinear section model tests was first reviewed, which was followed by the presentation of the experimental apparatus used for nonlinear section model tests. This section model test rig is able to model the nonlinear structural behavior of cable-supported bridges by suspending the bridge section model to a springing system comprised of inclined springs. Wind tunnel tests using this nonlinear section model test rig were conducted at the Boundary Layer Wind Tunnel Laboratory of the University of Western Ontario. At first, this bridge rig for nonlinear tests was validated by comparing linear dynamic test results for the old bridge rig and this new bridge rig using the single-box girder bridge model of a three-span suspension bridge. Using the new bridge rig, section model tests for a linear structural behavior were also conducted for two supplemental configurations, which are for a twin-box girder model considered for single-span suspension bridges with main spans of 2400 m and 3000 m. For these three bridge configurations, nonlinear section model tests were then conducted using inclined spring configurations.

The reliability of the new section model test rig for dynamic tests was validated since the flutter derivatives and linear dynamic responses measured with it compared well to those obtained using the old rig of the Boundary Layer Wind Tunnel Laboratory. Using the new bridge rig in the case of inclined spring configurations proved the possibility of conducting

nonlinear section model tests in the case of cable-supported bridges. It was demonstrated that the nonlinear structural behavior can have an influence on the critical wind speed for flutter, especially in the case of the twin-box girder bridge model of the two single-span suspension bridge configurations. This was in the case of an instability for the first symmetric modes. However, the nonlinear structural behavior did not have a significant effect on the wind dynamic response of a three-span suspension bridge, for which the bridge deck is a single-box girder, from the fact that this structural system is less nonlinear. Even though it would be of interest to conduct more nonlinear section model tests for different structural systems and bridge-deck cross sections, it is possible to recognize the fact that this work has made available to researchers and engineers an additional experimental tool to understand the effect of structural nonlinearities on the aeroelastic behavior of bridges. Future research should especially focus on whether the symmetric instability could be triggered for a wind speed lesser than the critical wind speed for the antisymmetric instability.

Chapter 7

Conclusion

7.1 Summary

From the fact that cable-supported bridges are getting longer, structural nonlinearities could play a more important role on the behavior of these bridges due to the greater contribution of the cable system to the stiffness of these bridges. The observations made by mathematicians regarding large oscillations in suspension bridges due to nonlinear structural dynamic phenomena also point in this direction. Therefore, it appears of interest to assess whether the nonlinear structural behavior could have an influence on the stability of cable-supported bridges when subjected to the effects of wind. For example, the critical wind speed for flutter could be influenced by such nonlinear structural behavior, and it is not impossible that structural nonlinearities could trigger nonlinear structural dynamic phenomena that have never been observed in bridges. This is why this doctoral research project aimed at assessing the effect of structural nonlinearities on flutter instability of long cable-supported bridges.

To answer this research problem, four separate objectives had to be met. The first objective was to provide an evaluation of structural nonlinearities in cable-supported bridges. The focus of this analysis was on geometric nonlinearities, which are of concern in cable-supported bridges because of their cable systems. This assessment especially focused on nonlinear structural vertical-torsional coupling in cable-supported bridges. Analyses were performed using a simplified practical approach relying on nonlinear pushover analysis. More specifically, modal loads were applied to geometrically nonlinear finite element models of cable-supported bridges. By doing so, nonlinear generalized stiffness parameters were determined for equivalent systems, which have from one to three degrees of freedom (lateral, vertical and torsional). They provide a comparison basis for identifying bridges that are more nonlinear, and thus more likely to have their flutter response impacted by nonlinear structural behavior.

Since it is difficult to analytically model the aerodynamic forces on bridges for large amplitudes of vibration, it was decided to utilize an experimental approach for the assessment of the effect of structural nonlinearities on flutter. Consequently, the second objective of this research was to make the theoretical developments required to account for structural nonlinearities when conducting wind tunnel tests of bridges, more specifically section model

tests. It was demonstrated that a two-mode nonlinear generalized stiffness behavior, obtained using nonlinear generalized stiffness analysis for a vertical mode and a torsional mode, can be considered to develop nonlinear section model tests for bridges. By comparing the full-bridge dynamic equations to the section-model equations, it was possible to develop a scaling procedure for the nonlinear generalized stiffness behavior to be considered for the vertical and torsional stiffnesses in nonlinear section model tests. This scaling procedure requires the use of mode correction factors and scaling factors. The assumptions made in the theory for nonlinear tests were validated, and the proposed scaling procedure to obtain the nonlinear structural behavior to be considered in nonlinear section model tests was also tested.

It was then found that a new experimental test rig was needed in order to conduct nonlinear section model tests for bridges. Therefore, it was required to develop a design for an experimental wind tunnel apparatus for section model tests of bridges able to represent the nonlinear structural behavior of a cable-supported bridge. This was also the third objective of this research project. First, the idea of using a nonlinear springing system composed of inclined springs was discussed. This was followed by the presentation of a numerical method to calibrate the nonlinear springing system so that its behavior matches the target behavior based on nonlinear generalized stiffness analysis. After testing the calibration method for different bridges, the design of a new section model test rig for bridges able of nonlinear tests was presented. With an easy adjustment of the attachment points of the inclined springs, this design of a new bridge test rig offers the flexibility required for a nonlinear springing system.

Following the fabrication of this section model test rig able of nonlinear section model tests, wind tunnel tests were conducted at the Boundary Layer Wind Tunnel Laboratory (BLWTL) of the University of Western Ontario. At first, linear section model tests were conducted for the single-box girder bridge model of a suspension bridge using the existing bridge rig as well as the new bridge rig. This procedure allowed to confirm the validity of the new bridge rig in the case of linear dynamic tests. Then, nonlinear section model tests were conducted at the BLWTL in order to study the effect of structural nonlinearities on the aeroelastic stability of cable-supported bridges, which corresponds to the fourth objective of this project. Supplemental to the test configuration of the single-box girder suspension bridge model, two additional test configurations for a twin-box girder suspension bridge model were utilized for the nonlinear tests. These three test configurations were first considered for linear dynamic section model tests. They were followed by nonlinear tests carried out using a nonlinear springing system with inclined springs. The effect of structural nonlinearities on flutter was

therefore assessed by comparing the results of the linear tests to those of the nonlinear tests.

7.2 Contributions

It is now of interest to summarize the main contributions of this research project, which is done in what follows.

1. The first contribution of this project is a numerical approach to quantify structural geometric nonlinearities in cable-supported bridges. It is a practical approach relying on nonlinear pushover analysis for modal loads that allows the determination of nonlinear generalized stiffnesses for equivalent reduce-order structural systems. Nonlinear generalized stiffness parameters can be utilized to quantify in a practical manner the level of nonlinearity and the nonlinear vertical-torsional coupling in cable-supported bridges.
2. The second contribution of this project is an assessment of structural nonlinearities in suspension bridges and cable-stayed bridges, which relied on nonlinear generalized stiffness analysis. This analysis demonstrated that vertical modes, especially symmetric vertical modes, are more nonlinear than lateral and torsional modes. Additionally, it confirmed nonlinear structural vertical-torsional coupling in cable-supported bridges. The suspension bridge system was also found to be more nonlinear in terms of geometric nonlinearity than the cable-stayed bridge system.
3. The third contribution of this Ph.D. project is a theory for section model tests of cable-supported bridges to account for the nonlinear structural behavior when conducting wind tunnel tests. The theory relies on the nonlinear generalized stiffness behavior of a cable-supported bridge that is modified using mode correction factors and scaling factors. It was demonstrated that the theory for nonlinear section model tests for small displacements is equivalent to the linear theory. This indicates that the nonlinear theory is an extension of the linear theory.
4. The fourth contribution is a demonstration that a springing system consisting of inclined springs can be utilized to represent the nonlinear structural behavior in nonlinear section model tests. To find how to arrange the inclined springs, it was required to utilize a numerical method based on the minimization of the error between the target nonlinear structural behavior and the nonlinear behavior from the inclined springs.

5. The fifth contribution of this research project is the development and fabrication of a new test rig that can be utilized for nonlinear section model tests of bridges. This experimental rig is suitable for a springing system composed of inclined springs.
6. The sixth and last contribution of this project is an experimental assessment of the influence of structural geometric nonlinearities on the aeroelastic stability of long-span bridges. This was done by using nonlinear section model tests. Such nonlinear tests account for a nonlinear structural behavior representative of a cable-supported bridge. The possibility of conducting nonlinear section model tests in the case of cable-supported bridges was therefore proved. These tests demonstrated that geometric nonlinearities can have an influence the critical wind speed for flutter.

7.3 Recommendations for Future Work

This research project provided an initial assessment of the effect of structural nonlinearities on the stability of cable-supported bridges when subjected to wind, and more specifically on flutter. The experimental approach based on nonlinear section model tests utilized in this research is a first step toward a better understanding of the effect of structural nonlinearities on flutter for cable-supported bridges. Consequently, it is interesting to briefly discuss in this section recommendations for further research on structural nonlinearities and flutter in the case of cable-supported bridges.

From the fact that the system modeled in nonlinear section model tests is a simplified representation of the problem, such tests are well suited for understanding the influence of specific effects like a nonlinear stiffness behavior and aerodynamic nonlinearities. With the same logic, numerical analysis could be utilized to simulate nonlinear section model tests. At first, it would be relevant to see whether harmonic vertical forces could lead to nonlinear dynamic phenomena for a 2-DOF dynamic system with a nonlinear behavior representative of a cable-supported bridge. The forcing amplitude and frequency would be parameters of interest to evaluate. Furthermore, 2D flutter analysis for a 2-DOF nonlinear dynamic system should also be conducted using time-domain dynamic analysis. It would be worth assessing the influence of using either linear or nonlinear aerodynamic force models for such time-domain flutter analyses. The effect of turbulence could also be studied. These numerical simulations would be compared to experimental results in order to be validated.

After, getting more insight on structural nonlinearities from 2D dynamic analysis, the next step could be to perform nonlinear dynamic analysis considering geometric nonlinearities

using numerical models of entire cable-supported bridges. Such numerical simulations would be carried out in the time domain for harmonic forces as well as for aerodynamic forces based on linear or nonlinear force models. It would also be relevant to use such numerical simulations to assess the effect of nonlinearities from the structural damping on the aeroelastic behavior of bridges. Additionally, using nonlinear finite element models of cable-supported bridges, it would be pertinent to calculate nonlinear normal modes. This should also provide more insight into the nonlinear dynamic behavior of cable-supported bridges.

In terms of experimental work, it would be recommended to conduct supplemental nonlinear section model tests using section models with bridge-deck cross sections that are different than those utilized in this project. With regard to the nonlinear behavior, it would be relevant to consider different structural systems such as simple suspension bridges and double-main-span suspension bridges. It would be interesting to see whether the effect of structural nonlinearities could be more apparent for some cross sections or structural systems. Additionally, it would be relevant to develop a full-aeroelastic model of a suspension bridge in which only the main span would be considered, i.e., only the main cables, hangers and bridge deck in the main span would be modeled. In such a model, the nonlinear geometric behavior would be represented correctly since the towers are excluded and that only the bending stiffness needs to be scaled for the deck of a suspension bridge. Nonlinear wind tunnel tests conducted using such a scale model would provide a reliable way to validate nonlinear numerical analyses. Finally, it is believed that such research that started with nonlinear section model tests will ensure the safe design of very long cable-supported bridges.

Bibliography

- [1] T. Kawada, *History of the modern suspension bridge: solving the dilemma between economy and stiffness*. Reston, Virginia: ASCE Press, 2010.
- [2] C.-L. Navier, “Rapport et mémoire sur les ponts suspendus: notice sur le pont des Invalides,” tech. rep., Corps royal des ponts et chaussées, Paris, 1830.
- [3] R. Scott, *In the wake of Tacoma: suspension bridges and the quest for aerodynamic stability*. Reston, Virginia: ASCE Press, 2001.
- [4] S. G. Buonopane and D. P. Billington, “Theory and history of suspension bridge design from 1823 to 1940,” *Journal of Structural Engineering*, vol. 119, no. 3, pp. 954–977, 1993.
- [5] D. B. Steinman, *A practical treatise on suspension bridges: their design, construction and erection*. New York: John Wiley & Sons, second ed., 1929.
- [6] L. S. Moisseiff and F. Lienhard, “Suspension bridges under the action of lateral forces,” *Transactions of the American Society of Civil Engineers*, vol. 98, no. 2, pp. 1080–1095, 1933.
- [7] K. Y. Billah and R. H. Scanlan, “Resonance, Tacoma Narrows Bridge failure, and undergraduate physics textbooks,” *American Journal of Physics*, vol. 59, no. 2, pp. 118–124, 1991.
- [8] A. Larsen, “Aerodynamics of the Tacoma Narrows Bridge - 60 years later,” *Structural Engineering International*, vol. 10, no. 4, pp. 243–248, 2000.
- [9] F. Farquharson, “Aerodynamic stability of suspension bridges,” *Journal of the Western Society of Engineers*, vol. 52, no. 3, pp. 141–152, 1947.
- [10] A. Davenport, “Buffeting of suspension bridge by storm winds,” *Journal of the Structural Division*, vol. 88, no. 3, pp. 233–270, 1962.
- [11] R. H. Scanlan and J. J. Tomko, “Airfoil and bridge deck flutter derivatives,” *Journal of the Engineering Mechanics Division*, vol. 97, no. EM6, pp. 1717–1737, 1971.
- [12] N. J. Gimsing, ed., *East Bridge*. Copenhagen, Denmark: A/S Storebæltsforbindelsen, second ed., 2006.
- [13] M. Kitagawa, “Technology of the Akashi Kaikyo Bridge,” *Structural Control and Health Monitoring*, vol. 11, no. 2, pp. 75–90, 2004.
- [14] M. Virlogeux, V. Bui, J. Jacob, H. Abel-Michel, J.-C. Foucriat, Y. Maury, T. Guyot, J. Lawnicki, L. Paulik, and A. Chauvin, “Design of the Normandie Bridge,” in *Pont Suspendus et à Haubans - Cable-Stayed and Suspension Bridges*, vol. 1, (Deauville), pp. 605–630, Association française pour la construction, 1994.

- [15] A. Pipinato, “Case study: the Russky Bridge,” in *Innovative Bridge Design Handbook (Second Edition)* (A. Pipinato, ed.), pp. 797–806, Kidlington, Oxford: Butterworth-Heinemann, 2022.
- [16] E. Arıoğlu, “Importance of “heuristics” in suspension bridge engineering and 1915 Çanakkale Bridge,” in *Developments in International Bridge Engineering: Selected Papers from Istanbul Bridge Conference 2018* (P. Gülkan, A. Caner, and N. Memisoglu Apaydin, eds.), Springer Tracts on Transportation and Traffic, pp. 19–41, Cham: Springer International Publishing, 2021.
- [17] F. Brancaloni, G. Diana, E. Faccioli, G. Fiammenghi, I. P. T. Firth, N. J. Gimsing, M. Jamiolkowski, P. Sluszka, G. Solari, G. Valensise, and E. Vullo, *The Messina Strait Bridge: a challenge and a dream*. Leiden, Netherlands: CRC Press/Balkema, 2010.
- [18] V. Boonyapinyo, H. Yamada, and T. Miyata, “Wind-induced nonlinear lateral-torsional buckling of cable-stayed bridges,” *Journal of Structural Engineering*, vol. 120, no. 2, pp. 486–506, 1994.
- [19] J. Cheng, J.-J. Jiang, R.-C. Xiao, and H.-F. Xiang, “Advanced aerostatic stability analysis of cable-stayed bridges using finite-element method,” *Computers & Structures*, vol. 80, no. 13, pp. 1145–1158, 2002.
- [20] J. Cheng, J.-J. Jiang, R.-C. Xiao, and H.-F. Xiang, “Nonlinear aerostatic stability analysis of Jiang Yin suspension bridge,” *Engineering Structures*, vol. 24, no. 6, pp. 773–781, 2002.
- [21] E. Simiu and R. H. Scanlan, *Wind effects on structures: fundamentals and applications to design*. New York: Wiley, third ed., 1996.
- [22] Y.-L. Xu, *Wind effects on cable-supported bridges*. Singapore: John Wiley & Sons, 2013.
- [23] R. Scanlan and A. Sabzevari, “Suspension bridge flutter revisited,” in *ASCE Structural Engineering Conference, May 8-12 1967*, ASCE Structural Engineering Conference – Preprint, p. 35, American Society of Civil Engineers (ASCE), 1967.
- [24] Y. Fujino, “Vibration, control and monitoring of long-span bridges—recent research, developments and practice in Japan,” *Journal of Constructional Steel Research*, vol. 58, no. 1, pp. 71–97, 2002.
- [25] O. H. Ammann, T. von Kármán, and G. B. Woodruff, “The failure of the Tacoma Narrows Bridge,” tech. rep., Federal Works Agency, Pasadena, California, 1941.
- [26] J. A. Jurado, S. Hernandez, F. Nieto, and A. Mosquera, *Bridge aeroelasticity: sensitivity analysis and optimum design*. Southampton, U.K. ; Boston, Mass: Wit Press, 2011.
- [27] G. Bartoli, S. Contri, C. Mannini, and M. Righi, “Toward an improvement in the

- identification of bridge deck flutter derivatives,” *Journal of Engineering Mechanics*, vol. 135, no. 8, pp. 771–785, 2009.
- [28] J. P. C. King, A. G. Davenport, and G. L. Larose, “A study of wind effects for the Storebaelt bridge tender design, Denmark,” Tech. Rep. BLWT-SS31-1991, Faculty of Engineering Science, The University of Western Ontario, London, Ontario, Canada, 1991.
- [29] P. A. Irwin, “Full aeroelastic model tests,” in *Aerodynamics of Large Bridges* (A. Larsen, ed.), (Copenhagen, Denmark), pp. 125–135, Balkema, 1992.
- [30] E. Hjorth-Hansen, “Section model tests,” in *Aerodynamics of Large Bridges* (A. Larsen, ed.), (Copenhagen, Denmark), pp. 95–112, Balkema, 1992.
- [31] A. G. Davenport and J. P. C. King, “The incorporation of dynamic wind loads into the design specifications for long span bridges,” in *Proceedings of ASCE Fall Convention and Structures Congress*, (New Orleans, Louisiana), 1982.
- [32] L. Singh, *Experimental determination of aeroelastic and aerodynamic parameters of long-span bridges*. Ph.D. thesis, Johns Hopkins University, Baltimore, Maryland, USA, 1997.
- [33] S. Prud’homme, F. Legeron, and A. Laneville, “Effect of sway movement and motion axis on flutter and vortex induced vibration in a 3 DOF wind tunnel sectional test,” *Journal of Wind Engineering and Industrial Aerodynamics*, vol. 136, pp. 82–88, 2015.
- [34] G. Diana, S. Bruni, A. Cigada, and E. Zappa, “Complex aerodynamic admittance function role in buffeting response of a bridge deck,” *Journal of Wind Engineering and Industrial Aerodynamics*, vol. 90, no. 12–15, pp. 2057–2072, 2002.
- [35] T. Argentini, D. Rocchi, S. Muggiasca, and A. Zasso, “Cross-sectional distributions versus integrated coefficients of flutter derivatives and aerodynamic admittances identified with surface pressure measurement,” *Journal of Wind Engineering and Industrial Aerodynamics*, vol. 104–106, pp. 152–158, 2012.
- [36] G. Diana, F. Resta, A. Zasso, M. Belloli, and D. Rocchi, “Forced motion and free motion aeroelastic tests on a new concept dynamometric section model of the Messina suspension bridge,” *Journal of Wind Engineering and Industrial Aerodynamics*, vol. 92, no. 6, pp. 441–462, 2004.
- [37] S. Prud’homme, F. Legeron, and A. Laneville, “Transient flutter analysis of bluff bodies,” *Journal of Wind Engineering and Industrial Aerodynamics*, vol. 145, pp. 139–151, 2015.
- [38] S. Maheux, S. Langlois, and F. Légeron, “Study on extraction parameters of flutter derivatives for the development of a time-domain formulation of self-excited forces,” in *Proceedings of the 7th European & African Conference on Wind Engineering*, (Liège, Belgium), 2017.

- [39] S. Maheux, S. Langlois, and F. Légeron, “Flutter analysis using quasi-steady time-domain flutter derivatives,” in *IABSE Reports*, vol. 114, (New York City, USA), pp. 2665–2671, 2019.
- [40] B. Siedziako, O. Øiseth, and A. Rønnquist, “An enhanced forced vibration rig for wind tunnel testing of bridge deck section models in arbitrary motion,” *Journal of Wind Engineering and Industrial Aerodynamics*, vol. 164, pp. 152–163, 2017.
- [41] B. Siedziako, O. Øiseth, and A. Rønnquist, “Wind tunnel testing of bridge deck section models with a new forced vibration rig,” in *Proceedings of the 7th European & African Conference on Wind Engineering*, (Liège, Belgium), 2017.
- [42] R. T. Starossek, S. Kim, and H.-K. Kim, “Section-model wind tunnel test for flexible suspended pedestrian bridges,” in *IABSE Reports*, vol. 114, (New York City, USA), pp. 2031–2037, 2019.
- [43] R. T. Starossek, *Aerodynamic behavior of simple suspension footbridges*. Master’s thesis, Seoul National University, Seoul, South Korea, 2020.
- [44] S. Pospíšil, R. Král, and J. Náprstek, “Multipurpose experimental rig for aeroelastic tests on bridge girders and slender beams,” in *Proceedings of 17th International Conference - Engineering Mechanics 2011* (V. Fuis, ed.), (Svratka, Czech Republic), pp. 483–486, Institute of Thermomechanics, Academy of Sciences of the Czech Republic, 2011.
- [45] R. Král, S. Pospíšil, and J. Náprstek, “Wind tunnel experiments on unstable self-excited vibration of sectional girders,” *Journal of Fluids and Structures*, vol. 44, pp. 235–250, 2014.
- [46] R. Král, S. Pospíšil, and J. Náprstek, “Experimental set-up for advanced aeroelastic tests on sectional models,” *Experimental Techniques*, vol. 40, no. 1, pp. 3–13, 2016.
- [47] F. Xu, J. Yang, Z. Zhang, and M. Zhang, “Investigations on large-amplitude vibrations of rigid models using a novel testing device,” *Journal of Bridge Engineering*, vol. 26, no. 5, p. 06021002, 2021.
- [48] F. Xu, J. Yang, M. Zhang, and H. Yu, “Experimental investigations on post-flutter performance of a bridge deck sectional model using a novel testing device,” *Journal of Wind Engineering and Industrial Aerodynamics*, vol. 217, p. 104752, 2021.
- [49] D. Stengel, K. Thiele, M. Clobes, and M. Mehdiانpour, “Aerodynamic damping of nonlinear movement of conductor cables in wind tunnel tests, numerical simulations and full scale measurements,” *Journal of Wind Engineering and Industrial Aerodynamics*, vol. 169, pp. 47–53, 2017.
- [50] Z. C. Yang and L. C. Zhao, “Analysis of limit cycle flutter of an airfoil in incompressible flow,” *Journal of Sound and Vibration*, vol. 123, no. 1, pp. 1–13, 1988.
- [51] D. M. Tang and E. H. Dowell, “Comparison of theory and experiment for non-linear

- flutter and stall response of a helicopter blade,” *Journal of Sound and Vibration*, vol. 165, no. 2, pp. 251–276, 1993.
- [52] C. C. Marsden and S. J. Price, “The aeroelastic response of a wing section with a structural freeplay nonlinearity: an experimental investigation,” *Journal of Fluids and Structures*, vol. 21, no. 3, pp. 257–276, 2005.
- [53] A. Abdelkefi, R. Vasconcellos, F. D. Marques, and M. R. Hajj, “Modeling and identification of freeplay nonlinearity,” *Journal of Sound and Vibration*, vol. 331, no. 8, pp. 1898–1907, 2012.
- [54] M. Schwartz, S. Manzoor, P. Hémon, and E. de Langre, “By-pass transition to airfoil flutter by transient growth due to gust impulse,” *Journal of Fluids and Structures*, vol. 25, no. 8, pp. 1272–1281, 2009.
- [55] Z. N. Gianikos, B. A. Kirschmeier, A. Gopalarathnam, and M. Bryant, “Limit cycle characterization of an aeroelastic wing in a bluff body wake,” *Journal of Fluids and Structures*, vol. 95, p. 102986, 2020.
- [56] B. Kirschmeier, G. Pash, Z. Gianikos, A. Medina, A. Gopalarathnam, and M. Bryant, “Aeroelastic inverse: estimation of aerodynamic loads during large amplitude limit cycle oscillations,” *Journal of Fluids and Structures*, vol. 98, p. 103131, 2020.
- [57] T. O’Neil and T. W. Strganac, “Aeroelastic response of a rigid wing supported by nonlinear springs,” *Journal of Aircraft*, vol. 35, no. 4, pp. 616–622, 1998.
- [58] J. Venkatramani, V. Nair, R. I. Sujith, S. Gupta, and S. Sarkar, “Multi-fractality in aeroelastic response as a precursor to flutter,” *Journal of Sound and Vibration*, vol. 386, pp. 390–406, 2017.
- [59] A. G. Davenport, J. P. C. King, and G. L. Larose, “Taut strip model tests,” in *Aerodynamics of Large Bridges* (A. Larsen, ed.), (Copenhagen, Denmark), pp. 113–124, Balkema, 1992.
- [60] S. Zhou, X. G. Hua, Z. Q. Chen, and W. Chen, “Experimental investigation of correction factor for VIV amplitude of flexible bridges from an aeroelastic model and its 1:1 section model,” *Engineering Structures*, vol. 141, pp. 263–271, 2017.
- [61] T. Wu, S. Li, and M. Sivaselvan, “Real-time aerodynamics hybrid simulation: a novel wind-tunnel model for flexible bridges,” *Journal of Engineering Mechanics*, vol. 145, no. 9, p. 04019061, 2019.
- [62] O.-S. Kwon, H.-K. Kim, U. Y. Jeong, Y.-C. Hwang, and M. Moni, “Design of experimental apparatus for real-time wind-tunnel hybrid simulation of bridge decks and buildings,” in *Proceedings of Structures Congress 2019*, (Orlando, Florida), pp. 235–245, American Society of Civil Engineers, 2019.
- [63] A. Larsen and J. H. Walther, “Aeroelastic analysis of bridge girder sections based on

- discrete vortex simulations,” *Journal of Wind Engineering and Industrial Aerodynamics*, vol. 67–68, pp. 253–265, 1997.
- [64] B. Kim and S. Yhim, “Buffeting analysis of a cable-stayed bridge using three-dimensional computational fluid dynamics,” *Journal of Bridge Engineering*, vol. 19, no. 11, p. 04014044, 2014.
- [65] R. Scotta, M. Lazzari, E. Stecca, J. Cotela, and R. Rossi, “Numerical wind tunnel for aerodynamic and aeroelastic characterization of bridge deck sections,” *Computers & Structures*, vol. 167, pp. 96–114, 2016.
- [66] I. Kavrakov and G. Morgenthal, “Aeroelastic analyses of bridges using a pseudo-3D vortex method and velocity-based synthetic turbulence generation,” *Engineering Structures*, vol. 176, pp. 825–839, 2018.
- [67] M. Zhang, F. Xu, Z. Zhang, and X. Ying, “Energy budget analysis and engineering modeling of post-flutter limit cycle oscillation of a bridge deck,” *Journal of Wind Engineering and Industrial Aerodynamics*, vol. 188, pp. 410–420, 2019.
- [68] L. A. Sangalli and A. L. Braun, “A fluid-structure interaction model for numerical simulation of bridge flutter using sectional models with active control devices. preliminary results,” *Journal of Sound and Vibration*, vol. 477, p. 115338, 2020.
- [69] T. Theodorson, “General theory of aerodynamic instability and the mechanism of flutter,” Tech. Rep. NACA-TR-496, National Advisory Committee for Aeronautics, Langley, VA, 1934.
- [70] P. P. Sarkar, N. P. Jones, and R. H. Scanlan, “Identification of aeroelastic parameters of flexible bridges,” *Journal of Engineering Mechanics*, vol. 120, no. 8, pp. 1718–1742, 1994.
- [71] Q. Li, “Measuring flutter derivatives for bridge sectional models in water channel,” *Journal of Engineering Mechanics*, vol. 121, no. 1, pp. 90–101, 1995.
- [72] X. Chen and A. Kareem, “Advances in modeling of aerodynamic forces on bridge decks,” *Journal of Engineering Mechanics*, vol. 128, no. 11, pp. 1193–1205, 2002.
- [73] R. H. Scanlan, J.-G. Beliveau, and K. S. Budlong, “Indicial aerodynamic functions for bridge decks,” *Journal of the Engineering Mechanics Division*, vol. 100, no. EM4, pp. 657–672, 1974.
- [74] Y. K. Lin and J. N. Yang, “Multimode bridge response to wind excitations,” *Journal of Engineering Mechanics*, vol. 109, no. 2, pp. 586–603, 1983.
- [75] R. Scanlan, “Role of indicial functions in buffeting analysis of bridges,” *Journal of Structural Engineering*, vol. 110, no. 7, pp. 1433–1446, 1984.
- [76] C. Bucher and Y. Lin, “Stochastic stability of bridges considering coupled modes,” *Journal of Engineering Mechanics*, vol. 114, no. 12, pp. 2055–2071, 1988.

- [77] K. Wilde, Y. Fujino, and J. Masukawa, "Time domain modeling of bridge deck flutter," *Structural Engineering/Earthquake Engineering*, vol. 13, no. 2, pp. 93s–104s, 1996.
- [78] X. Chen, M. Matsumoto, and A. Kareem, "Time domain flutter and buffeting response analysis of bridges," *Journal of Engineering Mechanics*, vol. 126, no. 1, pp. 7–16, 2000.
- [79] Z. Zhang, Z. Chen, Y. Cai, and Y. Ge, "Indicial functions for bridge aeroelastic forces and time-domain flutter analysis," *Journal of Bridge Engineering*, vol. 16, no. 4, pp. 546–557, 2011.
- [80] L. Caracoglia and N. P. Jones, "A methodology for the experimental extraction of indicial functions for streamlined and bluff deck sections," *Journal of Wind Engineering and Industrial Aerodynamics*, vol. 91, no. 5, pp. 609–636, 2003.
- [81] L. Caracoglia and N. Jones, "Time domain vs. frequency domain characterization of aeroelastic forces for bridge deck sections," *Journal of Wind Engineering and Industrial Aerodynamics*, vol. 91, no. 3, pp. 371–402, 2003.
- [82] T. Wu and A. Kareem, "Revisiting convolution scheme in bridge aerodynamics: comparison of step and impulse response functions," *Journal of Engineering Mechanics*, vol. 140, no. 5, p. 04014008, 2014.
- [83] B. Siedziako and O. Øiseth, "Superposition principle in bridge aerodynamics: modelling of self-excited forces for bridge decks in random vibrations," *Engineering Structures*, vol. 179, pp. 52–65, 2019.
- [84] M. Falco, A. Curami, and A. Zasso, "Nonlinear effects in sectional model aeroelastic parameters identification," *Journal of Wind Engineering and Industrial Aerodynamics*, vol. 42, no. 1-3, pp. 1321–1332, 1992.
- [85] G. L. Larose, A. G. Davenport, and J. P. C. King, "On the unsteady aerodynamic forces on a bridge deck in turbulent boundary layer flow," in *Proceedings of the 7th U.S. National Conference on Wind Engineering*, (UCLA, Los Angeles, CA), pp. 373–382, G.C. Hart, 1993.
- [86] M. Noda, H. Utsunomiya, F. Nagao, M. Kanda, and N. Shiraishi, "Effects of oscillation amplitude on aerodynamic derivatives," *Journal of Wind Engineering and Industrial Aerodynamics*, vol. 91, no. 1, pp. 101–111, 2003.
- [87] Z. Chen, X. Yu, G. Yang, and B. Spencer, "Wind-induced self-excited loads on bridges," *Journal of Structural Engineering*, vol. 131, no. 12, pp. 1783–1793, 2005.
- [88] F. Xu, X. Ying, and Z. Zhang, "Effects of exponentially modified sinusoidal oscillation and amplitude on bridge deck flutter derivatives," *Journal of Bridge Engineering*, vol. 21, no. 5, p. 06016001, 2016.
- [89] J. Guo, S. Zheng, J. Zhu, Y. Tang, and C. Hong, "Study on post-flutter state of

- streamlined steel box girder based on 2 DOF coupling flutter theory,” *Wind and Structures, An International Journal*, vol. 25, no. 4, pp. 343–360, 2017.
- [90] B. Wu, X. Chen, Q. Wang, H. Liao, and J. Dong, “Characterization of vibration amplitude of nonlinear bridge flutter from section model test to full bridge estimation,” *Journal of Wind Engineering and Industrial Aerodynamics*, vol. 197, p. 104048, 2020.
- [91] Y. Wu, X. Chen, and Y. Wang, “Identification of linear and nonlinear flutter derivatives of bridge decks by unscented Kalman filter approach from free vibration or stochastic buffeting response,” *Journal of Wind Engineering and Industrial Aerodynamics*, vol. 214, p. 104650, 2021.
- [92] G. Diana, F. Resta, and D. Rocchi, “A new numerical approach to reproduce bridge aerodynamic non-linearities in time domain,” *Journal of Wind Engineering and Industrial Aerodynamics*, vol. 96, no. 10–11, pp. 1871–1884, 2008.
- [93] R. Zhou, Y. Ge, Y. Yang, Y. Du, and L. Zhang, “Wind-induced nonlinear behaviors of twin-box girder bridges with various aerodynamic shapes,” *Nonlinear Dynamics*, vol. 94, no. 2, pp. 1095–1115, 2018.
- [94] R. Zhou, Y. Ge, Y. Yang, Y. Du, S. Liu, and L. Zhang, “Nonlinear behaviors of the flutter occurrences for a twin-box girder bridge with passive countermeasures,” *Journal of Sound and Vibration*, vol. 447, pp. 221–235, 2019.
- [95] W. Li and S. Laima, “Experimental investigations on nonlinear flutter behaviors of a bridge deck with different leading and trailing edges,” *Applied Sciences*, vol. 10, no. 21, p. 7781, 2020.
- [96] H. Skyvulstad, T. Argentini, A. Zasso, and O. Øiseth, “Nonlinear modelling of aerodynamic self-excited forces: an experimental study,” *Journal of Wind Engineering and Industrial Aerodynamics*, vol. 209, p. 104491, 2021.
- [97] M. Zhang, F. Xu, and X. Ying, “Experimental investigations on the nonlinear torsional flutter of a bridge deck,” *Journal of Bridge Engineering*, vol. 22, no. 8, p. 04017048, 2017.
- [98] K. Li, Y. Han, C. S. Cai, P. Hu, and C. Li, “Experimental investigation on post-flutter characteristics of a typical steel-truss suspension bridge deck,” *Journal of Wind Engineering and Industrial Aerodynamics*, vol. 216, p. 104724, 2021.
- [99] B. Wu, Q. Wang, H. Liao, and H. Mei, “Effects of vertical motion on nonlinear flutter of a bridge girder,” *Journal of Bridge Engineering*, vol. 25, no. 11, p. 04020093, 2020.
- [100] B. Wu, Q. Wang, H. Liao, and H. Mei, “Hysteresis response of nonlinear flutter of a truss girder: experimental investigations and theoretical predictions,” *Computers & Structures*, vol. 238, p. 106267, 2020.
- [101] L.-D. Zhu, G.-Z. Gao, and Q. Zhu, “Recent advances, future application and chal-

- lenges in nonlinear flutter theory of long span bridges,” *Journal of Wind Engineering and Industrial Aerodynamics*, vol. 206, p. 104307, 2020.
- [102] G. Gao and L. Zhu, “Nonlinearity of mechanical damping and stiffness of a spring-suspended sectional model system for wind tunnel tests,” *Journal of Sound and Vibration*, vol. 355, pp. 369–391, 2015.
- [103] G. Gao, L. Zhu, W. Han, and J. Li, “Nonlinear post-flutter behavior and self-excited force model of a twin-side-girder bridge deck,” *Journal of Wind Engineering and Industrial Aerodynamics*, vol. 177, pp. 227–241, 2018.
- [104] Y. Tang, X. G. Hua, Z. Q. Chen, and Y. Zhou, “Experimental investigation of flutter characteristics of shallow Π section at post-critical regime,” *Journal of Fluids and Structures*, vol. 88, pp. 275–291, 2019.
- [105] X. Chen and A. Kareem, “Nonlinear response analysis of long-span bridges under turbulent winds,” *Journal of Wind Engineering and Industrial Aerodynamics*, vol. 89, no. 14-15, pp. 1335–1350, 2001.
- [106] X. Chen and A. Kareem, “Aeroelastic analysis of bridges: effects of turbulence and aerodynamic nonlinearities,” *Journal of Engineering Mechanics*, vol. 129, no. 8, pp. 885–895, 2003.
- [107] G. Diana, D. Rocchi, and T. Argentini, “An experimental validation of a band superposition model of the aerodynamic forces acting on multi-box seck sections,” *Journal of Wind Engineering and Industrial Aerodynamics*, vol. 113, pp. 40–58, 2013.
- [108] G. Diana and S. Omarini, “A non-linear method to compute the buffeting response of a bridge validation of the model through wind tunnel tests,” *Journal of Wind Engineering and Industrial Aerodynamics*, vol. 201, p. 104163, 2020.
- [109] N. Barni, O. Øiseth, and C. Mannini, “Time-variant self-excited force model based on 2D rational function approximation,” *Journal of Wind Engineering and Industrial Aerodynamics*, vol. 211, p. 104523, 2021.
- [110] B. Wu, H. Liao, H. Shen, Q. Wang, H. Mei, and Z. Li, “Multimode coupled nonlinear flutter analysis for long-span bridges by considering dependence of flutter derivatives on vibration amplitude,” *Computers & Structures*, vol. 260, p. 106700, 2022.
- [111] Z. Zhang, “Multistage indicial functions and postflutter simulation of long-span bridges,” *Journal of Bridge Engineering*, vol. 23, no. 4, p. 04018010, 2018.
- [112] T. Wu and A. Kareem, “A nonlinear convolution scheme to simulate bridge aerodynamics,” *Computers and Structures*, vol. 128, pp. 259–71, 2013.
- [113] T. Wu and A. Kareem, “A low-dimensional model for nonlinear bluff-body aerodynamics: a peeling-an-onion analogy,” *Journal of Wind Engineering and Industrial Aerodynamics*, vol. 146, pp. 128–138, 2015.

- [114] H. Skyvulstad, Ø. W. Petersen, T. Argentini, A. Zasso, and O. Øiseth, “The use of a Laguerrian expansion basis as Volterra kernels for the efficient modeling of nonlinear self-excited forces on bridge decks,” *Journal of Wind Engineering and Industrial Aerodynamics*, vol. 219, p. 104805, 2021.
- [115] L. Carassale, T. Wu, and A. Kareem, “Nonlinear aerodynamic and aeroelastic analysis of bridges: frequency domain approach,” *Journal of Engineering Mechanics*, vol. 140, no. 8, p. 04014051, 2014.
- [116] G. Diana, D. Rocchi, T. Argentini, and S. Muggiasca, “Aerodynamic instability of a bridge deck section model: linear and nonlinear approach to force modeling,” *Journal of Wind Engineering and Industrial Aerodynamics*, vol. 98, no. 6–7, pp. 363–374, 2010.
- [117] T. Wu and A. Kareem, “Bridge aerodynamics and aeroelasticity: a comparison of modeling schemes,” *Journal of Fluids and Structures*, vol. 43, pp. 347–370, 2013.
- [118] T. Wu and A. Kareem, “Modeling hysteretic nonlinear behavior of bridge aerodynamics via cellular automata nested neural network,” *Journal of Wind Engineering and Industrial Aerodynamics*, vol. 99, no. 4, pp. 378–388, 2011.
- [119] T. Li, T. Wu, and Z. Liu, “Nonlinear unsteady bridge aerodynamics: reduced-order modeling based on deep LSTM networks,” *Journal of Wind Engineering and Industrial Aerodynamics*, vol. 198, p. 104116, 2020.
- [120] R. Zhou, Y. Ge, Y. Yang, S. Liu, Y. Du, and L. Zhang, “A nonlinear numerical scheme to simulate multiple wind effects on twin-box girder suspension bridges,” *Engineering Structures*, vol. 183, pp. 1072–1090, 2019.
- [121] G. Gao, L. Zhu, J. Li, and W. Han, “Application of a new empirical model of nonlinear self-excited force to torsional vortex-induced vibration and nonlinear flutter of bluff bidge sections,” *Journal of Wind Engineering and Industrial Aerodynamics*, vol. 205, p. 104313, 2020.
- [122] G. Gao, L. Zhu, J. Li, W. Han, and B. Yao, “A novel two-degree-of-freedom model of nonlinear self-excited force for coupled flutter instability of bridge decks,” *Journal of Sound and Vibration*, vol. 480, p. 115406, 2020.
- [123] A. Selberg, *Oscillation and aerodynamic stability of suspension bridges*. No. 13 in Civil Engineering and Building Construction Series, Trondheim, Norway: Knut Alming, 1961.
- [124] T. A. C. M. Van der Put, “Rigidity of structures against aerodynamic forces,” *IABSE Publications*, vol. 36, no. I, pp. 189–196, 1976.
- [125] R. H. Scanlan, “State-of-the-art methods for calculating flutter, vortex-induced, and buffeting response of bridge structures,” Technical Report FHWA/RD - 80/050, Federal Highway Administration, Washington, DC, 1981.

- [126] M. Matsumoto, Y. Kobayashi, Y. Niihara, and H. Shirato, "Flutter mechanism and its stabilization of bluff bodies," in *Proceedings of 9th International Conference on Wind Engineering*, (New Delhi, India), pp. 827–838, Wiley Eastern Science, 1995.
- [127] M. Matsumoto, H. Matsumiya, S. Fujiwara, and Y. Ito, "New consideration on flutter properties based on step-by-step analysis," *Journal of Wind Engineering and Industrial Aerodynamics*, vol. 98, no. 8–9, pp. 429–437, 2010.
- [128] F. Y. Xu, "System decoupling approach for 3-DOF bridge flutter analysis," *Journal of Structural Engineering*, vol. 141, no. 7, p. 04014168, 2015.
- [129] D. Lau, M. Cheung, and S. Cheng, "3D flutter analysis of bridges by spline finite-strip method," *Journal of Structural Engineering*, vol. 126, no. 10, pp. 1246–1254, 2000.
- [130] S. H. Cheng, D. T. Lau, and M. S. Cheung, "Comparison of numerical techniques for 3D flutter analysis of cable-stayed bridges," *Computers & Structures*, vol. 81, no. 32, pp. 2811–2822, 2003.
- [131] T. J. A. Agar, "Aerodynamic flutter analysis of suspension bridges by a modal technique," *Engineering Structures*, vol. 11, no. 2, pp. 75–82, 1989.
- [132] A. H. Namini, "Analytical modeling of flutter derivatives as finite elements," *Computers & Structures*, vol. 41, no. 5, pp. 1055–1064, 1991.
- [133] N. N. Dung, T. Miyata, H. Yamada, and N. Nguyen Minh, "Flutter responses in long span bridges with wind induced displacement by the mode tracing method," *Journal of Wind Engineering and Industrial Aerodynamics*, vol. 77–78, pp. 367–379, 1998.
- [134] A. Namini and P. Albrecht, "Finite element-based flutter analysis of cable-suspended bridges," *Journal of Structural Engineering*, vol. 118, no. 6, pp. 1509–1526, 1992.
- [135] Q. Ding, A. Chen, and H. Xiang, "A state space method for coupled flutter analysis of long-span bridges," *Structural Engineering and Mechanics, An International Journal*, vol. 14, no. 4, pp. 491–504, 2002.
- [136] Y. J. Ge and H. Tanaka, "Aerodynamic flutter analysis of cable-supported bridges by multi-mode and full-mode approaches," *Journal of Wind Engineering and Industrial Aerodynamics*, vol. 86, no. 2–3, pp. 123–153, 2000.
- [137] X. G. Hua and Z. Q. Chen, "Full-order and multimode flutter analysis using ANSYS," *Finite Elements in Analysis and Design*, vol. 44, no. 9–10, pp. 537–551, 2008.
- [138] C. Borri, C. Costa, and W. Zahlten, "Non-stationary flow forces for the numerical simulation of aeroelastic instability of bridge decks," *Computers & Structures*, vol. 80, no. 12, pp. 1071–1079, 2002.
- [139] X. Zhang, H. Xiang, and B. Sun, "Nonlinear aerostatic and aerodynamic analysis of long-span suspension bridges considering wind-structure interactions," *Journal of Wind Engineering and Industrial Aerodynamics*, vol. 90, no. 9, pp. 1065–1080, 2002.

- [140] X. Zhang, B. Sun, and W. Peng, "Study on flutter characteristics of cable-supported bridges," *Journal of Wind Engineering and Industrial Aerodynamics*, vol. 91, no. 6, pp. 841–854, 2003.
- [141] X.-J. Zhang and B.-N. Sun, "Study of design parameters on flutter stability of cable-stayed bridges," *Wind and Structures, An International Journal*, vol. 6, no. 4, pp. 279–290, 2003.
- [142] L. Salvatori and C. Borri, "Frequency- and time-domain methods for the numerical modeling of full-bridge aeroelasticity," *Computers & Structures*, vol. 85, no. 11–14, pp. 675–687, 2007.
- [143] L. Salvatori and P. Spinelli, "Effects of structural nonlinearity and along-span wind coherence on suspension bridge aerodynamics: some numerical simulation results," *Journal of Wind Engineering and Industrial Aerodynamics*, vol. 94, no. 5, pp. 415–430, 2006.
- [144] P. Chobsilprakob, S. Suthasupradit, and K.-D. Kim, "Aeroelastic analysis of long span bridges via indicial functions considering geometric and material nonlinearity," *International Journal of Steel Structures*, vol. 11, no. 2, pp. 215–226, 2011.
- [145] A. Arena, W. Lacarbonara, D. T. Valentine, and P. Marzocca, "Aeroelastic behavior of long-span suspension bridges under arbitrary wind profiles," *Journal of Fluids and Structures*, vol. 50, pp. 105–119, 2014.
- [146] A. Arena, W. Lacarbonara, and P. Marzocca, "Post-critical behavior of suspension bridges under nonlinear aerodynamic loading," *Journal of Computational and Nonlinear Dynamics*, vol. 11, no. 1, pp. 011005–1 – 011005–11, 2016.
- [147] C. C. Fu and S. Wang, *Computational analysis and design of bridge structures*. Boca Raton: CRC Press, 2014.
- [148] W.-X. Ren, "Ultimate behavior of long-span cable-stayed bridges," *Journal of Bridge Engineering*, vol. 4, no. 1, pp. 30–37, 1999.
- [149] N. J. Gimsing and C. T. Georgakis, *Cable supported bridges: concept and design*. West Sussex, UK: John Wiley & Sons, third ed., 2012.
- [150] R. Walther, B. Houriet, W. Isler, P. Moïa, and J.-F. Klein, *Cable stayed bridges*. London, UK: Thomas Telford Publishing, second ed., 1999.
- [151] N. Hussain, K. Falbe-Hansen, and S. Kite, eds., *Stonecutters Bridge, Hong Kong: design and construction*. Hong Kong: Arup and COWI, 2010.
- [152] P.-H. Wang and C.-G. Yang, "Parametric studies on cable-stayed bridges," *Computers & Structures*, vol. 60, no. 2, pp. 243–260, 1996.
- [153] M. Nagai, Y. Fujino, H. Yamaguchi, and E. Iwasaki, "Feasibility of a 1,400 m span steel cable-stayed bridge," *Journal of Bridge Engineering*, vol. 9, no. 5, pp. 444–452, 2004.

- [154] P. Lonetti and A. Pascuzzo, "A numerical study on the structural integrity of self-anchored cable-stayed suspension bridges," *Fracture and Structural Integrity*, vol. 0, no. 38, pp. 358–376, 2016.
- [155] J. M. W. Brownjohn, "Observations on non-linear dynamic characteristics of suspension bridges," *Earthquake Engineering & Structural Dynamics*, vol. 23, no. 12, pp. 1351–1367, 1994.
- [156] V. Boonyapinyo, Y. Lauhatanon, and P. Lukkunaprasit, "Nonlinear aerostatic stability analysis of suspension bridges," *Engineering Structures*, vol. 28, no. 5, pp. 793–803, 2006.
- [157] W.-X. Ren and M. Obata, "Elastic-plastic seismic behavior of long span cable-stayed bridges," *Journal of Bridge Engineering*, vol. 4, no. 3, pp. 194–203, 1999.
- [158] E. Caetano, A. Cunha, and C. A. Taylor, "Investigation of dynamic cable-deck interaction in a physical model of a cable-stayed bridge. part II: seismic response," *Earthquake Engineering & Structural Dynamics*, vol. 29, no. 4, pp. 499–521, 2000.
- [159] M. H. El Ouni, N. Ben Kahla, and A. Preumont, "Numerical and experimental dynamic analysis and control of a cable stayed bridge under parametric excitation," *Engineering Structures*, vol. 45, no. Supplement C, pp. 244–256, 2012.
- [160] C. Sun, Y. Zhao, J. Peng, H. Kang, and Y. Zhao, "Multiple internal resonances and modal interaction processes of a cable-stayed bridge physical model subjected to an invariant single-excitation," *Engineering Structures*, vol. 172, pp. 938–955, 2018.
- [161] Y. Cong, H. Kang, and T. Guo, "Planar multimodal 1:2:2 internal resonance analysis of cable-stayed bridge," *Mechanical Systems and Signal Processing*, vol. 120, pp. 505–523, 2019.
- [162] X. Su, H. Kang, J. Chen, T. Guo, C. Sun, and Y. Zhao, "Experimental study on in-plane nonlinear vibrations of the cable-stayed bridge," *Nonlinear Dynamics*, vol. 98, no. 2, pp. 1247–1266, 2019.
- [163] Y. Hui, H. J. Kang, S. S. Law, and Z. Q. Chen, "Modeling and nonlinear dynamic analysis of cable-supported bridge with inclined main cables," *Engineering Structures*, vol. 156, pp. 351–362, 2018.
- [164] Y. Hui, H. J. Kang, S. S. Law, and Z. Q. Chen, "Analysis on two types of internal resonance of a suspended sridge structure with inclined main cables based on its sectional model," *European Journal of Mechanics - A/Solids*, vol. 72, pp. 135–147, 2018.
- [165] Y. Hui, H. J. Kang, S. S. Law, and X. G. Hua, "Effect of cut-off order of nonlinear stiffness on the dynamics of a sectional suspension bridge model," *Engineering Structures*, vol. 185, pp. 377–391, 2019.
- [166] P. J. McKenna and C. Ó. Tuama, "Large torsional oscillations in suspension bridges

- visited again: vertical forcing creates torsional response,” *The American Mathematical Monthly*, vol. 108, no. 8, pp. 738–745, 2001.
- [167] K. Moore, “Large torsional oscillations in a suspension bridge: multiple periodic solutions to a nonlinear wave equation,” *SIAM Journal on Mathematical Analysis*, vol. 33, no. 6, pp. 1411–1429, 2002.
- [168] G. Arioli and F. Gazzola, “A new mathematical explanation of what triggered the catastrophic torsional mode of the Tacoma Narrows Bridge,” *Applied Mathematical Modelling*, vol. 39, no. 2, pp. 901–912, 2015.
- [169] G. Arioli and F. Gazzola, “Torsional instability in suspension bridges: the Tacoma Narrows Bridge case,” *Communications in Nonlinear Science and Numerical Simulation*, vol. 42, pp. 342–357, 2017.
- [170] A. Capsoni, R. Ardito, and A. Guerrieri, “Stability of dynamic response of suspension bridges,” *Journal of Sound and Vibration*, vol. 393, pp. 285–307, 2017.
- [171] W. M. Zhang and Y. J. Ge, “Flutter mode transition of a double-main-span suspension bridge in full aeroelastic model testing,” *Journal of Bridge Engineering*, vol. 19, no. 7, p. 06014004, 2014.
- [172] W. M. Zhang and Y. J. Ge, “Nonlinear flutter of a triple-tower suspension bridge via full aeroelastic model wind tunnel tests,” in *Proceedings of the 9th Asia-Pacific Conference on Wind Engineering*, (Auckland, New Zealand), 2017.
- [173] W.-m. Zhang, K.-r. Qian, and Y.-j. Ge, “Research on flutter-mode transition of a triple-tower suspension bridge based on structural nonlinearity,” *Structures*, vol. 34, pp. 787–803, 2021.
- [174] T. Argentini, G. Diana, D. Rocchi, and C. Somaschini, “A case-study of double multi-modal bridge flutter: experimental result and numerical analysis,” *Journal of Wind Engineering and Industrial Aerodynamics*, vol. 151, pp. 25–36, 2016.
- [175] A. H. Nayfeh and D. T. Mook, *Nonlinear oscillations*. New York: John Wiley & Sons, 1979.
- [176] M.-C. Tang, “Super-long span bridges,” *Structure and Infrastructure Engineering*, vol. 13, no. 6, pp. 722–730, 2017.
- [177] G. Diana, M. Falco, S. Bruni, A. Cigada, G. L. Larose, A. Darnsgaard, and A. Collina, “Comparisons between wind tunnel tests on a full aeroelastic model of the proposed bridge over Stretto di Messina and numerical results,” *Journal of Wind Engineering and Industrial Aerodynamics*, vol. 54–55, pp. 101–113, 1995.
- [178] G. Kerschen, M. Peeters, J. C. Golinval, and A. F. Vakakis, “Nonlinear normal modes, part I: a useful framework for the structural dynamicist,” *Mechanical Systems and Signal Processing*, vol. 23, no. 1, pp. 170–194, 2009.

- [179] M. Peeters, R. Vigiú, G. Sérandour, G. Kerschen, and J. C. Golinval, “Nonlinear normal modes, part II: toward a practical computation using numerical continuation techniques,” *Mechanical Systems and Signal Processing*, vol. 23, no. 1, pp. 195–216, 2009.
- [180] Electricité de France, “Finite element *Code_Aster*, analysis of structures and thermo-mechanics for studies and research.” Open source on www.code-aster.org, 1989–2022.
- [181] E. d. S. Caetano, *Cable vibration in cable-stayed bridges*. No. 9 in Structural Engineering Document, Zurich, Switzerland: IABSE, 2007.
- [182] D. J. Ewins, *Modal testing: theory, practice and application*. Baldock, UK: Research Studies Press, second ed., 2000.
- [183] A. Jain, N. Jones, and R. Scanlan, “Coupled flutter and buffeting analysis of long-span bridges,” *Journal of Structural Engineering*, vol. 122, no. 7, pp. 716–725, 1996.
- [184] W.-m. Zhang, K.-r. Qian, L. Wang, and Y.-j. Ge, “Aerostatic instability mode analysis of three-tower suspension bridges via strain energy and dynamic characteristics,” *Wind and Structures, An International Journal*, vol. 29, no. 3, pp. 163–175, 2019.
- [185] H. M. Irvine, *Cable structures*. Cambridge, Massachusetts: MIT Press, 1981.
- [186] X. Chen, A. Kareem, and M. Matsumoto, “Multimode coupled flutter and buffeting analysis of long span bridges,” *Journal of Wind Engineering and Industrial Aerodynamics*, vol. 89, no. 7–8, pp. 649–664, 2001.
- [187] X. Chen and A. Kareem, “Aeroelastic analysis of bridges under multicorrelated winds: integrated state-space approach,” *Journal of Engineering Mechanics*, vol. 127, no. 11, pp. 1124–1134, 2001.
- [188] U. Y. Jeong, J. P. C. King, and N. Isyumov, “A systematic finite element-based buffeting formulation,” in *Proceedings of the 10th Americas Conference on Wind Engineering*, (Baton Rouge, Louisiana), 2005.
- [189] J. M. W. Brownjohn, “Estimation of damping in suspension bridges,” *Proceedings of the Institution of Civil Engineers - Structures and Buildings*, vol. 104, no. 4, pp. 401–415, 1994.
- [190] A. A. Muravyov and S. A. Rizzi, “Determination of nonlinear stiffness with application to random vibration of geometrically nonlinear structures,” *Computers & Structures*, vol. 81, no. 15, pp. 1513–1523, 2003.
- [191] Computer and Structures Inc., “SAP2000 integrated software for structural analysis and design,” 2022.
- [192] A. Jain, N. Jones, and R. Scanlan, “Coupled flutter and buffeting analysis of long-span bridges,” *Journal of Structural Engineering*, vol. 122, no. 7, pp. 716–725, 1996.

- [193] C. Cremona and J.-C. Foucriat, *Comportement au vent des ponts*. Paris: Presses de l'école nationale des ponts et chaussées, 2002.
- [194] H. Katsuchi, N. Jones, and R. Scanlan, "Multimode coupled flutter and buffeting analysis of the Akashi-Kaikyo Bridge," *Journal of Structural Engineering*, vol. 125, no. 1, pp. 60–70, 1999.
- [195] W. M. Zhang, Y. J. Ge, and M. L. Levitan, "Aerodynamic flutter analysis of a new suspension bridge with double main spans," *Wind and Structures, An International Journal*, vol. 14, no. 3, pp. 187–208, 2011.
- [196] H. Tanaka and H. Yamada, "On predicting the performance under wind of full bridges from section model wind tunnel results," *Journal of Wind Engineering and Industrial Aerodynamics*, vol. 26, no. 3, pp. 289–306, 1987.
- [197] Z. Zhang, Y. Ge, and Z. Chen, "Vortex-induced oscillations of bridges: theoretical linkages between sectional model tests and full bridge responses," *Wind and Structures, An International Journal*, vol. 19, no. 3, pp. 233–247, 2014.
- [198] H. Tanaka, "Similitude and modelling in bridge aerodynamics," in *Aerodynamics of Large Bridges* (A. Larsen, ed.), (Copenhagen, Denmark), pp. 83–94, Balkema, 1992.
- [199] C. Mannini and G. Bartoli, "Investigation of the dependence of bridge deck flutter derivatives on steady angle of attack," in *Proceedings of 6th International Colloquium on Bluff Body Aerodynamics and Applications*, (Milano, Italy), 2008.
- [200] G. Diana, S. Stoyanoff, A. Allsop, L. Amerio, T. Argentini, M. Cid Montoya, S. Hernandez, J. Jurado, I. Kavrakov, G. Larose, A. Larsen, G. Morgenthal, s. Omarini, D. Rocchi, and M. Svendsen, "Super-long span bridge aerodynamics: on-going results of the TG3.1 benchmark test – step 1.2," in *IABSE Reports*, (New York City, USA), pp. 2644–2649, 2019.
- [201] G. Deodatis, "Simulation of ergodic multivariate stochastic processes," *Journal of Engineering Mechanics*, vol. 122, no. 8, pp. 778–787, 1996.
- [202] G. Solari and G. Piccardo, "Probabilistic 3-D turbulence modeling for gust buffeting of structures," *Probabilistic Engineering Mechanics*, vol. 16, no. 1, pp. 73–86, 2001.
- [203] R. H. Scanlan, "Problematics in formulation of wind-force models for bridge decks," *Journal of Engineering Mechanics*, vol. 119, no. 7, pp. 1353–1375, 1993.
- [204] B. Cao and P. Sarkar, "Time-domain aeroelastic loads and response of flexible bridges in gusty wind: prediction and experimental validation," *Journal of Engineering Mechanics*, vol. 139, no. 3, pp. 359–366, 2013.
- [205] R. Kiviluoma, "Coupled-mode buffeting and flutter analysis of bridges," *Computers & Structures*, vol. 70, no. 2, pp. 219–228, 1999.
- [206] S. Maheux, *Simulation dynamique du flottement d'un pont élancé à l'aide de coef-*

ficents instationnaires temporels. Master's thesis, Université de Sherbrooke, Sherbrooke, Québec, Canada, 2017.

Appendix A

Finite Element Models of Cable-Supported Bridges

A.1 Modeling and Validation of Finite Element Models

This appendix presents a description of the cable-supported bridges used for this research project as well as the corresponding finite element models. Nine suspension bridges with main spans between 1200 m and 4140 m and two cable-stayed bridges with main spans around 1 km were considered. As mentioned previously, such a wide range in terms of span lengths was used for the suspension bridges in order to identify any potential span length effect. Also, the cable-stayed bridges were included in this research for comparison purposes between the two most common structural systems used for long-span bridges, i.e., the suspension system and cable-stayed system. Detailed information for each of the eleven bridges is presented in sections A.2–A.12. Tables A.1, A.3, A.5, A.7, A.9, A.11, A.13, A.15, A.17, A.19 and A.21 present relevant information about the structural system and geometry of each bridge as well as the number of elements for the numerical models. The finite element models are shown in figs. A.1, A.3, A.5, A.7, A.9, A.11, A.13, A.15, A.17, A.19 and A.21.

It should be mentioned that suspension bridges SU1, SU2 and SU3b and cable-stayed bridges CS1 and CS2 are existing structures or existing detailed designs. Bridges SU3a and SU3c are preliminary bridge designs based on bridge SU3b, but with different span lengths. Compared to bridge SU3b, which has a main span of 3300 m, bridges SU3a (2460 m) and SU3c (4140 m) are respectively 25 % shorter and 25 % longer in terms of span length. For these bridges, the main cables and towers were redesigned considering the new span lengths, but the bridge-deck properties and hanger spacing were kept as in bridge SU3b. The same sag-to-span ratio of 1/10.5 was considered for bridges SU3a, SU3b and SU3c. These bridges provide a reliable way to judge on the span length effect as they originate from the same design concept.

Since it was found that single-span suspension bridges have a stronger nonlinear behavior, it was decided to develop four preliminary designs of single-span suspension bridges, which are bridges SU4a, SU4b, SU4c and SU4d. For this purpose, the design basis of bridge SU3b

was utilized with the exception that only vehicle usage was considered unlike bridge SU3b that has road and rail usages. The different span lengths considered for these bridges are 1200 m, 1800 m, 2400 m and 3000 m. For these four bridges, a sag-to-span ratio of 1/10 was utilized. The bridge deck used for these bridges, which is the same for bridges SU4a, SU4b, SU4c and SU4d, is a twin-box girder unlike the triple-box girder of bridge SU3b. This choice was made because railways are not present. Also, this is to ensure that the bridges are sufficiently stable against flutter since the applicability of a single-box girder would be questionable for the bridge designs with a main span of 1800 m and over [17]. The twin-box deck considered for these bridges was tested at the Boundary Layer Wind Tunnel Laboratory in 2001 for a proposed bridge project. Similar towers to bridge SU3b were used for these preliminary designs, but were resized accordingly. Similarly, the cable system was redesigned. These four single-span suspension bridges also offer a reliable way to assess the span length effect.

A.1.1 Modeling Approach of Suspension Bridges

For the suspension bridges, the fishbone modeling approach was used, i.e., each box girder of the bridge deck was modeled using Timoshenko beam elements connected to the cable system using rigid elements. For the towers, Timoshenko beam elements were also utilized. The main cables and hangers were modeled using tension-only truss elements, and cable preloads were applied using equivalent temperature loads. When active, the hydraulic buffers were represented using nonlinear truss elements having a bilinear material model. The suspension bridge models were analyzed considering geometric nonlinearities through large displacement analysis.

A.1.2 Modeling Approach of Cable-Stayed Bridges

Similar to the suspension bridges, the fishbone modeling approach was used for the cable-stayed bridges, and the bridge deck and towers were modeled with Timoshenko beam elements. Each stay cable was subdivided into 8 to 12 tension-only truss elements. This allows the cable sag effect to be represented adequately [181]. Temperature loads were used for the cable pretensions. Large displacement analysis is also considered for the cable-stayed bridge models.

For the purpose of dynamic analysis including modal analysis, two different modeling approaches were used to model the mass of the stay cables. The cable mass was uniformly distributed along each stay cable in the first approach, which is referred as the distributed cable mass (DCM) approach. In the second approach, half of the mass of each stay cable was

lumped at its ends and is referred as the lumped cable mass (LCM) approach. For the second approach, it is also required to apply the cable self-weight as a uniformly distributed load in order to have the correct geometric stiffness. Since the second approach allows disregarding cable modes and deck-cable modes, this approach is preferred for dynamic analysis over the first approach as it eases analysis. It should be noted that both modeling approaches for the cable mass do not have any incidence for static analysis and yield the same results. This is because in both approaches the self-weight is applied in the same manner and that the mass herein is referred in the context of dynamic analysis which does not influence the static behavior.

A.1.3 Validation Procedure of Finite Element Models

For comparison purposes, finite element models for the eleven cable-supported bridges were developed using two different finite element programs for a total of 22 numerical models. The programs used are *Code_Aster* [180], an open-source finite element software, and the commercial software *SAP2000* [191]. The finite element models for each bridge and each software are presented in figs. A.1, A.3, A.5, A.7, A.9, A.11, A.13, A.15, A.17, A.19 and A.21.


The first step in the validation of the bridge numerical models was to compare static pushover analysis results for the same bridge modeled in *Code_Aster* and *SAP2000*. Four different pushover analysis scenarios were considered. The first one corresponds to the application of a uniformly distributed load that is monotonically increased and applied to the bridge deck in the lateral direction. The second pushover load case is a uniformly distributed torsional moment applied to the deck. A distributed vertical load applied to the deck in the downward direction is the third scenario. The last case is a distributed vertical load applied upwards to the bridge deck. The maximum static loads for each scenario were chosen in order to observe some nonlinear behavior. They are therefore larger than the design loads, but these loads were only used for model validation purposes. The pushover analysis results were obtained considering large displacement analysis. The static pushover analysis results for each bridge are presented in figs. A.2, A.4, A.6, A.8, A.10, A.12, A.14, A.16, A.18, A.20 and A.22. These figures present the midspan deck displacement for an increasing load in the case of inactive hydraulic buffers where applicable. As it can be seen in these figures, the agreement for each bridge between *Code_Aster* and *SAP2000* is excellent. Additionally, it should be mentioned that the agreement between both programs is very good for the case of active buffers, but the results are not shown herein for the sake of brevity.

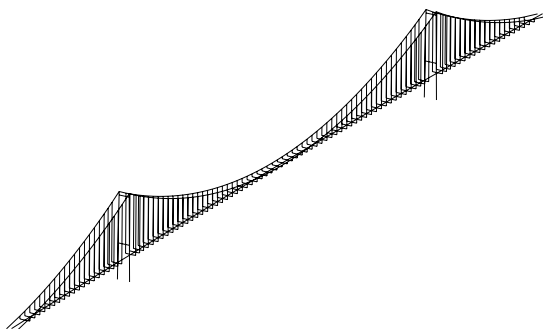
The second validation that was used consisted in comparing the natural frequencies calculated

using *Code_Aster* and *SAP2000* for the dead-load configuration. When applicable, the natural frequencies were also compared to the designer's values, which are not presented herein for confidentiality reasons. The natural frequencies and corresponding mode shapes for each bridge are shown in tables A.2, A.4, A.6, A.8, A.10, A.12, A.14, A.16, A.18, A.20 and A.22. The frequencies and mode shapes are shown up to the second symmetric mode (except for bridges CS1 and CS2), and they correspond to the modes used in this research. For the cable-stayed bridges, the natural frequencies shown below correspond to the LCM modeling approach. In these tables, the natural frequencies for inactive buffers (w/o buffers) and active buffers (w/ buffers) are presented. As for the static pushover analysis, the agreement for the natural frequencies of each bridge between *Code_Aster* and *SAP2000* is excellent. They also compare very well to the designer's values where applicable. Consequently, it is possible to state that the *Code_Aster* bridge numerical models used for this research are reliable.

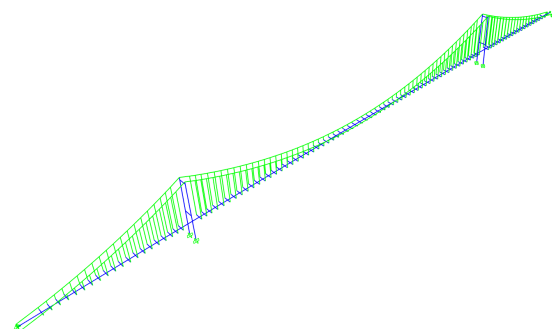
A.2 Suspension Bridge SU1

Table A.1: General information for suspension bridge SU1

Parameter	Value
Type	Three-span suspension bridge
Usage	Road traffic
Bridge deck	Steel single-box girder
Deck supports at towers	Continuous girder with lateral restraints
Longitudinal buffers?	Yes
Towers	Steel towers
Cables	Steel cables
Sag-to-span ratio	1/9
Spans (m)	566 + 1550 + 566
Hanger longitudinal spacing (m)	25.0
Main-cable lateral spacing (m)	30.1
Bridge-deck width (m)	35.93
Bridge-deck cross section	
Number of truss elements	410
Number of beam elements	462



(a) *Code_Aster*



(b) *SAP2000*

Figure A.1: Finite element models of suspension bridge SU1

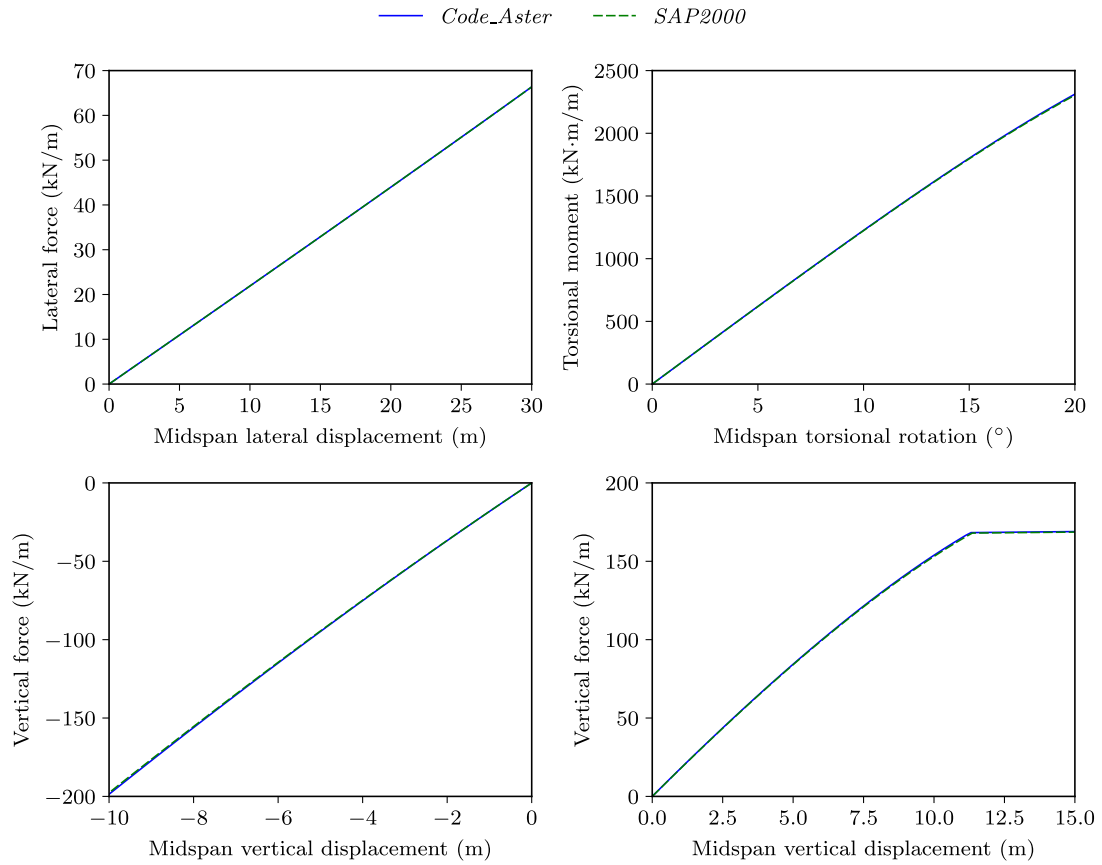
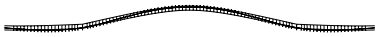





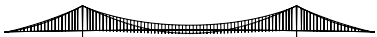




Figure A.2: Pushover analysis for suspension bridge SU1 (w/o buffers)

Table A.2: Natural frequencies and mode shapes for suspension bridge SU1 (L: lateral, V: vertical, θ : torsion, S: symmetric, A: antisymmetric)

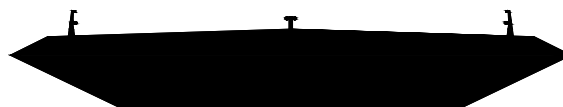
Mode	Frequency (Hz)				Mode shape (top view for L**, elevation view for V** and θ **)
	<i>Code_Aster</i> (w/o buffers)	<i>SAP2000</i> (w/o buffers)	<i>Code_Aster</i> (w/ buffers)	<i>SAP2000</i> (w/ buffers)	
LS1	0.053	0.053	0.053	0.053	
LA1	0.124	0.124	0.124	0.123	
LS2	0.207	0.206	0.207	0.206	
VS1	0.090	0.090	0.090	0.090	
VA1	0.107	0.107	0.095	0.095	
VS2	0.133	0.133	0.133	0.133	
θ S1	0.256	0.256	0.256	0.256	
θ A1	0.274	0.273	0.274	0.273	
θ S2	0.402	0.400	0.402	0.400	

A.3 Suspension Bridge SU2

Table A.3: General information for suspension bridge SU2

Parameter	Value
Type	Three-span suspension bridge
Usage	Road traffic
Bridge deck	Steel single-box girder
Deck supports at towers	Continuous girder with lateral restraints
Longitudinal buffers?	Yes
Towers	Concrete towers
Cables	Steel cables
Sag-to-span ratio	1/9
Spans (m)	536 + 1624 + 536
Hanger longitudinal spacing (m)	24.0
Main-cable lateral spacing (m)	27.0
Bridge-deck width (m)	31.0

Bridge-deck cross section

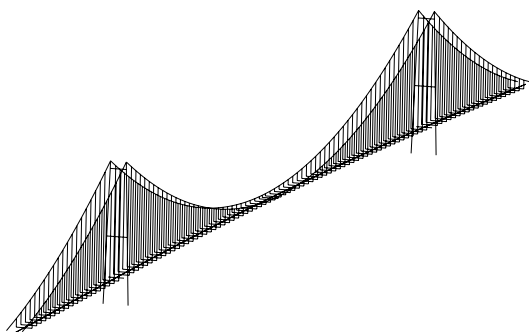


Number of truss elements

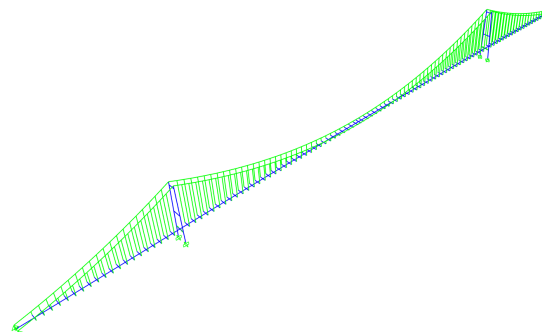
432

Number of beam elements

370



(a) *Code_Aster*



(b) *SAP2000*

Figure A.3: Finite element models of suspension bridge SU2

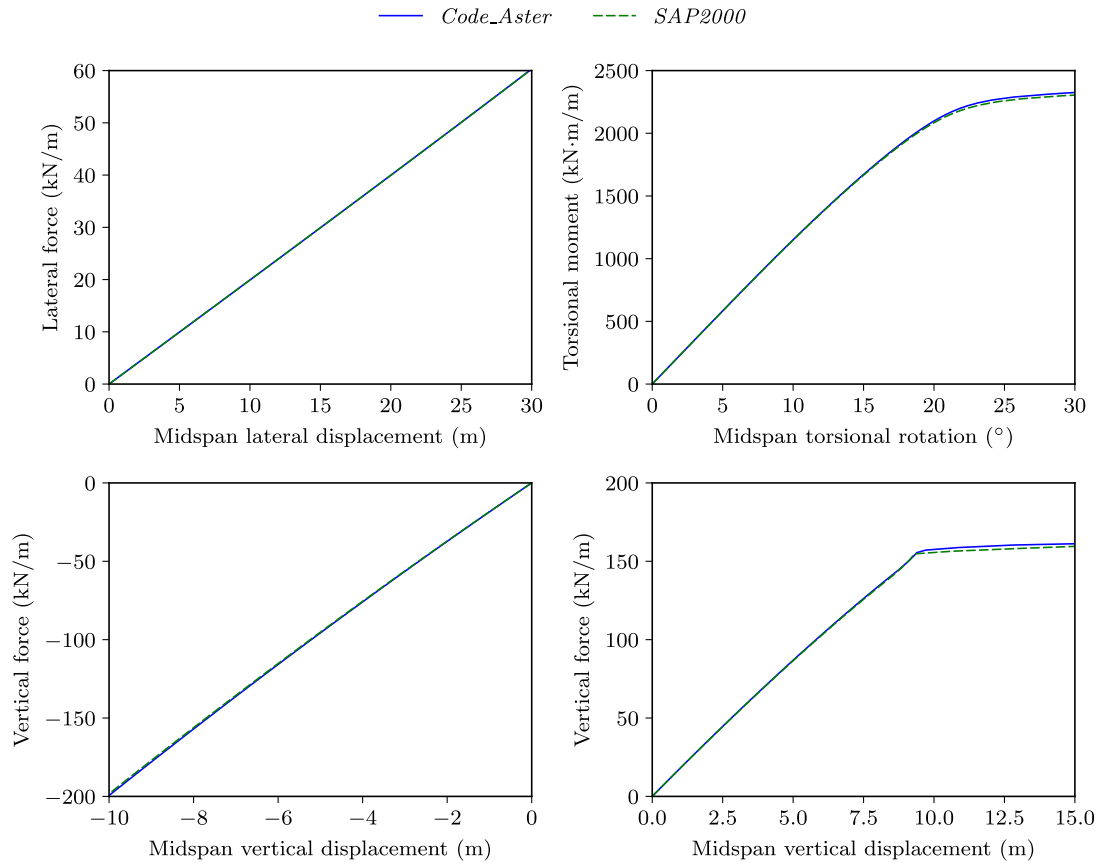











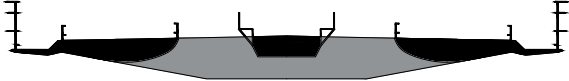
Figure A.4: Pushover analysis for suspension bridge SU2 (w/o buffers)

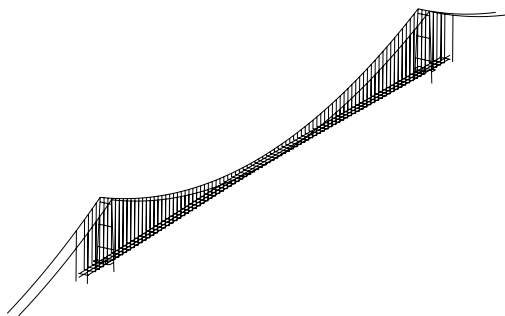
Table A.4: Natural frequencies and mode shapes for suspension bridge SU2 (L: lateral, V: vertical, θ : torsion, S: symmetric, A: antisymmetric)

Mode	Frequency (Hz)				Mode shape (top view for L**, elevation view for V** and θ **)
	<i>Code_Aster</i> (w/o buffers)	<i>SAP2000</i> (w/o buffers)	<i>Code_Aster</i> (w/ buffers)	<i>SAP2000</i> (w/ buffers)	
LS1	0.051	0.051	0.051	0.051	
LA1	0.116	0.116	0.116	0.116	
LS2	0.188	0.187	0.188	0.187	
VS1	0.097	0.097	0.098	0.097	
VA1	0.080	0.080	0.112	0.112	
VS2	0.131	0.131	0.131	0.131	
θ S1	0.279	0.278	0.279	0.278	
θ A1	0.358	0.357	0.358	0.357	
θ S2	0.411	0.409	0.411	0.409	

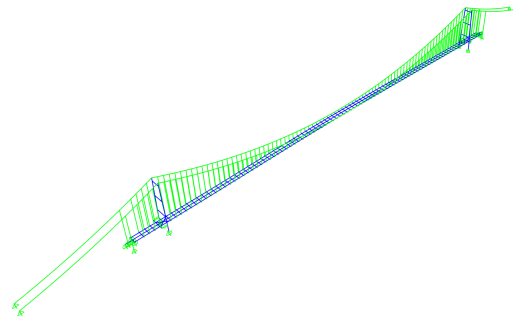
A.4 Suspension Bridge SU3a

Table A.5: General information for suspension bridge SU3a

Parameter	Value
Type	Three-span suspension bridge
Usage	Road traffic, rail traffic
Bridge deck	Steel triple-box girder
Deck supports at towers	Partially continuous girder with lateral restraints
Longitudinal buffers?	Yes
Towers	Steel towers
Cables	Steel cables
Sag-to-span ratio	1/10.5
Spans (m)	183 + 2460 + 183
Hanger longitudinal spacing (m)	30.0
Main-cable lateral spacing (m)	52.0
Bridge-deck width (m)	60.36
Bridge-deck cross section	
Number of truss elements	448
Number of beam elements	1443



(a) *Code_Aster*



(b) *SAP2000*

Figure A.5: Finite element models of suspension bridge SU3a

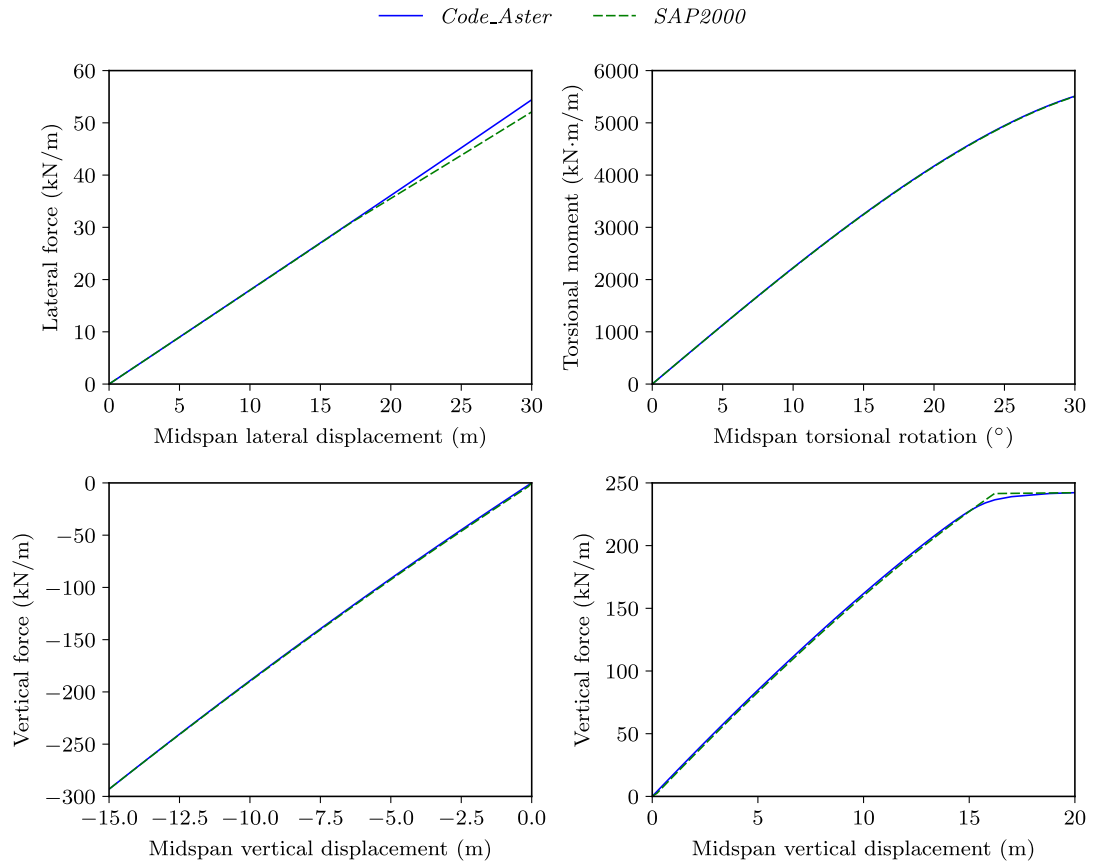











Figure A.6: Pushover analysis for suspension bridge SU3a (w/o buffers)

Table A.6: Natural frequencies and mode shapes for suspension bridge SU3a (L: lateral, V: vertical, θ : torsion, S: symmetric, A: antisymmetric)

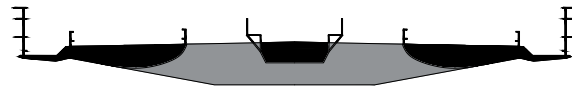
Mode	Frequency (Hz)				Mode shape (top view for L**, elevation view for V** and θ **)
	<i>Code_Aster</i> (w/o buffers)	<i>SAP2000</i> (w/o buffers)	<i>Code_Aster</i> (w/ buffers)	<i>SAP2000</i> (w/ buffers)	
LS1	0.037	0.037	0.037	0.037	
LA1	0.077	0.077	0.078	0.078	
LS2	0.143	0.143	0.143	0.143	
VS1	0.095	0.095	0.095	0.095	
VA1	0.065	0.065	0.076	0.076	
VS2	0.127	0.127	0.127	0.127	
θ S1	0.130	0.130	0.130	0.130	
θ A1	0.105	0.106	0.105	0.106	
θ S2	0.170	0.171	0.170	0.171	

A.5 Suspension Bridge SU3b

Table A.7: General information for suspension bridge SU3b

Parameter	Value
Type	Three-span suspension bridge
Usage	Road traffic, rail traffic
Bridge deck	Steel triple-box girder
Deck supports at towers	Partially continuous girder with lateral restraints
Longitudinal buffers?	Yes
Towers	Steel towers
Cables	Steel cables
Sag-to-span ratio	1/10.5
Spans (m)	183 + 3300 + 183
Hanger longitudinal spacing (m)	30.0
Main-cable lateral spacing (m)	52.0
Bridge-deck width (m)	60.36

Bridge-deck cross section

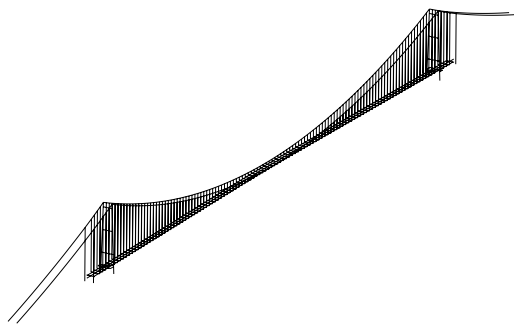


Number of truss elements

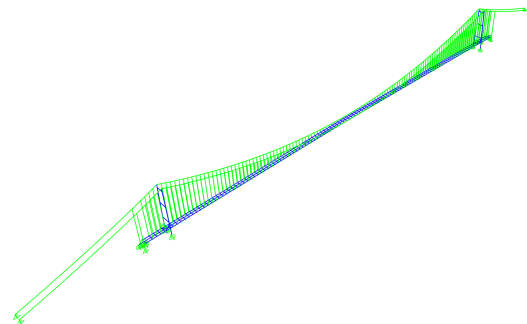
588

Number of beam elements

1835



(a) *Code_Aster*



(b) *SAP2000*

Figure A.7: Finite element models of suspension bridge SU3b

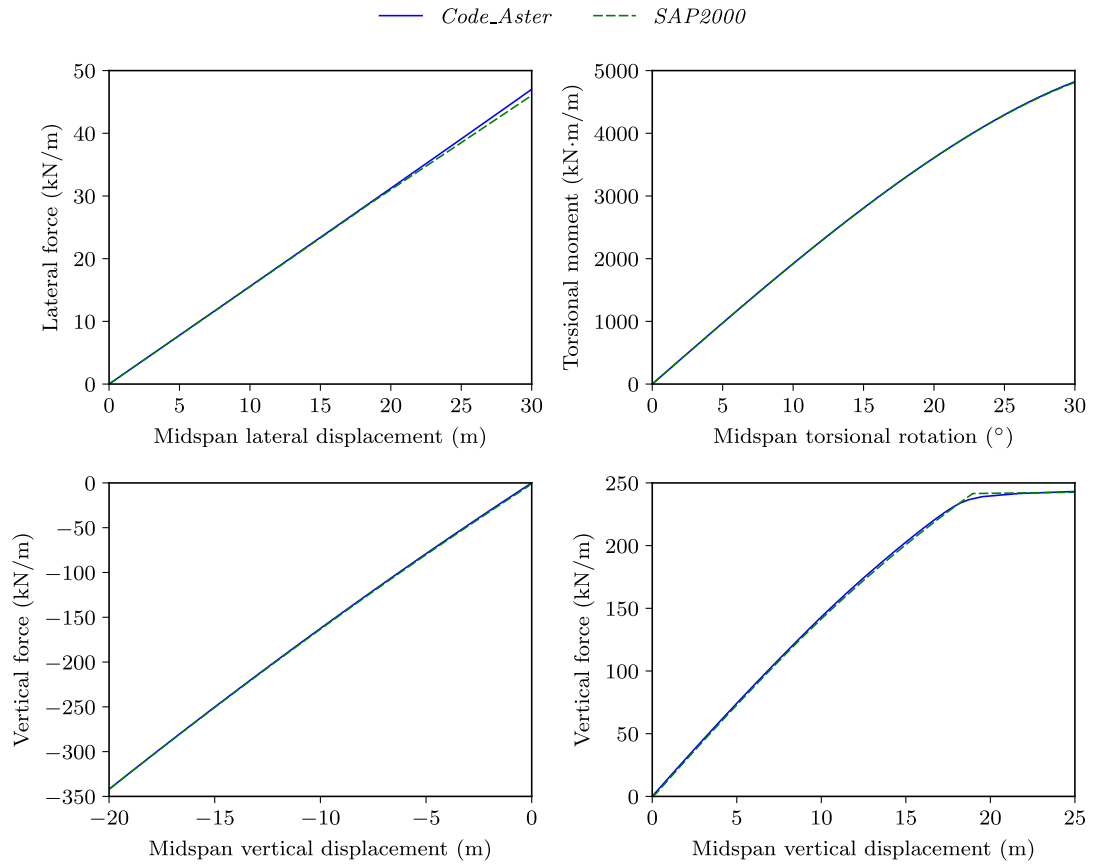











Figure A.8: Pushover analysis for suspension bridge SU3b (w/o buffers)

Table A.8: Natural frequencies and mode shapes for suspension bridge SU3b (L: lateral, V: vertical, θ : torsion, S: symmetric, A: antisymmetric)

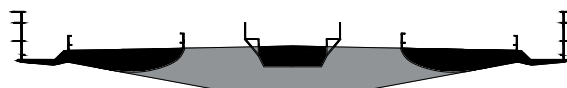
Mode	Frequency (Hz)				Mode shape (top view for L**, elevation view for V** and θ **)
	<i>Code_Aster</i> (w/o buffers)	<i>SAP2000</i> (w/o buffers)	<i>Code_Aster</i> (w/ buffers)	<i>SAP2000</i> (w/ buffers)	
LS1	0.030	0.030	0.030	0.030	
LA1	0.056	0.056	0.057	0.056	
LS2	0.083	0.083	0.084	0.083	
VS1	0.080	0.080	0.080	0.080	
VA1	0.058	0.058	0.065	0.064	
VS2	0.107	0.107	0.107	0.107	
θ S1	0.100	0.101	0.100	0.101	
θ A1	0.081	0.082	0.081	0.082	
θ S2	0.133	0.133	0.133	0.133	

A.6 Suspension Bridge SU3c

Table A.9: General information for suspension bridge SU3c

Parameter	Value
Type	Three-span suspension bridge
Usage	Road traffic, rail traffic
Bridge deck	Steel triple-box girder
Deck supports at towers	Partially continuous girder with lateral restraints
Longitudinal buffers?	Yes
Towers	Steel towers
Cables	Steel cables
Sag-to-span ratio	1/10.5
Spans (m)	183 + 4140 + 183
Hanger longitudinal spacing (m)	30.0
Main-cable lateral spacing (m)	52.0
Bridge-deck width (m)	60.36

Bridge-deck cross section

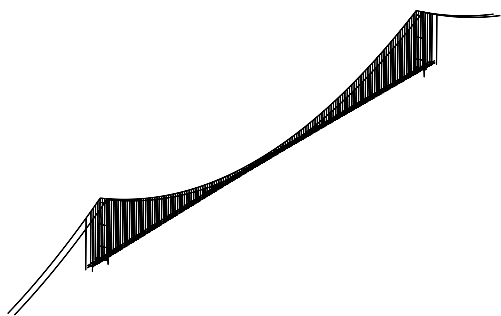


Number of truss elements

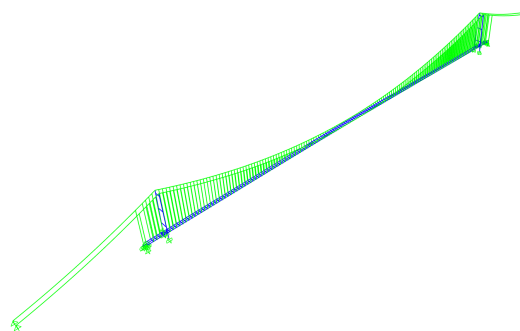
732

Number of beam elements

2227



(a) *Code_Aster*



(b) *SAP2000*

Figure A.9: Finite element models of suspension bridge SU3b

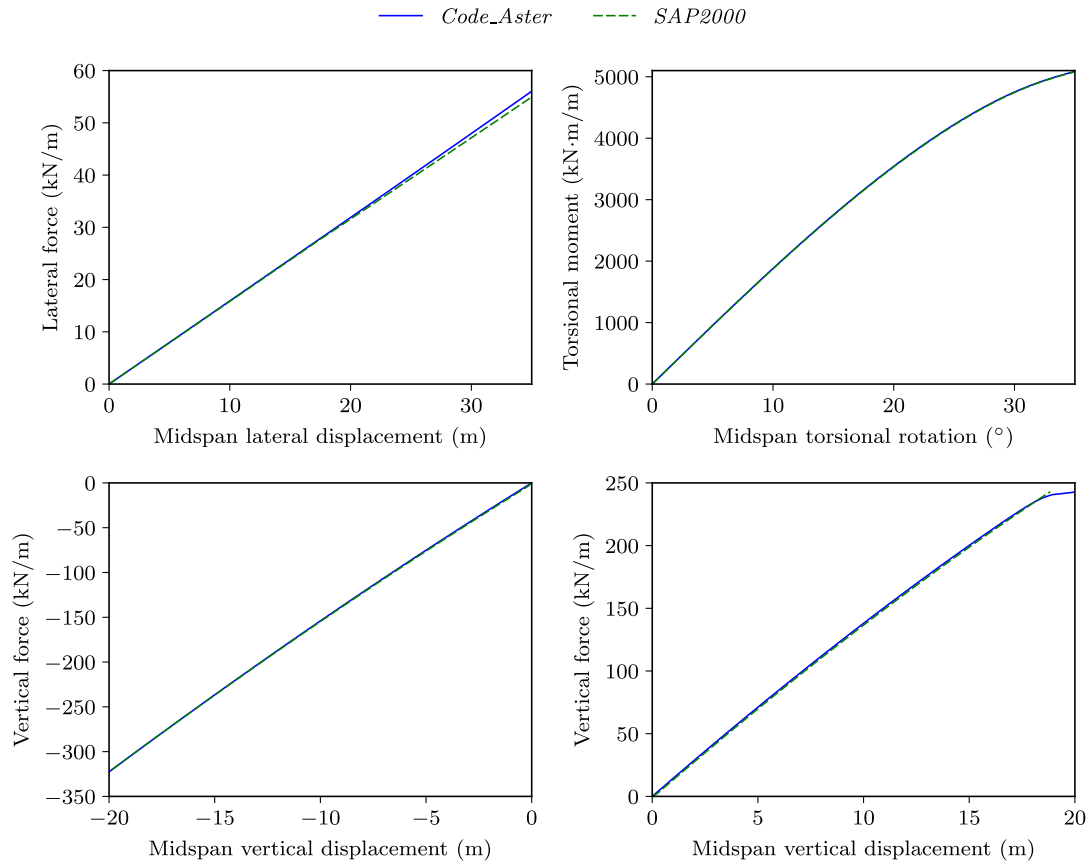












Figure A.10: Pushover analysis for suspension bridge SU3c (w/o buffers)

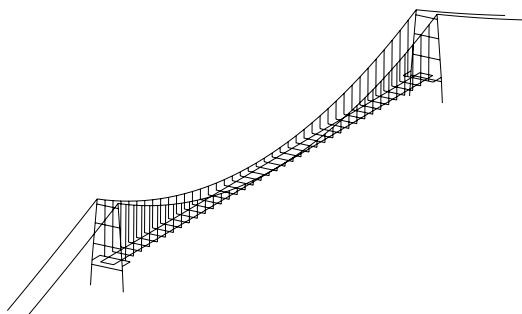
Table A.10: Natural frequencies and mode shapes for suspension bridge SU3c (L: lateral, V: vertical, θ : torsion, S: symmetric, A: antisymmetric)

Mode	Frequency (Hz)				Mode shape (top view for L**, elevation view for V** and θ **)
	<i>Code_Aster</i> (w/o buffers)	<i>SAP2000</i> (w/o buffers)	<i>Code_Aster</i> (w/ buffers)	<i>SAP2000</i> (w/ buffers)	
LS1	0.027	0.027	0.027	0.027	
LA1	0.047	0.047	0.047	0.047	
LS2	0.062	0.062	0.063	0.062	
VS1	0.070	0.070	0.070	0.070	
VA1	0.052	0.052	0.057	0.057	
VS2	0.093	0.093	0.093	0.093	
θ S1	0.083	0.083	0.083	0.083	
θ A1	0.067	0.067	0.067	0.067	
θ S2	0.109	0.110	0.109	0.110	

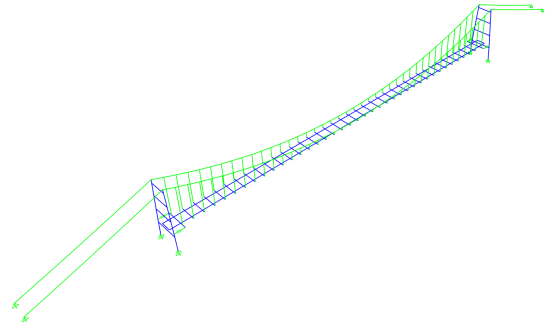
A.7 Suspension Bridge SU4a

Table A.11: General information for suspension bridge SU4a

Parameter	Value
Type	Single-span suspension bridge
Usage	Road traffic
Bridge deck	Steel twin-box girder
Deck supports at towers	Lateral, vertical and torsional restraints
Longitudinal buffers?	Yes
Towers	Steel towers
Cables	Steel cables
Sag-to-span ratio	1/10
Spans (m)	1200
Hanger longitudinal spacing (m)	30.0
Main-cable lateral spacing (m)	46.4
Bridge-deck width (m)	46.4
Bridge-deck cross section	
Number of truss elements	210
Number of beam elements	384



(a) *Code_Aster*



(b) *SAP2000*

Figure A.11: Finite element models of suspension bridge SU4a

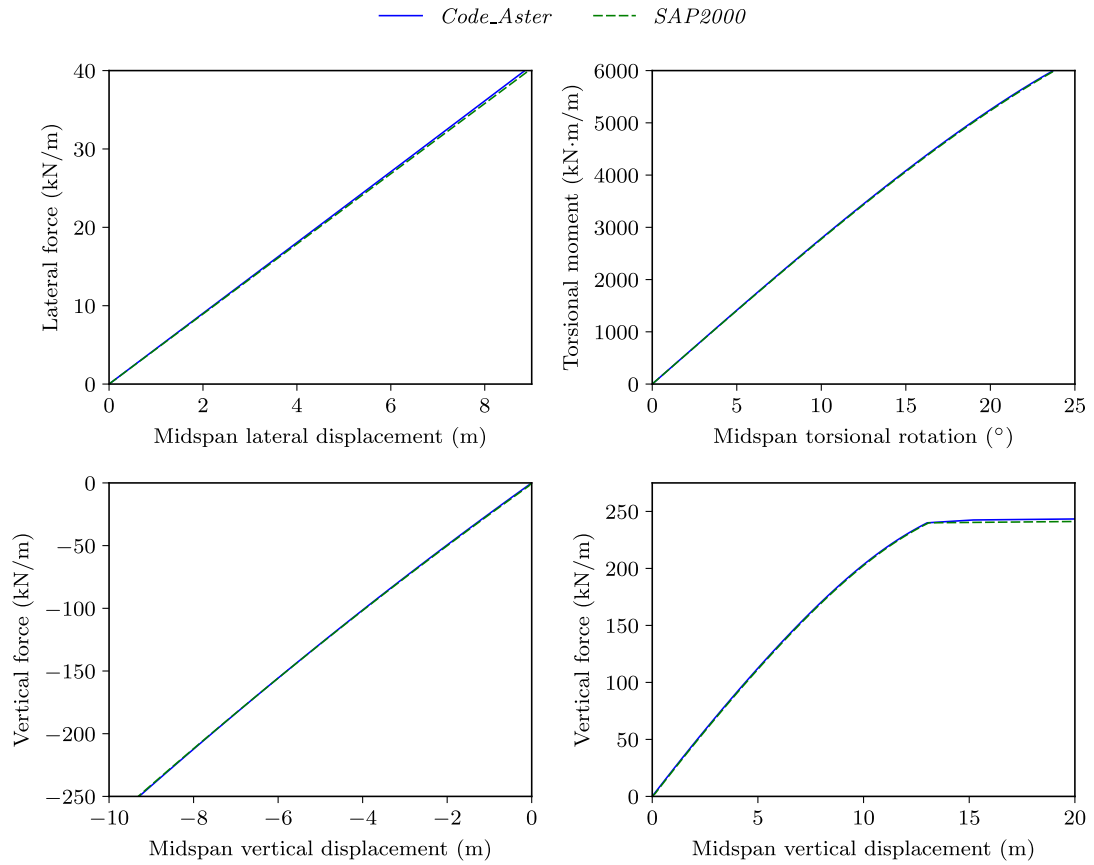












Figure A.12: Pushover analysis for suspension bridge SU4a (w/o buffers)

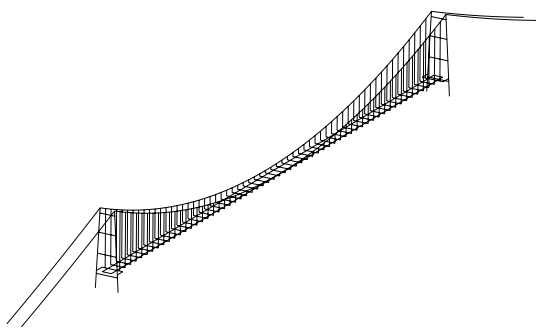
Table A.12: Natural frequencies and mode shapes for suspension bridge SU4a (L: lateral, V: vertical, θ : torsion, S: symmetric, A: antisymmetric)

Mode	Frequency (Hz)				Mode shape (top view for L**, elevation view for V** and θ **)
	<i>Code_Aster</i> (w/o buffers)	<i>SAP2000</i> (w/o buffers)	<i>Code_Aster</i> (w/ buffers)	<i>SAP2000</i> (w/ buffers)	
LS1	0.070	0.070	0.098	0.097	
LA1	0.203	0.201	0.235	0.231	
LS2	0.362	0.334	0.372	0.338	
VS1	0.136	0.136	0.136	0.136	
VA1	0.088	0.087	0.110	0.109	
VS2	0.182	0.182	0.182	0.182	
θ S1	0.244	0.241	0.244	0.242	
θ A1	0.252	0.250	0.252	0.250	
θ S2	0.384	0.381	0.386	0.381	

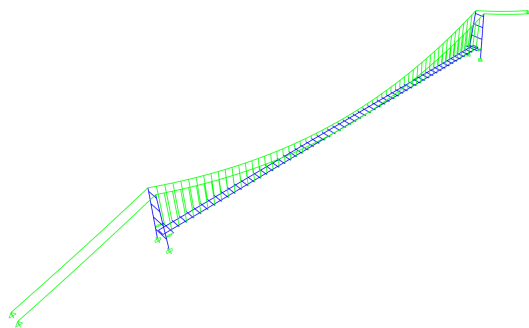
A.8 Suspension Bridge SU4b

Table A.13: General information for suspension bridge SU4b

Parameter	Value
Type	Single-span suspension bridge
Usage	Road traffic
Bridge deck	Steel twin-box girder
Deck supports at towers	Lateral, vertical and torsional restraints
Longitudinal buffers?	Yes
Towers	Steel towers
Cables	Steel cables
Sag-to-span ratio	1/10
Spans (m)	1800
Hanger longitudinal spacing (m)	30.0
Main-cable lateral spacing (m)	46.4
Bridge-deck width (m)	46.4
Bridge-deck cross section	
Number of truss elements	310
Number of beam elements	504



(a) *Code_Aster*



(b) *SAP2000*

Figure A.13: Finite element models of suspension bridge SU4b

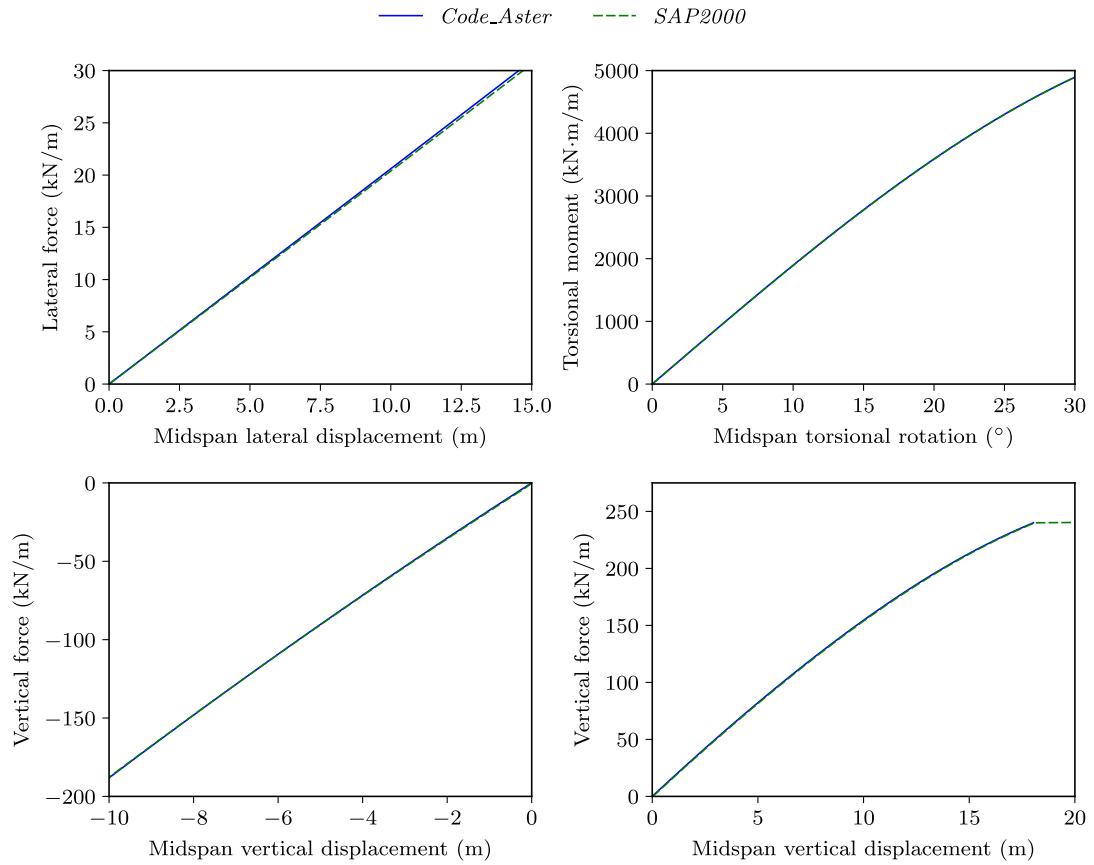












Figure A.14: Pushover analysis for suspension bridge SU4b (w/o buffers)

Table A.14: Natural frequencies and mode shapes for suspension bridge SU4b (L: lateral, V: vertical, θ : torsion, S: symmetric, A: antisymmetric)

Mode	Frequency (Hz)				Mode shape (top view for L**, elevation view for V** and θ **)
	<i>Code_Aster</i> (w/o buffers)	<i>SAP2000</i> (w/o buffers)	<i>Code_Aster</i> (w/ buffers)	<i>SAP2000</i> (w/ buffers)	
LS1	0.045	0.045	0.058	0.058	
LA1	0.110	0.110	0.134	0.133	
LS2	0.196	0.194	0.231	0.227	
VS1	0.109	0.109	0.109	0.109	
VA1	0.074	0.074	0.089	0.089	
VS2	0.145	0.145	0.146	0.145	
θ S1	0.178	0.176	0.178	0.177	
θ A1	0.168	0.167	0.168	0.167	
θ S2	0.257	0.256	0.257	0.256	

A.9 Suspension Bridge SU4c

Table A.15: General information for suspension bridge SU4c

Parameter	Value
Type	Single-span suspension bridge
Usage	Road traffic
Bridge deck	Steel twin-box girder
Deck supports at towers	Lateral, vertical and torsional restraints
Longitudinal buffers?	Yes
Towers	Steel towers
Cables	Steel cables
Sag-to-span ratio	1/10
Spans (m)	2400
Hanger longitudinal spacing (m)	30.0
Main-cable lateral spacing (m)	46.4
Bridge-deck width (m)	46.4
Bridge-deck cross section	
Number of truss elements	414
Number of beam elements	624

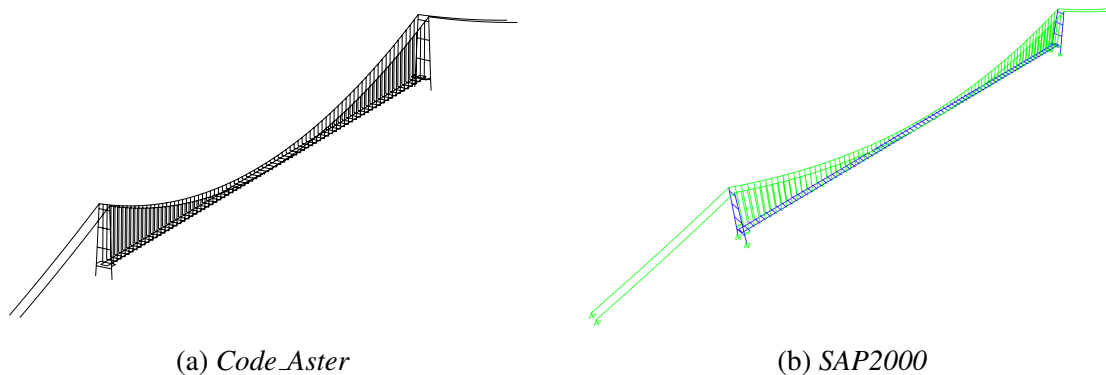


Figure A.15: Finite element models of suspension bridge SU4c

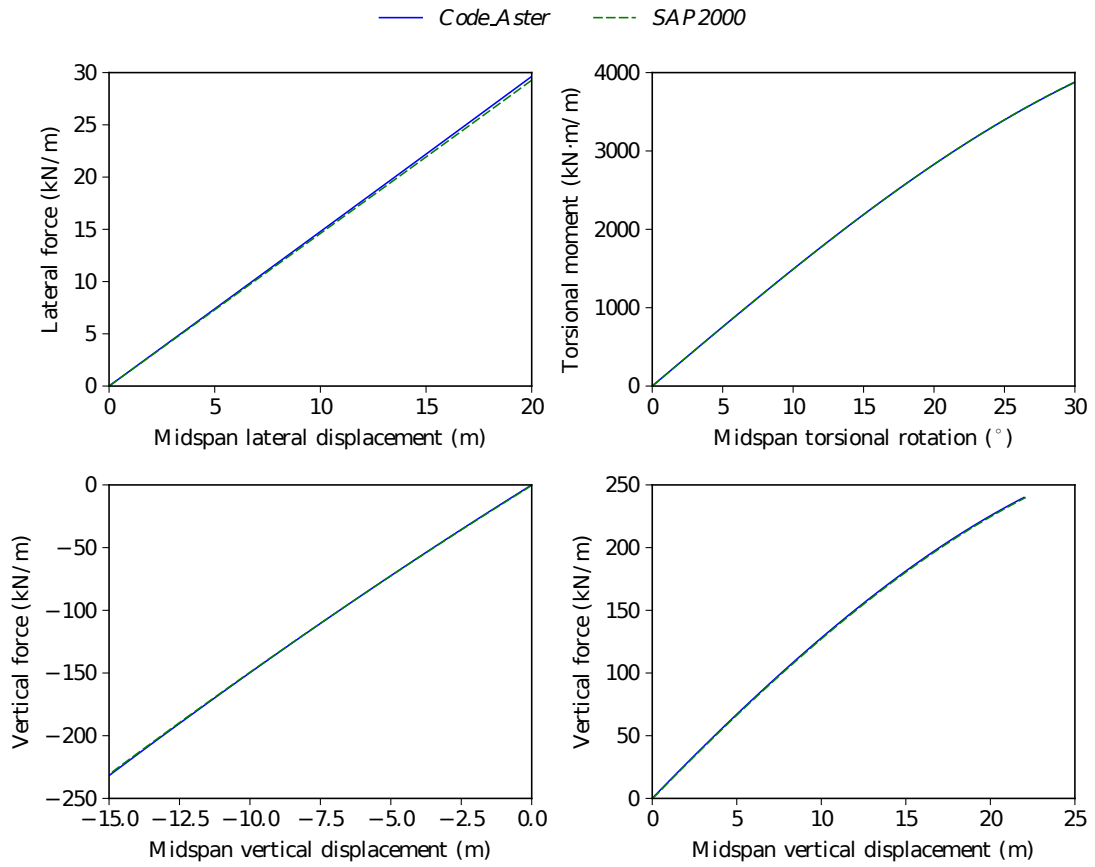











Figure A.16: Pushover analysis for suspension bridge SU4c (w/o buffers)

Table A.16: Natural frequencies and mode shapes for suspension bridge SU4c (L: lateral, V: vertical, θ : torsion, S: symmetric, A: antisymmetric)

Mode	Frequency (Hz)				Mode shape (top view for L**, elevation view for V** and θ **)
	<i>Code_Aster</i> (w/o buffers)	<i>SAP2000</i> (w/o buffers)	<i>Code_Aster</i> (w/ buffers)	<i>SAP2000</i> (w/ buffers)	
LS1	0.036	0.036	0.043	0.042	
LA1	0.075	0.074	0.091	0.090	
LS2	0.127	0.127	0.151	0.149	
VS1	0.093	0.093	0.093	0.093	
VA1	0.065	0.065	0.077	0.076	
VS2	0.124	0.124	0.124	0.124	
θ S1	0.140	0.139	0.140	0.139	
θ A1	0.126	0.125	0.127	0.125	
θ S2	0.194	0.190	0.195	0.193	

A.10 Suspension Bridge SU4d

Table A.17: General information for suspension bridge SU4d

Parameter	Value
Type	Single-span suspension bridge
Usage	Road traffic
Bridge deck	Steel twin-box girder
Deck supports at towers	Lateral, vertical and torsional restraints
Longitudinal buffers?	Yes
Towers	Steel towers
Cables	Steel cables
Sag-to-span ratio	1/10
Spans (m)	3000
Hanger longitudinal spacing (m)	30.0
Main-cable lateral spacing (m)	46.4
Bridge-deck width (m)	46.4

Bridge-deck cross section

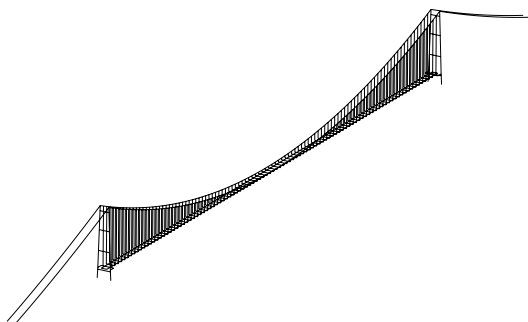


Number of truss elements

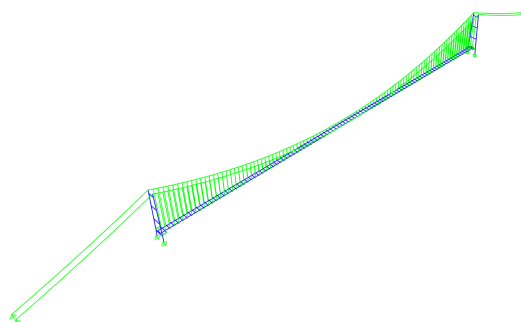
514

Number of beam elements

744



(a) *Code_Aster*



(b) *SAP2000*

Figure A.17: Finite element models of suspension bridge SU4d

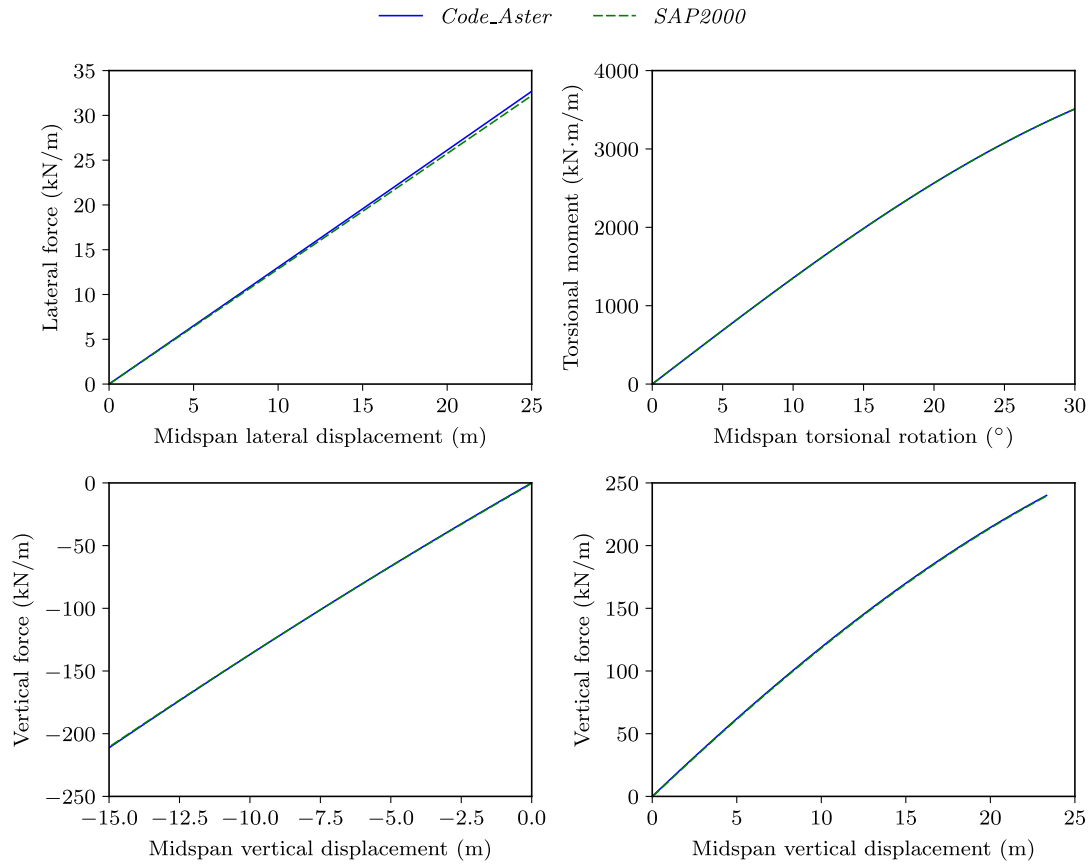











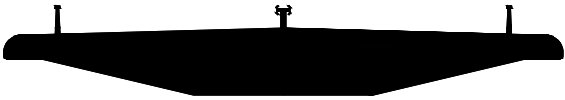
Figure A.18: Pushover analysis for suspension bridge SU4d (w/o buffers)

Table A.18: Natural frequencies and mode shapes for suspension bridge SU4d (L: lateral, V: vertical, θ : torsion, S: symmetric, A: antisymmetric)

Mode	Frequency (Hz)				Mode shape (top view for L**, elevation view for V** and θ **)
	<i>Code_Aster</i> (w/o buffers)	<i>SAP2000</i> (w/o buffers)	<i>Code_Aster</i> (w/ buffers)	<i>SAP2000</i> (w/ buffers)	
LS1	0.031	0.031	0.035	0.034	
LA1	0.058	0.058	0.069	0.069	
LS2	0.091	0.091	0.109	0.108	
VS1	0.083	0.083	0.083	0.083	
VA1	0.059	0.059	0.069	0.069	
VS2	0.110	0.110	0.110	0.110	
θ S1	0.115	0.115	0.115	0.115	
θ A1	0.100	0.100	0.100	0.100	
θ S2	0.155	0.154	0.155	0.154	

A.11 Cable-Stayed Bridge CS1

Table A.19: General information for cable-stayed bridge CS1

Parameter	Value
Type	Semi-fan cable-stayed bridge
Usage	Road traffic
Bridge deck	Steel single-box girder (main span) Concrete single-box girder (side spans)
Deck supports at towers	Rigid deck-tower connection
Longitudinal buffers?	No
Towers	Concrete towers
Cables	Steel cables
Cable crossies	Steel cables
Tower-to-span ratio (above deck)	1/5.46
Spans (m)	856
Cable long. spacing (at deck level) (m)	19.65
Cable lateral spacing (at deck level) (m)	21.2
Bridge-deck width (m)	23.5
Bridge-deck cross section	
Number of truss elements	1908
Number of beam elements	432

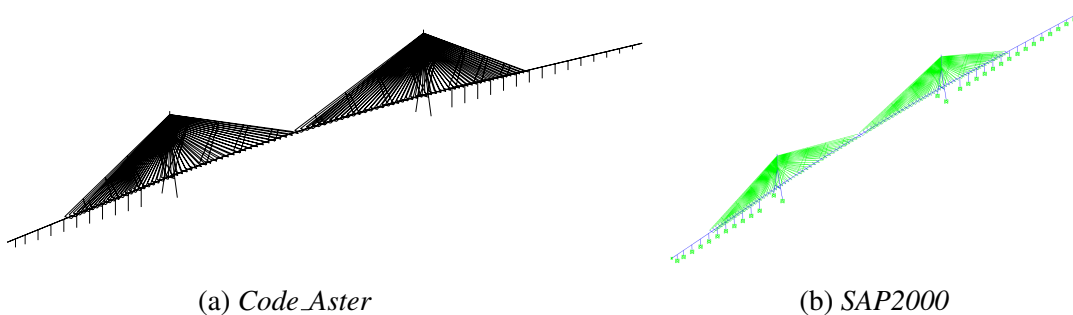


Figure A.19: Finite element models of cable-stayed bridge CS1

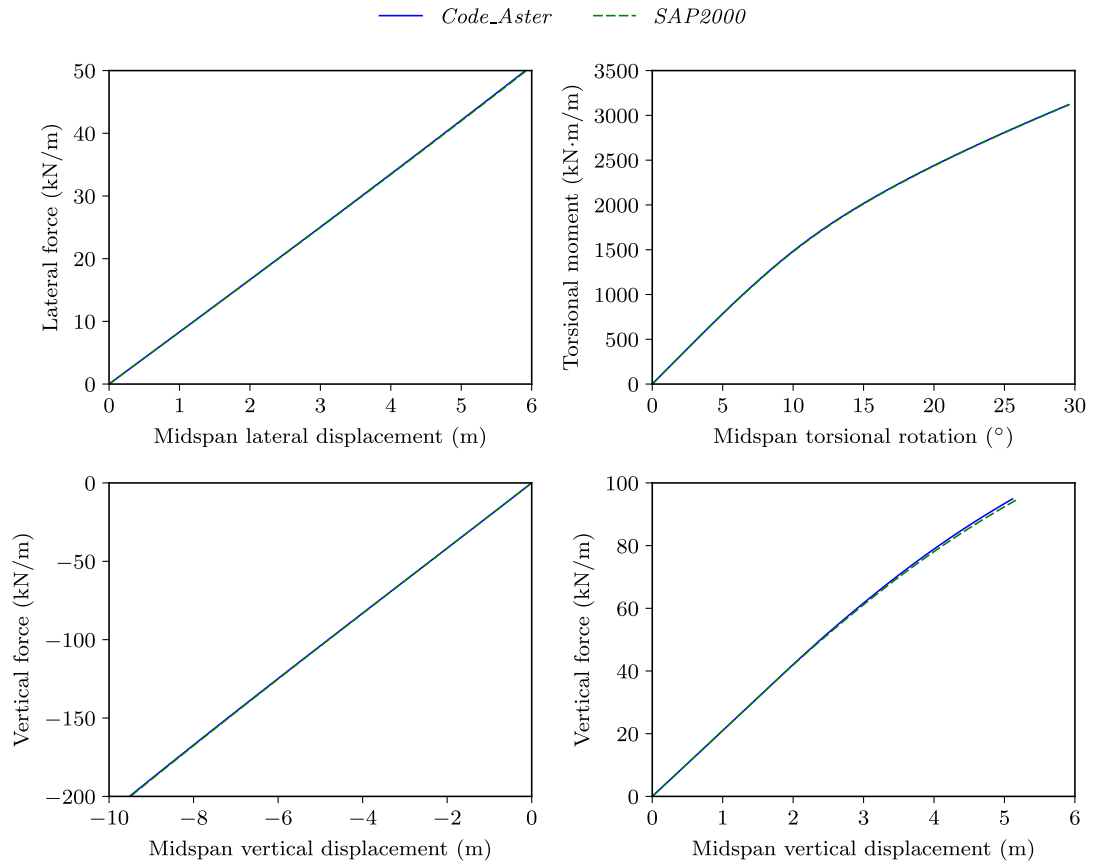









Figure A.20: Pushover analysis for cable-stayed bridge CS1

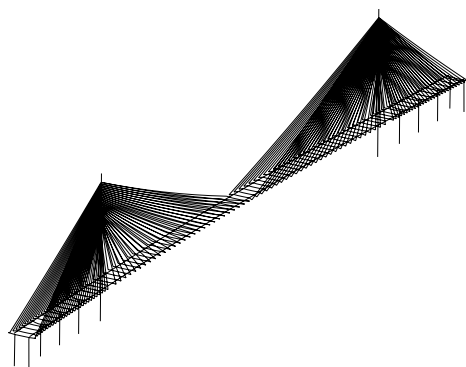
Table A.20: Natural frequencies and mode shapes for cable-stayed bridge CS1 (L: lateral, V: vertical, θ : torsion, S: symmetric, A: antisymmetric)

Mode	Frequency (Hz)		Mode shape (top view for L**, elevation view for V** and θ **)
	<i>Code_Aster</i>	<i>SAP2000</i>	
LS1	0.138	0.138	
LA1	0.338	0.338	
VS1	0.215	0.215	
VA1	0.271	0.270	
VS2	0.361	0.360	
θ S1	0.693	0.695	

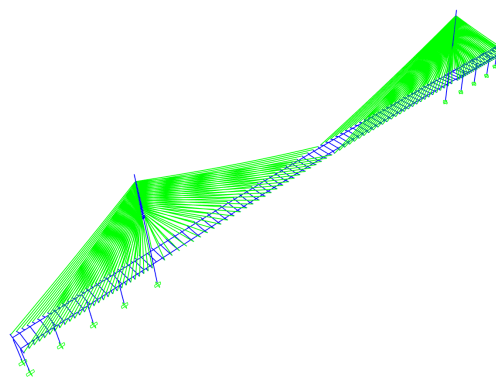
A.12 Cable-Stayed Bridge CS2

Table A.21: General information for cable-stayed bridge CS2

Parameter	Value
Type	Semi-fan cable-stayed bridge
Usage	Road traffic
Bridge deck	Steel twin-box girder (main span) Concrete twin-box girder (side spans)
Deck supports at towers	Continuous girder with lateral restraints
Longitudinal buffers?	Yes
Towers	Concrete towers
Cables	Steel cables
Cable crossies	None
Tower-to-span ratio (above deck)	1/4.62
Spans (m)	1018
Cable long. spacing (at deck level) (m)	18.17
Cable lateral spacing (at deck level) (m)	49.66
Bridge-deck width (m)	53.3
Bridge-deck cross section	
Number of truss elements	1792
Number of beam elements	1218



(a) *Code_Aster*



(b) *SAP2000*

Figure A.21: Finite element models of cable-stayed bridge CS2

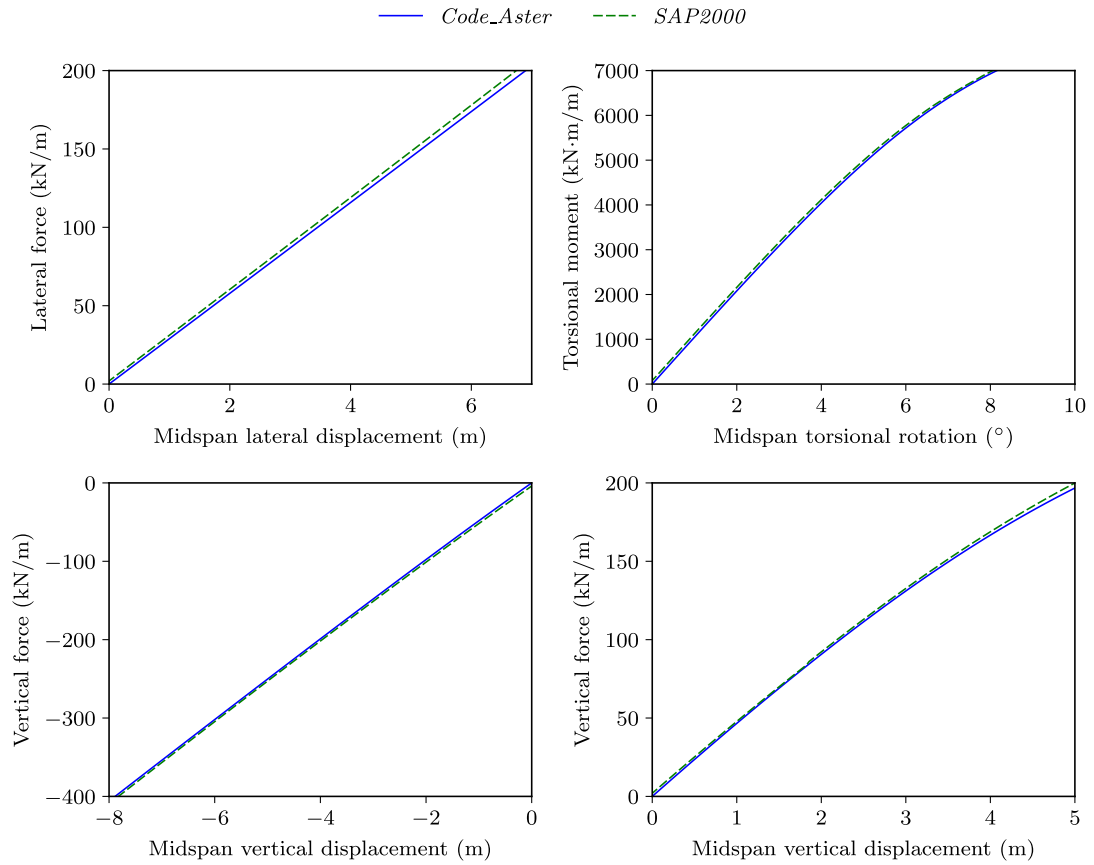

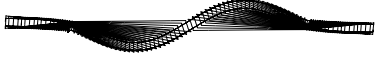







Figure A.22: Pushover analysis for cable-stayed bridge CS2 (w/o buffers)

Table A.22: Natural frequencies and mode shapes for cable-stayed bridge CS2 (L: lateral, V: vertical, θ : torsion, S: symmetric, A: antisymmetric)

Mode	Frequency (Hz)				Mode shape (top view for L**, elevation view for V** and θ **)
	<i>Code_Aster</i> (w/o buffers)	<i>SAP2000</i> (w/o buffers)	<i>Code_Aster</i> (w/ buffers)	<i>SAP2000</i> (w/ buffers)	
LS1	0.157	0.157	0.157	0.157	
LA1	0.393	0.384	0.393	0.384	
VS1	0.198	0.198	0.198	0.198	
VA1	0.240	0.238	0.239	0.238	
VS2	0.302	0.303	0.304	0.303	
θ S1	0.428	0.433	0.428	0.433	
θ A1	0.587	0.600	0.587	0.600	

Appendix B

Nonlinear Structural Coupling for Non-Analogous Modes

B.1 Introduction

The first few decades of the 20th century were marked by a rapid increase in span length for suspension bridges. This went on until dynamic wind effects were observed on some of the suspension bridges designed in this era, even those by prominent engineers like Othmar Amman and David B. Steinman. The collapse of the Tacoma Narrows Bridge is obviously the event that triggered what has been more than 80 years of research on the dynamic effects of wind on bridges. Going from wind tunnel testing, finite element analysis to computational fluid dynamics, this research has made possible super long-span bridges like the Çanakkale Bridge and Messina Strait Bridge. As span lengths are getting longer, nonlinear structural phenomena in cable-supported bridges could play a role on the safety and stability of these bridges when subjected to wind effects. Similar to what happened in the case of dynamic wind actions at the beginning of the 20th century, nonlinear structural phenomena have been omitted in the design process due to a lack of information about them.

Regarding nonlinear structural phenomena, there have been some demonstrations of nonlinear mode coupling made by mathematicians using nonlinear differential equations of continuum models of suspension bridges [166–169]. It has been shown that dynamic vertical forcing can induce large torsional oscillations due to nonlinear structural coupling. The nonlinear effect described previously seems to be attributed to a dynamic instability called internal parametric resonance [170]. To the author's knowledge, such nonlinear dynamic phenomena have never been demonstrated experimentally in a wind tunnel. However, a transition from an antisymmetric flutter mode to a symmetric flutter mode was observed on a full-aeroelastic model of a double-main-span suspension bridge [171]. A possible explanation for this would be internal resonance due to nonlinear effects of the aeroelastic-structural bridge system [172].

As nonlinear structural effects combined with aeroelastic effects could lead to unexpected instabilities, it appears that further research on structural nonlinearities in long-span bridges is needed, especially on nonlinear coupling between modes of vibration. Therefore, this

appendix presents an assessment of nonlinear mode coupling in cable-supported bridges. An emphasis is made on the coupling for non-analogous modal pairs, i.e., modes having a weak correlation along the bridge deck between the vertical displacement and torsional rotation.

First, the key aspects of nonlinear generalized stiffness analysis for cable-supported bridges in the case of vertical-torsional modal pairs are reviewed. Using this analysis technique, nonlinear generalized stiffness parameters for nine suspension bridges with main spans between 1.2 km and 4.14 km were calculated. Comparing the results for analogous modal pairs and non-analogous ones allows identifying the more critical modal pairs with regard to nonlinear structural coupling.

B.2 Two-mode Nonlinear Generalized Stiffness

Nonlinear generalized stiffness analysis provides a way to measure the nonlinear structural behavior of a bridge in terms of its dynamic properties or more specifically, its modes of vibration. This is achieved by applying static loads proportional to selected modes of vibration to a nonlinear finite element model of a cable-supported bridge. The reader is referred to chapter 3 for further information on nonlinear generalized stiffness analysis.

Since material nonlinearities are unlikely under wind loads in a properly designed cable-supported bridge, only geometric nonlinearities are of concern in this study. As shown in eqs. B.1 and B.2, nonlinear generalized stiffness analysis in this appendix accounts for two modes, i.e., mode ϕ_i and mode ϕ_j :

$$\mathbf{f}_{SG}(\mathbf{u}_{nl}) = \mathbf{p}_{ij} \quad (\text{B.1})$$

$$\mathbf{p}_{ij} = \mathbf{p}_i + \mathbf{p}_j = a_i \omega_i^2 \mathbf{M} \phi_i + a_j \omega_j^2 \mathbf{M} \phi_j \quad (\text{B.2})$$

where $\mathbf{f}_{SG}(\mathbf{u}_{nl})$ is the internal force vector of the nonlinear geometric system; \mathbf{u}_{nl} is the nonlinear displacement vector obtained from nonlinear static analysis; \mathbf{M} is the mass matrix calculated using the finite element method; a_i and a_j are respectively the modal load coefficients for mode ϕ_i and mode ϕ_j ; ω_i and ω_j are respectively the natural angular frequencies for mode ϕ_i and mode ϕ_j . The dead-load configuration of the bridge is used as the reference state for the nonlinear static equation in eq. B.1 and the calculations of the modal properties. Also, vertical and torsional modes are of interest for this study. They are normalized such that the maximum vertical displacement of the bridge deck is unity for vertical modes. For

torsional modes, the maximum torsional rotation is unity.

After solving eq. B.1, \mathbf{u}_{nl} can be approximated as follows:

$$\mathbf{u}_{nl} \approx \boldsymbol{\phi}_i z_i + \boldsymbol{\phi}_j z_j = \boldsymbol{\Phi}_{ij} \mathbf{z}_{ij} \quad (\text{B.3})$$

where $\boldsymbol{\Phi}_{ij} = [\boldsymbol{\phi}_i \ \boldsymbol{\phi}_j]$ and $\mathbf{z}_{ij} = [z_i \ z_j]^\top$; z_i and z_j are the generalized displacements for modes $\boldsymbol{\phi}_i$ and $\boldsymbol{\phi}_j$. Because of the mode normalization considered here, the generalized displacements correspond to the maximum deck displacement or rotation in the direction under consideration.

It is possible to rearrange eq. B.3 in order to find the generalized displacements (see chapter 3). By varying the modal load coefficients, a force-displacement relationship can be obtained for the generalized modal forces as functions of the generalized displacements. This relationship is utilized to calculate the two-mode tangent nonlinear generalized stiffness matrix $\tilde{\mathbf{K}}_{ij}^t$:

$$\tilde{\mathbf{K}}_{ij}^t(\mathbf{z}_{ij}) = \frac{\partial \tilde{\mathbf{p}}_{ij}}{\partial \mathbf{z}_{ij}} = \begin{bmatrix} \frac{\partial \tilde{p}_i}{\partial z_i} & \frac{\partial \tilde{p}_i}{\partial z_j} \\ \frac{\partial \tilde{p}_j}{\partial z_i} & \frac{\partial \tilde{p}_j}{\partial z_j} \end{bmatrix} \quad (\text{B.4})$$

It should be noted that $\tilde{\mathbf{p}}_{ij} = \boldsymbol{\Phi}_{ij}^\top \mathbf{p}_{ij} = [\tilde{p}_i \ \tilde{p}_j]^\top = [a_i \omega_i^2 \tilde{m}_i \ a_j \omega_j^2 \tilde{m}_j]^\top$. Also, we have that $\tilde{m}_i = \boldsymbol{\phi}_i^\top \mathbf{M} \boldsymbol{\phi}_i$ and $\tilde{m}_j = \boldsymbol{\phi}_j^\top \mathbf{M} \boldsymbol{\phi}_j$. By accounting for two modes in the modal load, it is possible to study the nonlinear structural coupling between these modes. This is demonstrated by the off-diagonal terms in the matrix shown in eq. B.4 as well as by the fact that the matrix entries are functions of both generalized displacements, z_i and z_j .

B.3 Numerical Models of Cable-Supported Bridges

This study focuses on suspension bridges since they showed a stronger nonlinear mode coupling than cable-stayed bridges. Table B.1 presents the nine suspension bridges considered for this analysis on nonlinear coupling between non-analogous modes. Finite element models were developed for these bridges using the fishbone modeling approach where the bridge deck, modeled as Timoshenko beam elements, is connected to the cable system through rigid elements. The cable system is modeled using tension-only truss elements, for which the cable pretensions are applied using temperature loads. As mentioned previously, the geometric nonlinearities are considered for these numerical models. It is also worth

Table B.1: Description of cable-supported bridges

Bridge	Type	Main span (m)	Buffers?	Elevation view
SU1	Three-span suspension Continuous girder	1550	Yes	
SU2	Three-span suspension Continuous girder	1624	Yes	
SU3a	Three-span suspension Partially continuous girder	2460	Yes	
SU3b	Three-span suspension Partially continuous girder	3300	Yes	
SU3c	Three-span suspension Partially continuous girder	4140	Yes	
SU4a	Single-span suspension Girder restrained at towers	1200	Yes	
SU4b	Single-span suspension Girder restrained at towers	1800	Yes	
SU4c	Single-span suspension Girder restrained at towers	2400	Yes	
SU4d	Single-span suspension Girder restrained at towers	3000	Yes	

noting that the hydraulic buffers, which are designed to limit longitudinal deck motions, are considered as inactive in this study.

B.4 Results

In this section are presented the nonlinear generalized stiffness analysis results for the dead-load configuration of the bridges in table B.1. First, section B.4.1 presents nonlinear generalized stiffness parameters in the case of modal pairs consisting of one vertical mode and its analogous torsional mode. Section B.4.1 serves as a basis of comparison for the results in sections B.4.2 and B.4.3. Section B.4.2 is used to assess the mode coupling caused by geometric nonlinearities between vertical and torsional effects for non-analogous modes. In the case of section B.4.3, the nonlinear coupling between pairs of modes of the same type are studied. For the sake of brevity, only results in the case of symmetric modes are included herein. Compared to symmetric modes, nonlinear coupling between antisymmetric modes is negligible (see chapter 3). This observation is also valid for nonlinear coupling between a symmetric mode and an antisymmetric mode.

For the calculation of the nonlinear generalized stiffness matrix $\tilde{\mathbf{K}}_{ij}^t$, the range of values for the modal load coefficients was chosen such that the nonlinear behavior can be observed. A total of 81 values for each of the modal load coefficients were used, therefore forming an 81×81 grid with a total of 6561 points. However, the presentation of the results in sections B.4.1–B.4.3 is limited to generalized displacement limits determined in chapter 3. They were determined based on the nonlinear static response under mean wind loads

calculated from finite element analysis. A displacement allowance was also included in order to account for the dynamic wind effects, which were estimated from wind tunnel results.

B.4.1 Nonlinear Coupling for Analogous Modes

For the sake of comparison with the case of non-analogous modes, fig. B.1 presents the terms of the nonlinear generalized stiffness matrix for analogous modes. Results for the modal pair formed by the first symmetric vertical mode (VS1) and the first symmetric torsional mode (θ S1) are shown. Results for mode VS2 and mode θ S2 are also included.

It is also worth noting that the results are presented in a normalized format. Diagonal terms are normalized with respect to the corresponding linear generalized stiffnesses. For example, the diagonal term relative to mode VS1 is presented as $\tilde{k}_{VS1,VS1}^t/\tilde{k}_{VS1}$ where $\tilde{k}_{VS1,VS1}^t$ and \tilde{k}_{VS1} are respectively the nonlinear generalized stiffness and linear generalized stiffness for mode VS1 ($\tilde{k}_{VS1} = \phi_{VS1}^T \mathbf{K} \phi_{VS1}$ with \mathbf{K} being the stiffness matrix of the bridge). In the case of modal pair VS1- θ S1, the off-diagonal terms are normalized as $(\tilde{k}_{VS1,\theta S1}^t/b_{cl})/\tilde{k}_{VS1}$ and $(\tilde{k}_{\theta S1,VS1}^t b_{cl})/\tilde{k}_{\theta S1}$, where b_{cl} is half of the distance between the main cables. This is done because $\tilde{k}_{VS1,\theta S1}^t$ and $\tilde{k}_{\theta S1,VS1}^t$ have different units than the linear generalized stiffnesses \tilde{k}_{VS1} and $\tilde{k}_{\theta S1}$. The quantity $\tilde{k}_{VS1,\theta S1}^t/b_{cl}$ can be seen as a vertical generalized stiffness at the location of the cable connections to the deck. The quantity $\tilde{k}_{\theta S1,VS1}^t b_{cl}$ represents an equivalent torsional generalized stiffness. In the case of modes VS1 and θ S1, these normalized stiffnesses are expressed as functions of the normalized generalized displacements z_{VS1}/L_{span} and $z_{\theta S1} b_{cl}/L_{span}$, where L_{span} is the main span length. The results for modes VS2 and θ S2 are also presented in a similar normalized format.

B.4.2 Nonlinear Coupling for Non-Analogous Modes

Figure B.2 presents the results of nonlinear generalized stiffness analysis in the case of non-analogous pairs formed by a vertical mode and a torsional mode. Modal pair VS1- θ S2 and modal pair VS2- θ S1 were considered. Results are presented in a normalized form similar to what is used in section B.4.1.

B.4.3 Nonlinear Coupling for Same-Type Modes

It is also of interest to assess the nonlinear coupling between modes of the same type, e.g., for two vertical modes or two torsional modes. Therefore, fig. B.3 presents the nonlinear generalized stiffnesses between modes VS1 and VS2 as well as those for modes θ S1 and θ S2. In this case, the diagonal and off-diagonal generalized stiffness terms are directly normalized

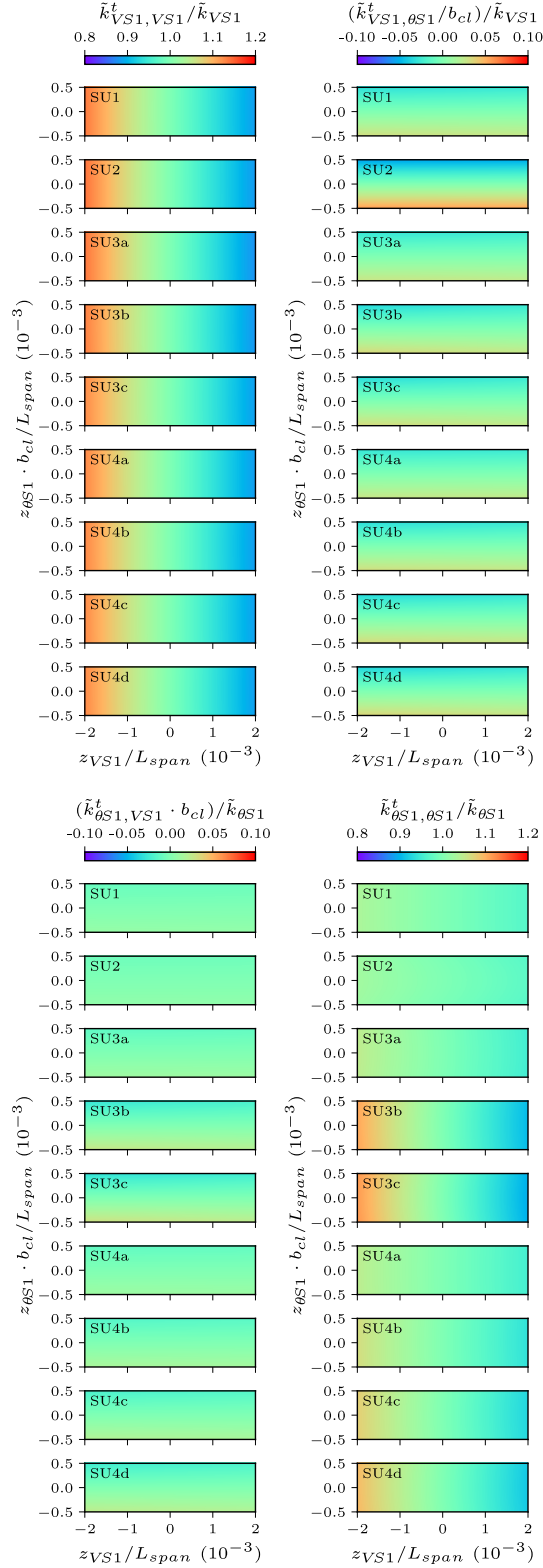
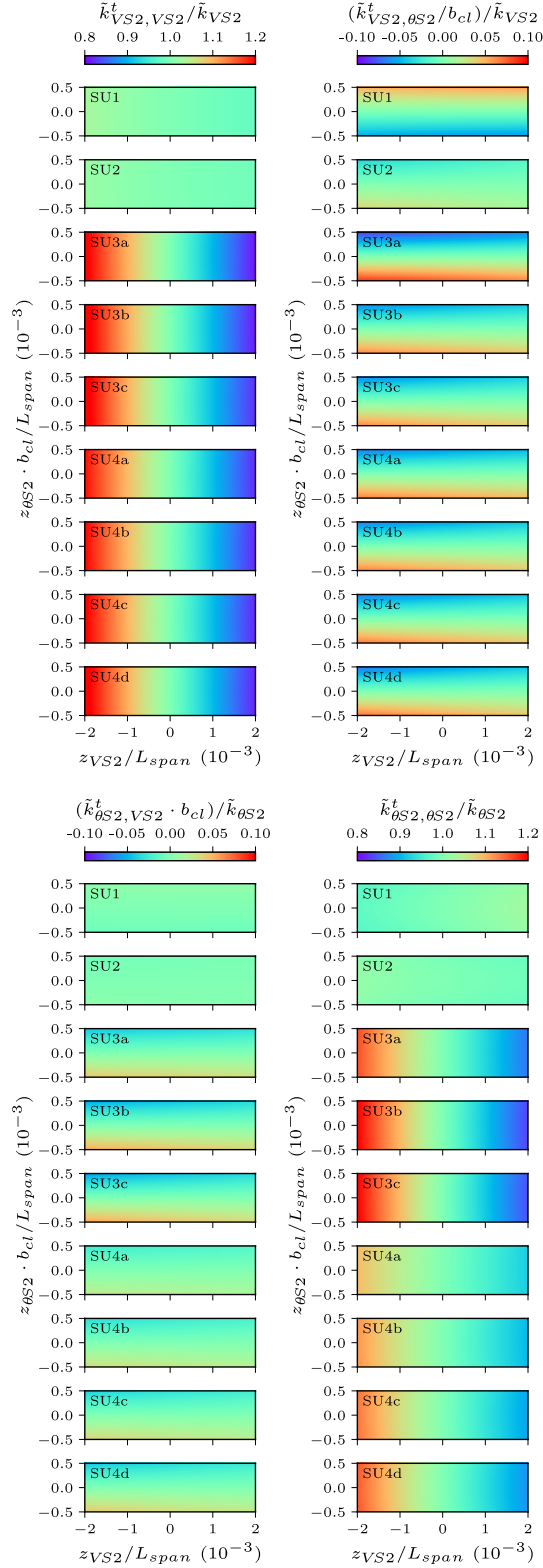
(a) Modes VS1 and $\theta S1$

Figure B.1: Nonlinear generalized stiffness terms of suspension bridges for analogous vertical and torsional modes



(b) Modes VS2 and θS2

Figure B.1: Nonlinear generalized stiffness terms of suspension bridges for analogous vertical and torsional modes (cont.)

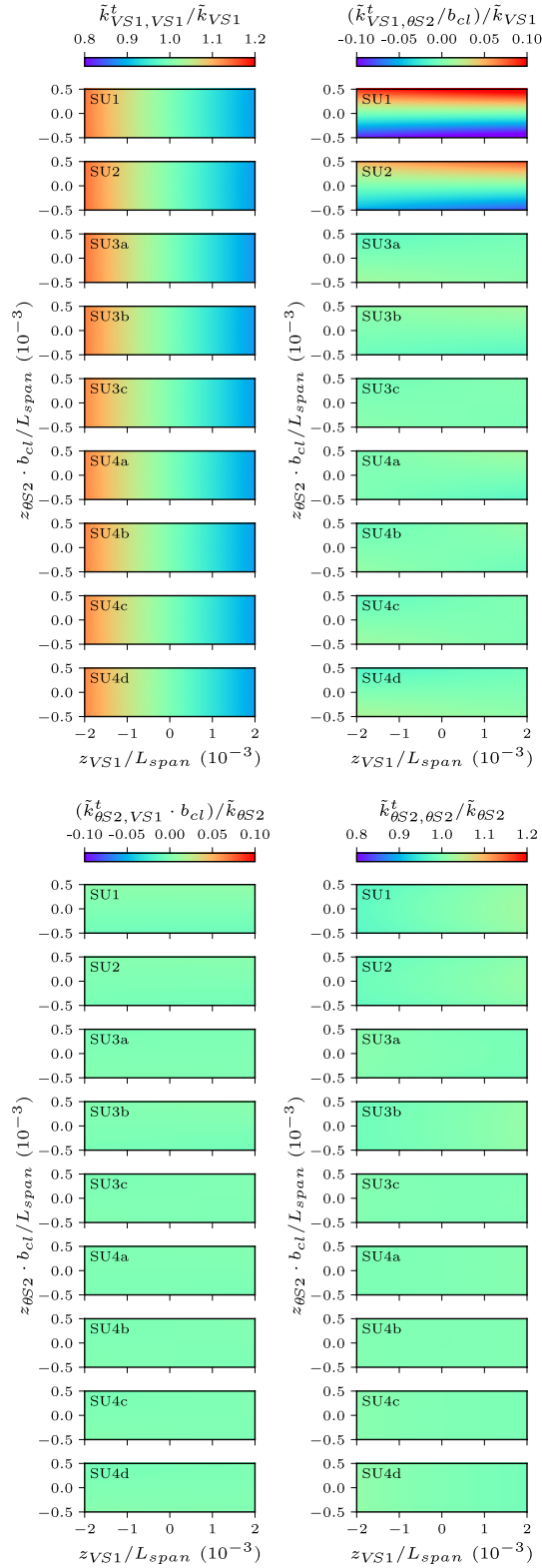
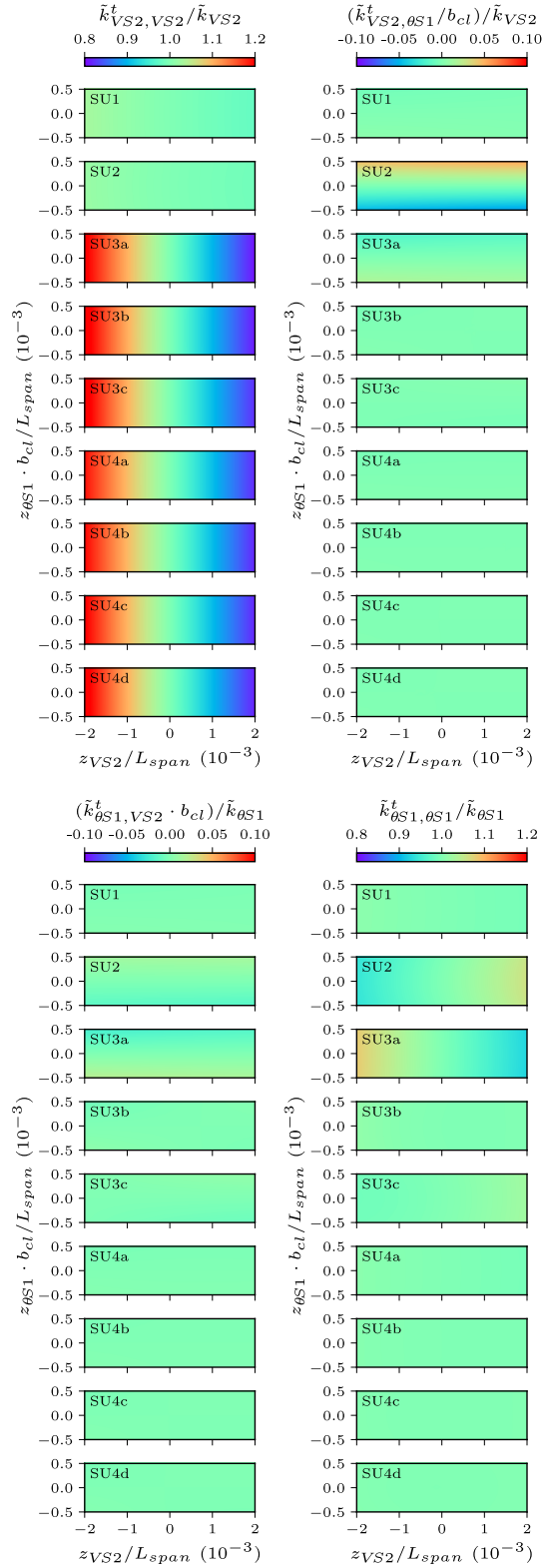
(a) Modes VS1 and $\theta S2$

Figure B.2: Nonlinear generalized stiffness terms of suspension bridges for non-analogous vertical and torsional modes



(b) Modes VS2 and $\theta S1$

Figure B.2: Nonlinear generalized stiffness terms of suspension bridges for non-analogous vertical and torsional modes (cont.)

with respect to the linear generalized stiffnesses because they have consistent units since modes of the same type are used.

B.5 Discussion

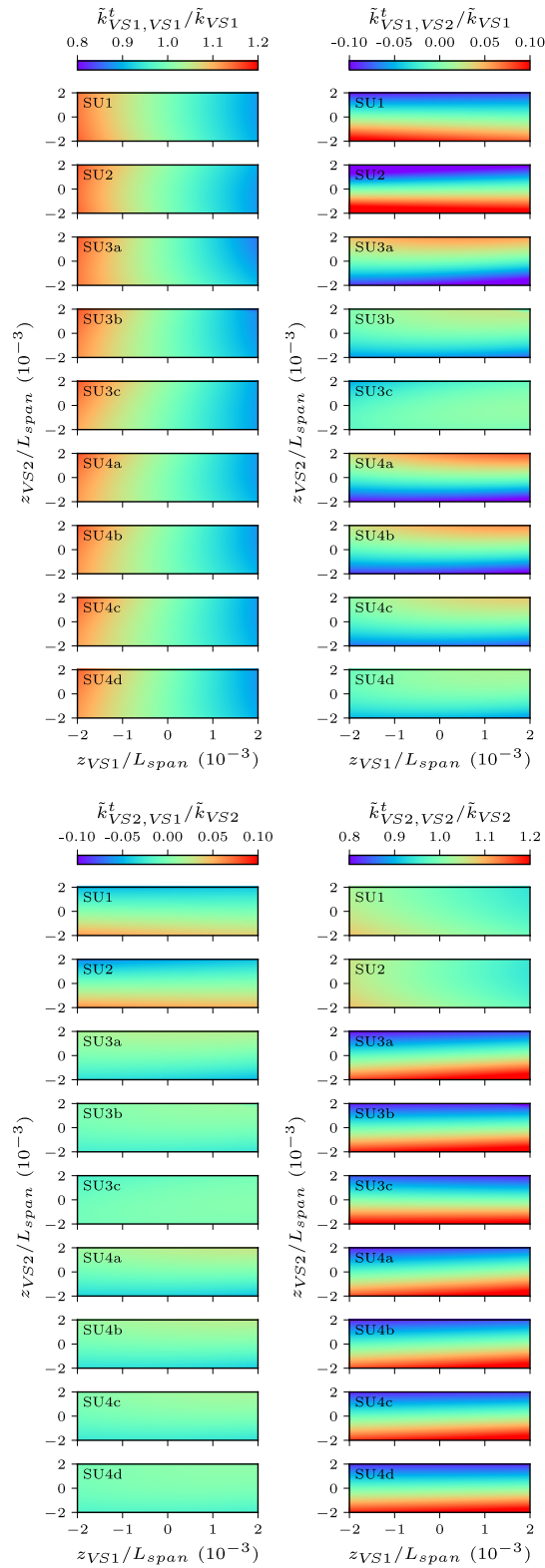
As in it can be observed in figs. B.1–B.3, the diagonal terms of $\tilde{\mathbf{K}}_{ij}^t$ relative to the vertical modes mainly show a one-mode nonlinear behavior. For example, $\tilde{k}_{VS1,VS1}^t$ varies with z_{VS1} , and it is only slightly affected by the second generalized displacement ($z_{\theta S1}$ for fig. B.1, $z_{\theta S2}$ for fig. B.2 and z_{VS2} for fig. B.3). This is explained by the fact that vertical cable modal displacements for symmetric modes involve a change of cable tension causing a variation of the geometric stiffness [185]. Additionally, from these results, it is evident that the three-span suspension bridges with short side spans (SU3a, SU3b and SU3c) and the single-span suspension bridges (SU4a, SU4b, SU4c and SU4d) show a stronger nonlinear modal coupling than the three-span suspension bridges (SU1 and SU2). Also, a span length effect can only be observed in fig. B.1.

By comparing fig. B.2 to fig. B.1, it is clear that the non-analogous case for one vertical mode and one torsional mode is less nonlinear compared to the analogous one. This is better demonstrated by the off-diagonal terms and the torsional diagonal terms. Regarding the modal coupling between modes of the same type, fig. B.3a for the vertical modes shows a stronger nonlinear coupling than for the torsional modes in fig. B.3b, which clearly shows a linear behavior. This indicates that the nonlinear behavior between modes of vibration mainly originates from the vertical movement of the bridge structure.

From this analysis, it appears that nonlinear mode coupling is stronger for pairs formed by analogous vertical and torsional modes. This indicates that further research on the effect of nonlinear structural coupling on the stability of bridges subjected to wind should focus on analogous modal pairs.

B.6 Conclusions

According to theoretical research, nonlinear structural coupling in cable-supported bridges could potentially lead to unexpected instabilities involving large torsional bridge-deck oscillations. Such coupling could have an effect on the stability of bridges subjected to wind. Therefore, this appendix presented an analysis of nonlinear coupling in the case of non-analogous modes. The procedure for nonlinear generalized stiffness analysis was applied to nine suspension bridges for different mode pairings. It was found that non-analogous modes



(a) Modes VS1 and VS2

Figure B.3: Nonlinear generalized stiffness terms of suspension bridges for same-type modes

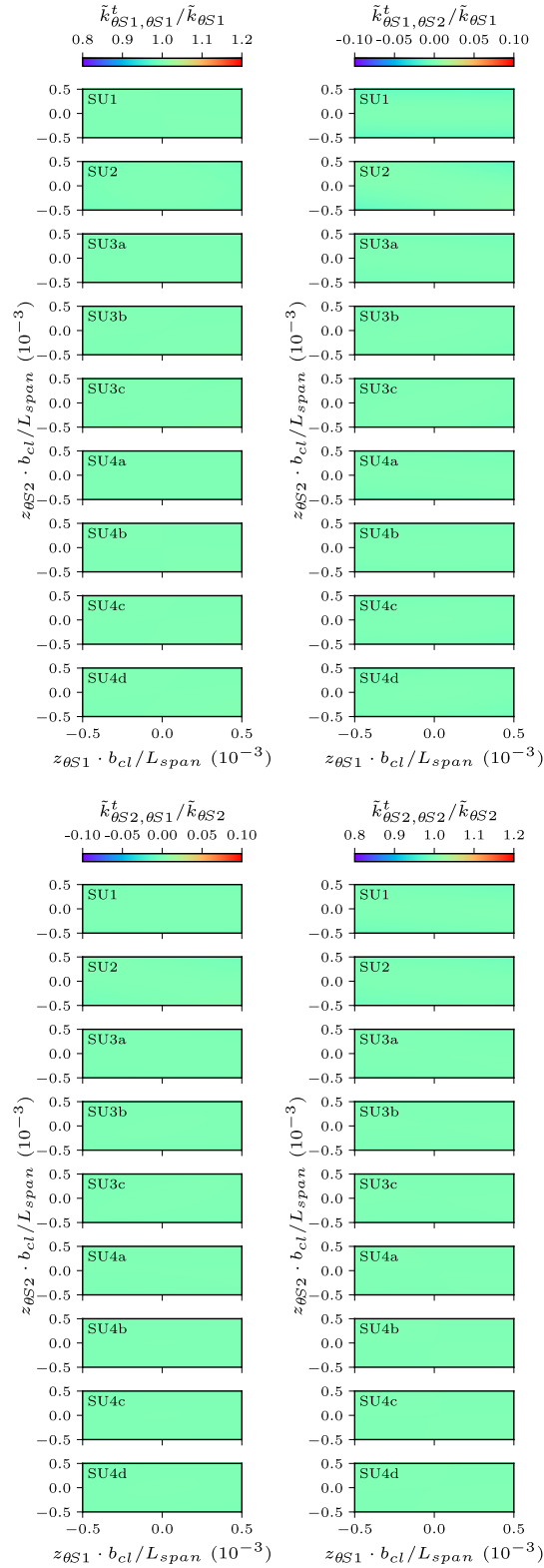
(b) Modes $\theta S1$ and $\theta S2$

Figure B.3: Nonlinear generalized stiffness terms of suspension bridges for same-type modes (cont.)

have a weaker nonlinear coupling than analogous modes. This indicates that future research should focus on analogous modes in the assessment of the effect of structural nonlinearities on the stability of bridges under wind effects.

Appendix C

Validation of New Experimental Bridge Rig

C.1 Introduction

It is well known that long cable-supported bridges, such as suspension bridges and cable-stayed bridges, are sensitive structures to the actions of wind, especially for dynamic phenomena like flutter. Flutter, which is a self-excited instability, can lead to major structural damages and even bridge collapse. For this reason, it has been common practice in the field of long-span bridge engineering to conduct wind tunnel tests in order to verify the soundness of bridge designs with respect to aerodynamic and aeroelastic phenomena. Different wind tunnel testing procedures can be utilized for bridges. In order of increasing complexity, the most common approaches are the section model tests [30], taut-strip model tests [59] and full-aeroelastic model tests [29]. Due to their versatility, simplicity and cost effectiveness in comparison to other testing procedures, section model tests have become the standard approach for wind tunnel tests of bridges.

Section model tests can be utilized to measure aerodynamic coefficients, measure the wind and motion-induced surface pressures and study the dynamic response of the bridge deck, especially with regard to instabilities like flutter. However, even with the improvements made in experimental apparatus over the years, section model tests still rely on the same simplifications with respect to the aerodynamic and structural behaviors. The fact that the aerodynamic contribution of the cable system is neglected is an example of such simplifications. Typically, only one vertical mode and an analogous torsional mode, which have uniform shapes, are considered in section model tests. Furthermore, the bridge structure is assumed to have a linear behavior because the modes represented in such tests are obtained considering linear structural dynamics theory.

Nevertheless, it is known that cable-supported bridges can show geometric nonlinearities [149] as well as material nonlinearities [151] and localized nonlinearities [17] in specific cases. Using advanced mathematical models of suspension bridges, mathematicians and engineers demonstrated that a dynamic vertical force can lead to large torsional oscillations due to nonlinear structural dynamic coupling [169, 170]. This coupling is caused by the intrinsic nonlinear geometric behavior of the suspension bridge system. In [170], it is mentioned that internal parametric resonance, a structural dynamic instability caused by

the nonlinear structural coupling between modes of vibration, would be responsible. To the author's knowledge, such large torsional oscillations due to nonlinear structural dynamic effects have never been witnessed on an actual bridge. Nonetheless, a transition from an antisymmetric instability mode to a symmetric instability mode occurred for a full-aeroelastic model of a double-main-span suspension bridge [171]. Internal resonance associated with the nonlinearities of the aeroelastic system would be responsible for the phenomenon observed on this full-aeroelastic bridge model [173]. This has led to recent studies on nonlinear flutter and aerodynamic nonlinearities [96, 101]. The main focus of these studies has been on aerodynamic nonlinearities, and structural nonlinearities are only discussed in verifications that section model test rigs behave linearly. However, in the field of aeronautics, it was demonstrated using nonlinear section model tests for airfoils that a nonlinear stiffness behavior can have an influence on flutter [54, 57].

Considering that the flutter response of airfoils can be impacted by a nonlinear stiffness behavior, it is worth asking whether this can also be the case for bridges. A section model test procedure for bridges able to represent the nonlinear structural behavior would be able to answer this question. The first step toward nonlinear section model tests for bridges was to develop a numerical procedure to study the nonlinear structural vertical-torsional coupling in cable-supported bridges (see chapter 3). The procedure in chapter 3 can also be used to determine the nonlinear structural behavior in stiffness to be considered for nonlinear section model tests. During the development of a scaling procedure for the nonlinear behavior obtained using the approach in chapter 3, it was determined that a new section model test rig is required in order to conduct nonlinear section model tests for bridges.

Therefore, this appendix presents the validation procedure of this new section model test rig in the case of standard linear tests. More specifically, a single-box girder bridge model was tested in two different wind tunnels, i.e., the main wind tunnel at the *Université de Sherbrooke* and the Boundary Layer Wind Tunnel Laboratory (BLWTL) at the University of Western Ontario. The new bridge rig of the BLWTL is validated by comparing the wind tunnel test results of the new bridge rig to those measured at the *Université de Sherbrooke* and those obtained at the BLWTL using the old bridge rig. First, the wind tunnels and section model test rigs considered in the validation procedure are presented. Then, the experimental program, which included static tests, flutter derivative tests and dynamic tests, is discussed. Finally, a presentation of the experimental results is made, which also includes a discussion of the results.

C.2 Experimental Apparatuses

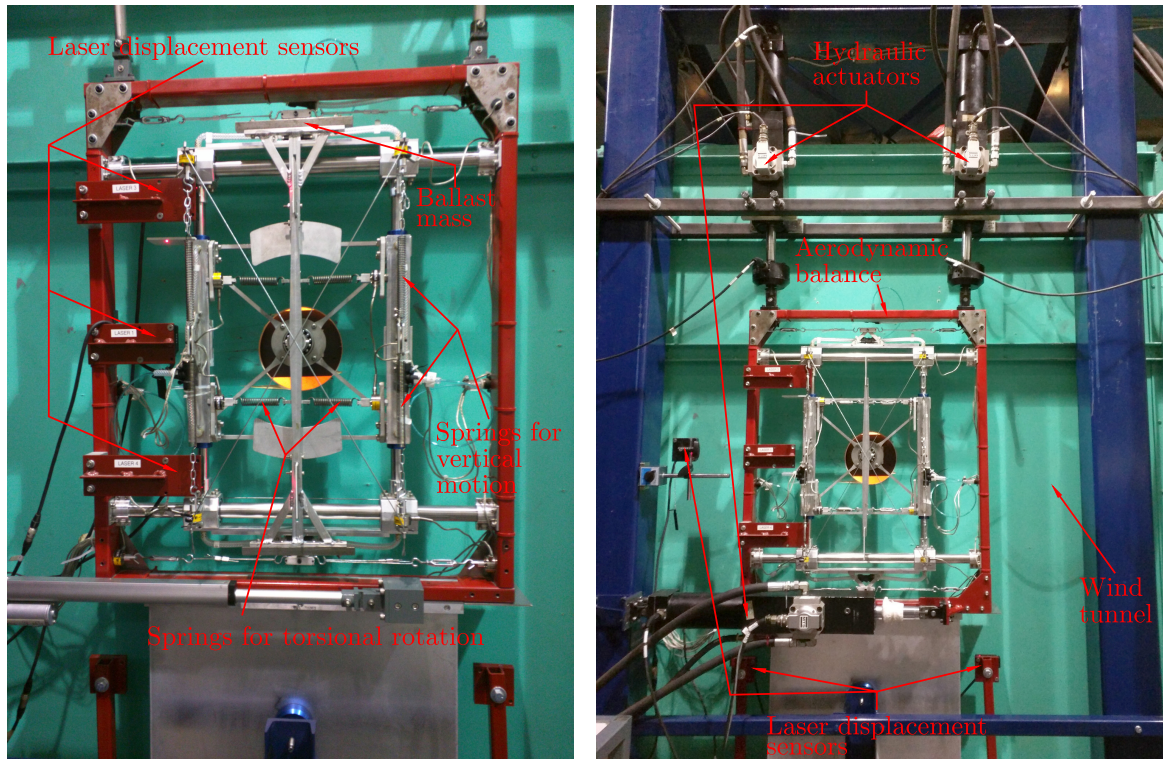
C.2.1 Wind Tunnel at the *Université de Sherbrooke*

For this validation of a new section model test rig, experimental results from two different wind tunnels are considered. The first one is the main wind tunnel at the *Université de Sherbrooke*, which is a closed-circuit wind tunnel with a maximum wind speed of 31 m/s. The 10 m-long test section is 1.83 m by 1.83 m. The mean wind speed was measured with two Pitot tubes located above and below the bridge section model. At the test location of section models, the longitudinal and vertical turbulence intensities are approximately 1.0 % under smooth flow conditions. For the turbulent flow conditions considered for some of the test runs, a grid positioned upstream was utilized. In this case, longitudinal and vertical turbulence intensities are respectively 7.1 % and 5.4 %.

In fig. C.1, the bridge section model test rig at the *Université de Sherbrooke* is presented. This rig is located outside the wind tunnel. As shown in fig. C.1, it can be used in two different configurations, which are a free-vibration test configuration and a force-vibration test configuration. The free-vibration configuration (fig. C.1a) can be used to measure the dynamic response of a sprung section model. Two degrees of freedom (DOF) are considered in this research, i.e., the vertical displacement and rotation. The free-vibration measurement of flutter derivatives is also possible in this configuration. In the forced-vibration configuration, the bridge model is attached to load cells through pretensioned cables, and dynamic hydraulic actuators are utilized to impose motion to the model (fig. C.1b). In this configuration, the test rig is typically used for a forced-vibration extraction of flutter derivatives. In both test configurations, laser displacement sensors are utilized to measure the displacements, whereas load cells are used for the forces. It is also worth noting that this test rig can also measure the static aerodynamic coefficients. More information about the experimental tests at the *Université de Sherbrooke* can be found in [206].

C.2.2 Boundary Layer Wind Tunnel Laboratory at the University of Western Ontario

Tests at the Boundary Layer Wind Tunnel Laboratory at the University of Western Ontario were conducted in the high-speed test section of the closed-circuit wind tunnel BLWT 2. For section model tests of bridges, the test rig units are installed inside two streamlined walls, one at each end of the bridge model (see fig. C.4b). Where the section model is mounted, a distance of 2.15 m between the walls is typically used, which is situated within



(a) Free-vibration tests

(b) Forced-vibration tests

Figure C.1: Section model test rig at the *Université de Sherbrooke*

the 3.35 m-wide test section. However, the width considered for the tests discussed herein was of 1.83 m since the bridge model considered is shorter than the models usually tested at the BLWTL. The overall height of the bridge test section is 1.77 m. The mean wind speed was measured with two Pitot tubes located above the bridge section model. The maximum wind speed achievable in the test section is 30 m/s. Smooth flow turbulence intensities are less than 0.5 %. For the turbulent tests, a longitudinal turbulence intensity of 4.8 % and a vertical turbulence intensity of 4.4 % were obtained using the grid shown in fig. C.4b.

The section model test rigs utilized at the BLWTL are shown in fig. C.2. Both are free-vibration test rigs equipped with torsion arms on which vertical springs are attached to provide vertical and torsional stiffness to the bridge model. Therefore, two DOFs, a vertical and a rotational, are possible with these rigs. For both test rigs, the displacements and rotations of the bridge model were measured using laser displacement sensors. In the case of the old bridge rig, the lateral movement of the model is restrained using leaf springs (see fig. C.2a). Also, the damping can be adjusted using pneumatic dampers in the old rig. For the new bridge rig (fig. C.2b), the lateral movement of the bridge model is made impossible by using air bushings able to move vertically along stainless-steel shafts but restrained in

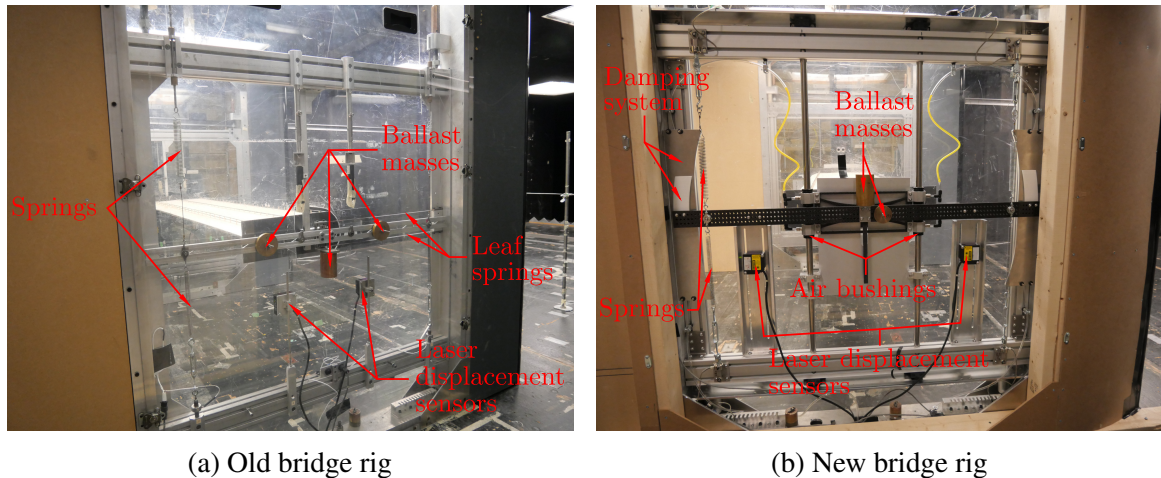


Figure C.2: Section model test rigs at the Boundary Layer Wind Tunnel Laboratory

the lateral direction. In the new bridge rig, a magnetic damping system is utilized to set the damping. Just like for the old rig, it is possible in the new bridge rig to adjust the horizontal position of the springs, but what differentiates the new bridge rig is that it is also possible to adjust the vertical position of the top and bottom attachment points of the springs. This is done by moving the top and bottom horizontal aluminum extrusions that are shown in fig. C.2b. This provides the flexibility to the new bridge rig that is required for a nonlinear device able to represent the nonlinear structural behavior in order to eventually conduct nonlinear section model tests for bridges.

C.3 Experimental Program

C.3.1 Bridge Section Model

The bridge section model utilized in the validation procedure of the new bridge rig is a box girder of a suspension bridge, which is referred herein as bridge SU2. The full-scale width of the bridge deck is 31 m. A geometric scale of $\lambda_L = 1/70$ is utilized, which gives a model width of 443 mm. As shown in fig. C.3, the section model consists of a carbon fiber frame that is clad with balsa wood sheets to form the bridge-deck cross section. Using this fabrication method allows the section model to be very light with a total mass of only 1.72 kg for a model that is 1806 mm long. Having a light model is particularly important for the extraction of flutter derivatives using forced-vibration tests as it reduces the model inertial forces that are measured by the load cells. This therefore facilitates the determination of the self-excited forces needed for the extraction of flutter derivatives. Additionally, the stiffness of the carbon fiber frame combined with the lightness of the model ensure that

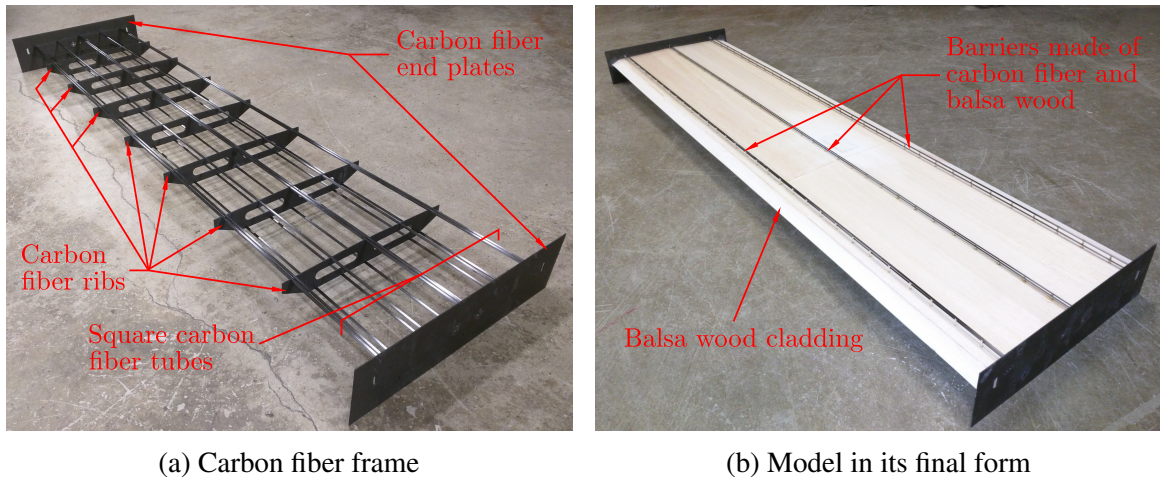


Figure C.3: Section model of bridge SU2 for $\lambda_L = 1/70$

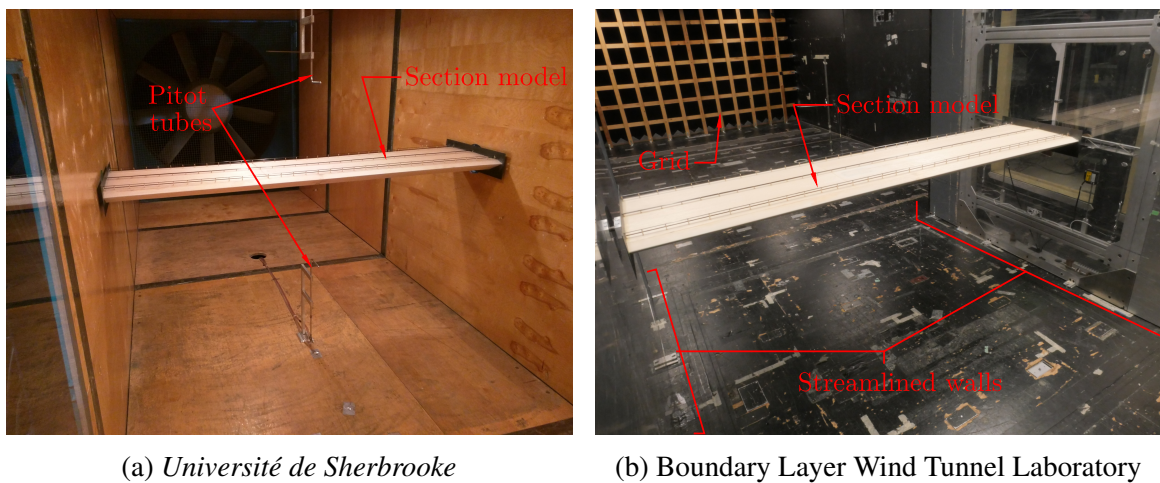


Figure C.4: Section model of bridge SU2 inside the wind tunnels

the model vibrations are minimal for free-vibration tests as well as for forced-vibration tests. Figure C.4a shows the bridge model when mounted on the section model test rig at the *Université de Sherbrooke*. The model when tested at the BLWTL is also presented in fig. C.4b.

C.3.2 Static Tests at the *Université de Sherbrooke*

In order to verify that the section model of bridge SU2 was not altered from its storage and its transportation between the two universities, it was first decided to compare the static coefficients measured at the *Université de Sherbrooke* and at the BLWTL. For the static tests at the *Université de Sherbrooke*, the static coefficients were measured for an angle of attack varying from -10° to 10° . Increments of 1° were used for angles of attack between

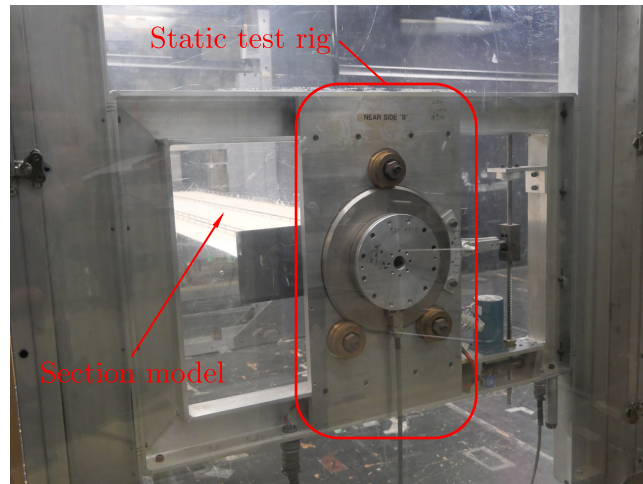


Figure C.5: Static test rig of the Boundary Layer Wind Tunnel Laboratory

-6° and 6° . Otherwise, increments of 2° were considered. Measurements were made for three different wind speeds in order to check for potential Reynolds number effects. This was done for a smooth flow and a turbulent flow.

C.3.3 Static Tests at the Boundary Layer Wind Tunnel Laboratory

For the static tests at the BLWTL, the angle of attack was varied between -10° and 10° with increments of 1° . Static coefficients were measured for two different mean wind speeds, which correspond to the two highest wind speeds considered in the static tests at the *Université de Sherbrooke*. At an angle of attack of 0° , the static coefficients were measured over the range of wind speeds achievable in BLWT 2. This was done to assess the Reynolds number dependence of the aerodynamic coefficients. All static tests at the BLWTL were conducted for a smooth flow as well as a turbulent flow using the static test rig presented in fig. C.5.

C.3.4 Free-Vibration Flutter Derivative Tests at the *Université de Sherbrooke*

The first step of the validation procedure for the new bridge rig is to compare the flutter derivatives measured using the different experimental rigs. At the *Université de Sherbrooke*, the flutter derivatives were first measured using the free-vibration procedure, which consists in measuring exponentially decaying displacement time histories of the sprung bridge model at different wind speeds. The full-scale dynamic properties of the sprung model used for these tests are shown in table C.1 (column UdeS). Flutter derivatives were measured for a

Table C.1: Full-scale test parameters for dynamic tests of bridge SU2 (\bar{m}_V^* : mass per unit length, \bar{m}_θ^* : mass moment of inertia per unit length, f_{VS1} : natural frequency of first symmetric vertical mode, ξ_{VS1} : damping ratio of first symmetric vertical mode, $f_{\theta S1}$: natural frequency of first symmetric torsional mode, $\xi_{\theta S1}$: damping ratio of first symmetric torsional mode, α_s : angle of attack)

Parameter	Target	UdeS		BLWTL–Old		BLWTL–New	
		Value	Error	Value	Error	Value	Error
\bar{m}_V^* (10^3 kg/m)	23.01	23.87	3.7 %	23.54	2.3 %	23.91	3.9 %
\bar{m}_θ^* (10^6 kg · m ² /m)	2.505	2.380	–5.0 %	2.482	–0.9 %	2.646	5.6 %
f_{VS1} (Hz)	0.097	0.101	4.1 %	0.097	0.0 %	0.098	1.0 %
ξ_{VS1} (%)	0.30	0.93	210 %	0.31	3.3 %	0.40	33.3 %
$f_{\theta S1}$ (Hz)	0.279	0.279	0.0 %	0.281	0.7 %	0.278	–0.4 %
$\xi_{\theta S1}$ (%)	0.30	0.91	203 %	0.37	23.3 %	0.28	–6.7 %
α_s (°)	0.0	0.0	-	0.0	-	0.0	-

smooth flow and a turbulent flow.

C.3.5 Forced-Vibration Flutter Derivative Tests at the *Université de Sherbrooke*

At the *Université de Sherbrooke*, the flutter derivatives were also measured using the forced-vibration procedure. For these tests, uncoupled harmonic motions were imposed to the bridge model, i.e., for one DOF at a time (vertical or torsional). By doing so for different wind speeds, it is possible to measure the corresponding self-excited forces, from which the flutter derivatives are calculated. The vertical amplitude and frequency for the vertical tests were 11 mm and 1.80 Hz. A torsional amplitude of 2.0° and a torsional frequency of 3.25 Hz were considered for the torsional tests. Smooth and turbulent flows were used for these tests.

C.3.6 Free-Vibration Flutter Derivative Tests at the Boundary Layer Wind Tunnel Laboratory

For the free-vibration tests at the BLWTL, the flutter derivatives were only measured for a smooth flow since turbulence did not have a significant effect on the flutter derivatives for the tests made at the *Université de Sherbrooke*. At the BLWTL, flutter derivatives tests were conducted for the old bridge rig and the new bridge rig. The full-scale dynamic properties of the sprung model considered in these tests for the old rig (column BLWTL–Old) and the new rig (column BLWTL–New) are presented in table C.1.

C.3.7 Dynamic Tests at the *Université de Sherbrooke*

As a second validation of the new bridge rig, a comparison is made for the dynamic responses of the sprung model of bridge SU2 measured using the different experimental rigs. Dynamic section model tests were performed considering the first symmetric vertical mode and first symmetric torsional mode, which are the critical modes with respect to flutter for bridge SU2. For the tests at the *Université de Sherbrooke*, the full-scale dynamic properties of the sprung model are presented in table C.1 (column UdeS). As it can be seen in this table, with the exception of the damping ratios, these dynamic parameters are close to the target values also shown in table C.1. For the UdeS damping ratios, it was required to use higher damping ratios due to limitations of the section model test rig. For these dynamic tests, time histories of the displacements of the sprung model were recorded for different mean wind speeds until the onset of flutter was reached. These tests were performed considering smooth and turbulent flows.

C.3.8 Dynamic Tests at the Boundary Layer Wind Tunnel Laboratory

Similar dynamic tests were conducted at the BLWTL using the old bridge rig and the new bridge rig. The full-scale dynamic properties for these tests are presented in table C.1. In this table, it can be seen that these test parameters are close to the full-scale target values. Dynamic tests at the BLWTL were also conducted for smooth and turbulent flows.

C.4 Results and Discussion

C.4.1 Results for Static Tests

First, the experimental results for the static coefficients for bridge SU2 are analyzed. Herein, the following formulation is utilized for the mean aerodynamic forces and static coefficients:

$$D_s = \frac{1}{2}\rho U^2 B C_D(\alpha_s) \quad L_s = \frac{1}{2}\rho U^2 B C_L(\alpha_s) \quad M_s = \frac{1}{2}\rho U^2 B^2 C_M(\alpha_s) \quad (\text{C.1})$$

where D_s , L_s and M_s are the mean aerodynamic drag force, mean aerodynamic lift force and mean aerodynamic moment per unit length; ρ is the density of air; U is the mean wind speed; B is the bridge-deck width; C_D , C_L and C_M are respectively the drag coefficient, lift coefficient and moment coefficient; α_s is the angle of attack. The sign convention for the

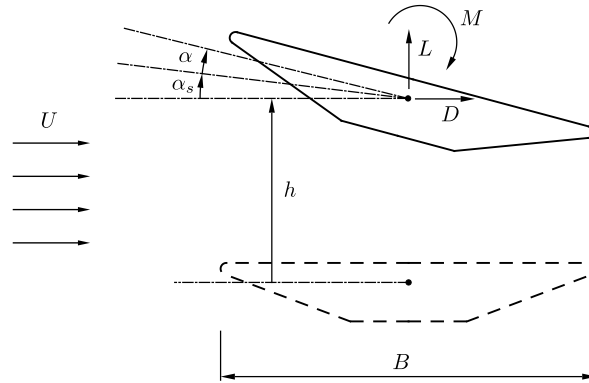


Figure C.6: Sign convention for displacements and forces

aerodynamic forces is shown in fig. C.6.

Figure C.7 presents a comparison of the static coefficients measured at the *Université de Sherbrooke* (UdeS) and the BLWTL for bridge SU2. Figures C.7a and C.7b show respectively the static coefficients for a smooth flow and a turbulent flow. Since it was found that the static coefficients are marginally impacted by the Reynolds number, results are only shown for a Reynolds number Re of approximately 3.4×10^5 (based on the bridge-deck width). As it can be seen in fig. C.7, there is a good agreement between the static coefficients measured from the two different wind tunnels, even though there are more noticeable discrepancies at large angles of attack. Nonetheless, it is possible to say that the section model of bridge SU2 was not altered from its storage and its transportation between the two universities.

C.4.2 Results for Flutter Derivative Tests

It is now of interest to examine the flutter derivatives measured using the different experimental rigs for bridge SU2. For the free-vibration tests, the flutter derivatives were calculated using the Modified Unifying Least-Squares (MULS) method [27]. In the case of the forced-vibration tests, a linear least-squares approach was utilized to obtain the flutter derivatives from the experimental results. In this appendix, the self-excited forces and flutter derivatives are defined as follows:

$$L_{se}(t) = \frac{1}{2}\rho U^2 B \left(KH_1^* \frac{\dot{h}}{U} + KH_2^* \frac{B\dot{\alpha}}{U} + K^2 H_3^* \alpha + K^2 H_4^* \frac{h}{B} \right) \quad (C.2)$$

$$M_{se}(t) = \frac{1}{2}\rho U^2 B^2 \left(KA_1^* \frac{\dot{h}}{U} + KA_2^* \frac{B\dot{\alpha}}{U} + K^2 A_3^* \alpha + K^2 A_4^* \frac{h}{B} \right) \quad (C.3)$$

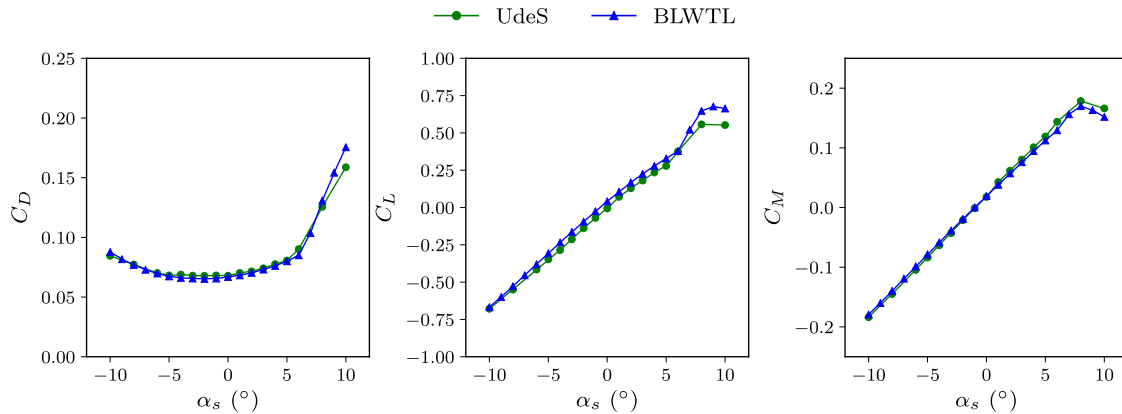
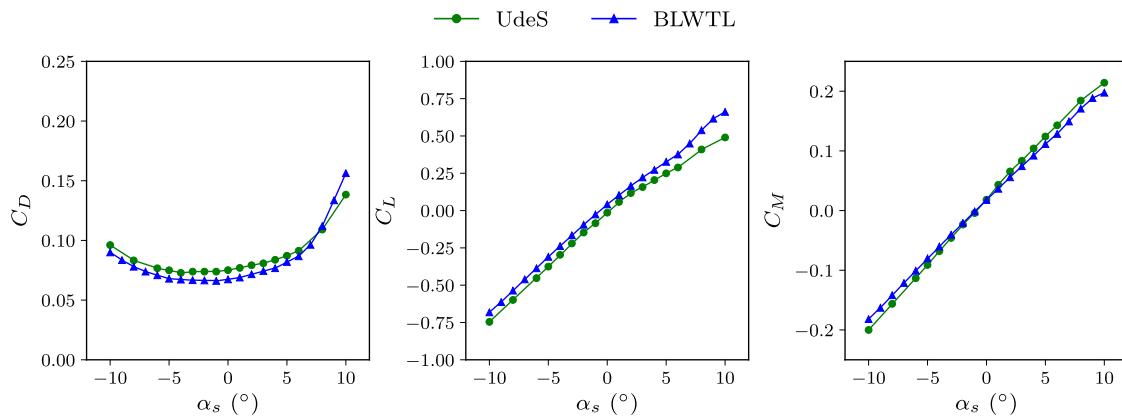
(a) Smooth flow and $Re = 3.4 \times 10^5$ (b) Turbulent flow and $Re = 3.3 \times 10^5$

Figure C.7: Static aerodynamic coefficients of bridge SU2

where $L_{se}(t)$ and $M_{se}(t)$ are the self-excited lift force and self-excited moment per unit length; t is the time; $h = h(t)$ and $\alpha = \alpha(t)$ are respectively the dynamic vertical displacement and dynamic rotation; $K = \omega B/U$ is the reduced frequency; $\omega = 2\pi f$ is the angular frequency of oscillation; H_i^* and A_i^* ($i = 1, \dots, 4$) are the flutter derivatives, which are functions of the reduced velocity $U_R = U/(fB)$; f is the frequency of oscillation; the overdot denotes the time derivative. The sign convention for the forces and displacements is shown in fig. C.6.

The flutter derivatives of bridge SU2 relative to the vertical motion are presented in fig. C.8, whereas those with respect to a rotational motion are shown in fig. C.9. These results are for a smooth flow. In these figures, a comparison is made for the free- and forced-vibration results measured at the *Université de Sherbrooke* (UdeS-Free and UdeS-Forced) as well as the results measured at the BLWTL using the old bridge rig (BLWTL-Old) and the new bridge rig (BLWTL-New). As observed in figs. C.8 and C.9, there is a good agreement

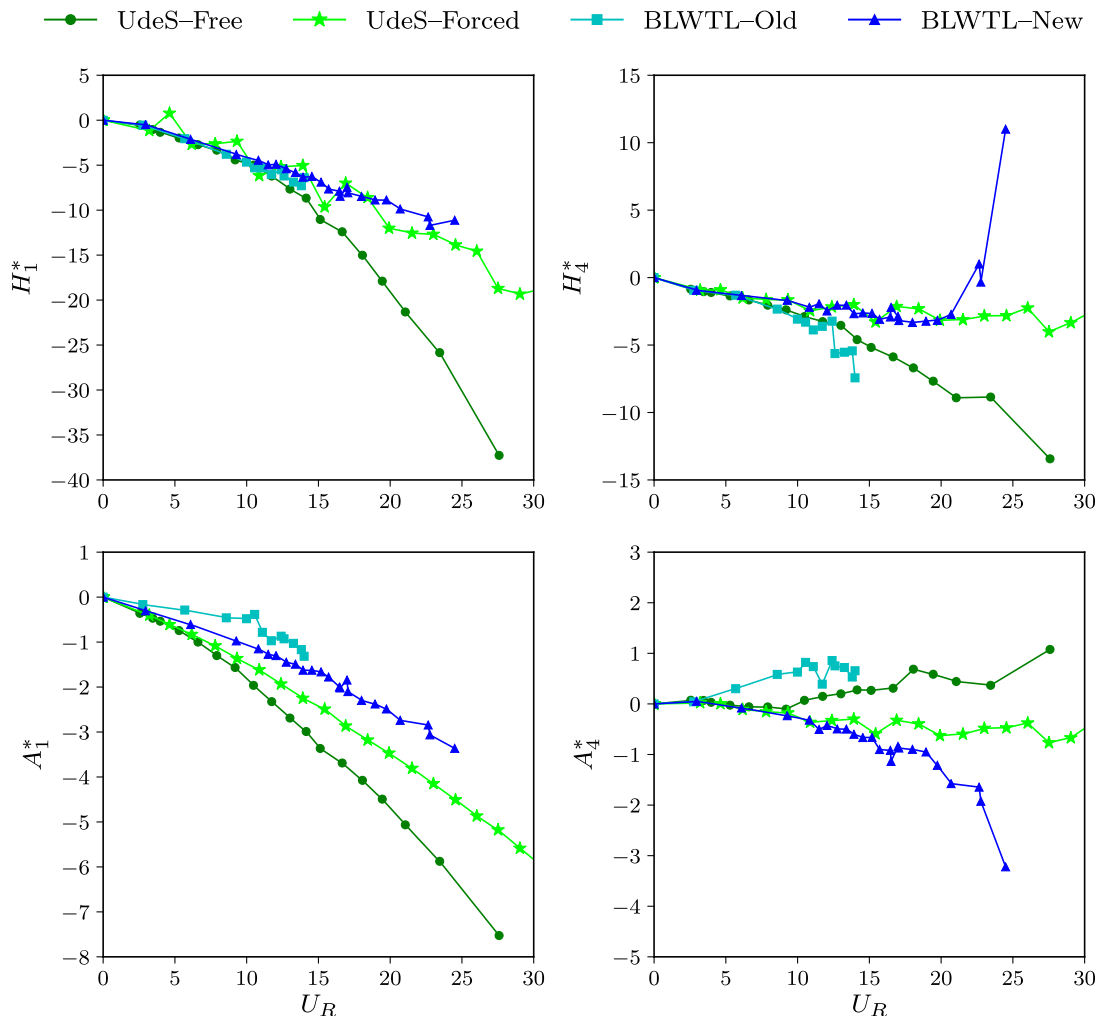


Figure C.8: Flutter derivatives of bridge SU2 for vertical motion (smooth flow)

between the different sets of flutter derivatives. This is especially the case for the flutter derivatives relative to the rotational motion. However, there are greater discrepancies for the derivatives with respect to the vertical motion. A possible explanation for this is that the aerodynamic damping is high for the vertical motion, therefore making difficult a reliable extraction of the derivatives using the free-vibration procedure. This could also be partially caused by different initial conditions considered in the free-vibration tests. Additionally, in some instances like for H_2^* in fig. C.9, the flutter derivatives measured from forced-vibration tests are different than those from free-vibration tests. This could be explained by the static rotation of the bridge model in the free-vibration tests (e.g. see fig. C.10a). Conversely, the mean angle of attack is imposed in forced-vibration tests to 0° . Nevertheless, it is possible to conclude that the new bridge rig is reliable for the measurement of flutter derivatives.

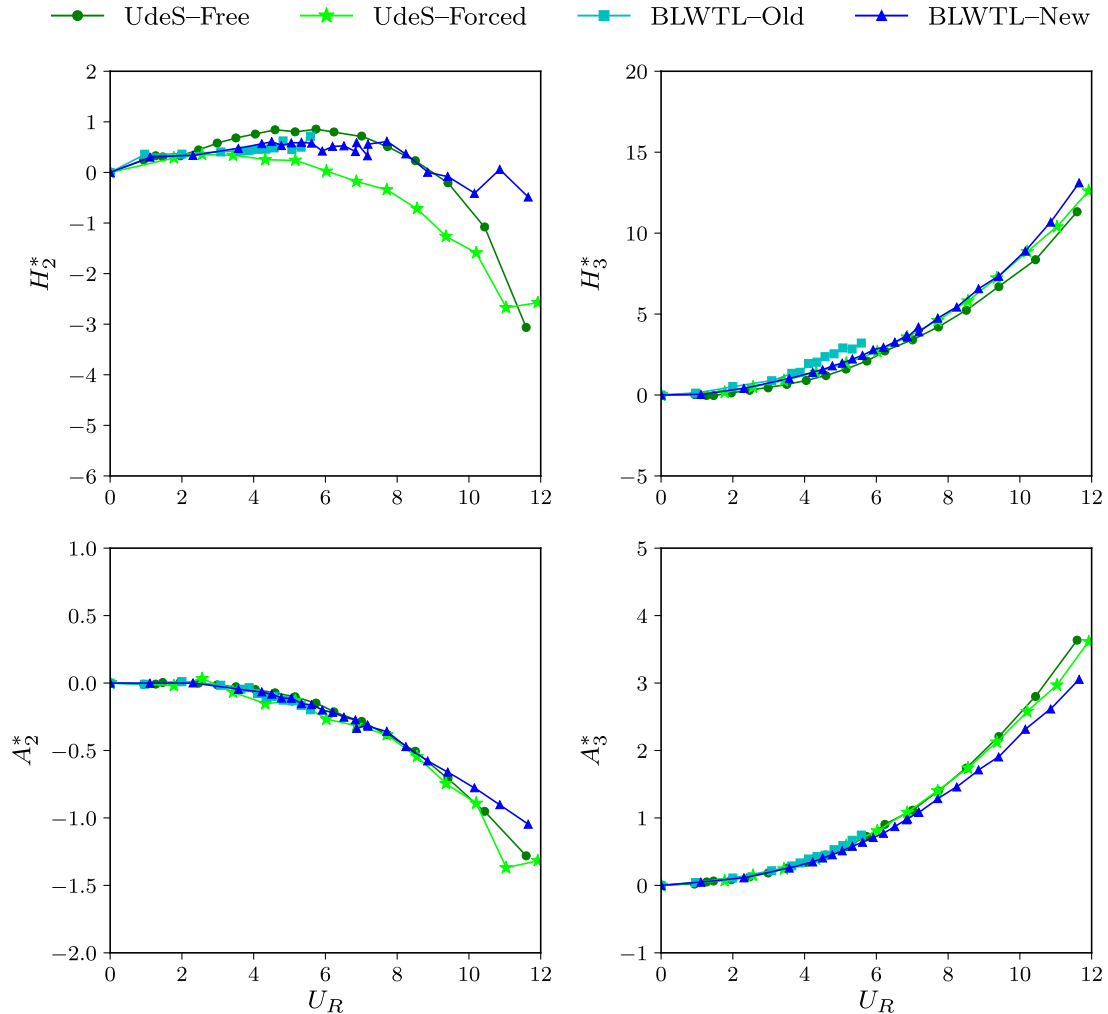


Figure C.9: Flutter derivatives of bridge SU2 for rotational motion (smooth flow)

C.4.3 Results for Dynamic tests

As mentioned previously, the second validation procedure of the new bridge rig consisted in comparing the dynamic response of the sprung model of bridge SU2 for the different free-vibration test rigs. Such comparisons are presented in figs. C.10 and C.11 for a smooth flow and a turbulent flow respectively. These figures include results measured at the *Université de Sherbrooke* (UdeS) and at the BLWTL for the old bridge rig (BLWTL-Old) and the new bridge rig (BLWTL-New). Figures C.10a and C.11a present the mean displacements, whereas the peak displacements are shown in figs. C.10b and C.11b.

In figs. C.10 and C.11, it can be observed that the dynamic responses for the old and new rigs of the BLWTL agree very well. For the bridge rig of the *Université de Sherbrooke*,

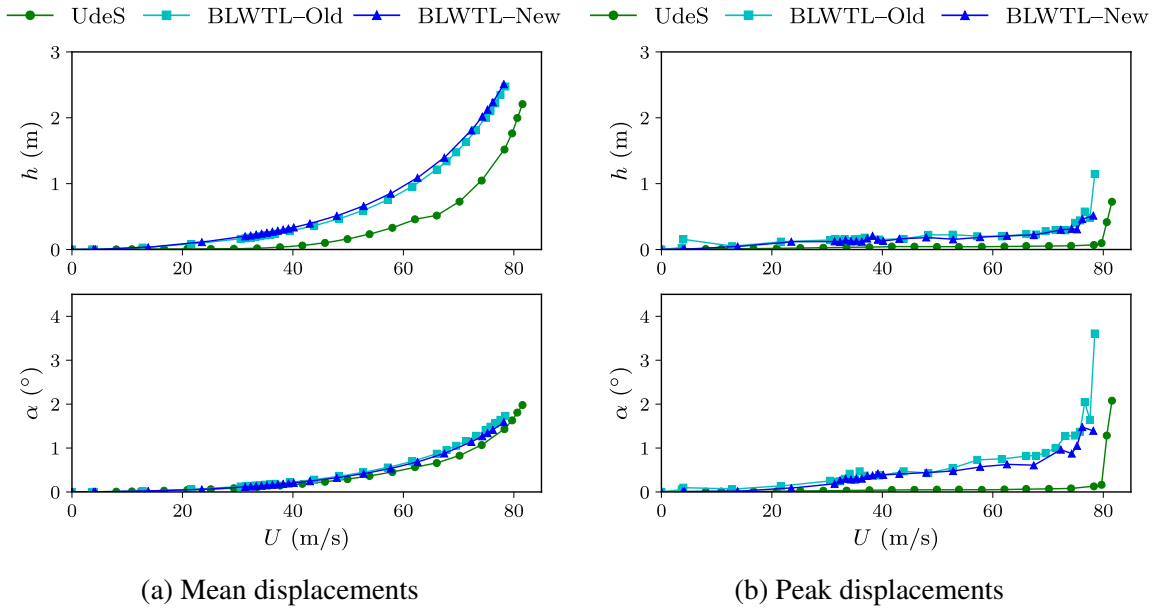


Figure C.10: Dynamic response of bridge SU2 for modes VS1 and TS1 and a smooth flow (full scale)

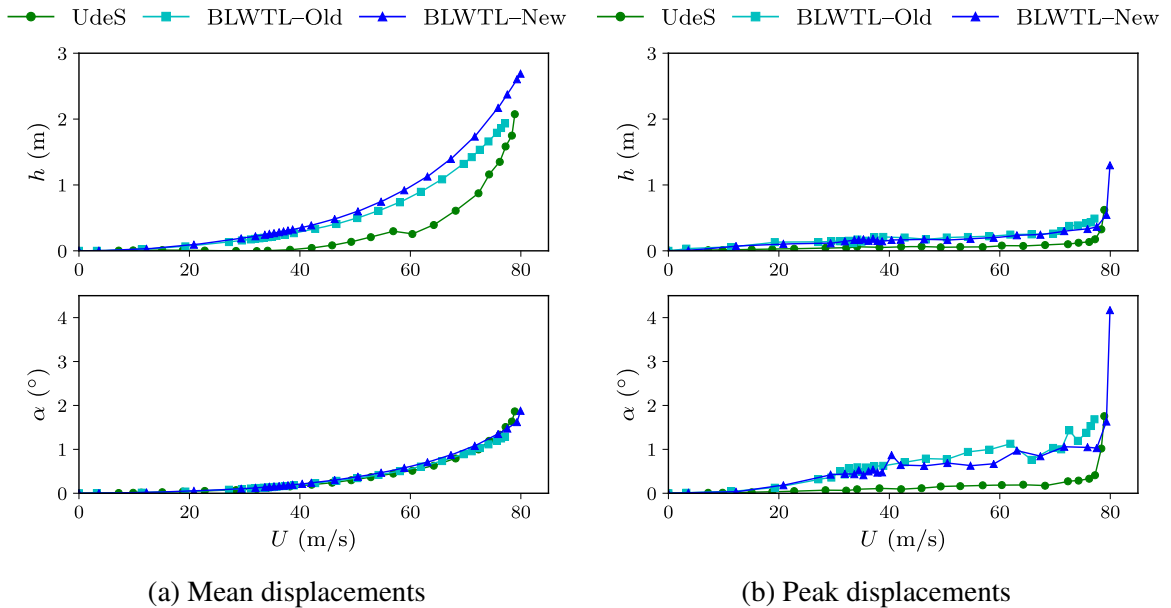


Figure C.11: Dynamic response of bridge SU2 for modes VS1 and TS1 and a turbulent flow (full scale)

figs. C.10b and C.11b show that the peak displacements are less than those for the BLWTL test rigs. This is attributed to the greater damping utilized for the tests at the *Université de Sherbrooke* (see table C.1). However, the larger damping for the UdeS dynamic response has a marginal effect on the onset of flutter since flutter occurs at relatively the same wind speed for the three experimental rigs. It is also worth noting that it was not always possible to measure the displacements when flutter occurred as the displacements would rapidly become very large, and the wind tunnel had to be stopped. This was the case for the results of the new BLWTL rig for a smooth flow and the old BLWTL rig for a turbulent flow. Regarding the mean displacements, the old and new BLWTL rigs have very similar results. However, in the case of the mean vertical displacement, there are discrepancies between the UdeS results and the results for the two other bridge rigs. Further investigation would be required in order to find an explanation for this behavior. This would likely require conducting additional wind tunnel tests at the *Université de Sherbrooke*. This was out of the scope of this research project since it is still possible to validate the new BLWTL rig by using the results measured for the old bridge rig of the BLWTL.

From this validation procedure based on standard linear section model tests, it is possible to conclude that the new BLWTL bridge rig is valid since it has demonstrated its reliability for the measurement of flutter derivatives and dynamic responses. The next step in this research project will be to replace the linear structural behavior by a nonlinear stiffness behavior in order to conduct nonlinear section model tests using the new bridge rig of the BLWTL. Such an experimental approach will allow an experimental investigation of the effect of structural nonlinearities on the aerodynamic and aeroelastic behavior of bridges.

C.5 Conclusions

Wind tunnel section model tests for cable-supported bridges are extensively used in industry and research. However, they rely on some assumptions. For example, they assume a linear structural behavior for the stiffness of the bridge. Considering theoretical demonstrations made regarding nonlinear structural dynamic phenomena in suspension bridges, it seems relevant to extend the capabilities of the section model test procedure for bridges by making such tests able to account for a nonlinear structural behavior. To achieve this, it was needed to design and fabricate a new section model test rig able to accommodate a nonlinear device representative of the nonlinear behavior of a bridge. Before using this new bridge rig for nonlinear section model tests, it was required to validate its usage by conducting linear section model tests. The results for this new bridge rig at the Boundary Layer Wind Tunnel

Laboratory of the University of Western Ontario were compared to results measured at the *Université de Sherbrooke* and results from the old bridge rig of the Boundary Layer Wind Tunnel Laboratory. This was done considering the same bridge section model. For the flutter derivatives and dynamic responses, a good agreement was obtained between the results of the different bridge rigs, therefore validating the reliability of the new bridge rig. This new bridge rig will be utilized in the near future to conduct nonlinear section model tests in order to provide an experimental assessment of the effect of structural nonlinearities on the aerodynamic and aeroelastic behavior of cable-supported bridges.

Curriculum Vitae

Name: Sébastien Maheux

**Post-Secondary
Education and
Degrees:** Université de Sherbrooke
Sherbrooke, Québec, Canada
2010–2014 B.Eng.

Université de Sherbrooke
Sherbrooke, Québec, Canada
2014–2016 M.A.Sc.

The University of Western Ontario
London, Ontario, Canada
2017–2022 Ph.D.

**Honours and
Awards:** Natural Sciences and Engineering Research Council (NSERC)
Alexander Graham Bell Canada Graduate Scholarship (Master's)
2014–2015

Fonds de recherche du Québec - Nature et technologies (FRQNT)
Master's Research Scholarship
2015–2016

Fonds de recherche du Québec - Nature et technologies (FRQNT)
Ministère des Transports Scholarship (Doctorate)
2017–2020

Natural Sciences and Engineering Research Council (NSERC)
Alexander Graham Bell Canada Graduate Scholarship (Doctorate)
2018–2021

+ 10 undergraduate awards

+ 10 graduate awards

Related Work Teaching Assistant
Experience: Université de Sherbrooke
 2015–2017

Teaching Assistant
 The University of Western Ontario
 2017–2021

Publications:

B. Kaabia, S. Langlois, S. Maheux, and F. Légeron, “Time-domain analysis of solar concentrator structure under gust wind,” in *Proceedings of the 13th Americas Conference on Wind Engineering*, (Gainesville, Florida, USA), 2017.

S. Maheux, S. Langlois, and F. Légeron, “Study on extraction parameters of flutter derivatives for the development of a time-domain formulation of self-excited forces,” in *Proceedings of the 7th European & African Conference on Wind Engineering*, (Liège, Belgium), 2017.

B. Kaabia, S. Langlois, and S. Maheux, “Effect of structure configurations and wind characteristics on the design of solar concentrator support structure under dynamic wind action,” *Wind and Structures, An International Journal*, vol. 27, no. 1, pp. 41–57, 2018.

S. Maheux, S. Langlois, and F. Légeron, “Flutter analysis using quasi-steady time-domain flutter derivatives,” in *IABSE Reports*, vol. 114, (New York City, USA), pp. 2665–2671, 2019.

S. Maheux, J. P. C. King, A. El Damatty, and F. Brancaloni, “Assessment of nonlinear structural vertical-torsional coupling in cable-supported bridges,” *Engineering Structures*, vol. 219, p. 110800, 2020.

M. AbuGazia, M. El-Sefy, M. El-Kateb, S. Maheux, T. El-Afandy, and A. Abdelrahman, “Flexural behavior of RC continuous slabs strengthened by external prestressing systems,” in *Proceedings of the Canadian Society of Civil Engineering Annual Conference 2021*, p. STR095, Springer, 2021.